Dissertation

Results on Neutrinoless Double Beta Decay Search in GERDA: Background Modeling and Limit Setting

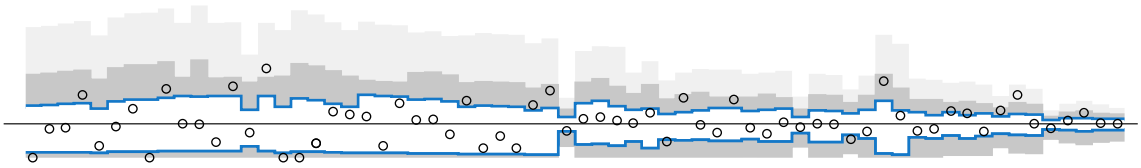

von

Neslihan Becerici Schmidt

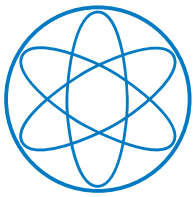

München

2014

Fakultät für Physik der Technischen Universität München

Max-Planck-Institut für Physik
(Werner-Heisenberg-Institut)

Results on Neutrinoless Double Beta Decay Search in GERDA: Background Modeling and Limit Setting

Neslihan Becerici Schmidt

Vollständiger Abdruck der von der Fakultät für Physik der Technischen Universität München zur Erlangung des akademischen Grades eines

Doktors der Naturwissenschaften (Dr. rer. nat.)

genehmigten Dissertation.

Vorsitzender:	Univ.-Prof. Dr. Björn Garbrecht
Prüfer der Dissertation:	
1.	Priv.-Doz. Dr. Béla Majorovits
2.	Univ.-Prof. Dr. Stefan Schönert
3.	Hon.-Prof. Allen C. Caldwell, Ph.D.

Die Dissertation wurde am 30.06.2014 bei der Technischen Universität München eingereicht und durch die Fakultät für Physik am 22.07.2014 angenommen.

For my dear son Theo

Her zaman sorular sorman ve
"Kral çıplak!" diyebilmen dileğiyle.

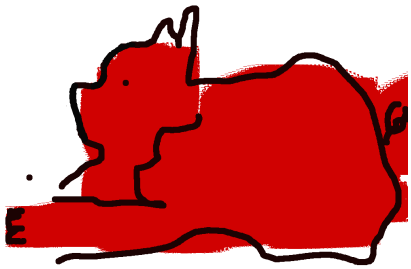

Abstract

The search for the neutrinoless double beta decay ($0\nu\beta\beta$) process is primarily motivated by its potential of revealing the possible Majorana nature of the neutrino, in which the neutrino is identical to its antiparticle. It has also the potential to yield information on the intrinsic properties of neutrinos, if the underlying mechanism is the exchange of a light Majorana neutrino. The GERDA experiment is searching for $0\nu\beta\beta$ decay of ^{76}Ge by operating high purity germanium (HPGe) detectors enriched in the isotope ^{76}Ge ($\sim 87\%$), directly in ultra-pure liquid argon (LAr). The first phase of physics data taking (Phase I) was completed in 2013 and has yielded 21.6 kg·yr of data. A background index of $B \approx 10^{-2}$ cts/(keV·kg·yr) at $Q_{\beta\beta} = 2039$ keV has been achieved. A comprehensive background model of the Phase I energy spectrum is presented as the major topic of this dissertation. Decomposition of the background energy spectrum into the individual contributions from different processes provides many interesting physics results. The specific activity of ^{39}Ar has been determined. The obtained result, $A = (1.15 \pm 0.11)$ Bq/kg, is in good agreement with the values reported in literature. The contribution from ^{42}K decays in LAr to the background spectrum has yielded a ^{42}K (^{42}Ar) specific activity of $A = \left(106.2\,^{+12.7}_{-19.2}\right)$ μBq/kg, for which only upper limits exist in literature. The analysis of high energy events induced by α decays in the ^{226}Ra chain indicated a total ^{226}Ra activity of (3.0 ± 0.9) μBq and a total initial ^{210}Po activity of (0.18 ± 0.01) mBq on the p^+ surfaces of the enriched semi-coaxial HPGe detectors. The half life of the two-neutrino double beta ($2\nu\beta\beta$) decay of ^{76}Ge has been determined as $T^{2\nu}_{1/2} = (1.926 \pm 0.094) \cdot 10^{21}$ yr, which is in good agreement with the result that was obtained with lower exposure and has been published by the GERDA collaboration. According to the model, the background in $Q_{\beta\beta} \pm 5$ keV window is resulting from close-by decays of ^{214}Bi, ^{228}Th, ^{60}Co, ^{42}K and the α-emitting isotopes, i.e ^{210}Po and the isotopes in the ^{226}Ra sub-chain. Given the background expectation from the background model, no indication for a $0\nu\beta\beta$ decay signal has been found. A Bayesian analysis of data from GERDA alone has yielded $T^{0\nu}_{1/2} > 1.85 \cdot 10^{25}$ yr at 90% C.I., and GERDA data in combination with data from the past HPGe $0\nu\beta\beta$ experiments resulted in $T^{0\nu}_{1/2} > 2.86 \cdot 10^{25}$ yr at 90% C.I. The longstanding claim for observation of a ^{76}Ge $0\nu\beta\beta$ decay signal reported by a subgroup of the HdM collaboration has been disfavored with a Bayes factor of 0.02.

Zusammenfassung

Die Suche nach dem neutrinolosen Doppelbetazerfall ($0\nu\beta\beta$) ist in erster Linie motiviert durch den potenziellen Nachweis des Majorana-Charakter von Neutrinos. Dabei werden Neutrinos mit ihrem eigenen Antiteilchen identisch. Darüber hinaus kann der $0\nu\beta\beta$–Zerfall Informationen über die intrinsischen Eigenschaften von Neutrinos liefern, sofern der zugrunde liegende Mechanismus im Austausch eines leichten Majorana-Neutrinos besteht. Beim GERDA Experiment wird nach dem $0\nu\beta\beta$–Zerfall von ^{76}Ge gesucht, wobei hochreine Germanium (HPGe)-Detektoren, die mit dem Isotop ^{76}Ge ($\sim 87\%$) angereichert sind, direkt in hochreinem Flüssigargon (LAr) betrieben werden. In der 2013 abgeschlossenen ersten Phase der physikalischen Datenerhebung (Phase I) wurden 21.6 kg·yr an Daten aufgenommen. Es wurde ein Untergrundindex von $B \approx 10^{-2}$ cts/(keV·kg·yr) bei $Q_{\beta\beta} = 2039$ keV erreicht. In dieser Dissertation wird ein umfassendes Untergrundmodell des Phase-I-Energiespektrums präsentiert. Die Zerlegung des Untergrund-Energiespektrums in die einzelnen Beiträge der verschiedenen Prozesse liefert interessante physikalische Ergebnisse. Die spezifische Aktivität von ^{39}Ar wurde ermittelt. Das Ergebnis, $A = (1.15 \pm 0.11)$ Bq/kg, deckt sich gut mit den in der Literatur zu findenden Werten. Der Beitrag des ^{42}K-Zerfalls im Flüssigargon zum Untergrundspektrum ergab eine ^{42}K (^{42}Ar) – spezifische Aktivität von $A = \left(106.2\,^{+12.7}_{-19.2}\right)$ μBq/kg, für die in der Literatur nur Obergrenzen zu finden sind. Die Analyse hochenergetischer Ereignisse hervorgerufen durch α Zerfälle in der ^{226}Ra Kette zeigte eine Aktivität von (3.0 ± 0.9) μBq und eine ^{210}Po Anfangsaktivität von (0.18 ± 0.01) mBq auf den p^+ Oberflächen der angereicherten semicoaxial HPGe Detektoren. Die Halbwertszeit des zwei-Neutrino Doppelbetazerfalls ($2\nu\beta\beta$) von ^{76}Ge wurde mit $T^{2\nu}_{1/2} = (1.926 \pm 0.094) \cdot 10^{21}$ yr bestimmt, was gut mit früheren von der GERDA Kollaboration veröffentlichten Ergebnissen mit geringerer Datenmenge übereinstimmt. Entsprechend dem Modell ist der Untergrund im $Q_{\beta\beta} \pm 5$ keV Energiefenster zusammengesetz aus Ereignissen resultierend aus Zerfällen von ^{214}Bi, ^{228}Th, ^{60}Co, ^{42}K und den α-strahlenden Isotopen, d.h. ^{210}Po und den Isotopen der ^{226}Ra Subkette. Ausgehend von den Vorhersagen des Untergrundmodells wurde kein Hinweis für ein $0\nu\beta\beta$ Zerfallssignal gefunden. Eine Bayessche Analyse der GERDA Daten allein ergab $T^{0\nu}_{1/2} > 1.85 \cdot 10^{25}$ yr im 90% C.I., und GERDA Daten zusammen mit Daten von vorangegangenen HPGe $0\nu\beta\beta$ Experimenten ergaben $T^{0\nu}_{1/2} > 2.86 \cdot 10^{25}$ yr im 90% C.I. Die seit langem bestehende Behauptung, ein ^{76}Ge $0\nu\beta\beta$ Zerfallssignal beobachtet zu haben, wie von einer Untergruppe der HdM Kollaboration gemeldet wurde, wurde mit einem Bayes-Faktor von 0.02 verworfen.

Table of Contents

List of abbreviations

BAT	Bayesian Analysis Toolkit
C.I.	Credible Interval
C.L.	Confidence Level
FWHM	Full Width at Half Maximum
GERDA	Germanium Detector Array
HPGe [detector]	High Purity Germanium [detector]
IH	Inverted neutrino mass Hierarchy
LAr	Liquid Argon
NH	Normal neutrino mass Hierarchy
NME	Nuclear Matrix Elements
PSD	Pulse Shape Discrimination
ROI	Region Of Interest
SM	Standard Model of particle physics

$\beta\beta$ [decay]	Double beta [decay]
$2\nu\beta\beta$ [decay]	Two-neutrino double beta [decay]
$0\nu\beta\beta$ [decay]	Neutrinoless double beta [decay]
$Q_{\beta\beta}$	Q-value of double beta decay
$\langle m_{\beta\beta} \rangle$	Effective Majorana neutrino mass
$G_{0\nu}$	Phase space factor
$M_{0\nu}$	Nuclear matrix element

Introduction

In 1928, Dirac formulated the relativistic quantum mechanical wave equation [1] that describes the behavior of fermions and, as a consequence of the unphysical negative energy solutions, implies the existence of antiparticles, which were discovered after this epochal work. Nine years later, Majorana found a different representation that "somewhat modified the meaning of Dirac equations" [2]. Unlike Dirac's equation, the formulation of Majorana allows a fermion to be its own antiparticle. Majorana suggested the electrically neutral neutrino as a natural candidate. Like all other fermions, neutrinos are considered as Dirac type particles in the Standard Model of particle physics (SM), and were assumed to have zero rest mass until the experiments studying neutrinos from different sources have demonstrated their nonzero mass through the observation of neutrino flavor oscillations [3]. We know now that the observed neutrino flavor eigenstates in weak interactions are combinations of three neutrino mass eigenstates, at least two of which have nonzero mass. Oscillation experiments cannot measure absolute mass values, but only the differences between the squared masses. Nevertheless, the results imply that the heaviest mass eigenstate cannot be lighter than 0.05 eV. On the other hand, the sum of neutrino masses is constrained by cosmology in a model dependent way, with the current best upper limit of 0.23 eV [4]. In light of these empirical facts, it is now accepted knowledge that neutrinos have nonzero but surprisingly small mass, i.e. at least 6 orders of magnitude smaller compared to that of the electron. An extension of the SM is necessary for accommodating the neutrino masses. This can be done through the seesaw mechanism [5, 6], which comes naturally with Majorana type neutrinos, and can also explain the smallness of the neutrino masses. Majorana neutrinos can provide an explanation to yet another intriguing phenomenon. The Universe is known to be composed of matter that forms the galaxies, planets and us, although an equal number of matter and antimatter particles should have been created in the very early Universe. Some mechanism must have caused an initial imbalance between the two that led more matter particles to be created, preventing all matter from annihilating with antimatter. If neutrinos are Majorana particles, the theory of leptogenesis [7, 8] might explain this asymmetry. So far, a Majorana fermion has not been found [1], but the unceasing search for it is motivated by its profound implications for particle physics, cosmology and other fields like solid state physics [10].

A discovery of neutrinoless double beta ($0\nu\beta\beta$) decay would truly establish that Majorana fermions exist and that the neutrino is one of them, regardless of the underlying

[1] Neither Ettore Majorana himself has ever been found again, after disappearing in 1938 without leaving a trace [9].

mechanism(s) mediating the process [11]. Another direct consequence of $0\nu\beta\beta$ decay is the violation of the lepton number by two units, which is a conserved quantity in all observed SM particle physics processes. One can also learn about neutrino masses through the observation of $0\nu\beta\beta$ decay. The neutrino oscillation measurements, being insensitive to the absolute mass scale, allow for two different orderings of the neutrino mass states, known as the *neutrino mass hierarchy problem*. A measurement of the $0\nu\beta\beta$ decay rate, which is proportional to the squared effective Majorana neutrino mass, can yield information on the mass spectrum, in the case that the $0\nu\beta\beta$ process is mediated by a light Majorana neutrino exchange.

There are numerous experiments searching for $0\nu\beta\beta$ decay using different candidate isotopes and different detection techniques [10, 12–16]. So far, only upper limits on the half life of the decay have been provided, with the exception of a positive claim for observation [17] that has recently been refuted by the GERDA experiment [18]. The most stringent half life limits are of the order of 10^{25} years, which correspond to upper limits on the effective Majorana neutrino mass in the 0.1 eV range [14]. A significant improvement of the sensitivity to longer half lives requires increased exposures, lower background levels combined with optimal detection techniques which provide high energy resolution, maximal detection efficiency and allowing for scalability of the experiment.

The GERDA experiment [19] is searching for $0\nu\beta\beta$ decay of the candidate isotope ^{76}Ge, by operating high purity germanium (HPGe) detectors directly in ultra-pure liquid argon (LAr). The detector material is enriched in the isotope ^{76}Ge ($\sim 87\%$). The HPGe detectors with excellent energy resolution also serve as the source, maximizing the detection efficiency of a $0\nu\beta\beta$ signal. GERDA is located at the underground laboratory LNGS in Italy and pursued its first phase of physics data taking (Phase I) between 2011 and 2013, after being commissioned for about a year. Phase I has demonstrated that, HPGe detectors can be operated in LAr with good performance and under sufficiently stable conditions for long measurement periods. A total exposure of 21.6 kg·yr was acquired and a background level of $B \simeq 10^{-2}$ cts/(keV·kg·yr) at $Q_{\beta\beta}$ of ^{76}Ge has been achieved, which is an order of magnitude lower than the levels observed in the previous HPGe experiments. In Phase I, GERDA adopted a blind analysis strategy in order to avoid bias in the analysis, which has never been done before in this research field.

Chapter 1 gives a short review of the theoretical motivation and experimental aspects of the $0\nu\beta\beta$ decay search discussed above, while Chapter 2 presents the GERDA experiment along with a detailed description of the Phase I data taking period. The following chapters present the analyses performed on GERDA data.

Chapter 3 describes the commissioning phase of the experiment and the background studies performed on commissioning data for gaining knowledge on the background sources in the setup before the start of Phase I. The GERDA collaboration effort on the study of unexpectedly high ^{42}K background observed in the commissioning is summarized (Section 3.2). Investigation of the ^{208}Tl background and the location of the contaminations in the setup using the data taken in different configurations (Section 3.3), as well as an analysis of the low energy region of the spectrum dominated by the ^{39}Ar background along with the determination of the ^{39}Ar specific activity (Section 3.4), both performed as part of this dissertation work, are described.

Chapter 4 gives a detailed study of the background sources in GERDA Phase I: the γ-ray line intensities; characterization of the background sources and Monte Carlo simulations of all possible contributions; investigation of the location of ^{238}U / ^{232}Th contaminations through the intensity of the observed γ-ray lines from ^{214}Bi and ^{208}Tl; analysis of the α-induced events in the high energy region and detector surface contaminations; and finally a global background model that describes the whole energy spectrum above the endpoint of ^{39}Ar β spectrum. The decomposition of the background energy spectrum into the individual contributions from different processes provides many important results, such as knowledge on the background sources and their locations in the setup. Also, quantification of the individual background contributions in the energy region of interest (ROI) around $Q_{\beta\beta}$ allows to find strategies for further mitigating the background in Phase II. The obtained background model gives a prediction of the expected number of background events and the spectral shape of the background in the ROI, which are essential inputs for the $0\nu\beta\beta$ signal analysis. The predictions of the background model were used in the $0\nu\beta\beta$ analysis published by the GERDA collaboration in [18]. The studies described in this chapter were carried out within this dissertation work (except Section 4.6.6 [20] and Section 4.7.3 [21]) and have been published (except Section 4.7.6) in [22].

Chapter 5 presents the determination of $2\nu\beta\beta$ decay half life of ^{76}Ge using GERDA Phase I data, according to the contribution of $2\nu\beta\beta$ spectrum to the measured total energy spectrum as derived by the background model developed in Chapter 4. A full systematic uncertainty evaluation is also described. The previous analysis performed by the GERDA analysis team (coordinator L. Pandola) using the early Phase I data, reported in [23], is briefly described in Section 5.1, and the results from the two analyses are compared.

Chapter 6 summarizes the studies for determining the input parameters for the $0\nu\beta\beta$ signal analysis, such as the expected number of background events, the detection efficiency and acceptance of $0\nu\beta\beta$ signal after analysis cuts, that were carried out before opening the blinding window around $Q_{\beta\beta}$. The experimental sensitivity of GERDA Phase I is evaluated given the determined analysis parameters. All studies described in this chapter were performed by the GERDA analysis team with contributions from this thesis work.

Finally, Chapter 7 describes the analyses for estimating (or setting a limit on) the $0\nu\beta\beta$ decay half life, performed on the GERDA Phase I data after opening the blinding window. These analyses were carried out with contributions from the whole GERDA collaboration and the results are published in [18, 24]. The contribution of this dissertation work was to the Bayesian analysis. The complete analysis is re-performed, using mostly common GERDA analysis tools, and reported in detail. For completeness, also a brief description of the Frequentist analysis and its results are reported.

Chapter 1

Theoretical and experimental aspects of neutrinoless double beta decay

This introductory chapter motivates the search for neutrinoless double beta decay and gives an overview of the experimental aspects that are relevant for the following chapters. The double beta ($\beta\beta$) decay process in its observed "neutrino accompanied" final state ($2\nu\beta\beta$) and hypothetical "neutrinoless" final state ($0\nu\beta\beta$) is introduced (Section 1.1). Implications of $0\nu\beta\beta$ in neutrino physics are reviewed (Section 1.2). The experimental signature, sensitivity and the status concerning the $0\nu\beta\beta$ decay searches, along with a brief discussion on potential background sources that limit the sensitivity to a $0\nu\beta\beta$ signal and the advantages of using high purity germanium (HPGe) detectors in this research field are given (Section 1.3).

1.1 Double beta decay

Double beta decay is a weak process that converts an initial nucleus of mass number A and atomic number Z, (A, Z), into a nucleus of $(A, Z-2)$ or $(A, Z+2)$, considering the two possible modes $\beta^+\beta^+$ and $\beta^-\beta^-$, respectively. Similar processes changing a nucleus of (A, Z) to $(A, Z-2)$ are double electron capture ($ECEC$) and simultaneous occurrence of a β^+ decay and a EC process (β^+EC). The available phase space is smaller for the decay modes that involve emission of positron(s) compared to the most commonly considered mode $\beta^-\beta^-$ decay. In the following, decay modes other than $\beta^-\beta^-$ (simply denoted as $\beta\beta$) are either not considered or not explicitly mentioned. Two different final states of $\beta\beta$ decay, i.e. with ($2\nu\beta\beta$) and without ($0\nu\beta\beta$) emission of two neutrinos, are described in detail.

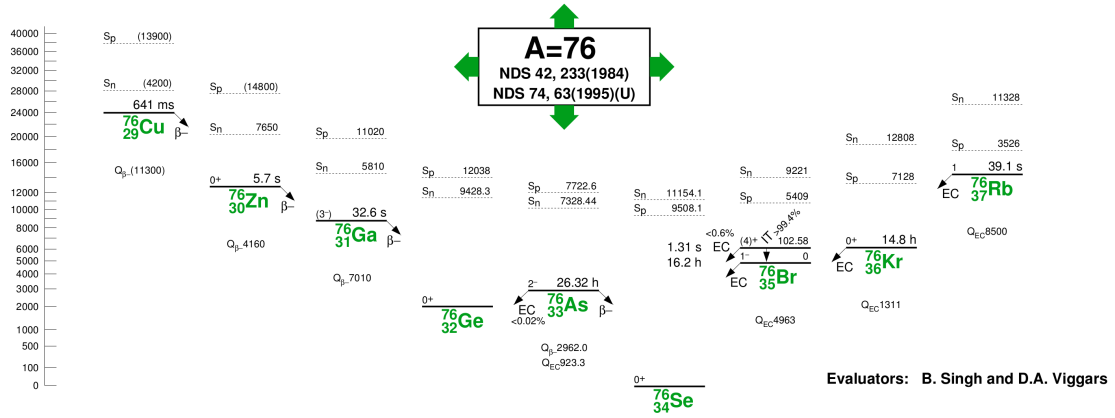

Figure 1.1: Isobars for $A = 76$ [26]. The energy of $^{76}_{32}$Ge is less than that of $^{76}_{33}$As, which forbids its β^- decay. The $\beta\beta$ decay of $^{76}_{32}$Ge to $^{76}_{34}$Se is however energetically allowed.

1.1.1 Final state with two neutrinos

The possibility of a $\beta\beta$ decay with simultaneous emission of two electrons (e^-) and two antineutrinos ($\bar{\nu}_e$), referred to as *two-neutrino double beta decay* (Eq. (1.1)), was first considered in 1935 [25], shortly after Fermi's β decay theory.

$$2\nu\beta\beta \text{ decay}: \ (A, Z) \rightarrow (A, Z+2) + 2e^- + 2\bar{\nu}_e \tag{1.1}$$

It is predicted to occur in certain even-even nuclei, (A, Z), i.e. with even numbers of neutrons and protons, that are more bound than the odd-odd nucleus, $(A, Z+1)$, of the neighboring isotope due to pairing interaction, but less so than the even-even nucleus, $(A, Z+2)$, of the next neighboring isotope. An example of such even-even nuclei is $^{76}_{32}$Ge (see Fig. 1.1), the binding energy of which is lower than that of $^{76}_{33}$As, thus its β decay to $^{76}_{33}$As is energetically forbidden, whereas, its $\beta\beta$ decay to $^{76}_{34}$Se is allowed. Fig. 1.2 (left) shows the Feynman diagram for $2\nu\beta\beta$ decay process.

Obeying all conservation laws, $2\nu\beta\beta$ decay is an allowed process in the Standard Model of particle physics (SM), and has been observed in eleven isotopes so far [14, 27, 28]. The measured half lives ($T^{2\nu}_{1/2}$) for different isotopes are in the range of $7 \cdot 10^{18} - 2 \cdot 10^{24}$ yr [14]. Being a second-order weak process, $2\nu\beta\beta$ decay is characterized by an extremely low decay rate ($\Gamma_{2\nu}$) that can be factorized as

$$\Gamma_{2\nu} = (T^{2\nu}_{1/2})^{-1} = G_{2\nu}(Q_{\beta\beta}, Z)|M_{2\nu}|^2 \ , \tag{1.2}$$

where $G_{2\nu}(Q_{\beta\beta}, Z)$ is the four particle phase-space factor and $M_{2\nu}$ is the nuclear matrix element. A recent calculation of $G_{2\nu}(Q_{\beta\beta}, Z)$, including $T^{2\nu}_{1/2}$, single electron spectra, summed electron spectra and electron angular correlations, by using improved electron wave functions is given for $2\nu\beta\beta$ decay of different isotopes in [29]. Using the measured values of $T^{2\nu}_{1/2}$ through the detection of $2\nu\beta\beta$ process and the calculated $G_{2\nu}(Q_{\beta\beta}, Z)$, $M_{2\nu}$ can be determined, which supports the theoretical schemes for its calculation. It

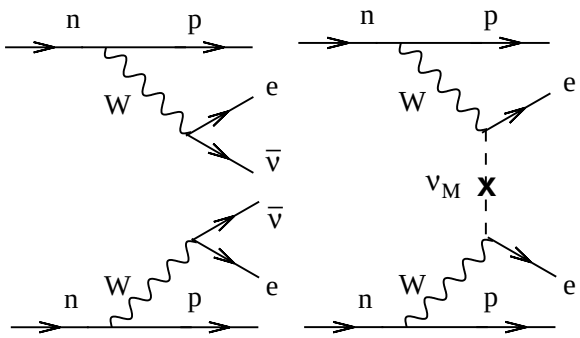

Figure 1.2: Feynman diagrams for $2\nu\beta\beta$ (left) and Majorana neutrino exchange driven $0\nu\beta\beta$ (right) decays. Taken from [33].

also provides an important input for the nuclear matrix element calculations for $0\nu\beta\beta$ decay which, due to the relation between $2\nu\beta\beta$ and $0\nu\beta\beta$ processes, can be performed using similar methods by defining the neutrino potential separately for each process (see e.g. [30]).

1.1.2 Final state without neutrinos

The possibility of $\beta\beta$ decay with no neutrinos in the final state, the so-called *neutrinoless double beta decay* (Eq. (1.3)), was considered [31, 32] for testing Majorana's neutrino theory [2] soon after its formulation in 1937. According to Majorana's formalism, the neutrino and the antineutrino are indistinguishable.

$$0\nu\beta\beta \text{ decay}: \ (A, Z) \rightarrow (A, Z+2) + 2e^- \tag{1.3}$$

In this process, the lepton numbers in the initial (L_i) and final (L_f) states are not equal; the lepton number conservation law in the SM is violated by two units, i.e. $|\Delta L_{if}| = 2$. Its observation would thus demonstrate the existence of physics beyond the SM. Fig. 1.2 (right) shows the Feynman diagram of Majorana neutrino exchange driven $0\nu\beta\beta$ decay, i.e. exchange of a light Majorana neutrino being responsible for the process. There are other lepton number violating mechanisms in the extensions of the SM that can mediate $0\nu\beta\beta$ process [13, 33, 34], e.g. the ones involving exchange of super-symmetric particles or right-handed weak currents. However, they require the existence of new particles and/or interactions in addition to Majorana nature of neutrinos. The exchange of light Majorana neutrinos is the most commonly considered mechanism [10, 33]. Besides, regardless of what the actual mechanism is, the occurrence of $0\nu\beta\beta$ decay implies that neutrinos have Majorana character with nonzero mass [11]; any diagram contributing to $0\nu\beta\beta$ decay can be inserted into a neutrino propagator [33] as shown in Fig. 1.3.

The best present limits on the half life of $0\nu\beta\beta$ decay ($T^{0\nu}_{1/2}$) from the current high sensitivity experiments are in the range of $2.8 \cdot 10^{24}$ (^{130}Te) – $2.1 \cdot 10^{25}$ yr (^{76}Ge) [14]. A claim of a (^{76}Ge) $0\nu\beta\beta$ decay signal has been reported [17], which is in strong tension with the results of recent experiments that are sensitive to the claimed $0\nu\beta\beta$ signal rate but have not observed it (see Section 1.3.3).

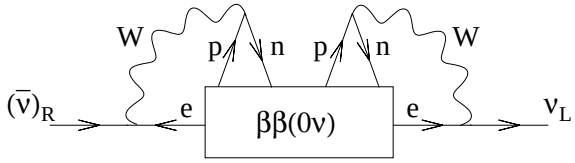

Figure 1.3: Majorana propagator resulting from $0\nu\beta\beta$ amplitude (the black-box $0\nu\beta\beta$ argument [11]). Taken from [33].

The decay rate of $0\nu\beta\beta$ ($\Gamma_{0\nu}$) can be, in general, written as the sum of the contributions from different underlying lepton number violating mechanisms. In this case, for each contributing mechanism x, it is factorized in terms of the phase-space factor $G_{0\nu,x}(Q,Z)$, nuclear matrix element $M_{0\nu,x}$ and an additional term representing the particle physics parameters, η_x, responsible for the decay [34]. If the exchange of light Majorana neutrinos with left-handed interactions contributes dominantly, then the decay rate is approximately [33]:

$$\Gamma_{0\nu} = (T^{0\nu}_{1/2})^{-1} = G_{0\nu}(Q_{\beta\beta}, Z)|M_{0\nu}|^2\langle m_{\beta\beta}\rangle^2 \tag{1.4}$$

where $\langle m_{\beta\beta}\rangle$ is the effective Majorana mass of the electron neutrino. Determination of $\langle m_{\beta\beta}\rangle$ would have profound implications on neutrino physics which are discussed in the following section. In order to relate the measured $T^{0\nu}_{1/2}$ to $\langle m_{\beta\beta}\rangle$, and also to compare the results of experiments that are using different isotopes, the knowledge of $G_{0\nu}$ and $M_{0\nu}$ is essential. An analytical computation of $G_{0\nu}$ with a good accuracy is possible. A complete calculation is given in [29], which makes use of exact Dirac wave functions with finite nuclear size and electron screening. The uncertainties introduced to $G_{0\nu}$ due to different input parameters, such as the Q-value of $\beta\beta$ decay ($Q_{\beta\beta}$), nuclear radius, etc., are around 7% [29]. The calculation of $M_{0\nu}$, that connects the initial and final state wavefunctions, cannot be done exactly, due to the complicated nuclear many-body nature of the problem. Different methods are used for the calculations, Comparing different nuclear model evaluations indicates a factor ~ 3 spread in the calculated $M_{0\nu}$. If the results of the major nuclear structure approaches which share certain common ingredients are considered for the quantification, such that the remaining discrepancies between different approaches are only due to the different nuclear wave functions they employ, the uncertainties in the calculations are in the 20–30% range [13]. The uncertainties on $M_{0\nu}$ make the comparison of limits from different isotopes difficult and, in case of a positive observation, will make the physical interpretation nontrivial.

1.2 Neutrino physics and the role of $0\nu\beta\beta$

The neutrino is an electrically neutral, massless, Dirac type particle in the SM, with three active families, referred to as flavors, ν_e, ν_μ and ν_τ ($L = +1$) and their corresponding antiparticles ($L = -1$), which take part only in the weak interactions. The weak interaction violates parity, therefore, right-handed [1] neutrinos (and left-handed antineutrinos)

[1] A particle is referred to as right-handed (left-handed) if its spin points in the same (opposite) direction as its momentum.

have no interaction and have not been observed so far. The absence of right-handed neutrinos led to the assumption that neutrinos are massless. In contradiction to this assumption in the SM, observation of neutrino flavor oscillations has established that neutrinos do have nonzero rest mass, albeit very small [3]. Although absolute masses cannot be measured in the oscillation experiments, observations imply that the mass of the heaviest neutrino mass eigenstate cannot be less than 0.05 eV. The most stringent (model dependent) upper limits come from cosmology on the sum of neutrino masses, e.g. $< 0.23\,\text{eV}$ [4]. This empirical fact requires an extension of the SM to accommodate the small but nonzero mass of neutrino.

The fact that neutrinos have no electric charge allows to write two kinds of Lorentz invariant mass terms: Dirac and Majorana masses. Whereas, conservation of electric charge allows only Dirac type mass terms for charged fermions. In the case of neutrinos, the Lagrangian density includes the mass terms [10]:

$$\begin{aligned}\mathcal{L}_{mass} &= m_D\left[\bar{\nu_R}\nu_L + (\bar{\nu_L})^c\nu_R^c\right] + m_L\left[(\bar{\nu_L})^c\nu_L + \bar{\nu_L}\nu_L^c\right] + m_R\left[(\bar{\nu_R})^c\nu_R + \bar{\nu_R}\nu_R^c\right] \\ &= -\frac{1}{2}(\ (\bar{\nu_L})^c\ \bar{\nu_R}\ )\begin{pmatrix} m_L & m_D \\ m_D & m_R \end{pmatrix}\begin{pmatrix} \nu_L \\ (\bar{\nu_R})^c \end{pmatrix},\end{aligned} \tag{1.5}$$

where ν_L and ν_R are the left- and right-handed components of the neutrino field and m_D is the Dirac mass. The Majorana masses m_L and m_R are not required to be equal since the Majorana equation decouples. In the seesaw mechanism [5,6], it is assumed that $m_L = 0$ and $m_R \gg m_D$, motivated by the non-observation of ν_R. Under these assumptions, diagonalizing $\mathcal{L}_{mass}$ results in two mass eigenvalues: m_R and $m_\nu \sim m_D^2/m_R$. Thus, the seesaw mechanism predicts one light and one heavy Majorana neutrino, and provides a natural explanation to the smallness of m_ν compared to m_D, which should naturally have a value close to the mass of the charged Dirac fermions, e.g. the electron. A direct consequence of the Majorana mass term in the Lagrangian is that neutrinos are their own antiparticles. Terms like $(\bar{\nu_L})^c\nu_L$ in $\mathcal{L}_{mass}$ result in interactions that change lepton number by two units. The seesaw model also provides an explanation to the matter-antimatter asymmetry of the Universe through leptogenesis [7,8], which requires CP violation in the lepton sector and prefers neutrinos to be Majorana particles.

Being insensitive to the Majorana/Dirac nature of neutrinos, oscillation experiments provide important information on the neutrino masses and have potential to measure possible CP violation in the lepton sector. There are different experimental approaches to measure the absolute mass scale of neutrinos, such as direct measurement from the study of β decay kinematics and inference on the sum of the neutrino masses from cosmology. Currently, the only feasible experimental test of the Majorana nature of neutrinos is the search for the lepton number violating $0\nu\beta\beta$ decay. It has also the potential to yield information on the neutrino mass spectrum, in case the process is mediated by light Majorana neutrino exchange. These experimental and phenomenological aspects are described in the following.

Neutrino oscillations and neutrino mass spectrum

Experiments studying neutrinos from different sources – sun, atmosphere, reactors and

accelerators – have yielded compelling evidence that neutrinos change flavor while propagating in vacuum or in matter [3, 35]. This observation implies that *a*) neutrinos have mass: there is a spectrum of three (or more) neutrino mass eigenstates, ν_i, $i = 1, 2, 3$, that are the analogues of the charged-lepton mass eigenstates, l_α, $\alpha = e, \mu, \tau$; and *b*) leptons mix: the weak interaction, coupling the W boson to a charged lepton and a neutrino, can couple any l_α to any ν_i. The amplitude of a specific combination is $U^*_{\alpha i}$, where U is the unitary neutrino mixing matrix (PMNS [2] matrix). Thus, a neutrino of flavor α produced in weak interactions in association with the charged lepton of flavor α is

$$|\nu_\alpha\rangle = \sum_i U^*_{\alpha i} |\nu_i\rangle \ , \tag{1.6}$$

and U can written as [3]

$$\begin{aligned} U &= \begin{pmatrix} c_{12}c_{13} & s_{12}c_{13} & s_{13}e^{-i\delta} \\ -s_{12}c_{23} - c_{12}s_{23}s_{13}e^{i\delta} & c_{12}c_{23} - s_{12}s_{23}s_{13}e^{i\delta} & s_{23}c_{13} \\ s_{12}s_{23} - c_{12}c_{23}s_{13}e^{i\delta} & -c_{12}s_{23} - s_{12}c_{23}s_{13}e^{i\delta} & c_{23}c_{13} \end{pmatrix} \times P \ , \\ P &= \mathrm{diag}(1, e^{i\alpha_{21}/2}, e^{i\alpha_{31}/2}) \ , \end{aligned} \tag{1.7}$$

where s_{ij} and c_{ij} stand for the sine and cosine of the mixing angles $\theta_{ij} \in [0, \pi/2]$, $\delta \in [0, 2\pi]$ is the CP violating Dirac phase and α_{21}, α_{31} are two CP violating Majorana phases. If massive neutrinos are Dirac particles, only δ is physical and can be responsible for CP violation in the lepton sector. The additional phases α_{21}, α_{31} have physical consequences only if neutrinos are Majorana particles [38, 39]. Assuming CPT invariance, unitarity of U guarantees that the created charged lepton l_α will have the same flavor as ν_α.

In the neutrino flavor change process, referred to as *neutrino oscillation*, a neutrino created as ν_α changes into a different flavor ν_β after traveling a distance L, e.g. from the source to the detector. The amplitude for the oscillation in vacuum is written as

$$\mathrm{Amp}(\nu_\alpha \to \nu_\beta) = \sum_i U^*_{\alpha i}\, \mathrm{Prob}(\nu_i)\, U_{\beta i} = \sum_i U^*_{\alpha i}\, e^{-i m_i^2 L/2E}\, U_{\beta i} \ , \tag{1.8}$$

where $\mathrm{Prob}(\nu_i)$ is the propagation amplitude for ν_i, m_i is the mass of ν_i, L is the lab-frame distance between the source and the detector and E is the beam energy (see [3, 35] for the derivation). Then, the oscillation probability can be written as:

$$\begin{aligned} P(\nu_\alpha \to \nu_\beta) = |\mathrm{Amp}(\nu_\alpha \to \nu_\beta)|^2 = \delta_{\alpha\beta} - 4 \sum_{i>j} \mathbf{R}\{U^*_{\alpha i}\, U^*_{\beta j}\, U_{\beta i}\, U_{\alpha j}\} \sin^2 \frac{\Delta m^2_{ij} L}{4E} \\ + 2 \sum_{i>j} \mathbf{I}\{U^*_{\alpha i}\, U^*_{\beta j}\, U_{\beta i}\, U_{\alpha j}\} \sin \frac{\Delta m^2_{ij} L}{2E} \ , \end{aligned} \tag{1.9}$$

where $\Delta m^2_{ij} \equiv m^2_i - m^2_j$. In the oscillation probability, only the relative phases of the propagation amplitudes for different mass eigenstates have physical consequences. Oscillation

[2] Abbreviation for Pontecorvo-Maki-Nakagawa-Sakata [36, 37].

experiments measure the probability, and therefore, have only access to the squared mass differences Δm^2_{ij} and the parameters of the mixing matrix U, that are the mixing angles θ_{ij} and the Dirac phase δ. The oscillation probability for neutrinos propagating in matter, e.g. in the sun, earth, or a supernova, can be different compared to the one in vacuum, since the propagation can be modified by the coherent forward-scattering from particles in the medium, known as the Mikheyev-Smirnov-Wolfenstein (MSW) effect [40, 41].

Results on neutrino oscillations from the majority of experiments can be consistently described within the three-neutrino oscillation framework. These experiments have measured two independent differences between squared masses: the so-called *solar mass splitting*, $\delta m^2 = m^2_2 - m^2_1 > 0$ and *atmospheric mass splitting*, $\Delta m^2 = m^2_3 - (m^2_1 + m^2_2)/2$. Currently, five of the oscillation parameters are determined with an accuracy dominated by specific class of experiments: θ_{12} by solar data, θ_{13} by short-baseline (SBL) reactor data (Daya Bay, RENO, Double Chooz), θ_{23} by atmospheric data, mainly from Super-Kamiokande, δm^2 by long-baseline reactor data from KamLAND, and Δm^2 by long-baseline (LBL) accelerator data (K2K, T2K, MINOS). The sign of $\delta m^2 > 0$ is determined by the MSW effect in solar matter [3]. However, the sign of Δm^2 is currently unknown and allows for two possible neutrino mass spectra: $+\Delta m^2$ corresponds to the *normal mass hierarchy* (NH) and $-\Delta m^2$ to the *inverted mass hierarchy* (IH). Also, the status of CP symmetry in the lepton sector is unknown. Knowing $\theta_{13} \neq 0$, the phase δ can generate CP violation effects in neutrino oscillations. However, at present no experimental information on δ is available. Unknown parameters may be constrained through a global neutrino data analysis, as was successfully done for θ_{13}, e.g. in [42], before the discovery of $\theta_{13} > 0$ at reactor experiments.

Table 1.1 lists the best-fit values and allowed 3σ ranges for the 3ν mass-mixing parameters obtained by a global 3ν oscillation analysis [43]. The analysis includes the recent measurements (until 2014): e.g. SBL reactor data from Daya Bay [44] and RENO [45], which improve θ_{13}; the latest appearance and disappearance event spectra by the LBL accelerator experiments T2K [46] and MINOS [47], which constrain the parameters (Δm^2, θ_{23}, θ_{13}) and provide guidance on the θ_{23} octant and δ. The global analysis does not show any preference of NH vs IH. However, it gives an intriguing hint of nonzero CP violation around $\delta \sim 1.4\pi$ (with $\sin\delta < 0$) at $\gtrsim 1\sigma$ level.

Precision oscillation searches can probe the neutrino mass hierarchy (IH or NH), if interference of oscillation driven by $\pm\Delta m^2$ with oscillation driven by another quantity with strong sign can be measured [48]. Some of the approaches are studying neutrino oscillations in medium baseline reactor experiments like JUNO [49] and RENO experiments, and studying the earth matter effects on atmospheric neutrinos, e.g. PINGU [50] (sensitivity may exceed 3σ) or on the accelerator neutrinos with LBL neutrino oscillation experiments at accelerators, e.g. NOvA [51] (sensitivity $> 2\sigma$). The CP violation effect in neutrino oscillations is planned to be studied in the experiments with high intensity accelerator neutrino beams, like T2K and NOvA.

Absolute mass observables

The absolute neutrino mass scale is not accessible from neutrino oscillation measure-

Table 1.1: Results of the global 3ν oscillation analysis, in terms of best-fit values and allowed 3σ ranges for the 3ν mass-mixing parameters. Here, $\Delta m^2 \equiv m_3^2 - (m_1^2 + m_2^2)/2$, with $+\Delta m^2$ for NH and $-\Delta m^2$ for IH. The CP violating phase is taken in the (cyclic) interval $\delta/\pi \in [0, 2]$. The overall χ^2 difference between IH and NH is insignificant ($\Delta\chi^2_{\mathrm{I-N}} = -0.3$). Taken from [43].

Parameter		Best fit	3σ range
$\delta m^2/10^{-5}\,\mathrm{eV}^2$	NH, IH	7.54	6.99 – 8.18
$\sin^2\theta_{12}/10^{-1}$	NH, IH	3.08	2.59 – 3.59
$\Delta m^2/10^{-3}\,\mathrm{eV}^2$	NH	2.43	2.23 – 2.61
	IH	2.38	2.19 – 2.56
$\sin^2\theta_{23}/10^{-1}$	NH	4.37	3.74 – 6.26
	IH	4.55	3.80 – 6.41
$\sin^2\theta_{13}/10^{-2}$	NH	2.34	1.76 – 2.95
	IH	2.40	1.78 – 2.98
δ/π	NH	1.39	—
	IH	1.31	

ments. However, it can be probed through complementary experimental approaches that measure different mass observables: 1) the rest mass of electron neutrino, $\langle m_\beta \rangle$, by studying the β decay kinematics; 2) the sum of the neutrino masses, M, from cosmological observations; and 3) the effective Majorana mass of the electron neutrino, $\langle m_{\beta\beta} \rangle$, through searches for $0\nu\beta\beta$ process.

Direct determination of m_β is the most model independent one among the three methods. In this approach, high precision measurement of the kinematics of β decay allows for reconstructing the electron neutrino mass,

$$\langle m_\beta \rangle \equiv \sqrt{\sum_{i=1}^{3} |U_{ei}|^2 m_i^2} = \sqrt{c_{12}^2\, c_{13}^2 m_1^2 + s_{12}^2\, c_{13}^2 m_2^2 + s_{13}^2 m_3^2}\,, \tag{1.10}$$

since the endpoint region of a β decay spectrum is affected directly by the rest mass of the emitted neutrino. Obtaining high statistics close to the β decay endpoint constitutes an experimental challenge. β emitters with a low endpoint energy such as ^{187}Re, ^{3}H and ^{163}Ho are favorable in such experiments. The upper limits on m_β at 95% C.L. from past spectroscopic measurements are 2.3 eV and 2.1 eV, obtained by the Mainz [52] and Troitsk [53] collaborations, respectively. The KATRIN experiment aims at pushing the sensitivity down to $m_\beta = 0.2\,\mathrm{eV}$ (90% C.L.) and is scheduled for initial data taking in 2015 [54]. There are also planned experiments, like MARE [55] and ECHO [56], that use a calorimetric approach where the β emitter is embedded into or is identical to the detector. These experiments are promising to reach sensitivities in the sub-eV region. A recent review on the status and perspectives of direct neutrino mass experiments can be found in [57].

In the second approach, cosmological and astrophysical observations set constraints on the sum of the neutrino masses:

$$M \equiv \sum_i m_i \ . \tag{1.11}$$

In the standard model of cosmology, the structure formation is mainly influenced by the neutrino contribution to the cosmic energy density, Ω, and the influence of neutrinos can be described in terms of M [58]. Currently, only upper limits on M are available, which vary strongly with the data combination adopted and depend on the cosmological model used in the data analysis. A limit of $M < 0.23\,\text{eV}$ [4] has been recently (March 2014) reported by the Planck collaboration as their most reliable limit, and is obtained using the baryon acoustic oscillations (BAO) and cosmic microwave background (CMB) data. Future large scale surveys, such as Euclid [59] (foreseen launch date 2019), may allow for the detection of a nonzero neutrino mass, even with hierarchical neutrino masses in the NH. According to a detailed estimation on how well a Euclid-like survey will constrain the neutrino parameters [60], M can be measured with a 1σ precision of $0.015\,\text{eV}$ and combination of Euclid with Planck CMB data may be able to probe neutrino masses at 3σ precision or better.

The third approach allows for the determination of $\langle m_{\beta\beta}\rangle$ through the measurement of $0\nu\beta\beta$ decay rate $\Gamma_{0\nu}$ (Eq. (1.4)), under the assumption that light Majorana neutrino exchange is the leading contribution to the process. The effective Majorana neutrino mass is then defined as

$$m_{\beta\beta} = \left|\sum_{i=1}^{3} U_{ei}^2 m_i\right| = \left|\mathrm{e}^{i\alpha_1}|U_{e1}^2|m_1 + \mathrm{e}^{i\alpha_2}|U_{e2}^2|m_2 + \mathrm{e}^{-2i\delta}|U_{e3}^2|m_3\right| , \tag{1.12}$$

where m_i are the masses of the individual neutrino mass eigenstates ν_i, and U_{ei} are the elements of the mixing matrix U (Eq. (1.7)) that define the composition of the electron neutrino:

$$|\nu_\mathrm{e}\rangle = \sum_{i=1}^{3} U_{ei}^* |\nu_i\rangle \ . \tag{1.13}$$

Fig. 1.4 shows the relation between $\langle m_{\beta\beta}\rangle$ and the mass of the lightest neutrino m_min in the left, M in the middle and $\langle m_\beta\rangle$ in the right panel, given the values of the neutrino oscillation parameters [61], for the three mass hierarchies allowed by the oscillation data: NH ($m_1 < m_2 < m_3$), IH ($m_3 < m_1 < m_2$), and degenerate ($m_1 \approx m_2 \approx m_3$). The width of the hatched bands is due to the uncertainty introduced by the unknown CP violating Majorana ($\alpha_2 1$, $\alpha_3 1$) and Dirac phases (δ) (Eq. (1.7)). The allowed areas become wider as represented by the outer solid lines, if the uncertainties on the oscillation parameters are taken into account. The systematic uncertainties on $M_{0\nu}$ are not folded into the mass projections, which would further widen the areas. The allowed ranges for $m_{\beta\beta}$, given the neutrino oscillation parameters, are $(0.1 - 5.1)\,\text{meV}$ in NH and $(15 - 51)\,\text{meV}$ in IH. The current limits on $m_{\beta\beta}$ are of the order $0.1\,\text{eV}$ (with significant uncertainties due to $M^{0\nu}$), which may be improved by an order of magnitude by the next generation experiments (Section 1.3.3), allowing to start exploring part of the IH parameter space.

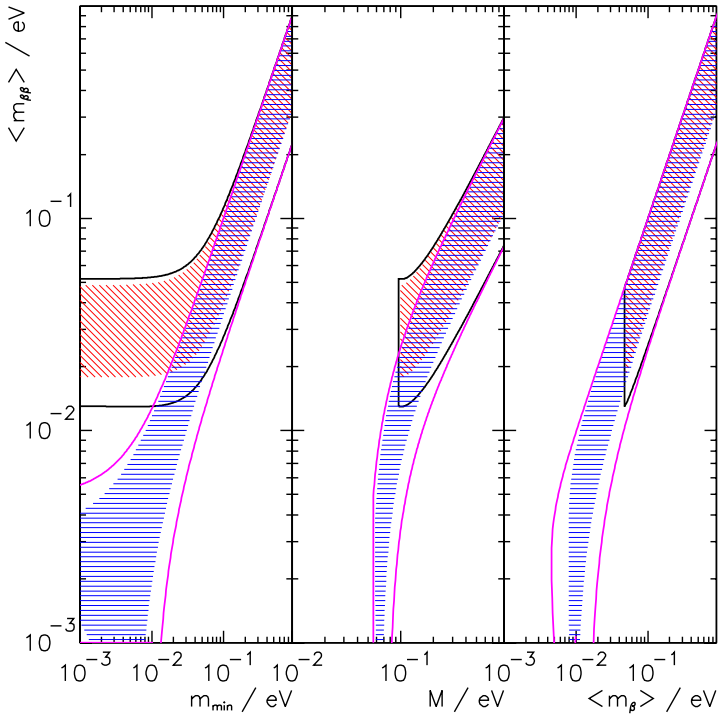

Figure 1.4: $m_{\beta\beta}$ as a function of the absolute mass of the lightest neutrino m_{min} (left panel), the summed neutrino mass m_{tot} (middle panel) and the mass m_β (right panel). In all panels the width of the hatched areas is due to the unknown Majorana phases. The allowed areas given by the solid lines are obtained by taking into account the uncertainties of the oscillation parameters (at the 3σ level [61]). The two sets of solid lines correspond to the normal and inverted hierarchies. These sets merge into each other for $m_{\beta\beta} \geq 0.1\,\text{eV}$, which corresponds to the degenerate mass pattern. Taken from [61].

Observation of $0\nu\beta\beta$ decay will make it possible to fix a range of the absolute values of m_{ν_i}. However, a limit on $m_{\beta\beta}$ does not allow to constrain the individual mass values.

1.3 The search for $0\nu\beta\beta$ decay

The search for $0\nu\beta\beta$ decay has been a compelling field of research that gained more relevance after the establishment of nonzero neutrino mass by the neutrino oscillation experiments. The most sensitive $0\nu\beta\beta$ experiments so far have been the ones searching for this process using the isotopes ^{76}Ge and ^{136}Xe [18, 62]. They provided lower limits on $T^{0\nu}_{1/2}$ of the order of $10^{25}\,\text{yr}$ at 90% C.L., setting the most stringent limits on $\langle m_{\beta\beta}\rangle$. Achieving a significant improvement in the experimental sensitivity for exploring longer $T^{0\nu}_{1/2}$ is a challenge due to the extremely low expected decay rates, and is possible only if very demanding requirements are fulfilled. In this section, experimental aspects of $0\nu\beta\beta$ searches such as the experimental signature, requirements for higher sensitivities and its dependence on experimental parameters are addressed. Also, a selection of experiments

using different experimental approaches and potential background sources for $0\nu\beta\beta$ decay searches are discussed.

1.3.1 Signal detection

The total energy released in $0\nu\beta\beta$ decay is shared between the two electrons in the final state, if the recoil energy of the daughter nucleus is neglected. For an experiment that measures the total energy of the emitted electrons, the signature of $0\nu\beta\beta$ decay is a peak at $Q_{\beta\beta}$ in the energy spectrum. Several parameters determine the intensity of the expected $0\nu\beta\beta$ signal. **Larger mass (M) of the source material** that contains a **high fraction (κ) of the candidate $0\nu\beta\beta$ isotope** will increase the signal intensity. Larger M means a larger setup which can require a more complicated technology and higher costs. For some elements κ can be naturally high, whereas for others it needs to be increased through an isotopic enrichment process. **Longer measuring times (t)** will also naturally increase the number of signal events. Any radioactive decay follows the exponential decay law and is characterized by its decay constant that is proportional to the inverse half life of the process. The number of decayed nuclei after time t given by the radioactive decay law is

$$N(t) = N_0 \left(1 - e^{-(\ln 2)t/T_{1/2}}\right) , \tag{1.14}$$

where N_0 is the initial number of nuclei. For rare processes, like $0\nu\beta\beta$ decay with expected half lives on the order of minimum 10^{25} years, N is approximately linear in time given the measuring times in experiments. For $t \ll T_{1/2}$ the above expression becomes

$$N(t) = \frac{N_0 \left(\ln 2\right) t}{T_{1/2}} . \tag{1.15}$$

For the number of $0\nu\beta\beta$ events, ν, expected to be measured in an experimental setup, the above formula can be re-expressed as

$$\nu = \frac{M\, N_A}{m_A} \cdot \kappa \cdot \epsilon \cdot \frac{(\ln 2)\, t}{T^{0\nu}_{1/2}} , \tag{1.16}$$

where N_A is Avogadro's constant, m_A the molar mass of the material and ϵ the signal detection efficiency. The latter also accounts for the signal acceptance of the analysis cuts, the fraction of the signal distribution in the analysis energy window, etc. The product of M and t, called exposure $\mathcal{E}$, is a frequently used term in experiments as the measure of accumulated data.

In $0\nu\beta\beta$ experiments the parameter of interest that is inferred from the observed number of events is $T^{0\nu}_{1/2}$. The sensitivity of an experiment to $T^{0\nu}_{1/2}$ can be calculated with Eq. (1.16) only in an ideal world. The only requirement would be to have large enough M, κ, t and ϵ to measure an event given $T^{0\nu}_{1/2}$. However, in real world the experiments additionally measure a continuum of events in the same energy region as the expected signal but produced by other processes than $0\nu\beta\beta$ decay. This background continuum is one of the biggest limitation for the sensitivity of experiments. For being sensitive to the explored ranges of $T^{0\nu}_{1/2}$, the experimental requirement is to have a background level

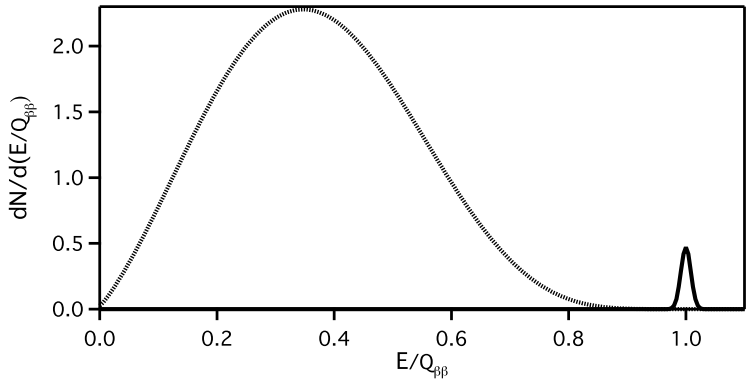

Figure 1.5: Distribution of the sum of electron energies for $2\nu\beta\beta$ (continuous curve until $E/Q_{\beta\beta} = 1.0$) and $0\nu\beta\beta$ (Gaussian shaped curve at 1.0). The curves are drawn assuming that $0\nu\beta\beta$ rate is 1% of $2\nu\beta\beta$ rate and for a 1-σ energy resolution of 2% [33].

which satisfies that ν is significantly higher than the statistical fluctuations in the expected number of background events λ. The background rate at $Q_{\beta\beta}$ is defined by a parameter called background index, B, and is expressed as

$$B = \frac{\lambda}{M\,t\,\Delta E}, \tag{1.17}$$

where ΔE is the analysis energy window around $Q_{\beta\beta}$ for the signal search. The choice of the width of ΔE will depend on the energy resolution at $Q_{\beta\beta}$, since a narrower ΔE will lead to an increase in the signal-to-background ratio (s/b). Thus, **high energy resolution** at $Q_{\beta\beta}$ is an important factor for high sensitivity experiments. Moreover, events near the $Q_{\beta\beta}$ of the continuous energy spectrum of $2\nu\beta\beta$ process will contribute less to the background in ΔE for higher energy resolution (see Fig. 1.5). This is especially an important concern because $2\nu\beta\beta$ events have an indistinguishable topology from the $0\nu\beta\beta$ events and, thus, they constitute an irreducible background source. Last but not least, $0\nu\beta\beta$ experiments should be designed to achieve a very **low-background environment** in order to have low B. While designing $0\nu\beta\beta$ experiments, these parameters are taken into account and optimized for exploring the aimed $T^{0\nu}_{1/2}$ region.

1.3.2 Experimental sensitivity

In this section the experimental sensitivity is formulated based on [63]. Currently, the best achieved B in $0\nu\beta\beta$ experiments with ^{76}Ge is of the order of 10^{-2} cts/(keV·kg·yr). Given an exposure of 20 kg·yr and an energy resolution of 2.0 keV at $Q_{\beta\beta}$, very few background events are expected, e.g. 2.4 events in $Q_{\beta\beta} \pm 3\sigma$ window according to Eq. (1.17). When the most stringent lower ^{76}Ge $T^{0\nu}_{1/2}$ limit of $3{\cdot}10^{25}$ yr [18] is considered, the maximum expected number of $0\nu\beta\beta$ events is very low as well. Assuming an enriched Ge material ($^{\text{enr}}$Ge) with $\kappa = 0.86$ and a maximal signal detection efficiency of $\epsilon = 1.0$, only 3.2 signal events are expected for the same exposure according to Eq. (1.16). With such small

numbers, the statistical analysis can only be correctly done by using Poisson statistics. Example sensitivity calculations are given for ^{76}Ge $0\nu\beta\beta$ decay search with the parameters like energy resolution and B representing the state-of-the-art in this field. Neither the exact values of the parameters nor the choice of the isotope or the experimental approach plays an important role in the examples given below. The aim is to demonstrate the dependence of the sensitivity of a $0\nu\beta\beta$ experiment on the parameters discussed in the previous section.

Formulation

The observed events in ΔE are assumed to originate from both signal and background processes. The probability of observing x events resulting from the sum of two indistinguishable processes, each of which follows a Poisson distribution, is a Poisson distribution with mean μ that is equal to the sum of the individual process means, $\mu = \nu + \lambda$, and can be written as

$$P(x|\mu) = \frac{e^{-(\nu+\lambda)}(\nu+\lambda)^x}{x!} \ , \tag{1.18}$$

where ν is the expected number of signal and λ the expected number of background events. Having measured x events and knowing λ, the probability distribution for ν can be obtained using Bayes' Theorem as

$$P(\nu|x,\lambda) = \frac{\left(e^{-(\nu+\lambda)}(\nu+\lambda)^x/x!\right) P_0(\nu)}{\int_0^\infty \left(e^{-(\nu+\lambda)}(\nu+\lambda)^x/x!\right) P_0(\nu) d\nu} \ , \tag{1.19}$$

where $P_0(\nu)$ is the prior probability on the expected number of signal events. Assuming equal probabilities for different ν, Eq. (1.19) becomes

$$P(\nu|x,\lambda) = \frac{e^{-\nu}(\nu+\lambda)^x}{x! \sum_{n=0}^{x} \frac{\lambda^n}{n!}} \ . \tag{1.20}$$

An upper limit on ν can be determined by finding the value of ν that equals the cumulative pdf $F(\nu|x,\lambda)$ to the desired probability, i.e. 0.90 for a 90% upper limit,

$$F(\nu|x,\lambda) = \int_{\nu'=0}^{\nu} P(\nu'|x,\lambda) d\nu' = 1 - \frac{e^{-\nu} \sum_{n=0}^{x} \frac{(\lambda+\nu)^n}{n!}}{\sum_{n=0}^{x} \frac{\lambda^n}{n!}} = 0.90 \ . \tag{1.21}$$

The 90% probability upper limit on ν can be translated to a 90% probability lower limit on $T_{1/2}^{0\nu}$ using Eq. (1.16).

Prior to an experimental measurement, the average of the expected lower limit on $T_{1/2}$ can be calculated by considering each possible outcome and weighting the result of an outcome with its probability. The average of the expected lower limit, called experimental sensitivity, will then be

$$\langle T_{1/2}^{0\nu} \rangle = \sum_{x=0}^{\infty} P(x|\nu=0,\lambda) \cdot \frac{M \cdot N_A}{m_A} \cdot \kappa \cdot \epsilon \cdot \frac{\ln 2 \cdot t}{\nu(F=0.90)} \ . \tag{1.22}$$

Example analysis

In the following analysis, the average 90% lower limit on the $T^{0\nu}_{1/2}$ is obtained for a set of example parameter values and by solving Eq. (1.21) numerically to find the value of ν that gives $F = 0.90$. When the analysis is performed on the number of events in ΔE, the signal efficiency ϵ will, in addition to other factors, also depend on the chosen width of ΔE and the energy resolution σ at $Q_{\beta\beta}$. The signal efficiency is parameterized by truncating the Gaussian in the range ΔE:

$$\varepsilon_{res} = \frac{1}{\sqrt{2\pi}\sigma} \int_{Q_{\beta\beta}-\Delta E/2}^{Q_{\beta\beta}+\Delta E/2} e^{-\frac{(x-Q^2_{\beta\beta})}{2\sigma^2}} dx. \tag{1.23}$$

Figure 1.6 shows the average expected 90% probability lower limit on $T^{0\nu}_{1/2}$ as a function of ΔE for $B = 10^{-2}$ cts/(keV·kg·yr), $\mathcal{E} = 20$ kg·yr, $\kappa = 0.86$, $\epsilon = 0.72$ and for two different energy resolutions $\sigma = 1.0$ keV and $\sigma = 2.0$ keV. As can be seen from this example, the optimum size of ΔE for a given σ is a trade-off between the final signal efficiency, which improves for a larger window, and the number of expected background events, which increases with the window size worsening the s/b. Also, a comparison of the cases for $\sigma = 1.0$ keV and $\sigma = 2.0$ keV clearly shows that a higher sensitivity can be achieved with higher energy resolution, due to better s/b in the optimum ΔE.

Two other important parameters influencing the sensitivity of an experiment are $\mathcal{E}$ and B. The dependence of $\langle T^{0\nu}_{1/2} \rangle$ limit on these parameters is demonstrated in Fig. 1.7 for the same example case of $\sigma = 2.0$ keV and always the optimum ΔE width. The increase in the sensitivity with $\mathcal{E}$ approaches to a linear increase as B decreases and will be linear in a background free experiment. The most sensible thing to do for improving the sensitivity of $0\nu\beta\beta$ experiments is to achieve a reduction in B and an increase in $\mathcal{E}$ simultaneously. Achievable exposures and background levels as well as the other parameters, such as signal efficiency, fraction of the isotope under study and energy resolution at $Q_{\beta\beta}$, are determined by the choice of the candidate isotope, the applicable detection technique and current technological limits. These will be addressed in the following section.

1.3.3 Experiments

Among 35 candidate $0\nu\beta\beta$ decay isotopes in nature, the ones with relatively high $Q_{\beta\beta}$ values, e.g. ^{76}Ge, ^{82}Se, ^{100}Mo, ^{130}Te, ^{136}Xe, etc. ($Q_{\beta\beta} > 2.0$ MeV), are more suitable to be studied in experiments (see [12]). It brings advantages in terms of phase space, since $G_{0\nu}(Q_{\beta\beta}, Z) \propto (Q_{\beta\beta})^5$ [33], and background level at $Q_{\beta\beta}$, due to having less contributions from natural decay chains at higher energies $\gtrsim 2$ MeV (Section 1.3.4). Most of these candidate isotopes have low ($< 10\%$) natural isotopic abundance which necessitates isotopic enrichment processes, since the experimental sensitivity scales with the number of candidate nuclei (Eq. (1.16), while increasing the detector mass might result in increased background levels at $Q_{\beta\beta}$. In most cases enrichment is possible (see [12]), e.g. for ^{76}Ge and ^{136}Xe through centrifugation, and has been used in many experiments. Also, the applicable detection technique for the $0\nu\beta\beta$ isotope under study determines two important parameters, detection efficiency and energy resolution. Whether large source masses can

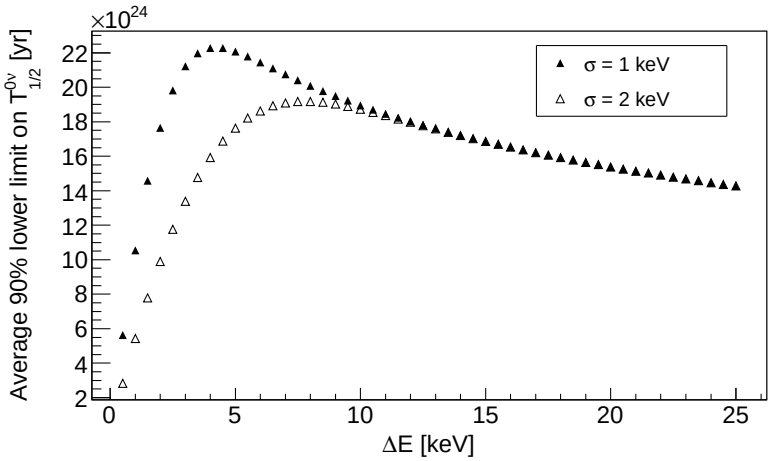

Figure 1.6: The average 90% probability lower limit on $T^{0\nu}_{1/2}$ as a function of the width of ΔE for $B = 10^{-2}\,\mathrm{cts/(keV{\cdot}kg{\cdot}yr)}$, $\mathcal{E} = 20\,\mathrm{kg{\cdot}yr}$, $\kappa = 0.86$, initial $\epsilon = 0.72$ and for two different energy resolutions $\sigma = 1.0\,\mathrm{keV}$ and $\sigma = 2.0\,\mathrm{keV}$.

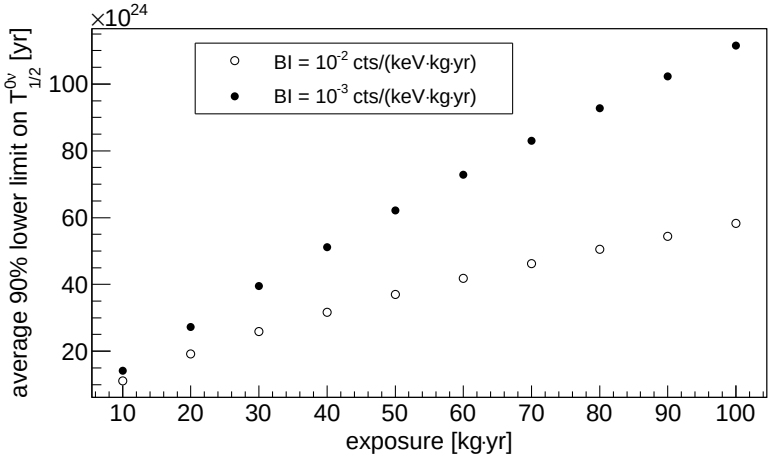

Figure 1.7: The average 90% probability lower limit on $T^{0\nu}_{1/2}$ as a function $\mathcal{E}$ and for two different background indices $B = 10^{-2}\,\mathrm{cts/(keV{\cdot}kg{\cdot}yr)}$ and $B = 10^{-3}\,\mathrm{cts/(keV{\cdot}kg{\cdot}yr)}$, given $\kappa = 0.86$, initial $\epsilon = 0.72$ and $\sigma = 2.0\,\mathrm{keV}$. Note that always optimum ΔE was considered.

Table 1.2: Best present results on $0\nu\beta\beta$ decay (limits at 90% C.L.) and a selection of high sensitivity projects in progress (sensitivity at 90% C.L.). Adapted from [14].

Experiment	Isotope	$T^{0\nu}_{1/2}$ [yr]	$\langle m_{\beta\beta}\rangle$ [eV]	Detection technique
		Results		
GERDA [18]	^{76}Ge	$> 2.1 \cdot 10^{25}$	$< 0.25 - 0.62$	enr. HPGe detector
NEMO3 [64]	^{100}Mo	$> 1.1 \cdot 10^{24}$	$< 0.34 - 0.87$	Track. & calorimeter
CUORICINO [65]	^{130}Te	$> 2.8 \cdot 10^{24}$	$< 0.31 - 0.76$	TeO_2 bolometer
KAMLAND-ZEN [62]	^{136}Xe	$> 1.9 \cdot 10^{25}$	$< 0.14 - 0.34$	Xe loaded liquid scint.
		Projected sensitivity		
GERDA [19]	^{76}Ge	$2.0 \cdot 10^{26}$	$0.08 - 0.19$	enr. HPGe detector
MAJORANA [66]	^{76}Ge	$1.5 \cdot 10^{26}$	$0.09 - 0.20$	enr. HPGe detector
KAMLAND-ZEN [67]	^{136}Xe	$2.0 \cdot 10^{26}$	$0.04 - 0.11$	Xe loaded liquid scint.
EXO [68]	^{136}Xe	$4.0 \cdot 10^{25}$	$0.10 - 0.24$	Xe loaded liquid scint.
SUPERNEMO [69]	^{82}Se	$1.0 \cdot 10^{26}$	$0.04 - 0.14$	Track. & calorimeter
CUORE [70]	^{130}Te	$1.0 \cdot 10^{26}$	$0.05 - 0.13$	TeO_2 bolometer

be achieved depends on the detection technique as well, which is very important for future large scale experiments aiming at significant improvements in sensitivity. Depending on the properties of the isotope, detectors can be built out of material containing the $0\nu\beta\beta$ isotope(s) under study. In this "source = detector" approach, the detection efficiency is maximized and also building setups with large source masses is feasible. Some examples for this approach are ^{76}Ge and ^{116}Cd with semiconductor detectors, ^{48}Ca with CaF_2 scintillating crystals, ^{130}Te with TeO_2 bolometers, ^{136}Xe with liquid scintillators, etc. [12,33]. In "source $\neq$ detector" approach, all available isotopes can be investigated using different detection techniques [12]. In such setups, the source material containing the $0\nu\beta\beta$ isotope is prepared as thin foils to prevent self absorption, which are then placed in between tracking detectors. Certain drawbacks of this approach are the challenge for building large scale experiments and the intrinsic limitations on the energy resolution and detection efficiency. As an important advantage, this detection technique allows for tracking the two emitted electrons in $0\nu\beta\beta$ process separately and makes it possible to identify most of the background sources. Ultimately, it maybe possible to measure the opening angle of the electrons, thus, it potentially allows for studying the underlying mechanism in $0\nu\beta\beta$ decay.

Reviews on $0\nu\beta\beta$ experiments studying different isotopes by employing numerous detection techniques can be found in [10,12–16]. Only some leading projects in terms of the achieved or aimed sensitivity, as summarized in [14], are discussed briefly in the following. Table 1.2 lists the best present results on $0\nu\beta\beta$ decay with limits at 90% C.L. and a selec-

tion of high sensitivity projects that are currently in progress with estimated sensitivities at 90% C.L. Both the results and the sensitivities to $\langle m_{\beta\beta} \rangle$ are calculated [14] using $M_{0\nu}$ values from [71–76] and $G_{0\nu}(Q_{\beta\beta}, Z)$ values from [29].

Until the GERDA experiment and the ^{136}Xe experiments provided results in the last couple of years, the most sensitive results in $0\nu\beta\beta$ decay searches were provided by the ^{76}Ge experiments HDM and IGEX i.e. $T^{0\nu}_{1/2} > 1.9 \cdot 10^{25}$ yr and $T^{0\nu}_{1/2} > 1.6 \cdot 10^{25}$ yr, respectively (90% C.L.) [77, 78]. Both experiments operated HPGe detectors, enriched in the isotope ^{76}Ge, in ultra-low background vacuum cryostats at cryogenic temperatures and used lead shieldings, allowing them to reach background indices of the order of 10^{-1} cts/(keV·kg·yr). A subgroup of the HDM experiment claimed an observation of $0\nu\beta\beta$ signal with $T^{0\nu}_{1/2} = (1.19^{+0.37}_{-0.23}) \cdot 10^{25}$ yr [17], that has been criticized by the scientific community (see e.g. [79–81]). The claimed $T^{0\nu}_{1/2}$ value is in some tension with the KAMLAND-ZEN result [62] (uncertainties on $M_{0\nu}$ makes the comparison difficult), and has been refuted by the GERDA experiment in a model independent way [18]. The GERDA experiment searches for $0\nu\beta\beta$ decay of ^{76}Ge using an array of HPGe detectors enriched in ^{76}Ge and operated in ultra-pure LAr. The experimental design and the Phase I data taking period are described in Chapter 2. In Phase II, the goal is to explore $T^{0\nu}_{1/2} > 10^{26}$ yr with $B < 10^{-3}$ cts/(keV·kg·yr) and ~ 100 kg·yr of exposure. The MAJORANA experiment [66] aims at a similar sensitivity to GERDA Phase II and is currently being assembled. It will operate a mixed array of enriched and natural HPGe detectors inside Cu cryostats built from ultra-pure electroformed copper. The primary goal of the experiment is to demonstrate the feasibility of a definitive next-generation experiment in terms of backgrounds and scalability. A joint collaboration between GERDA and MAJORANA is conceived for achieving sensitivity to $T^{0\nu}_{1/2}$ of the order of 10^{27} yr using tonne-scale detectors in nearly background-free conditions, which will allow to start exploring the IH region (see Fig. 1.4).

Both KAMLAND-ZEN and EXO experiments use xenon as source and detector. The KAMLAND-ZEN experiment has provided the best lower limit on $T^{0\nu}_{1/2}$ of ^{136}Xe. It consists of 13 tons of Xe-loaded (300 kg of $^{\text{enr}}$Xe) liquid scintillator contained in a spherical inner balloon, suspended at the center of the KAMLAND [82] detector. The inner balloon is surrounded by an outer balloon containing 1 kton of liquid scintillator which acts as a powerful active shield. The EXO experiment consists of time projection chambers (TPC) filled with 200 kg of liquid xenon enriched to 81% in ^{136}Xe in its first phase. Energy depositions in TPC produce both ionization and scintillation signals. By forming the linear combination of both measurements, an energy resolution of 3.9% (FWHM) at 2.6 MeV has been achieved. For a future phase of EXO, the possibility of tagging the $\beta\beta$ decay daughter barium ion by means of atomic laser spectroscopy methods is considered for improving background rejection.

The NEMO3 experiment, completed in 2011, has employed an external source approach allowing the study of seven candidate $0\nu\beta\beta$ isotopes, and provided the best lower limit on $T^{0\nu}_{1/2}$ of ^{100}Mo. Its main design feature is the tracking capability, allowing to detect separately the two electrons emitted in the $0\nu\beta\beta$ decay. The NEMO3 detector was composed of drift chambers (Geiger cells) for tracking and plastic scintillators for the calorimetry part. An energy resolution 8% (FWHM) at $Q_{\beta\beta} = 3034$ keV of ^{100}Mo has

been achieved. The main background contributions at $Q_{\beta\beta}$ are ascribed to $2\nu\beta\beta$ decay and ^{222}Rn induced events, all other contributions are efficiently suppressed by the topological reconstruction. The successor SuperNEMO experiment will use the same design and technology. The baseline target isotope will be ^{82}Se. The energy resolution has been improved by a factor of two compared to NEMO3. If the design specifications can be met, SuperNEMO can achieve background-free conditions for 7 kg of ^{82}Se and two years of data taking [15].

1.3.4 Potential background sources

$0\nu\beta\beta$ experiments are located in deep underground laboratories for shielding the setup from cosmic-rays. Without the shielding rock, the background levels due to cosmic-ray interactions would make the search for the extremely rare $0\nu\beta\beta$ decay unthinkable. E.g, in the underground laboratory LNGS of INFN, the Gran Sasso overburden of 3500 m.w.e. reduces the flux of cosmic muons to about $1.2/(\mathrm{h}\cdot\mathrm{m}^2)$ [19]. Muons are the only surviving cosmic-ray particles at such depths, but their interactions can produce high energy secondaries of neutrons, bremsstralung γ-rays, and electromagnetic showers [33]. In most experiments, the setup includes a muon veto system for eliminating signals produced by the muon itself, or by any of its prompt emissions from interactions in the setup, through an anticoincidence requirement. Significantly lower levels of muon induced background compared to other background components can be achieved [22].

Neutrons produced by fission and (α, n) reactions in the cavity rock have $E < 10\,\mathrm{MeV}$ and can be shielded from the detector with hydrogenous material. On the other hand, neutrons produced from muon interactions can have $E > 1\,\mathrm{GeV}$ and may penetrate the shield, resulting in potential background causing reactions near the detector [33]. These high energy neutrons can be reduced by going deeper underground.

Cosmic-ray spallation of the material used in the experimental setup is also a potential background. High energy neutrons can produce radioactive nuclei that can create background for $0\nu\beta\beta$ [83, 84]. For the searches of ^{76}Ge $0\nu\beta\beta$ decay using Ge detectors, the dangerous cosmogenically produced isotopes are ^{68}Ge ($T_{1/2} = 270.8\,\mathrm{d}$) and ^{60}Co ($T_{1/2} = 5.3\,\mathrm{yr}$) produced in Ge (^{60}Co also in Cu), with significant production rates above ground. Due to the Q-value of ^{60}Co ($Q_\beta = 2823.9\,\mathrm{keV}$) well above $Q_{\beta\beta} = 2039\,\mathrm{keV}$ of ^{76}Ge, its decays can contribute to the background in the energy region of interest. ^{60}Co β decays are followed by emission of two γ-rays with 1173.2 and 1332.5 keV (both with 100% probability). In addition to the β spectrum, the two γ-rays with a total energy of 2505.7 keV can also contribute to the background at $Q_{\beta\beta}$. ^{68}Ge decays to ^{68}Ga ($T_{1/2} = 67.6\,\mathrm{m}$), which then undergoes β^+ with $Q_\beta = 2921.1\,\mathrm{keV}$, thus, constitutes a potential background source at $Q_{\beta\beta}$ as well. Once these isotopes are cosmogenically produced in material above ground, due to their half lives in the range of years, they will remain also after the underground installation of the material. Thus, such background sources can be mitigated by minimizing the exposures of materials above ground and by storing them underground and waiting for the isotopes to decay away before the physics data taking.

An irreducible background comes from the $2\nu\beta\beta$ decays of the candidate $0\nu\beta\beta$ isotope. Events in the energy region near the endpoint of the $2\nu\beta\beta$ spectrum can contribute to

the region of interest around $Q_{\beta\beta}$ (Fig. 1.5). Due to the same topology of these two types of events, this contribution cannot be reduced by background discrimination techniques. Depending on the energy resolution, it can be a significant contribution to background at $Q_{\beta\beta}$ like in the NEMO3 experiment [64], or completely negligible like in GERDA [22].

In most of the $0\nu\beta\beta$ experiments, the primary background contributions come from the ^{238}U (Fig. A.1) and ^{232}Th (Fig. A.2) decay chain isotopes, which are present in all materials. An initial contamination of materials in the setup with the radioisotopes in these natural decay chains lead to a continuum background spectrum, arising from Compton-scattered γ-rays, β-rays and α particles, that extends to and beyond the energy region at $Q_{\beta\beta}$ of most of the $0\nu\beta\beta$ candidates. In particular, the 2614.5 keV γ-ray line ($I_\gamma = 0.99$) of ^{208}Tl in the ^{232}Th decay chain, which is above $Q_{\beta\beta}$ for most of the promising candidate isotopes, is a common background concern. The Compton continuum of this γ-ray can result in a significant contribution around $Q_{\beta\beta}$, depending on the location and concentration of the contamination in the setup. In order to reduce the level of contaminations, all materials used in the setup are screened for radio-purity and radio pure enough materials are selected.

There are experiment specific background sources, depending on the setup and detection technique employed. For example, an important background contribution in the GERDA experiment comes from the ^{42}Ar in LAr, as the Ge detectors are directly immersed in LAr. ^{42}Ar is expected to be present in small concentrations in natural argon, hence, also in LAr produced from atmospheric argon. ^{42}Ar is produced through cosmic ray interactions in the atmosphere by the ^{40}Ar(α,2p)^{42}Ar process, and can also originate from ^{40}Ar(n,γ)(n,γ)^{42}Ar reaction in strong neutron fields (e.g. nuclear weapon explosions), or from ^{40}Ar(t,p)^{42}Ar process [26]. The long-lived β-emitter ^{42}Ar ($T_{1/2} = 32.9$ yr, $Q_\beta = 600$ keV) decays directly to the ground state of ^{42}K, without emission of γ-rays. Its short-lived progeny ^{42}K ($T_{1/2} = 12.4$ h, $Q_\beta = 3525.4$ keV) decays through β-decay with 81.9% probability to the ground state of ^{42}Ca, and with 17.6% probability to the first excited state of ^{42}Ca that promptly emits a 1525 keV γ-ray (see Fig. A.3). The decays of ^{42}K can significantly contribute to the background at $Q_{\beta\beta}$ of ^{76}Ge due to the Q-value of ^{42}K well above 2039 keV. The specific activity of ^{42}Ar obtained from computed ^{42}Ar production rates largely vary from one another: two different computations for the reaction ^{40}Ar(n,γ)(n,γ)^{42}Ar lead to an activity of 140 μBq/l of LAr [85] and 10 μBq/l of LAr [86]. Moreover, measurements reported in literature provide only upper limits for the ^{42}Ar concentration, e.g. $4.3 \cdot 10^{-21}$ g/g at 90% C.L. [87] and $3.0 \cdot 10^{-21}$ g/g at 90% C.L. [88]. The ^{42}Ar mass fraction assumed for the GERDA design was taken as the upper limit given in [88], which corresponds to 42 μBq/l of LAr at 90% C.L. The estimated background contribution given this upper limit value is within the GERDA Phase I specifications.

1.3.5 High purity Ge detectors in $0\nu\beta\beta$ decay searches

The experiments searching for $0\nu\beta\beta$ decay of the isotope ^{76}Ge using high purity germanium (HPGe) detectors have been among the most sensitive ones (see Table 1.2). HPGe is a semiconductor material used to manufacture detectors with very high energy resolution, i.e. $\sim 0.1\%$ at $Q_{\beta\beta} = 2039$ keV of ^{76}Ge. As a well established technology, HPGe detectors

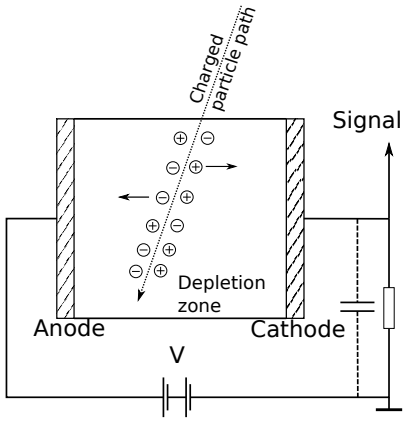

Figure 1.8: Working principle of a semiconductor detector. Taken from [90].

are widely used for γ-ray spectroscopy and also in various applications in particle and nuclear physics [89]. Being used as detector and source simultaneously in $0\nu\beta\beta$ experiments, the detection efficiency of the two emitted electrons in $0\nu\beta\beta$ decay is maximized. The low natural abundance of ^{76}Ge (7.6%) is one of the drawbacks of this choice. The most sensitive experiments, i.e. IGEX, HDM, GERDA, have used detectors produced from material with increased ^{76}Ge fraction ($\sim 87\%$). Another disadvantage of the searches with ^{76}Ge is the relatively low $Q_{\beta\beta}$ of 2039 keV, which means more background contribution from ^{238}U and ^{232}Th decay chains (see Section 1.3.4). However, using HPGe detectors for detection brings important advantages in terms of energy resolution, intrinsic radio-purity, detection efficiency compared to other techniques, which makes ^{76}Ge a good candidate for $0\nu\beta\beta$ search. The detection principle of Ge detectors and their background suppression power through pulse shape discrimination (PSD) methods are discussed briefly in the following.

Detection principle

For an ideal germanium crystal at 0 K, the conduction band is empty and the valence band is completely filled with electrons. The probability that electrons are thermally excited from the valence to the conduction band, thus leaving positively charged holes in the valence band, increases with temperature. Electrons in the conduction band and holes in the valence band, so-called charge carriers, contribute to the electric conductivity. For germanium, the gap between the valence and the conduction bands is 0.67 eV at room temperature. The energy needed to create an electron-hole pair is higher than this energy, i.e. 2.95 eV at 80 K, since also some energy goes into the excitation of phonons. Electrons can be excited to the conduction band through ionizing radiation as well. By applying a reverse bias voltage as shown in Fig. 1.8, the electrons and holes created by the passage of particles interacting with the detector material can be collected on the corresponding electrodes. The region between the contacts becomes depleted with increasing bias voltage V, and acts as the active volume of the detector. The bias voltage at which the depletion

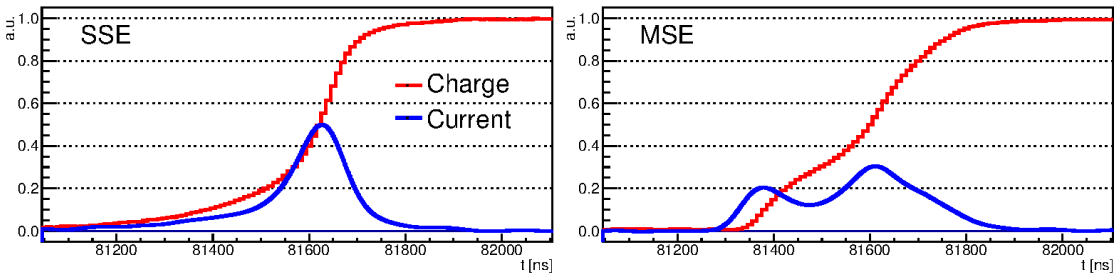

Figure 1.9: Candidate pulse traces taken from GERDA Phase I BEGe data for a SSE (left) and MSE (right). The maximal charge pulse amplitudes are set equal to one for normalization and current pulses have equal integrals. The current pulses are extracted from the recorded charge pulses by differentiation. Taken from [97].

zone extends over the entire detector volume is referred to as full depletion voltage. The drift of the charge carriers towards the corresponding electrodes in the electric field induce a mirror charge (charge pulse) on the readout electrode. The signal readout is then performed with charge sensitive pre-amplifiers, and finally the signals are digitized and recorded for offline analysis. The maximum amplitude of the charge pulse is proportional to the deposited energy, i.e the total number of electron-hole pairs generated, while the time structure contains information on the event topology.

Background discrimination capability

The time structure of the recorded pulses can be analyzed offline for background discrimination. Event topologies for background and $0\nu\beta\beta$ signal events can be significantly different. The $0\nu\beta\beta$ decay events have mostly localized energy deposition within few mm^3 in the detector volume, if the electrons lose little energy by bremsstrahlung, and are often referred to as single-site events (SSE). Whereas, most of the background events, e.g. photons interacting via multiple Compton scattering, deposit energy in several locations, well separated by few cm in the detector, and are referred to as multi-site events (MSE). The difference in drift paths and times of the charge carriers of SSE and MSE results in different pulse shapes. PSD methods use these features to distinguish between background- and signal-like events, and have been used in the $0\nu\beta\beta$ experiments [91–97].

An example PSD method for BEGe type detectors use the parameter A/E ratio, i.e. ratio of the maximum of the current pulse (A) to the energy (E), for discriminating SSE and MSE motivated by the differences in the current pulses for the two type of events [98,99]. Fig. 1.9 shows an example of a possible SSE (left) and MSE (right) charge and current pulses with same event energy, recorded by one of the BEGe detectors in GERDA Phase I [97].

Chapter 2

The Germanium Detector Array: Design, Setup and Data Taking

The GERDA (GERmanium Detector Array) experiment is conducting a search for $0\nu\beta\beta$ decay of the isotope ^{76}Ge, using an array of germanium detectors isotopically enriched in ^{76}Ge. It is located in an ultra-low-background environment with 1.4 km rock overburden (3800 m.w.e.), at the Laboratori Nazionali del Gran Sasso (LNGS) in Italy. The design and the physics goals of the experiment, as well as the efforts that went into background reduction, are discussed in the following sections. The first phase of physics data taking (Phase I) discussed in this thesis has been pursued between November 2011 and May 2013. The detectors operated in Phase I, off-line processing of the data, energy calibration, determination of the energy resolution, operational configuration during data taking, parameters of the Phase I data set, and finally, the blinding procedure adopted in Phase I are described.

2.1 Design and physics goals

As a main design feature, GERDA operates bare Ge detectors directly in LAr, which evolved from a proposal in [100]. The ultra-pure cryogenic liquid does not only provide the cooling medium necessary for the operation of the detectors, but also shields the detector array from external radiation. Detection of the LAr scintillation light can also allow for an active background veto system (planned for Phase II). In this concept, the amount of high-Z material in the vicinity of the detector array is minimized compared to the conventional shielding, which significantly reduces the background.

Fig. 2.1 shows the GERDA experimental setup with its main components. The germanium detectors mounted on strings are suspended in the LAr, contained in a vessel made from specially selected and screened low-background stainless steel, with an additional lining made from electroplated low background copper. The copper lining reduces the γ radiation from the vessel itself. The detectors are lowered into the LAr volume using a lock system located in a clean room. The LAr cryostat is placed inside a tank filled with ultra-pure water. The water tank is instrumented with photo-multipliers and functions as

Figure 2.1: Cutaway view of the GERDA experiment (Ge array not to scale), showing the main hardware components: the germanium detector array (1); the LAr cryostat (2) with its internal copper shield (3) and the surrounding water tank (4) housing the Cherenkov muon veto; the GERDA building with the superstructure supporting the clean room (5) and the lock (6). Various laboratories behind the staircase include the water plant and a radon monitor, control rooms, cryogenic infrastructure and the electronics for the muon veto. Taken from [19].

a Cherenkov detector to reject high energy muon events. The ultra-pure water in the tank also functions as a shield against external neutrons and γ-rays. Additionally, an array of plastic scintillators instrumented with PMTs are placed on top of the clean room, in order to veto the muons that are penetrating through the neck region of the cryostat.

The experiment is carried out in phases in terms of the goal sensitivity to $0\nu\beta\beta$ decay half life ($T^{0\nu}_{1/2}$). The goal of GERDA Phase I was to reach B of 10^{-2} cts/(keV·kg·yr) and an exposure of 20 kg·yr. This allows for a sensitivity, sufficient to scrutinize the positive claim for $0\nu\beta\beta$ signal, i.e. $T^{0\nu}_{1/2} = 1.19^{+0.37}_{-0.23} \cdot 10^{25}$ yr [17], reported by a group from the HDM collaboration. This goal has been accomplished with the data acquired in November 2011–May 2013, using eight semi-coaxial $^{\text{enr}}$Ge detectors previously operated by the HDM and IGEX experiments, as well as five newly produced enriched BEGe detectors [101]. With a total exposure of $\mathcal{E} = 21.6$ kg·yr and a background index of $B = 1.1 \cdot 10^{-2}$ cts/(keV·kg·yr) (with PSD, reduced signal efficiency $\sim 90\%$), the long-standing claim has been refuted by GERDA using the same candidate isotope ^{76}Ge, thus, in a model independent way [18]. The details of the $0\nu\beta\beta$ decay analysis and results from Phase I are given in Chapter 7.

A further exploration of $0\nu\beta\beta$ decay will be pursued in GERDA Phase II, with B of 10^{-3} cts/(keV·kg·yr) and an exposure of 100 kg·yr, improving the sensitivity by a factor of about 10. This is planned to be achieved by employing additionally about 30 newly produced enriched BEGe detectors (~ 20 kg of ^{76}Ge) and making use of their enhanced PSD capabilities, as well as using LAr instrumentation to detect coincident scintillation light and reject background events. Transition from Phase I to Phase II setup is currently ongoing.

2.2 Background reduction strategies and estimated background levels

In GERDA Phase I, the achieved background level around $Q_{\beta\beta}$ is an order of magnitude lower with respect to the previous $0\nu\beta\beta$ HPGe experiments, HDM and IGEX. A factor of 10 suppression in B succeeded by operating Ge detectors in a cryostat that holds $64\,\mathrm{m}^3$ of LAr, used as cooling medium and shielding material simultaneously. This allows for a significant reduction in cladding and shielding material around the detector array, and hence in the accompanying background sources. In this concept, the background produced by interactions of cosmic rays is reduced with respect to the conventional shielding concept of HDM, IGEX or MAJORANA, due to the lower Z of the shielding material [19]. About a 2 m thick LAr shields the detectors against the remnants of the external γ background penetrating the surrounding water, and against the radioactivity of the cryostat itself. In addition, about a 3 m thick pure water buffer surrounding the LAr cryostat moderates and absorbs neutrons and attenuates the flux of external γ radiation.

The instrumentation of the water tank with PMTs (together with the plastic scintillator panels above the neck of the cryostat) provides a high muon-veto efficiency, through the identification of muons by the detection of their Cherenkov light. The muon rejection efficiency (ϵ_{MR}) was estimated from the data acquired during the GERDA commissioning. The efficiency is defined as the probability that an event induced in the Ge detectors by a cosmic-ray muon is accompanied by a valid trigger of the Cherenkov veto system. The resulting efficiency is $\epsilon_{MR} = (97.9^{+1.2}_{-2.0})\%$ (median with 68% central interval), or $\epsilon_{MR} > 94.2\%$ (95% credibility interval) [19, 102]. The muon-induced background index at $Q_{\beta\beta}$, due to muon-induced single-detector events in Ge not tagged by the muon-veto, is estimated to be $B_\mu < 2.0 \cdot 10^{-4}\,\mathrm{cts/(keV{\cdot}kg{\cdot}yr)}$ at 95% C.L. [103], which meets the background requirement for Phase I (and Phase II).

The Phase I detectors, used previously in the HDM and IGEX experiments, were stored at an underground facility whenever possible, in order to avoid exposure to cosmic rays, and hence, to minimize the cosmogenic production of ^{68}Ge and ^{60}Co, which contribute to the background in the region of interest around $Q_{\beta\beta}$. Also, in between various reprocessing operations, the detectors were stored underground at the HADES facility [104]. The total exposure above ground during the reprocessing of the Phase I detectors, including the transportation from LNGS to HADES and back, was ~ 5 days [105]. Total specific activity of the internal ^{60}Co and ^{68}Ge contaminations of all the Phase I (enriched semi-coaxial) detectors were calculated for the reference date of July 2010, and were summarized in Table 6.5 and 6.6 of [105]: it varies between $0.09 - 0.49\,\mu$Bq/kg for ^{60}Co and $0.03 - 0.07\,\mu$Bq/kg for ^{68}Ge. In these calculations, the cosmogenic production rate of ^{60}Co and ^{68}Ge in germanium isotopically enriched to 86% in ^{76}Ge, and at sea level, was assumed to be about 4 atoms/(kg·d) and 1 atom/(kg·d), respectively [106]. Also, all the periods of time spent above ground, starting from the crystal growth until the final transport to LNGS, were considered. The background index, B, due to the internal ^{60}Co and ^{68}Ge contamination of individual detectors, given the calculated activities and using Monte Carlo simulation for efficiencies, was given in [105] as $(1.0 - 2.2) \cdot 10^{-3}$ and $(0.2 - 0.5) \cdot 10^{-3}\,\mathrm{cts/(keV{\cdot}kg{\cdot}yr)}$, respectively. These estimations are valid for the reference date of July 2009. Considering

the actual beginning date of Phase I data taking, i.e. November 2011, the activity, hence the expected B, of ^{60}Co ($T_{1/2} = 5.3\,\mathrm{yr}$) has decreased by a factor of 0.74, and that of ^{68}Ge ($T_{1/2} = 271\,\mathrm{d}$) by a factor of 0.12. The contribution from ^{60}Co, although still within Phase I specifications with $B < 10^{-2}\,\mathrm{cts/(keV{\cdot}kg{\cdot}yr)}$, is a relevant one in Phase I. Whereas, the contribution from ^{68}Ge is negligible. The total activity of the internal ^{60}Co and ^{68}Ge for the newly produced BEGe detectors is calculated to be 0.58 and $3.70\,\mu$Bq (for November 2011), respectively, given the assumed activation rate for these isotopes according to [107] and the known histories of exposure to cosmic rays of the individual detectors. The calculated activities of the internal ^{60}Co and ^{68}Ge contaminations of the individual detectors are used as constraints on the contribution of these backgrounds, while modeling the Phase I background spectrum (see Section 4.7).

Another important step for achieving a low background level was the careful selection of radio-pure materials, carried out by using state-of-the-art screening techniques [19]. The hardware components used in the setup were tested for their radio-purity prior to installation: parts close to (up to 2 cm) and at medium distance (up to 30 cm) from the detectors, as well as the stainless steel and the copper used for construction of the cryostat, were screened using HPGe screening facilities or ICP-MS measurements. The cryostat volume with its copper lining and material in the lock system installed were tested for ^{222}Rn emanation [110]. Table 2.1 lists the total measured activities (or limits) of the most relevant components, as well as their expected B contributions obtained by using efficiencies derived from MC simulations [108, 109]. The measured activities lead to a total expected contribution of $B \approx 3 \cdot 10^{-3}\,\mathrm{cts/(keV{\cdot}kg{\cdot}yr)}$ from the close-by sources, $B \approx 10^{-3}\,\mathrm{cts/(keV{\cdot}kg{\cdot}yr)}$ from the medium distance sources and $B < 10^{-3}\,\mathrm{cts/(keV{\cdot}kg{\cdot}yr)}$ from the far sources, which are tolerable for Phase I, i.e. $B < 10^{-2}\,\mathrm{cts/(keV{\cdot}kg{\cdot}yr)}$.

^{222}Rn can be continuously produced in the LAr by emanation from the material with ^{226}Ra contamination. The ^{222}Rn emanation rate of the cryostat in its final configuration is $(54.7 \pm 3.5)\,\mathrm{mBq}$, and that of the lock system is $< 17\,\mathrm{mBq}$. Given this activity and according to the evaluations based on MC simulation [111], a background contribution of B most likely less than $\approx 0.7 \cdot 10^{-3}\,\mathrm{cts/(keV{\cdot}kg{\cdot}yr)}$ is expected, as not all ^{222}Rn from lock system will end up in the LAr. In this evaluation, only the contribution from ^{214}Bi originating from ^{222}Rn were taken into account (α emitters drifting towards the detector surfaces were neglected) and the ^{222}Rn in LAr was assumed to be uniformly distributed. A higher contribution could be expected, if ^{222}Rn in LAr could be transported close to the detector array by convection; the convection turn around time is expected to be similar to the ^{222}Rn half life, i.e. most of the ^{222}Rn will not decay before reaching the detectors [112]. In order to prevent this, a central volume of about 3 m height and 750 mm diameter around the detector array is separated from the rest of the LAr volume by a $30\,\mu$m thick cylindrical copper foil, called radon shroud in the following. The radon shroud is expected to reduce this background contribution by up to a factor of seven [19].

Li salt used to dope the n^+ surfaces of detectors was screened. The measurements yielded a ^{226}Ra contamination of $(17 \pm 5)\,\mathrm{mBq/kg}$. Assuming an n^+ Li doping of 10^{16} Li nuclei per cm^3 germanium, an overall Li weight per detector is expected to be $\approx 5\,\mu$g. This results in a negligible contribution to the total B at $Q_{\beta\beta}$, even under the assumption that the ^{226}Ra contamination diffuses into germanium with the same efficiency as Li.

Table 2.1: Gamma ray screening and ^{222}Rn emanation measurement results for hardware components, and estimated contribution to background index at $Q_{\beta\beta}$, B, from each component. The activity of the mini shroud was derived from ICP-MS measurement assuming secular equilibrium of the ^{238}U decay chain. Estimates of the B are based on efficiencies obtained by MC simulations [108, 109] of the GERDA setup. Table adapted from [19, 22].

Component	Units	^{40}K	^{214}Bi and ^{226}Ra	^{228}Th	^{60}Co	^{222}Rn	B [10^{-3} cts/(keV·kg·yr)]
Close sources: up to 2 cm from detectors							
Copper det. support	μBq/det.	< 7	< 1.3	< 1.5			< 0.2
PTFE det. support	μBq/det.	6.0 (11)	0.25 (9)	0.31 (14)			0.1
PTFE in array	μBq/det	6.5 (16)	0.9 (2)				0.1
Mini shroud	μBq/det.		22 (7)				2.8
Li salt	mBq/kg		17(5)				$\approx 0.003^{\dagger}$
Medium distance sources: 2–30 cm from detectors							
CC2 preamps	μBq/det.	600 (100)	95 (9)	50 (8)			0.8
Cables and suspension	mBq/m	1.40 (25)	0.4 (2)	0.9 (2)	76 (16)		0.2
Distant sources: further than 30 cm from detectors							
Cryostat	mBq					54.7 (35)	< 0.7
Copper of cryostat	mBq	< 784	264 (80)	216 (80)	288 (72)		] < 0.05
Steel of cryostat	kBq	< 72	< 30	< 30	475		
Lock system	mBq					< 17	< 0.03
^{228}Th calib. source	kBq			20			< 1.0

† Value derived for 1 mg of Li salt absorbed into the surface of each detector.

In the first months of data taking during the GERDA commissioning phase (started in July 2010), the 1525 keV γ-ray line of ^{42}K (progeny of ^{42}Ar) was measured with an intensity well above the expected value adopted in the GERDA proposal [106]. Also, the B at $Q_{\beta\beta}$ was higher than expected, which was later found to be correlated with the ^{42}K background. In many runs with different configurations, it could be demonstrated that the count rate of the 1525 keV γ-ray line is influenced by the electric field generated in the LAr volume by the detector array; the positive ^{42}K ions in LAr drift towards the detector surfaces at negative potential. In order to prevent the collection of ^{42}K from a large volume, the detector strings were enclosed in a 60 μm thick cylindrical Cu foil with 113 mm diameter, called mini-shroud. The mini-shroud was not present in the original design of GERDA. Its presence has significantly suppressed the ^{42}K background. The measurements and studies concerning the ^{42}K background, performed during commissioning, are described in Section 3.2.

The background index of the GERDA Phase I enriched detectors, considering both semi-coaxials and BEGes, is $B = (24 \pm 2) \cdot 10^{-3}$ cts/(keV·kg·yr) after applying data quality, detector anti-coincidence and muon veto cuts, and for the full data set with a total exposure 21.6 kg·yr. It reduces to $B = (11^{+2}_{-1}) \cdot 10^{-3}$ cts/(keV·kg·yr) after applying PSD cuts, resulting in a $\sim 90\%$ reduction in the $0\nu\beta\beta$ decay signal efficiency. The details of the B evaluation in Phase I are given in Section 6.4.

2.3 Phase I detectors and data taking

GERDA Phase I data taking, pursued between November 2011 and May 2013, is described along with the employed detectors, the reference off-line signal processing, data quality cuts, data quality monitoring, energy calibration and resolution. More detailed information on the experimental performance of Phase I data taking can be found in [19]. The operational configuration of the detectors in the data taking runs and the experimental parameters of the official Phase I data set are summarized. The blinding procedure adopted in Phase I is also discussed.

2.3.1 Detectors and signal read-out

Different types of HPGe detectors were operated in GERDA Phase I: semi-coaxial type ($^{\text{enr}}$Ge-coax) and broad energy germanium (BEGe) detectors, both produced from material isotopically enriched in ^{76}Ge; as well as semi-coaxial type with natural isotopic abundance ($^{\text{nat}}$Ge-coax). All eight $^{\text{enr}}$Ge-coax detectors were previously employed in the HDM [113] and IGEX [114] experiments, and all three $^{\text{nat}}$Ge-coax ones in the GENIUS-TF experiment [115]. Prior to their operation in LAr in GERDA, they underwent specific refurbishing processes [105, 116] at Canberra Semiconductor NV, Olen. In total five new custom-made BEGe detectors [101], originally produced for GERDA Phase II, were employed in Phase I as well, both for testing their operation in LAr and for increasing the Phase I exposure.

All Phase I detectors are p-type diodes. The $^{\text{enr}}$Ge-coax detectors have a cylindrical geometry with a closed-end coaxial bore hole, and a "wrap around" n^+ conductive lithium layer (~ 1 mm) that is separated from the boron implanted p^+ contact by a circular groove

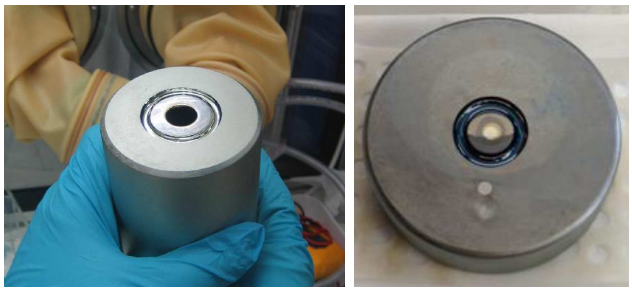

Figure 2.2: An ^{enr}Ge-coax (left) and a BEGe (right) detector operated in Phase I.

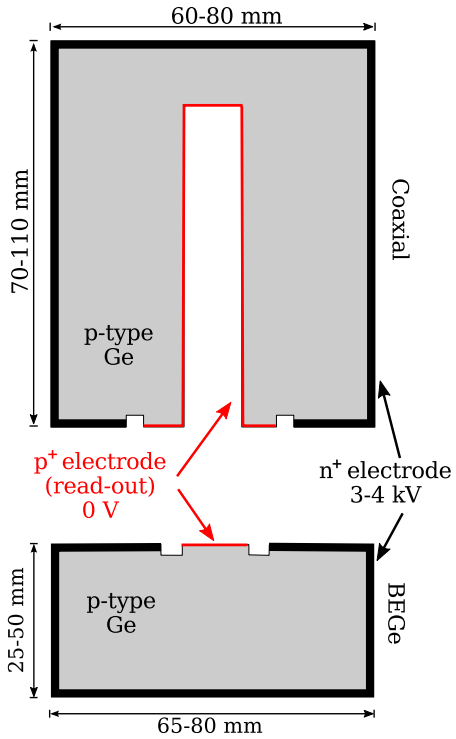

Figure 2.3: Schematic drawing of a ^{enr}Ge-coax (top) and a BEGe detector (bottom) operated in GERDA Phase I. The conductive lithium layer (n^+ electrode) and the boron implanted layer (p^+ electrode) are separated by a groove [22].

(see Fig. 2.2 left). The custom-made BEGe detectors have a small p^+ electrode, while the n^+ electrode is covering the whole rest of the surface, separated from the p^+ electrode by a groove (see Fig. 2.2 right). A schematic drawing of both types, indicating also the dimensions, is depicted in Fig. 2.3. The main parameters of all the detectors, such as the enrichment fraction f_{76}, total mass M, active mass M_{act}, active volume fraction f_{AV}, and the thickness of the effective n^+ dead layer d_{dl}, are listed in Table 2.2. The d_{dl} on the p^+ surface of ^{enr}Ge-coax detectors is expected to be around 300 nm, based on the calculation of the penetration depth of B ions given the ion energy used for the implantation.

Table 2.2: Main parameters for the Ge detectors employed in GERDA commissioning and Phase I: isotopic abundance for ^{76}Ge (f_{76}), total mass (M), active mass (M_{act}), active volume fraction (f_{AV}) and the effective thickness of the n^+ dead layer (d_{dl}). The numbers in parentheses give the 1σ uncertainties. Table adapted from [22].

Detector	f_{76} (Δf_{76})	M [g]	M_{act} (ΔM_{act}) [g]	f_{AV} (Δf_{AV})	$\Delta f_{AV,u}$	$\Delta f_{AV,c}$	d_{dl} [mm]
Enriched semi-coaxial detectors							
ANG1	0.859 (29)	958	795 (50)	0.830 (52)	0.045	0.027	1.8 (5)
ANG2	0.866 (25)	2833	2468 (145)	0.871 (51)	0.043	0.028	2.3 (7)
ANG3	0.883 (26)	2391	2070 (136)	0.866 (57)	0.049	0.028	1.9 (7)
ANG4	0.863 (13)	2372	2136 (135)	0.901 (57)	0.049	0.029	1.4 (7)
ANG5	0.856 (13)	2746	2281 (132)	0.831 (48)	0.040	0.027	2.6 (6)
RG1	0.855 (15)	2110	1908 (125)	0.904 (59)	0.052	0.029	1.5 (7)
RG2	0.855 (15)	2166	1800 (115)	0.831 (53)	0.046	0.027	2.3 (7)
RG3	0.855 (15)	2087	1868 (113)	0.895 (54)	0.046	0.029	1.4 (7)
Enriched BEGe detectors							
GD32B	0.877 (13)	717	638 (19)	0.890 (27)			1.0 (2)
GD32C	0.877 (13)	743	677 (22)	0.911 (30)			0.8 (3)
GD32D	0.877 (13)	723	667 (19)	0.923 (26)			0.7 (2)
GD35B	0.877 (13)	812	742 (24)	0.914 (29)			0.8 (3)
GD35C	0.877 (13)	635	575 (20)	0.906 (32)			0.8 (3)
Natural semi-coaxial detectors							
GTF32	0.078 (1)	2321	2251 (116)	0.97 (5)			0.4 (8)
GTF45	0.078 (1)	2312					
GTF112	0.078 (1)	2965					

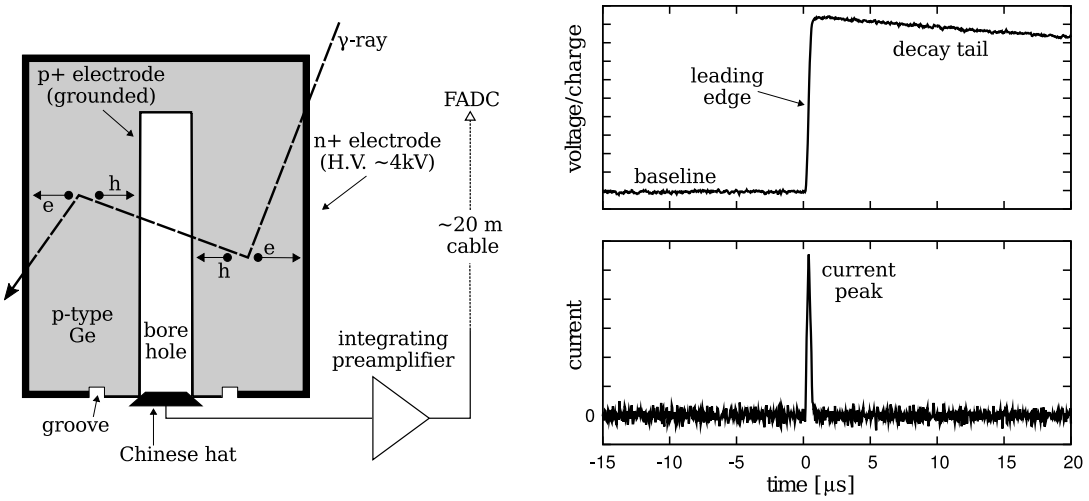

Figure 2.4: Left: Vertical section of a Phase I $^{\text{enr}}$Ge-coax detector showing the electrode scheme and the read-out chain. Right: Traces containing a characteristic pulse induced by the collection of electron-hole pairs created by interactions of γ-rays or charged particles in the detector. Figure from [20]

In the normal readout scheme (DC coupled), the detectors are operated by applying high voltage to the n^+ electrode and grounding the p^+ electrode, which is connected to a charge sensitive amplifier. An alternative readout scheme, AC coupling, is possible by grounding the n^+ contact and applying negative high voltage to the p^+ contact, which has been used in Phase I commissioning. In this read-out mode, the analog signal is still read out from the p^+ contact but coupled with a HV capacitor to the amplifier. Fig. 2.4 shows a drawing of an $^{\text{enr}}$Ge-coax detector with the electrode scheme and the read-out chain in the left panel. The right panel shows an example charge pulse (upper plot), and also the first derivative of the charge pulse (lower plot) which corresponds to the current pulse.

The signals are digitized by 14-bit flash-ADCs (FADC), running at 100 MHz sampling frequency and equipped with integrated anti-aliasing bandwidth filters [117–119]. The FADC computes in run-time two traces for each event: a high-frequency-short (HFS) trace, sampled at 100 MHz and 4 μs long; and a low-frequency-long (LFL) trace, sampled at 25 MHz and 160 μs long. The HFS trace is used for studying the time-structure of the pulse leading edge, i.e. for pulse shape analysis. The LFL trace is used for tasks that do not require high time resolution, such as analyzing the baseline or pulse decay tail and energy reconstruction. Eventually, both types of FADC traces are written to disk for off-line analysis.

2.3.2 Off-line signal processing

The off-line processing of the FADC traces is performed with the GERDA software framework GELATIO [120]. The procedure is described in [20,121]. The signal processing is performed along chains of modules, with each module being in charge for a unique task. The output of a module can be scalar parameters, like the amplitude of the pulse, as

well as new traces obtained by applying shaping filters such as smoothing, deconvolution, etc. The first module (*TopModule*) extracts the traces from the input file. It performs preprocessing operations like changing the pulse polarity if needed. After the *TopModule*, the LFL and HFS traces go through two different chains of modules. The HFS traces are processed along a chain tailored to study the time structure of the pulses, like computing the current signal and extracting its basic features, and will not be discussed further. The chain that process the LFL traces provides the parameters that are used for data selection, quality monitoring and spectral analysis. Its modules are briefly described in the following.

BaselineModule analyzes the baseline of the signal, i.e. computing the average value, the root-mean-square deviation (RMS) and the linear slope before the leading edge, and also performs a baseline restoration.

TriggerModule identifies the beginning of the pulse leading edge, i.e. the trigger position. It implements a leading-edge discriminator, with a threshold dynamically defined as three times the RMS of the signal baseline. The trigger is accepted if the signal remains for at least 40 μs above threshold.

FTTriggerModule is used to identify pile-up events, i.e. multiple physical pulses occurring within the same trace. The module applies to the input signal a 1.5 μs moving differentiation filter and a 1 μs moving average filter for noise reduction. The resulting trace has a peak for each sharp variation of the signal, such as the leading edge of a pulse. The number and the position of the peaks are estimated by applying a leading-edge discriminator. The signal has to remain at least 1 μs above the threshold, which is four times the RMS of the baseline.

EnergyGaussModule reconstructs the event energy using an approximate Gaussian filter [122, 123]. The pulse is differentiated by a moving differentiation filter and then integrated 20 times by a moving average filter (5 μs width) to achieve an approximated Gaussian shape. The energy information is stored in the maximum amplitude of the final quasi-Gaussian pulse.

RiseTimeModule computes the rise time between 10% and 90% of the maximum amplitude of the pulse. The maximum amplitude is determined as the difference between the maximum of the pulse and the average baseline value. The 10% and 90% of the maximum amplitude are found by starting from this maximum position.

2.3.3 Data quality cuts

The parameters obtained along the signal processing chain described in the previous section were used to apply a set of quality cuts on the signals [20,121]. The quality cuts aim to reject: *a*) corrupted signals or signals due to non-physical events like discharges, cross-talk, pick-up noise; *b*) particular type of signals like from pile-up events and accidental coincidences. The parameters used to identify and remove these signals have well-defined ranges for the properly processed physical events, that are meant to be kept in the data set for further physics analysis.

a) type events can have anomalous decay tails, leading edge positions and widths

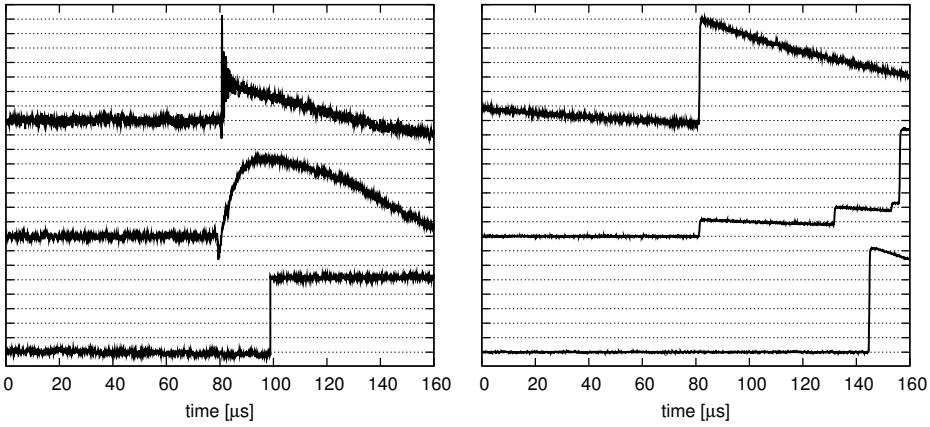

Figure 2.5: Illustrative traces generated by non-physical events (left), pile-up events (right, top-middle trace) and accidental coincidences (right, bottom trace) [20, 121].

different than expected, or over/under shots (see Fig. 2.5 left). They are rejected by applying cuts on the position of the leading edge, the maximum amplitude of the Gaussian pulse, the 10-90% rise time (for pulses inconsistent with the detector charge collection time) and the maximum value of the trace samples (for pulses that exceed the dynamic range of the FADC).

b) type events consist of signals generated by the superposition of multiple physical pulses (pile-up), or that have a leading edge not aligned with the center of the trace (see Fig. 2.5 right). They are rejected by placing cuts on the values of the baseline slope, the number of triggers and the position of the main leading edge. The fraction of such events can reach up to 15% in a calibration run, which has a rate of ~ 100 events/s above 500 keV. Whereas, it is negligible in the physics run, where the count rate is $\sim 10^{-2}$ events/s above ~ 30 keV. The pile-up rejection cuts in Phase I were tuned to remove $\sim 100\%$ of the signals, for which the secondary event induces an increase of > 20 keV in the pulse amplitude and has a time difference of $\geq 2\,\mu$s from the main trigger.

2.3.4 Data quality monitoring

In order to monitor the stability of the data taking conditions and the data quality, several parameters, like the counting rates of different type of events, noise levels, baseline parameters, etc., were daily checked off-line by the analysis team [124, 125].

The count rates of the Ge detector, and events flagged by the muon veto, are expected to be approximately constant in time. A significant deviation from their average value can indicate problems in the operational performance of detectors or in the muon veto system. The occurrence of noise bursts can also cause a substantial increase of the event rate. In order to monitor the stability of the electronics, test pulses with fixed amplitude were produced by a pulser and fed to all DAQ channels during the entire data taking period. Test pulses were issued at a rate of 0.1 Hz (0.05 Hz in the last period). Since the pulser signal injected in the electronic chain is constant, a variation in its amplitude with

respect to time indicates a change in the global response of the electronic chain, e.g. gain drift, change in the system capacitance, etc. Also, fluctuations of the width of the test pulse line can be related to the electronic noise of the chain.

The position and RMS of the baseline as a function of time were daily monitored as well. Since the baseline is proportional to the detector leakage current, its parameters are sensitive to the variations in the noise and gain of the read-out chain.

Data taking periods with significant fluctuations in the monitored parameters, usually caused by hardware operations or sudden temperature variations, were removed from the data set.

2.3.5 Energy calibration and resolution

The energy scales of the individual detectors were determined by performing calibration runs with ^{228}Th sources once every one or two weeks during Phase I. After applying the data quality cuts (Section 2.3.3), the γ-ray peaks in the calibration spectrum are fitted with a Gaussian plus a sigmoid function defined as

$$f(x) = \frac{A}{\sqrt{2\pi}\sigma} e^{-(x-\bar{x})^2/2\sigma^2} + (B_L - B_R)\left[e^{(x-\bar{x})/2\sigma} + 1\right]^{-1} + B_R, \tag{2.1}$$

where $\bar{x}$ is the centroid of the peak, A the net area and σ the standard deviation. The parameters B_L and B_R indicate the background rate on the left and right side of the peak. Fig. 2.6 shows the energy spectra of the individual $^{\text{enr}}$Ge-coax detectors from a calibration run with ^{228}Th source. The subplots on the right side show the 583 and 2615 keV γ-ray peaks of ^{228}Th together with the best fit model (red lines), obtained by fitting the peaks with the function given in Eq. (2.1).

The energy resolution of the fitted γ-ray peaks in terms of FWHM ($= 2.35\,\sigma$) are indicated on the subplots as well. The FWHM of different detectors in this calibration run varies between 4.5 and 5.1 keV at 2614 keV and between 3.6 to 4.4 keV at 583 keV.

The energy calibration curve for each detector is extracted using the γ-ray lines of ^{228}Th at 583, 727, 861, 1620, 2104 and 2615 keV. The centroids of the six peaks are determined as described above, and the calibration curve is obtained by fitting these six points with a 2nd order polynomial. An example calibration curve is shown in the upper left plot in Fig. 2.7. The two residual plots shown in the same figure – the left one for fitting a linear function and the right one for fitting the reference 2nd order polynomial – demonstrates that, assuming only a linear function is not good enough to describe the data; its residual plot shows a parabolic behavior. The deviation from linearity is $< 0.1\%$ and likely to be related to the read-out electronic chain or the data acquisition system. The energy resolution of the ^{228}Th γ-ray line peaks as a function of energy is shown in the right plot of Fig. 2.7. The energy resolution function is obtained by fitting the points with the function

$$\sigma(E) = d + e \cdot \sqrt{E}, \tag{2.2}$$

where d and e are scalar parameters. The fit result shows that the zero point energy resolution, $\sigma(0\,\text{keV})$, achieved with this analysis in the presence of intrinsic noise of the read-out chain and data acquisition system is ~ 3 keV. The term $e \cdot \sqrt{E}$ accounts for the

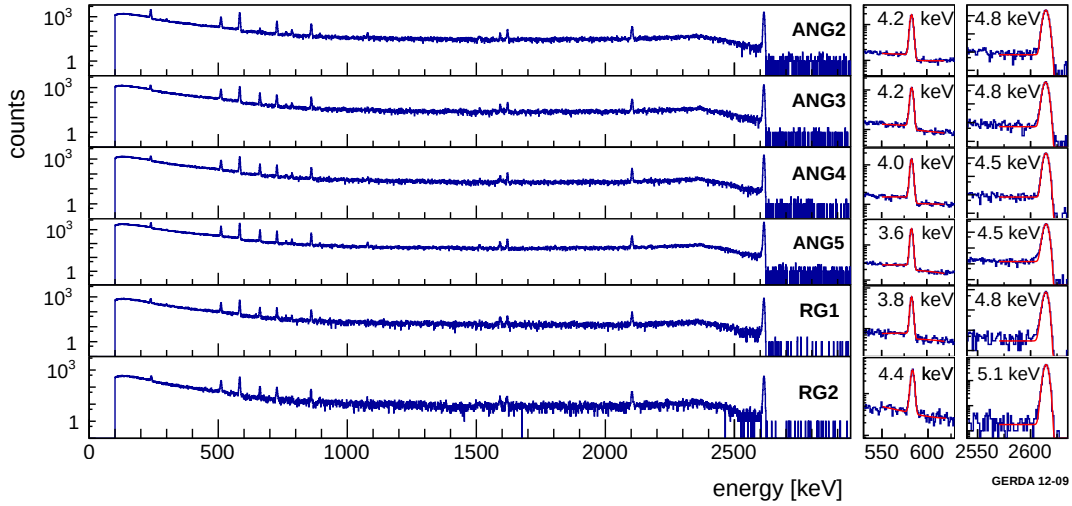

Figure 2.6: The energy spectra of the six $^{\text{enr}}$Ge-coax detectors from a calibration with ^{228}Th source. The blow-ups on the right show the fit results for the 583 keV and the 2615 keV γ-ray lines, also indicating the FWHM values resulting from the best fit [19].

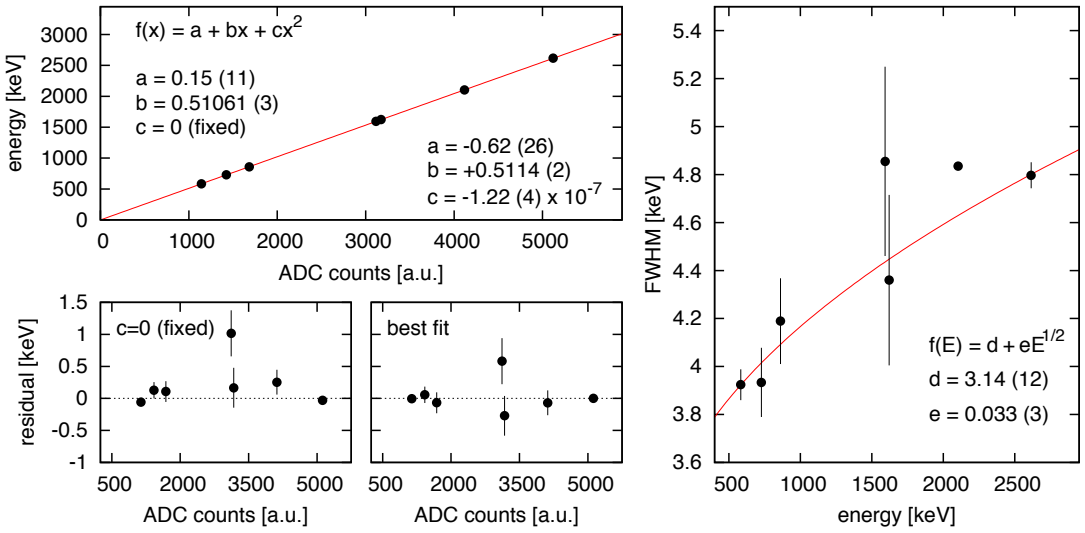

Figure 2.7: Upper left: A calibration curve obtained by fitting a second order polynomial to the data points of ^{228}Th γ-ray line positions (in ADC channel) as a function of the corresponding γ-ray energy. Lower left: The residuals for fitting a linear function by fixing $c = 0$ (left) and for fitting a quadratic function (right). Right: The energy resolution (FWHM) as a function of energy obtained by fitting the σ values of the ^{228}Th γ-ray lines. The point at 2103 keV is not included in the fit; this single escape peak is widened by Doppler effect [126]. Figure taken from [20].

statistical fluctuations in the number of produced charge pairs. The coefficient e includes also the Fano factor.

Fig. 2.8 shows the variation of the 2615 keV γ-ray line positions between consecutive calibrations performed during the first months of Phase I. The energy scale is stable within ± 1.3 keV (indicated with horizontal green lines), with a maximum deviation of 2 keV. The gain variations are assumed to be partly related to temperature changes in the clean room. The variations of the energy scale at $Q_{\beta\beta}$, if linearly scaled from those of the 2615 keV γ-ray peak, corresponds to ± 1 keV, which is smaller than the average FWHM of ~ 4.5 keV. The energy resolution at 2615 keV is also stable in the same period for all detectors within less than ± 0.5 keV, as demonstrated in Fig. 2.9.

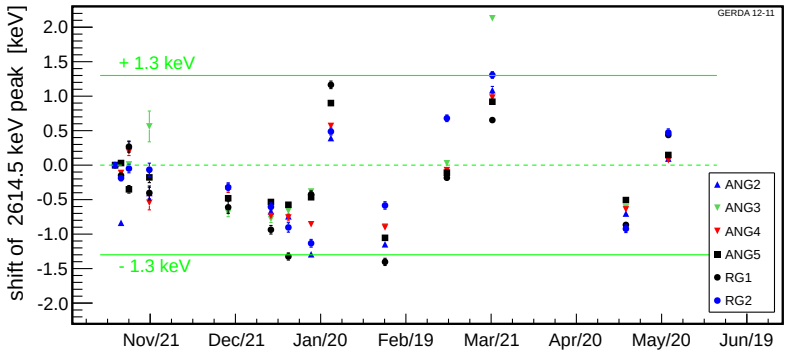

Figure 2.8: Shifts in the 2614.5 keV γ-ray line position (variations in gain) between successive calibrations performed during the first months of GERDA Phase I. The horizontal green lines indicate the ± 1.3 keV shifts, and correspond to ± 1 keV variations at $Q_{\beta\beta}$ for linear scaling. Figure from [19].

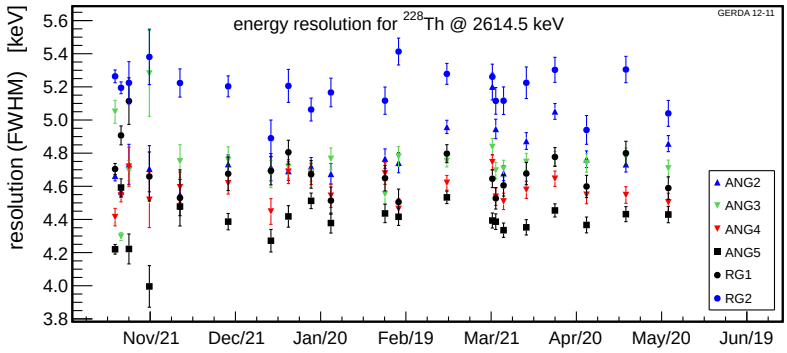

Figure 2.9: The energy resolution of the $^{\text{enr}}$Ge-coax detectors at 2615 keV in successive calibration runs with a ^{228}Th source. Figure from [19].

2.3.6 Phase I runs and configurations

After the completion of commissioning and meeting the design specifications, physics data taking of Phase I was started in November 2011. The detector array configuration in Phase I consisted of a 3 string setup, with each string carrying three detectors, and a 1 string setup used for employing different detectors in different periods, with a maximum of five detectors.

In the first part of Phase I data taking, pursued between 9.11.2011–22.05.2012 (Runs 25–32), all eight $^{\text{enr}}$Ge-coax detectors and a $^{\text{nat}}$Ge-coax detector were mounted on the 3 string setup, and two $^{\text{nat}}$Ge-coax detectors on the 1 string setup, in the following configuration:

- 1 string setup (no mini-shroud, AC coupled read-out mode)
  1. string: GTF45 (top), GTF32 (middle)
- 3 string setup (with mini-shrouds, DC coupled read-out mode)
  2. string: GTF112 (top), ANG2 (middle), ANG1 (bottom)
  3. string: RG1 (top), ANG4 (middle), RG2 (bottom)
  4. string: ANG3 (top), ANG5 (middle), RG3 (bottom)

All detector strings, except the 1. string carrying GTF45 and GTF32, were enclosed with individual mini-shrouds (see Fig. 2.10). The detectors in the mini-shrouds were operated in DC coupled read-out mode, i.e. positive HV was applied to the n^+ electrode (2500–4500 V) [1]. The $^{\text{nat}}$Ge-coax detectors on the string without mini-shroud were AC coupled (-3000 V), using a specially developed low background capacitor [127]. AC coupling minimizes the electric field in the LAr volume, and, as does the mini-shroud, prevents the drift of positive ^{42}K ions from LAr volume towards the detector surfaces. The unexpectedly high count rates of the 1525 keV γ-ray line of ^{42}K and the high background level around $Q_{\beta\beta}$ observed in the first measurements, could be mitigated through addition of a mini-shroud or AC coupling (see Section 3.2).

Two of the $^{\text{enr}}$Ge-coax detectors, ANG1 and RG3, started to draw too high leakage current shortly after their deployment. Their HVs were decreased gradually and both were eventually switched off. These detectors are completely omitted in the physics analysis. At the beginning of Run 27 (started in 11/01/2012), the 40 keV energy interval around $Q_{\beta\beta}$ was blinded. The details of the blinding procedure are described in Section 2.3.8. In Run 29 (started in 26/01/2012), the energy threshold of all the channels was set to 35 keV. Before, all had different thresholds between 50 and 100 keV. Also, the rate of the test pulse was reduced to 0.05 Hz, which was initially 0.1 Hz.

In Run 33 (02/06–15/06/2012) and Run 34 (15/06–02/07/2012), data taking continued without the 1 string arm as the installation of the five BEGe detectors was prepared. In these runs, the DAQ had only 9 channels. As Run 33 was very unstable and noisy run with many gain drifts, it was completely removed from the Phase I data set.

[1] ANG2: 3500 V, ANG3: 3500 V, ANG4: 3500 V, ANG5: 2500 V, RG1: 4500 V, RG2: 4000 V (later reduced), GTF112: 3000 V

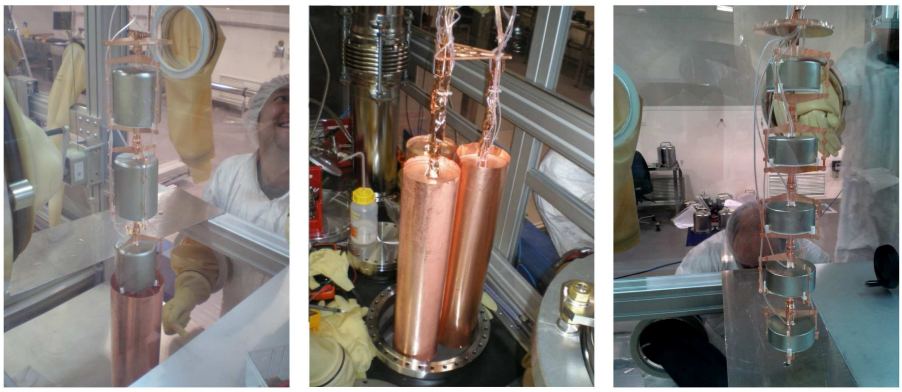

Figure 2.10: Left: Three $^{\text{enr}}$Ge-coax detectors mounted on a string. Middle: The 3 string setup with each string enclosed in their individual mini-shrouds. Right: Five BEGe detectors employed in GERDA Phase I.

The 1 string setup was operational again in Run 35, started in 08/07/2012, and was re-mounted with five BEGe detectors (see Fig. 2.10 right) in the following configuration:

1. string (top to bottom): GD32B, GD32C, GD32D, GD35B, GD35C

All BEGe detectors were operated in the normal read-out mode; 3500 V was applied on the n^+ contact. Starting from Run 35, the DAQ had 14 channels. This configuration did not change until the end of the Phase I data taking (21/05/2013).

One BEGe detector, GD35C, showed unstable behavior from the beginning on and was omitted from Phase I data analysis. Also, some other detectors showed unstable performance for certain periods: GD32B in Run 37 (03/09–27/09/2012, live time: 23.46 days); GD32D in Run 38 (27/09–11/10/2012, live time: 13.88 days) and in the last part of Run 46 (15/05–21/05/2013, live time: 5.61 days), and the corresponding data files were removed from the data set. Starting from March 2013, RG2 was operated below its full depletion voltage, and not considered for the data analysis in the rest of the data taking period.

2.3.7 Parameters of the Phase I data set

The Phase I data set used for the $0\nu\beta\beta$ decay analysis reported in [18] and discussed in more detail in Chapters 6 and 7, includes Runs 25–46, excluding Run 33. The important parameters of the considered data taking period were given in [128]. The operational time, i.e. in which DAQ was taking valid data, is 492.3 days. The ratio of the operational time to the total time elapsed, the duty factor, is 88.1%. Since some of the detectors were switched off and data from some detectors were tagged as invalid for some runs as discussed above, the valid measurement times (live times) differ from detector to detector. Table 2.3 lists the live times and the exposures calculated in terms of the total mass M ($\mathcal{E} = M \cdot t$), the active mass M_{act} ($\mathcal{E}_{AV} = M \cdot t \cdot f_{AV}$) and the ^{76}Ge active mass M_{76} ($\mathcal{E}_{76} = M \cdot t \cdot f_{AV} \cdot f_{76}$),

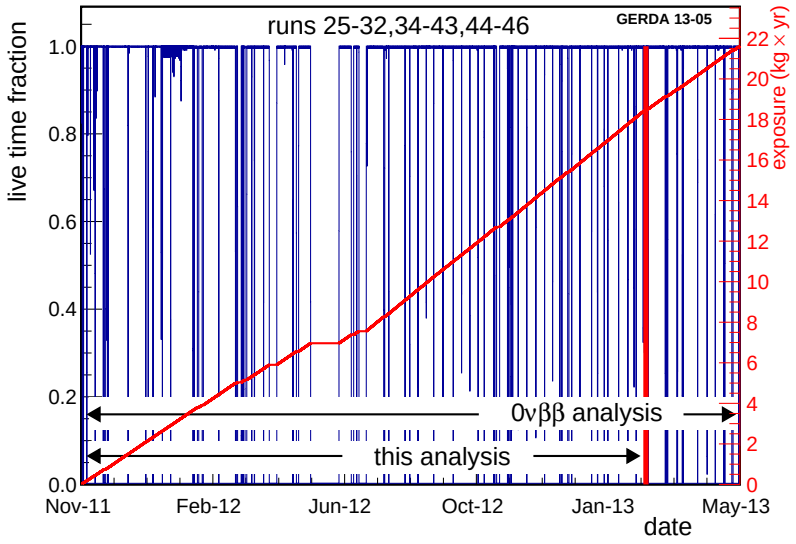

Figure 2.11: Live time fraction for the ^{enr}Ge detectors during the entire Phase I data taking period [22]. The spikes in the live time fraction distribution arise from the regular calibration measurements. The development of the exposure is also shown (red curve) with the right axis. See text for further details.

for the individual detectors. The live time is calculated using the monitoring test pulses (see Section 2.3.4), which had a rate of 0.1 Hz up to Run 28, and 0.05 Hz from Run 29 on. The data files were written to disk every 2 hours, thus, the uncertainty on the live time evaluated from this procedure is about $0.3 - 0.5\%$. Fig. 2.11 shows the live time fraction (left axis) and the total exposure $\mathcal{E}$ (right axis) for the ^{enr}Ge detectors as a function of time during entire Phase I data taking period. The spikes in the live time fraction distribution arise from the regular calibration measurements. The interruption of $\sim$ 10 days at the end of May 2012 together with the following 13 days was due to the decommissioning of the 1 string arm and the discarded Run 33 which follows that. There are also interruptions due to temperature instabilities in the Gerda clean room and due to operations for employing the 1 string arm re-mounted with the BEGe detectors (02–08/07/2012). The vertical red line indicates the end of the considered data taking period (03/03/2013) for the evaluation of the background model described in Chapter 4.

A significantly higher background level has been observed after the removal of the GTF detectors in the 1 string arm and deployment of the BEGe detectors in the GERDA cryostat in July 2012. Fig. 2.12 shows the observed background rate of the ^{enr}Ge-coax detectors in the energy region between 1550 and 3000 keV, in 15 day intervals. This period corresponds to Run 34 (15/06–02/07/2012) and Run 35 (08/07–27/07/2012), which are not discarded, but treated separately from the rest of the data set in physics analysis. Plausible explanations for the increased background level are possible non-uniformities of the contaminations in LAr and additional ^{222}Rn activity in the LAr introduced during the modification of the experimental surrounding. Possible scenarios are investigated in the background characterization and modeling described in Section 4.7.2.

Table 2.3: Phase I live times (t) and exposures calculated using the total mass M ($\mathcal{E}$), the active mass M_{act} ($\mathcal{E}_{AV}$) and the ^{76}Ge active mass M_{76} ($\mathcal{E}_{76}$) of the individual detectors.

Detector	t [days]	$\mathcal{E}$ [kg·yr]	$\mathcal{E}_{AV}$ [kg$_{AV}$ yr]	$\mathcal{E}_{76}$ [kg$_{76}$ yr]	$\mathcal{E}_{76}$ [mol yr]
Enriched semi-coaxial ($^{\text{enr}}$Ge-coax) *detectors*					
ANG2	490.9	3.81	3.32	2.88	37.9
ANG3	490.9	3.21	2.78	2.46	32.4
ANG4	490.9	3.19	2.87	2.49	32.7
ANG5	490.9	3.69	3.07	2.63	34.7
RG1	490.9	2.84	2.56	2.20	29.0
RG2	417.2	2.47	2.06	1.76	23.2
sum $^{\text{enr}}$Ge-coax		19.21			
Enriched BEGe detectors					
GD32B	280.0	0.55	0.49	0.43	5.7
GD32C	303.4	0.62	0.56	0.49	6.5
GD32D	284.0	0.56	0.52	0.46	6.0
GD35B	303.4	0.67	0.62	0.54	7.1
sum BEGe		2.40			
sum $^{\text{enr}}$Ge		21.61			

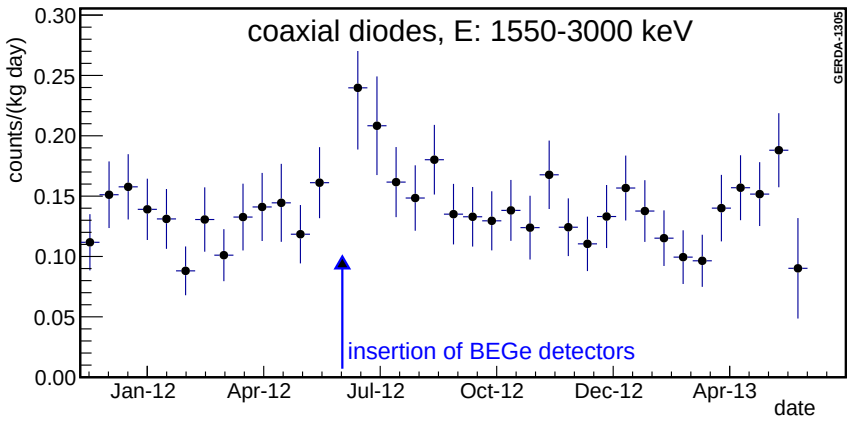

Figure 2.12: Development of the observed background rate of the $^{\text{enr}}$Ge-coax detectors in the energy region between 1550 and 3000 keV, in 15 days intervals [22]. A significant increase in the background level after modification of the setup in July 2012 can be seen.

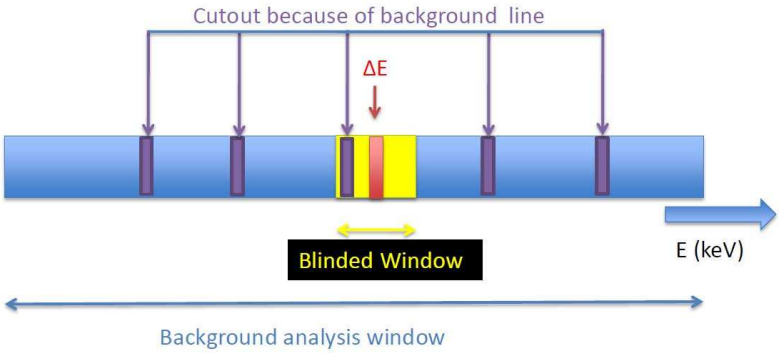

Figure 2.13: Representation of energy spectrum for definition of the energy windows used in the blind analysis [22]. See text for details.

2.3.8 Blind analysis strategy

GERDA adopted a blind analysis strategy in Phase I, in order to avoid bias in the event selection criteria. This has not been done before in the field of the search for $0\nu\beta\beta$ decay. Three different energy regions, as indicated in Fig. 2.13, are defined: background analysis window (blue region); blinding window (yellow region); and the energy interval ΔE around $Q_{\beta\beta}$, where $0\nu\beta\beta$ decay signal is expected (red region). All studies concerning background and signal studies, such as energy calibration, selection of valid runs, grouping of data from different runs or detectors into subsets, modeling the background spectrum, etc., were performed using the energy spectrum minus the blinding window, i.e. $Q_{\beta\beta} \pm 20\,\text{keV}$. The background level in ΔE was determined by the analysis of the events in the blue region. Unblinding was performed in two steps: first the blinding window except for the region ΔE, i.e. $Q_{\beta\beta} \pm 5\,\text{keV}$, was opened to see if there are any unexpected γ-ray lines; finally, ΔE was opened to analyze the entire spectrum for estimation of (or setting limit on) the $0\nu\beta\beta$ decay signal rate, given the background level evaluated from the blue region.

Blinding was carried out by making the raw data unavailable to the collaboration. Raw data were written to disk and events with energies $Q_{\beta\beta} \pm 20\,\text{keV}$, according to the DAQ reconstruction, were removed from the data files available for analysis. Blinding of the $Q_{\beta\beta} \pm 20\,\text{keV}$ window was started on 11/01/2012 (Run 27). After the finalization of the energy calibration and the background model, the blinding window was partially opened on 02/05/2013 (Run 46), except for the ΔE of $Q_{\beta\beta} \pm 5\,\text{keV}$ ($\pm 4\,\text{keV}$) window for the $^{\text{enr}}$Ge-coax (BEGe) detectors. Finally, after all data selection methods and cuts for the $0\nu\beta\beta$ analysis had been frozen, events in ΔE were made available for analysis on June 14th, 2013.

Chapter 3

Background studies in the commissioning phase

The GERDA experiment was commissioned for about a year before the start of Phase I. The commissioning data taking was dedicated to characterizing the background in the setup and finding the best operational configuration, both for good performance of the detectors and for achieving the background index (B) goal of Phase I. The data taking conditions (Section 3.1) and the background studies carried out during the commissioning phase are described in this chapter.

The first data collected using ^{nat}Ge-coax detectors revealed an unexpectedly high intensity of the 1525 keV γ-ray line from ^{42}K and a higher B than expected related to the high ^{42}K activity. The collaboration effort for understanding this background and finding methods for its mitigation are reported in detail in [129], and are briefly summarized in Section 3.2. Studies for gaining knowledge on the ^{228}Th background and investigating possible ^{228}Th contaminations in the upper parts of the setup (Section 3.3), as well as the ^{39}Ar background and determination of the ^{39}Ar specific activity from GERDA data (Section 3.4), are described.

3.1 Commissioning data taking

Commissioning of the GERDA experiment was carried out between July 2010 and November 2011. Data taking started with three ^{nat}Ge-coax detectors – GTF32, GTF45, GTF112 – mounted on 1 string arm (Runs 1–13) and continued with an additional string of ^{enr}Ge-coax detectors – RG1, ANG4, RG2 – installed in June 2011 (Runs 14–22). In Runs 8 and 9, GTF112 was replaced with a natural BEGe type detector. The main parameters for all detectors employed in commissioning are given in Table 2.2. The energy resolution of the detectors was between 4.5–6.0 keV (FWHM) at 2.6 MeV. The data taking runs with the parameters of interest for the considered background study are listed and described in the following sections. The last two data taking runs (Runs 23 and 24) performed in October – November 2011, before the start of GERDA Phase I, were dedicated to preparing and testing the Phase I setup with all ^{enr}Ge-coax detectors, and are not used

in physics analysis.

In order to investigate the background sources in the setup, various operational configurations were tested in different runs. For mitigating the ^{42}K background, the detector string was enclosed in a 60 μm cylindrical Cu foil with 113 mm diameter, called mini-shroud, that prevents the collection of ^{42}K from a large LAr volume. In some runs, GTF45 and GTF112 detectors were encapsulated with a thin copper foil, also for investigating a possible background suppression. The polarities of voltages of the Rn-shroud and mini-shroud and operational voltage of the detectors were varied, in order to change the surrounding electric field and study the drift of ^{42}K ions in LAr towards detector surfaces. Also, an alternative readout scheme (AC coupled), in which negative HV is applied to the p^+ electrode, was tested in some runs with the same motivation. This electrode scheme prevents the formation of electric field in the LAr volume. The detector string position in the cryostat was varied in many runs, for investigating the locations of the background sources in the setup, especially the contributions from the ^{238}U/^{232}Th decay chains. All these configurations are discussed in the following, while describing the dedicated background studies.

3.2 Investigation of the ^{42}K background by changing its distribution in LAr

^{42}K is a progeny of ^{42}Ar, which is expected to be present in the GERDA LAr that is produced from atmospheric argon (see Section 1.3.4). ^{42}K decays with 81.9% probability through β-decay, $Q_\beta = 3525.4$ keV, to the ground state of ^{42}Ca, and with 17.6% probability to the first excited state of ^{42}Ca, that promptly emits a 1525 keV γ-ray (Fig. A.3). The decays of ^{42}K can contribute to the background at $Q_{\beta\beta}$ due to the Q-value of ^{42}K well above 2039 keV.

In the first GERDA commissioning runs, the 1525 keV γ-ray line of ^{42}K had 20 times higher count rate compared to the expectation. The expected rate was ~ 0.1 cts/(kg·day), as estimated through a MC simulation of the realistic experimental setup and by assuming a uniform ^{42}K distribution in LAr [129], given the upper limit on the ^{42}Ar specific activity in [88]. The observed B at $Q_{\beta\beta}$ was ~ 0.15 cts/(keV·kg·yr), which is an order of magnitude higher than the goal B of GERDA Phase I. The high count rate can be explained by the drift of ^{42}K ions (positively charged after the decay of ^{42}Ar) towards the detector surfaces at negative potential (holder and readout contact) due to the electric field dispersed in the LAr. Several different configurations to change the surrounding electric field were tested, in order to minimize the count rate at 1525 keV γ-ray line of ^{42}K (R_{1525}) and in the energy region of interest around $Q_{\beta\beta}$.

Fig. 3.1 shows the measured R_{1525} in cts/(kg·day) and B in cts/(keV·kg·yr) in the commissioning Runs 1–13. Table 3.1 lists those runs together with the measurement date, the detectors and their operational voltage, and the voltages applied on the mini-shroud and the Rn-shroud. In Runs 2, the Rn-shroud was biased at -400 V, trying to drift positively charged ^{42}K ions towards the Rn-shroud and, thus, to reduce R_{1525} which is 2.0 cts/(kg·day) in the first run. The detector operating voltage was reduced

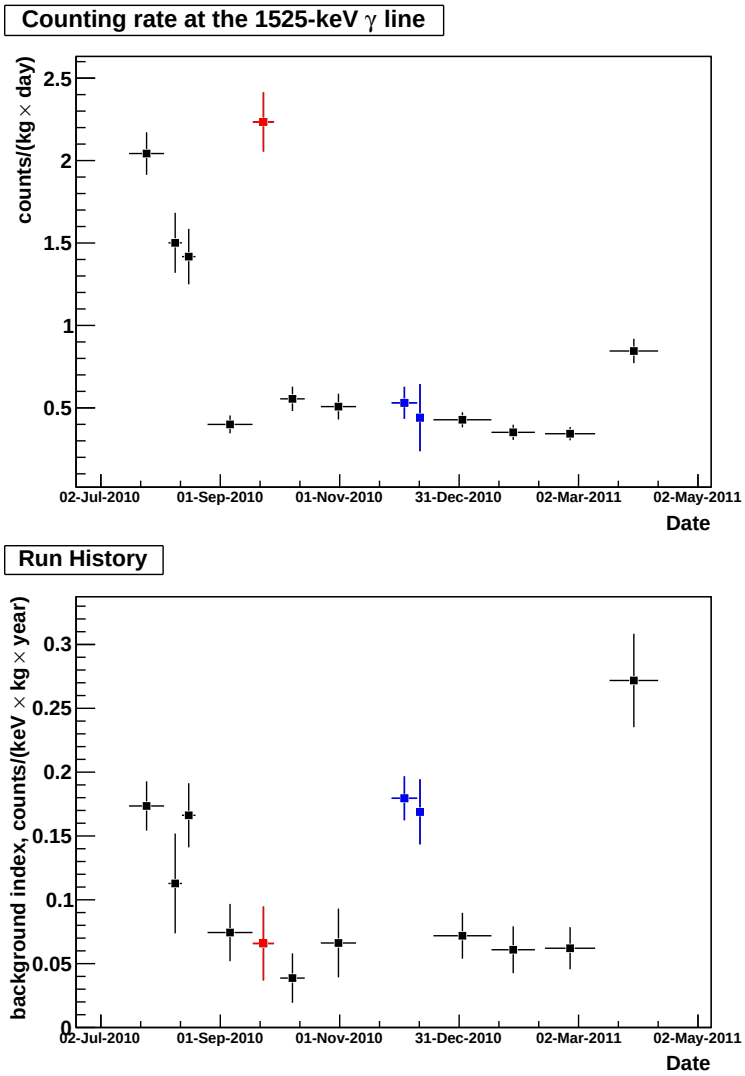

Figure 3.1: The measured count rate of the 1525 keV γ-ray line of ^{42}K (top) and the background index at $Q_{\beta\beta}$ (bottom) in the commissioning Runs 1–13. The points in the plots correspond to the data taking runs listed in Table 3.1. See text for details.

Table 3.1: GERDA commissioning runs along with the measurement date, detectors and their operational voltage and the voltage applied on the mini-shroud, M, and Rn-shroud, R (F stands for floating).

Runs	Date	Detectors	Det. voltage [V]	Shroud M / R [V]
1	16/07/10 – 03/08/10	GTF45, GTF32, GTF112	3000	- / F
2	05/08/10 – 10/08/10	GTF45, GTF32, GTF112	3000	- / −400
3	12/08/10 – 16/08/10	GTF45, GTF32, GTF112	2500	- / −400
4	25/08/10 – 17/09/10	GTF45*, GTF32, GTF112	3500	0 / −400
5	17/09/10 – 28/09/10	GTF45*, GTF32, GTF112	3500	−200 / +500
6	01/10/10 – 14/10/10	GTF45*, GTF32, GTF112	3500	0 / 0
7	21/10/10 – 09/11/10	GTF45*, GTF32, GTF112	3500	−200 / −400
8‡	27/11/10 – 10/12/10	GTF45†, GTF32, BEGe	3500	0 / −400
9	10/12/10 – 13/12/10	GTF45†, GTF32, BEGe	3500	0 / −400
10	18/12/10 – 17/01/11	GTF45†, GTF32, GTF112†	3500	0 / −400
11	17/01/11 – 08/02/11	GTF45†, GTF32, GTF112†	3500	0 / 0
12	13/02/11 – 16/03/11	GTF45, GTF32, GTF112	−3500	0 / −400
13	18/03/11 – 12/04/11	GTF45, GTF32, GTF112	−3500	- / −400

* HV = 1500 V.
† Encapsulated.
‡ Muon veto not active.

to 2500 V in Run 3, in order to change the surrounding electric field as well. In these runs, $R_{1525} \approx 1.5\,\mathrm{cts/(kg{\cdot}day)}$. There were also many events at higher energies, even above the 2615 keV ^{208}Tl line. These events can be partly attributed to ^{42}K decays β spectrum. Changing the position of the detector string (moving it 50 cm higher) did neither change the 1525 keV line count rate nor the event rate at higher energies. The count rates for different detectors were consistent with each other. No source except ^{42}K could be identified. In Run 4, the mini-shroud was installed and resulted in a significant decrease in both rates: $R_{1525} = 0.40 \pm 0.05\,\mathrm{cts/(kg{\cdot}day)}$ and $B \sim 0.8\,\mathrm{cts/(keV{\cdot}kg{\cdot}yr)}$, as shown in Fig. 3.1. In order to see if R_{1525} can be enhanced, the Rn-shroud was biased to +500 V and the mini-shroud to −200 V in Run 5. In this configuration, the ^{42}K ions drifted towards the mini-shroud, thus, an increased R_{1525} of $2.2 \pm 0.2\,\mathrm{cts/(kg{\cdot}day)}$ is observed, while B did not change significantly (red points in Fig. 3.1). These tests demonstrated that R_{1525} can be manipulated by changing the potential configuration of the shrouds, and that positively charged ^{42}K after the decay of ^{42}Ar drift in the electric field dispersed in LAr. In the following runs, different electric field configurations, encapsulation of some of the detectors GTF45 and GTF112 (Runs 8–11), AC coupled readout mode (Runs 12–13) were tested to see their impact on R_{1525} and B. In Runs 8 and 9, the BEGe detector was mounted on the string, which exhibited a higher B compared to the coaxial detectors (blue points in Fig. 3.1). In Run 13, the detectors were operated in AC coupled mode without

mini-shroud, which resulted in a higher count rate compared to with mini-shroud.

In the commissioning runs, a clear correlation between the measured count rates (R_{1525}, B) and the electric field generated by the detector array in the LAr has been observed. A major improvement of B is achieved by enclosing the detector string with the mini-shroud and grounding the mini-shroud. This configuration is also adopted in the Phase I setup. The intensity of the 1525 keV γ-ray line is still about four times higher than the expected $\sim$ 0.1 cts/(kg·day) given the upper limit on the ^{42}Ar specific activity in literature and assuming that ^{42}K is homogeneously distributed outside the mini-shroud. The specific activity of ^{42}K (^{42}Ar) determined using GERDA Phase I data is described in Section 4.7.6.

3.3 Investigation of the ^{208}Tl background

An initial ^{232}Th/^{228}Th contamination of materials in the setup is a potential background source at $Q_{\beta\beta}$ = 2039 keV, due to the 2614.5 keV γ-ray of ^{208}Tl in the decay chain (Section 1.3.4). A dedicated study of the ^{208}Tl background was carried out during the commissioning runs of GERDA. The Z-position of the detector string was varied, in order to investigate its effects on the measured energy spectrum. This allowed to gain knowledge on the location of the contaminations. This study was reported in [130] and is briefly described below.

In the data taking period from Run 14 to Run 22, the position of the string with three $^{\text{enr}}$Ge-coax detectors, RG1 (top), ANG4 (middle), and RG2 (bottom), was changed between $z = -1700$ mm and $z = -3150$ mm. The z position corresponds to the distance from the bottom of the bottom detector on the string to the LAr fill level. Table 3.2 lists the live time, position of the detector string (z), observed number of counts in the (2614.5 ± 10) keV peak region (N_{peak}) and in Compton continuum (N_{cont}) in the 1550–2595 keV interval for each run. The energy interval for the continuum is maximized in order to have enough statistics allowing for an interpretation, while keeping the 1525 keV γ-ray line of ^{42}K outside of the interval. The number of counts are obtained from the measured energy spectra, after applying muon veto and detector anti-coincidence cuts. The peak counts N_{peak} were determined without background subtraction. Only the detectors RG1 and ANG4 are considered in the analysis; the third detector RG2 showed problems, i.e. its energy scale was uncertain at a level of 20 keV, and was not used for physics analysis.

A significantly higher number of counts, both in the peak region and in the continuum, was observed in Run 20, when the detector string was moved to $z = -1700$ mm, i.e. closer to the neck of the cryostat. The increase in the number of counts can be due to contaminations in different locations at the upper parts of the setup – namely, the clean room floor, the upper part of the Rn-shroud, the stainless steel walls of the cryostat or the heat exchanger and its support. The heat exchanger is the cryostat's active cooling unit to reduce evaporation losses. It consists of two parts: the upper one in the cryostat's neck at about the LAr level; and the lower one $\sim$ 1100 mm below the LAr level. Fig. 3.2 shows a drawing of the GERDA cryostat, indicating the LAr fill level (the reference position) and specifying the distance of the heat exchanger (both upper and lower parts) from this reference point. The heat exchanger is made out of copper, which was not screened for

Table 3.2: Live time, position of the detector string (z, nominal -2900 mm), observed number of counts in the (2614.5 ± 10) keV peak region (N_{peak}) and in Compton continuum in the $(1550 - 2595)$ keV interval (N_{cont}) for GERDA commissioning runs with $^{\text{enr}}$Ge-coax detectors. Note that N_{peak} and N_{cont} are not normalized to live time or detector mass.

Runs	Date	Live time [days]	z [mm]	N_{peak} [cts]		N_{cont} [cts]	
				RG1	ANG4	RG1	ANG4
Run 14	23/06–30/06/2011	7.11	−2400	0	1	11	4
Run 15	01/07–25/07/2011	16.02	−2900	0	0	8	3
Run 16	01/08–10/08/2011	8.90	−2900	0	1	3	2
Run 17	11/08–17/08/2011	5.96	−2900	0	0	2	2
Run 18	17/08–23/08/2011	6.15	−2900	0	1	4	1
Run 20	29/08–05/09/2011	6.71	−1700	13	15	89	53
Run 21	05/09–19/09/2011	13.65	−2900	0	0	2	2
Run 22	19/09–16/10/2011	15.73	−3150	0	1	5	4

radio-purity, hence, possible contaminations of this component are not known. In the following analysis, a potential ^{228}Th contamination of the heat exchanger is assumed to account for all the counts in the 2614.5 keV γ-ray peak in Run 20, given that it is the only run where this γ-ray line is observed significantly. The ^{228}Th activity of the heat exchanger is determined by means of a Monte Carlo simulation under this assumption.

The simulation was performed in MAGE using the GERDA setup, after implementing the heat exchanger geometry with its realistic dimensions and in its proper position. For simplicity, in stead of a spiral geometry, a cylindrical shell made out of copper with 800 mm height, 700 mm diameter and 1 mm thickness, positioned 1100 mm below the LAr fill level, was implemented. The vertical position of the detector string was set such that, the bottom of the bottom detector was at 1700 mm distance from the LAr fill level and the radial distance of the string from the center of the cryostat neck was set to 190 mm, as a realistic representation of Run 20. In this configuration, the detector string is inside the heat exchanger (see Fig. 3.3). The ^{232}Th decay chain was simulated in the heat exchanger material starting from ^{228}Ac. This is justified as ^{228}Ac is the first isotope in the decay chain emitting γ-rays with relevant energy. In total $2 \cdot 10^7$ decays were generated and were uniformly distributed in the material. The energy spectra of the detectors resulting from the simulation were smeared using the energy resolution function determined from calibrations. Detector anti-coincidence was applied both to the simulated and measured spectra.

Fig. 3.4 shows the measured and simulated spectra of the sum of the two considered detectors, with the simulated one scaled to match the number of counts in the (2615 ± 10) keV interval of the measured one. The ratio of the number of counts in the peak region to the one in the continuum is $(N_{\text{peak}}/N_{\text{cont}})_{\text{data}} = 28/142 = 0.20^{+0.09}_{-0.05}$ for the measured spectrum, while it is $(N_{\text{peak}}/N_{\text{cont}})_{\text{MC}} = 1847/6635 = 0.28 \pm 0.01$ for the simulated spec-

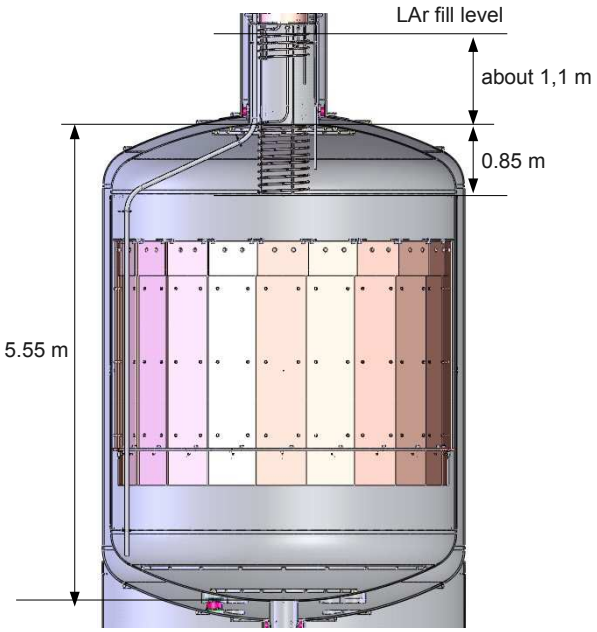

Figure 3.2: Drawing of the GERDA cryostat. The upper part of the heat exchanger is located in the cryostat's neck at about the LAr fill level. The lower part is ∼1.1 m below the LAr fill level.

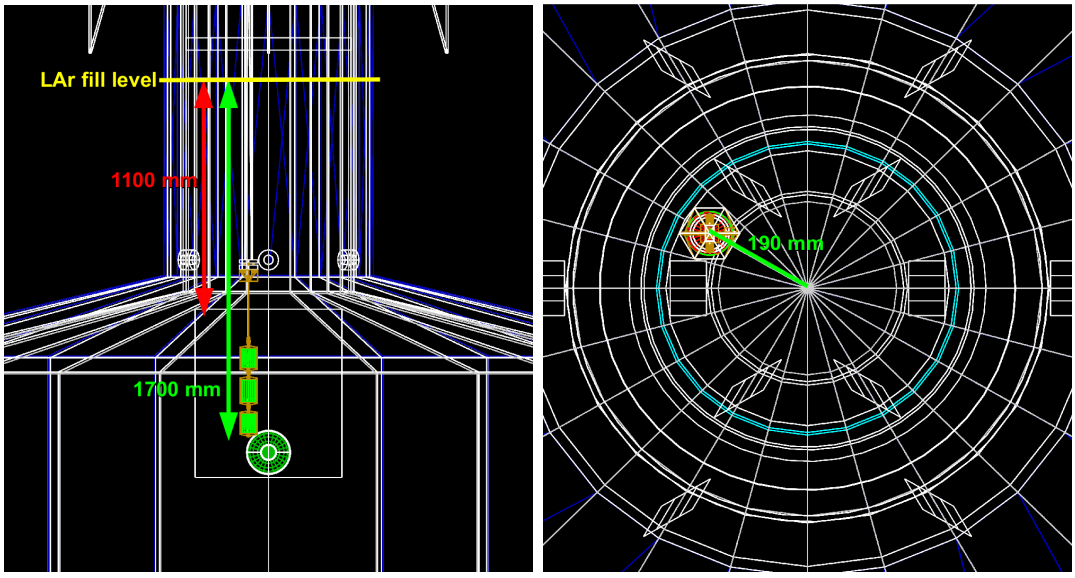

Figure 3.3: Part of the GERDA setup in MAGE representation (left: side view, right: top view), showing the configuration in Run 20, used for the simulation of background contribution from the heat exchanger. The detector string carrying the three ^{enr}Ge-coax detectors (RG1, ANG4 and RG2) is inside the heat exchanger in this configuration. The z-position of the detector string (-1700 mm) and the distance of the heat exchanger from the LAr fill level are indicated.

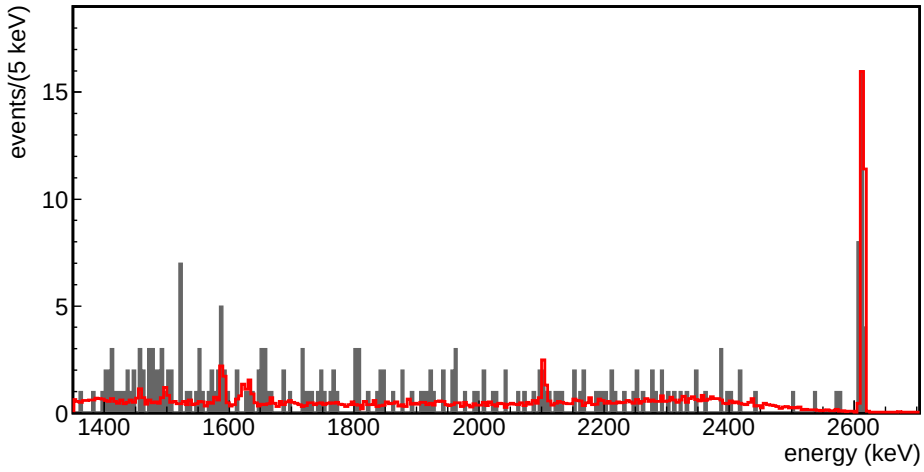

Figure 3.4: The sum energy spectrum (filled gray) of the RG1 and ANG4 detectors in Run 20 in comparison to the simulated spectrum (red histogram) obtained from the ^{228}Th decay chain simulation in the heat exchanger, using a realistic implementation of the GERDA setup in Run 20. The simulated spectrum is scaled to match the number of observed counts in the (2615 ± 10) keV interval.

trum. A small discrepancy could be expected, since background sources other than ^{232}Th decay chain, like ^{214}Bi (^{238}U), ^{42}K, ^{60}Co, etc., possibly contribute to the counts in the 1550–2595 keV interval. The ratio for the measured spectrum is smaller than that for the simulated one, as expected. Nevertheless, they do not significantly differ. This indicates that, the major contribution in the continuum comes from the ^{232}Th decay chain in this specific run.

The specific activity of ^{228}Th in the heat exchanger was derived by attributing the origin of all the observed counts in the (2614.5 ± 10) keV peak region in Run 20, i.e. $\mathrm{N_{peak}} = 28$, to the decays taking place in the heat exchanger. Given the total number of simulated decays, $N_{\mathrm{MC}} = 2 \cdot 10^7$, the normalization factor between the simulated and measured spectra due to the above assumption, $F = N_{\mathrm{peak,data}}/N_{\mathrm{peak,MC}} = (15 \pm 3) \cdot 10^{-3}$, the live time of Run 20, $t = 6.71$ days, the (simulated) volume of the heat exchanger, $V = 1.76$ dm^3, and the density of copper, $\rho_{Cu} = 8.94$ kg/dm^3, the resulting specific activity is:

$$A = \frac{N_{MC} \cdot F}{t \cdot V \cdot \rho_{Cu}} = (33 \pm 6)\ \mathrm{mBq/kg}\ . \tag{3.1}$$

Since the specific activity is derived by neglecting the contributions from ^{228}Th contamination of components other than the heat exchanger, it must be considered as an upper limit. It is important to mention that only the lower part of the heat exchanger is considered in this evaluation. The contribution from the upper heat exchanger was simulated as well, and was found to be negligible.

The same analysis was performed for the upper part (neck) of the cryostat. For this component the specific activity needed to account for all the counts in the (2614.5 ± 10) keV

peak region in Run 20 was derived to be $\sim$ 100 mBq/kg. However, the ^{228}Th activity from the screening of the stainless steel of the cryostat is 2-3 mBq/kg. Thus, the ^{208}Tl background observed in Run 20 is unlikely to originate from cryostat's steel wall, although it may give a small contribution.

Also increased count rates of the γ-ray lines at 1173.2 keV and 1332.3 keV from ^{60}Co were observed in Run 20. A dedicated study similar to the one described above was performed to determine the ^{60}Co specific activity in the heat exchanger, which yielded (26.2 ± 2.7) mBq/kg [131]. Yet another similar study for both ^{208}Tl and ^{60}Co contributions from the heat exchanger was reported in [132], showing consistent results with the other works. In the same report, the contributions to the background indices for Phase I and Phase II were evaluated as $B \leq (1.0 \pm 0.3) \cdot 10^{-4}$ and $B \leq (1.6 \pm 0.5) \cdot 10^{-5}$ cts/(keV·kg·yr), respectively. Considering the goal of achieving $B = 10^{-3}$ cts/(keV·kg·yr) in Phase II, the above mentioned contribution from the heat exchanger is only of minor importance.

Background contributions from ^{208}Tl decays in different parts of the setup, including the heat exchanger, are further discussed in Sections 4.7.5 and 4.7.7, where the GERDA Phase I energy spectrum is decomposed into individual background contributions through a global fit.

3.4 Measurement of the ^{39}Ar specific activity

As the Ge detectors are directly submerged in LAr, the low energy part of the measured spectrum in GERDA is dominated by the β decay of ^{39}Ar up to its Q-value of 565 keV. ^{39}Ar is mainly produced through cosmic rays in the atmosphere by the ^{40}Ar(n,2n)^{39}Ar process. It is present in LAr produced from the atmospheric gas. The specific activity of ^{39}Ar measured in LAr is (1.01 ± 0.08) Bq/kg corresponding to a fraction of $(8.0 \pm 0.6) \cdot 10^{-16}$ g/g, as reported in [133]. This measurement is in very good agreement with the ^{39}Ar contamination of $^{\text{nat}}$Ar in the troposphere, reported as $[7.9 \pm 0.3(\text{stat})] \cdot 10^{-16}$ g/g in [134].

The measured energy spectrum in the GERDA commissioning runs was analyzed to study this background component. A dedicated Monte Carlo simulation of ^{39}Ar β decays in the LAr in GERDA was performed, using the realistic experimental setup implemented in MAGE [135]. The simulated spectrum was compared to the measured one, which allowed for determining the ^{39}Ar specific activity from the GERDA commissioning data, as well as for gaining knowledge on the thickness of the dead layer (d_{dl}) on the n^+ surface.

The data taking period from Run 10 to Run 13, with a total live time of 100.14 days, is considered for this study. The energy threshold in the previous runs was not sufficiently low, i.e. 200–300 keV, and was also different from run to run, which led to artificial structures in the low energy part of the sum spectrum of all runs, i.e. Runs 1–13. Whereas, for the Runs 10–13, the energy threshold was around 100 keV. Thus, the sum spectrum from those runs in the energy region above 100 keV is considered in the analysis. Moreover, among the three $^{\text{nat}}$Ge-coax detectors that were deployed in the setup, only the data from GTF32 is used; the other two detectors were encapsulated, and hence, are not suitable for this study.

The β decay of ^{39}Ar is classified as a forbidden unique transition and, hence, the β

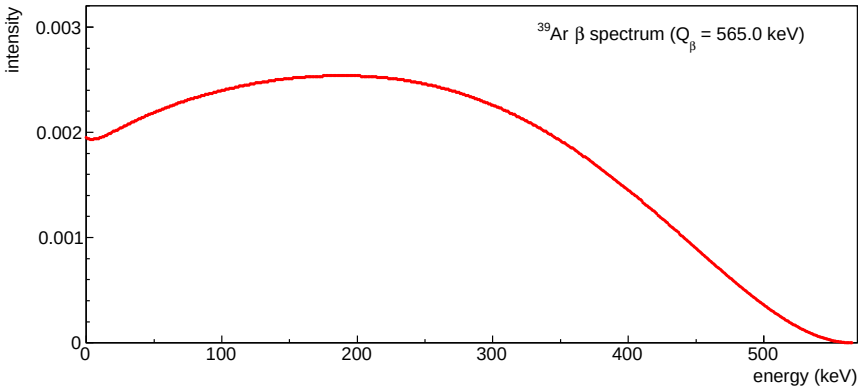

Figure 3.5: ^{39}Ar β-decay spectrum obtained from the Table of Radioactive Isotopes, LBNL [136].

spectrum is not described by the usual Fermi function. A semi-empirical β spectrum from [136] (shown in Fig. 3.5) is used as the initial spectrum for simulating the β decays of ^{39}Ar. The simulation was performed in MaGe, using a realistic implementation of the experimental setup in Runs 10–13 with the three $^{\text{nat}}$Ge-coax detectors placed on a central string. The decays were sampled inside a cylindrical volume with 145 mm outer radius and 566 mm height surrounding the detectors, that corresponds to about 36 liters of LAr. A uniform distribution of ^{39}Ar within that volume was assumed. Since the mean range of 600 keV electrons in LAr is about 2.7 mm, the decays that deposit energy in the detectors are expected to mostly take place in the close vicinity of the detector surfaces. The sampling volume is large enough to also account for the Bremsstrahlung gammas. The geometry of the detectors included the groove part (see Fig. 2.3) as well. The dead layers, their extensions and thicknesses play an essential role in this study. The β-rays with energies lower than 565 keV have less than 0.8 mm range in Ge, and thus, their energies are significantly degraded within the dead layer on the n^+ surface, which is $d_{dl}(n^+) = (0.4 \pm 0.08)$ mm for GTF32 (see Table 2.2). Different values of $d_{dl}(n^+)$, i.e. 0.2, 0.4, 0.8 and 1.6 mm, and $d_{dl}(p^+)$, i.e. 0.1, 1 and 10 μm, were assumed in the simulation, in order to investigate the effect on the spectral shape. While the variations of $d_{dl}(p^+)$ has practically no effect on the spectral shape, variations of $d_{dl}(n^+)$ significantly influences it, especially below $\sim$ 200 keV (see Fig. 3.6): the low energy part of the spectrum gets more suppressed for a thicker $d_{dl}(n^+)$. Fig. 3.7 shows the primary vertex position of the simulated ^{39}Ar decays in LAr within the sampling volume (left) and the position of the interactions (hits) inside the detector active volume (right) in a central slice of 1 cm in the $x - z$ plane. The right plot demonstrates that most of the events that deposit energy in the active volume are due to β-rays passing through the thin dead layer on the p^+ surface (and groove), while a smaller fraction pass through the n^+ surface.

A χ^2 fit to the measured spectrum is performed with a model consisting of the simulated ^{39}Ar spectrum plus a constant background component, in the energy range from 105 keV to 570 keV with 15 keV binning. The lower energy boundary of the fit window is well above the energy threshold of the considered runs. The upper energy boundary is higher

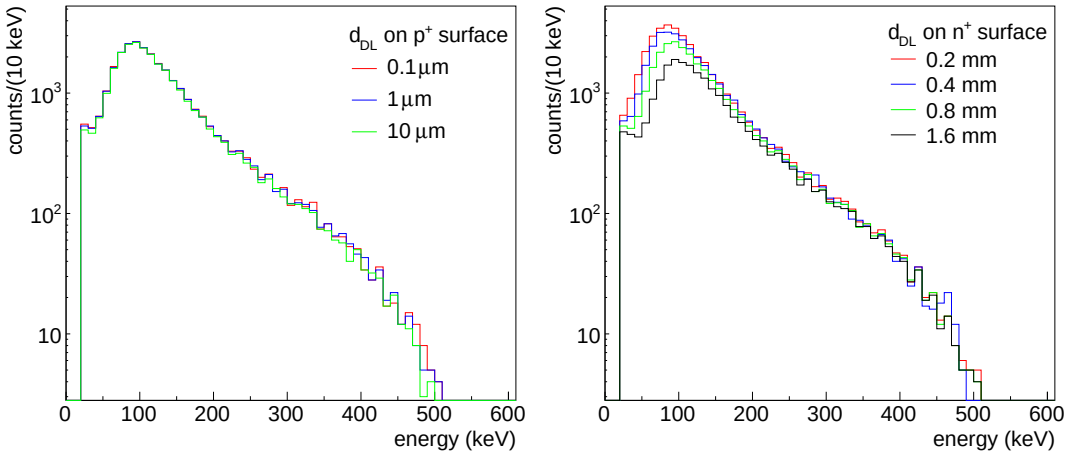

Figure 3.6: Simulated ^{39}Ar spectra for different d_{DL} assumptions on the p^+ surface (left) and on the n^+ surface (right).

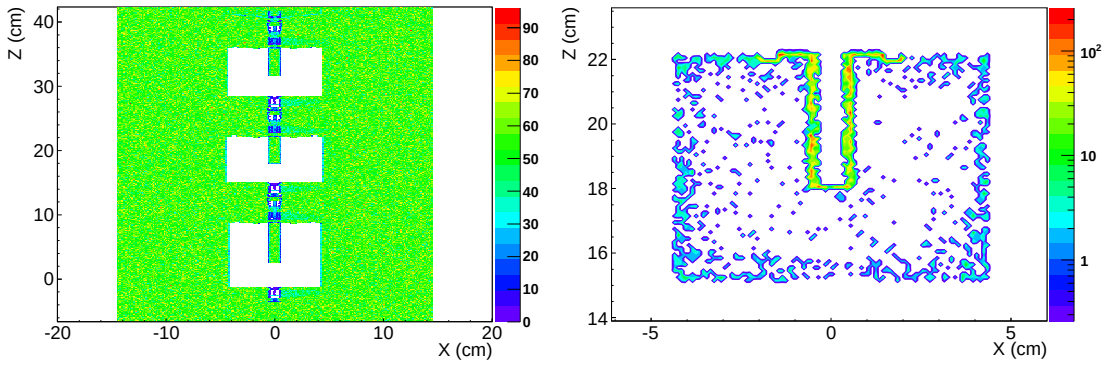

Figure 3.7: Primary vertex position of the simulated ^{39}Ar decays in LAr within the sampling volume (left) and the position of the interactions inside the detector active volume (right) shown in a central slice of 1 cm in the $x - z$ plane.

than $Q_\beta = 565\,\text{keV}$ of ^{39}Ar, but lower than the 609 keV γ-ray line of ^{214}Bi which is not accounted for in the fit model. The nominal $d_{dl} = 0.4\,\text{mm}$ on the n^+ and $d_{dl} = 1\,\mu\text{m}$ on the p^+ surface and on the groove are assumed for the reference fit. The fit model has two free parameters: a constant term that accounts for the contribution from background sources other than ^{39}Ar, approximated as a flat distribution; and the specific activity of ^{39}Ar, $A(^{39}\text{Ar})$, that scales the simulated ^{39}Ar spectrum. The simulated spectrum is normalized to $A(^{39}\text{Ar}) = 1\,\text{Bq/kg}$, thus, the best fit parameter for the ^{39}Ar component gives the specific activity in units of Bq/kg.

Fig. 3.8 shows the measured energy spectrum of GTF32 together with the best fit model. The reference fit results in a $\chi^2/\text{NDF} = 30/29$. For d_{dl} of 0.2 and 0.8 mm, the model still describes the spectrum well and gives χ^2/NDF of 34/29 and 31/29, respectively. The specific activity of ^{39}Ar that results from the analysis is

$$A(^{39}\text{Ar}) = 1.15 \pm 0.05\,(\text{stat}) \pm 0.10\,(\text{syst}) = (1.15 \pm 0.11)\,\text{Bq/kg}\ . \tag{3.2}$$

The systematic uncertainty is due to different assumptions on $d_{dl}(n^+)$, i.e. 0.2 and 0.8 mm that also describes the data adequately. Another important systematic uncertainty contribution, which is not accounted for in the analysis, might be coming from the shape of the initial spectrum. The spectral fit shows some indications for a slight disagreement in the simulated and observed spectral shapes, i.e. between ~ 100 and 250 keV. Different choice of fit windows and binning are found to be negligible compared to the systematic uncertainty due to $d_{dl}(n^+)$. The constant term resulting from the best fit is $1.56\,\text{cts}/(\text{keV}\cdot\text{kg}\cdot\text{yr})$. The results show that there are only minor contributions from other background sources in the energy region below 565 keV, where ^{39}Ar β decay dominates the energy spectrum of GERDA. The derived $A(^{39}\text{Ar})$ from GERDA data is in good agreement with the result of [133], i.e. $A(^{39}\text{Ar}) = (1.01 \pm 0.08)\,\text{Bq/kg}$, within 1σ uncertainty.

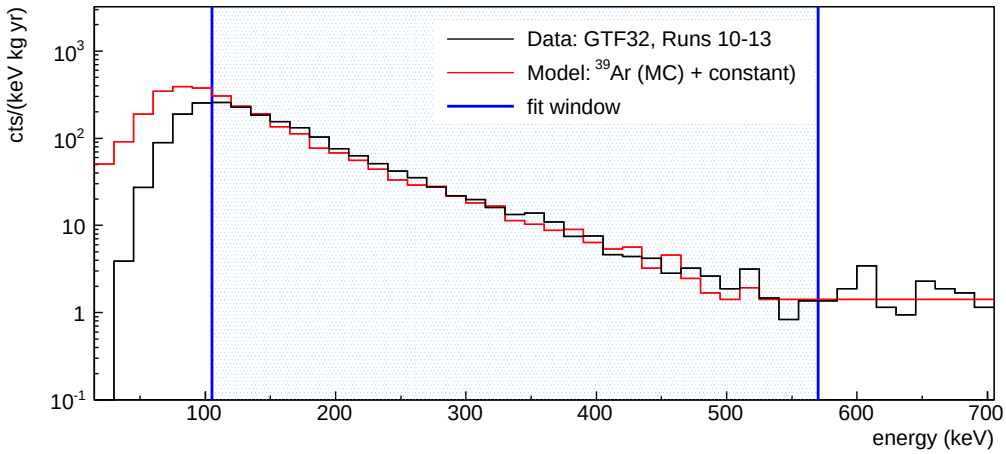

Figure 3.8: The sum energy spectrum of GTF32 in GERDA Runs 10–13 (black histogram) together with the best fit model (red histogram) which consists of the simulated ^{39}Ar spectrum plus a constant term. The nominal $d_{dl}(\mathrm{n}^+)$ of 0.4 mm (see Table 2.2) was assumed in the ^{39}Ar β decay simulation.

Chapter 4

Background model of the GERDA Phase I energy spectrum

The observed energy spectrum in GERDA Phase I induced by processes other than $0\nu\beta\beta$ decay, referred to as the background spectrum, has been analyzed and a comprehensive background model has been developed. Preliminary results of this work were reported in [137–140] and the final results in [22]. Details of the background analysis and results are explained in this chapter.

As GERDA adopted a blind analysis in Phase I, all the work concerning background model had to be finalized and prepared for a publication before opening the final blinding window $Q_{\beta\beta} \pm 5\,\mathrm{keV}$, which was planned and performed in June 2013. Therefore, the data set considered for the background modeling was frozen in March 3rd, 2013. The validity of the background model for the complete Phase I data is demonstrated at the end of this chapter.

The statistical methods used in the analysis are described in Section 4.1. The main steps of the background analysis can be summarized as follows:

- Detectors and run periods are grouped to form sets of data with similar qualities such as background level and energy resolution (Section 4.2).
- Energy spectra of the data sets are obtained after the energy calibration and the data quality selection as described in Section 2.3.2. Count rates of all expected and/or observed γ-ray lines are determined and background sources are discussed (Section 4.3).
- Monte Carlo simulations are performed to obtain the spectral shape of individual background components, which were expected due to contamination of the material known from the screening measurements (Table 2.1) and/or identified from their prominent structures in the energy spectrum. Different source locations for the background sources are considered to account for possible contaminations of different parts that can result in different spectral shapes (Section 4.4).
- ^{214}Bi and ^{208}Tl backgrounds are analyzed individually to determine the main location of the contamination in the setup by comparing the intensity of their prominent γ-ray

lines in the observed and simulated spectra (Section 4.5).

- Events at the high energy region of the spectrum, i.e. E $>$ 3.5 MeV, referred to as *α-induced events*, are analyzed individually to infer to their origin and source location in the setup. The count rate distribution of the events as a function of time is compared to the models due to the assumptions on the origin of these events. A model that describes the energy spectrum in the α-induced event region is obtained using the simulated energy spectra (Section 4.6).
- Finally, the entire background spectrum above the endpoint energy of ^{39}Ar (Q_β = 565 keV) is modeled through a global fit, using the simulated spectra of the identified background components. The global fit is repeated with different set of background sources and different source location assumptions. The effect of these variation on the results is evaluated as part of the systematic uncertainty on the model predictions (Section 4.7).

Important information are extracted from the global background model, such as the expected total background index, γ-ray lines and shape of the background spectrum in the region of interest around $Q_{\beta\beta}$, as well as the contributions from individual background components in this energy region. While the former being an essential input for the $0\nu\beta\beta$ analysis, the latter is important for understanding and further mitigating the background in GERDA Phase II and beyond.

4.1 Statistical methods

The data analysis is carried out using Bayesian approach. The posterior probability distribution for the model M under study is evaluated using the Bayesian Analysis Toolkit (BAT) [141]. The posterior for a fixed model, $P(\vec{\lambda}|\vec{D}, M)$, is proportional to the product of the likelihood $P(\vec{D}|\vec{\lambda}, M)$, i.e. the probability of observing D given M and its parameters $\vec{\lambda}$, and the prior probability for the parameters, $P(\vec{\lambda}|M)$:

$$P(\vec{\lambda}|\vec{D}, M) \propto P(\vec{D}|\vec{\lambda}, M) \cdot P(\vec{\lambda}|M) \ . \tag{4.1}$$

The likelihood $P(\vec{D}|\vec{\lambda}, M)$ and the priors $P(\vec{\lambda}|M)$ are defined for each specific analysis. All quantities of interest such as the expected values and uncertainty intervals of the parameters or limits, and correlations between the parameters are derived using $P(\vec{\lambda}|\vec{D}, M)$. Also, the probability distribution for a function of the model parameters is evaluated using the obtained sampling of the parameters according to $P(\vec{\lambda}|\vec{D}, M)$, which allows for a straightforward uncertainty propagation. The result of the analysis is given as the best fit value (the global mode) of the parameters, which maximizes $P(\vec{\lambda}|\vec{D}, M)$. The uncertainty interval of a parameter value is obtained as the smallest interval containing the 68% probability of the marginalized posterior probability distribution of the parameter, and quoted as the 68% credibility interval (C.I.). If the mode of the marginalized distribution significantly differs from the global mode, both are quoted. For the cases where the marginalized mode is zero, or 68% C.I. extends down to zero, an upper limit at 90% C.I. is quoted instead.

In Section 4.1.1, the Bayesian approach for determining the γ-ray line count rates is described. The method and the formulation is adapted from the "Mesuring a decay rate" tutorial given in the BAT home page [142]. The binned distributions of observed events, i.e. energy spectra and count rate distributions, are compared to models as described in Section 4.1.2. The analysis methods were implemented as dedicated applications in BAT Version 0.9.2.

4.1.1 Estimation of the γ-ray line count rates

The background spectrum consists of contributions from the decay processes of different radioisotopes. Thus, the γ-ray events from a certain isotope have been measured in the presence of other background events. For estimating the count rate of a γ-ray line, the total number of events (N_T) in the γ-ray peak region, i.e. in $E_\gamma \pm 3\sigma$ interval, and the number of events in the side bands of the peak region (N_B) are determined first. While, N_T is due to both γ-ray signal and other background processes, N_B is assumed to be due to background processes only. The estimation of the background rate in the γ-ray signal region is done using N_B, assuming that the continuous background spectrum is a linear distribution, by choosing the width of the side bands such that this assumption holds. The number of expected background (λ_B) and total (λ_T) events in the peak region are defined as

$$\lambda_B = R_B \cdot C_B \tag{4.2}$$

and

$$\lambda_T = (R_S + R_B) \cdot C_T, \tag{4.3}$$

where R_B is the expected background and R_S the expected signal count rate in units of counts in the peak region per exposure, i.e. cts/kg·yr. The scale factors C_B and C_T are the constants of proportionality, i.e. product of the corresponding exposure and energy window.

The possible values of the parameter of interest, R_S, are obtained using Bayes' Theorem. The posterior probability for R_B and R_S is

$$P(R_B, R_S|N_B, N_T) = \frac{P(N_T|R_B, R_S)P(R_S)P(R_B|N_B)}{\int P(N_T|R_B, R_S)P(R_S)P(R_B|N_B)dR_B dR_S} \ , \tag{4.4}$$

with

$$P(R_B|N_B) = \frac{P(N_B|R_B)P(R_B)}{\int P(N_B|R_B)P(R_B)dR_B} \ . \tag{4.5}$$

Combining Eqs. (4.4) and (4.5) gives

$$P(R_B, R_S|N_B, N_T) = \frac{P(N_T|R_B, R_S)P(N_B|R_B)P(R_S)P(R_B)}{\int P(N_T|R_B, R_S)P(N_B|R_B)P(R_S)P(R_B)dR_B dR_S} \ . \tag{4.6}$$

Using a flat probability distribution for the priors $P(R_S)$ and $P(R_B)$, Eq. (4.6) reduces to

$$P(R_B, R_S|N_B, N_T) \propto P(N_T|R_B, R_S)P(N_B|R_B) \ . \tag{4.7}$$

Given that the events arise from a Poisson process, the likelihood for the background event is written as

$$P(N_B|R_B) = \frac{e^{-\lambda_B} \cdot \lambda_B^{N_B}}{N_B!} \ , \tag{4.8}$$

and for the γ-ray signal plus background events as

$$P(N_T|R_B, R_S) = \frac{e^{-\lambda_T} \cdot \lambda_T^{N_T}}{N_T!} \ . \tag{4.9}$$

The probability distribution for R_S is obtained by marginalizing the posterior probability distribution, i.e. by integrating out the parameter R_B:

$$P(R_S|N_B, N_T) = \int P(R_B, R_S|N_B, N_T) dR_B \ , \tag{4.10}$$

which is then used for determining R_S and uncertainties or for limit setting.

4.1.2 Analysis of the binned distributions of observed events

Both count rate distributions and energy spectra are binned and analyzed using Bayesian approach. The likelihood is defined as the product of Poisson probabilities in each bin

$$P(\vec{D}|\vec{\lambda}) = \prod_i P(n_i|\lambda_i) = \prod_i \frac{e^{-\lambda_i} \lambda_i^{n_i}}{n_i!}, \tag{4.11}$$

where n_i is the observed and λ_i the expected number of events in the i-th bin. The priors, $P(\vec{\lambda})$, are defined according to the information on the possible values of the parameters whenever available, e.g due to previous measurements. Otherwise a flat prior probability distribution in the parameter range is assigned.

Count rate analysis: A model is defined according to the assumptions on the origin of events and fitted to the observed count rate distributions. Depending on $T_{1/2}$ of the radioisotope assumed to induce the observed events, the model is defined as a constant decay rate, if $T_{1/2}$ is much longer than the measurement time, or as an exponentially decreasing decay rate, if they are comparable. The predictions from the models can not be directly compared to the observed distributions, before the data taking interruptions (see Section 2.3.6) are taken into account. The live time distribution ϵ (Fig. 2.11), in the same time window and with the same binning as the observed count rate distributions, is used to correct the expected number of counts from the model, such that it is comparable to the observed one. Thus, the number of expected counts in the i-th bin is defined as

$$\lambda_i = \epsilon_i \int_{\Delta t_i} f(t) dt, \tag{4.12}$$

where Δt_i the time interval in the i-th bin and $f(t)$ is the model under study.

Spectral analysis: The model spectrum, consists of different contributions obtained from Monte Carlo simulations, is fitted to the observed energy spectrum. The expected number of events in the i-th bin is defined as the sum of the expected number of events from each model component in that bin:

$$\lambda_i = \sum_C \lambda_{i,C} \ , \tag{4.13}$$

with

$$\lambda_{i,C} = N_C \int_{\Delta E_i} f_C(E) dE \ , \tag{4.14}$$

where $f_C(E)$ is the normalized simulated spectrum of the model component C, N_C the scaling parameter, i.e. the integral of the spectrum, and ΔE_i the energy interval of the i-th bin.

4.1.3 Goodness-of-fit and model comparison

The goodness-of-fit test implementation in BAT [141] is used for drawing conclusions on the validity of a model under study as a representation of the data. It is performed by evaluating the likelihood, $f^*(\vec{x}) = P(\vec{x}|\vec{\lambda}^*, M)$, for an ensemble of data sets, $\vec{x}$, which are generated under the assumption of the model M and the best fit parameters $\vec{\lambda}^*$. The p-value is then defined (Eq. (4.15)) as the probability to have found a result with likelihood lower than the one for the observed data, $f^D = P(\vec{D}|\vec{\lambda}^*, M) = f^*(\vec{x} = \vec{D})$, assuming the model and parameter values are valid.

$$p = \frac{\int_{f^*(\vec{x})<f^D} f^*(\vec{x}) d\vec{x}}{\int f^*(\vec{x}) d\vec{x}} \ . \tag{4.15}$$

The p-value will be a small number, i.e. < 0.1, if the model does not give a good representation of the data. This argumentation is only valid for the model with the current values of the parameters compared to a future data set. Note that, p-value is not used for model comparison, but only for evaluating the model validity.

For model comparison, Bayes factor is evaluated,

$$K = \frac{P(\bar{M}|\vec{D})}{P(M|\vec{D})} \ , \tag{4.16}$$

where $P(\bar{M}|\vec{D})$ and $P(M|\vec{D})$ are the conditional probabilities for the models $\bar{M}$ or M to be true given data. E.g. $P(M|\vec{D})$ is expressed as

$$P(M|\vec{D}) = \frac{P(\vec{D}|M)P_0(M)}{P(\vec{D}|\bar{M})P_0(\bar{M}) + P(\vec{D}|M)P_0(M)} \ . \tag{4.17}$$

The evaluation of K, thus, requires the normalization of the posterior probability, which is not necessary for the estimation of the parameters of a given model, thus, only done in case a model comparison was needed. The prior probabilities for $\bar{M}$ and M can be chosen according to the initial knowledge if available, or can be given equal values, i.e. $P_0(M) = P_0(\bar{M}) = 0.5$.

4.1.4 Color-coded data/model comparison plots

The results of the performed fits are demonstrated by showing the best fit model and data plotted together, with uncertainty intervals placed on the model predictions, i.e. no error bars on the observed number of events, as proposed in [143]. The uncertainty intervals are modeled with a Poisson distribution, the mean of which is the model prediction. Three uncertainty intervals corresponding to the smallest sets containing minimum 68%, 95% and 99.9% probability for the expectations are shown with green, yellow and red bands, respectively. The intervals generally cover a larger probability than the indicated ones, due to the discreteness of Poisson distribution. The comparison plots with the color-coded uncertainty intervals give an indication whether the observations are within reasonable statistical fluctuations of the expectations, and hence also allows for judging the validity of a model.

4.2 Data sets

The measurement period between November 2011 and March 2013 is considered for the background analysis. Data taking runs and detector configurations were described in Section 2.3.6. Some run periods were discarded due to temperature related instabilities as explained in the same section. Considered run period corresponds to GERDA Runs 25–43, excluding Run 33. Considered data do not include the events in $Q_{\beta\beta} \pm 20\,\text{keV}$ window due to the blind analysis strategy (Section 2.3.8) adopted in GERDA.

Data from $^{\text{enr}}$Ge and $^{\text{nat}}$Ge detectors are treated separately in the analysis. The main goal is to obtain a background model and consequently a background index (B) prediction for the $^{\text{enr}}$Ge detectors, which are the ones used for the $0\nu\beta\beta$ signal search. Data from the $^{\text{nat}}$Ge detectors are analyzed in a separate data set, which provides a consistency check of the model developed for the $^{\text{enr}}$Ge detectors. The global model consists of background components common to both $^{\text{enr}}$Ge and $^{\text{nat}}$Ge detectors, since they experience the same environment. Also, most of the background sources, their locations and activities are expected to be comparable for the two detector types.

Furthermore, data from different type of $^{\text{enr}}$Ge detectors, i.e. enriched semi-coaxial ($^{\text{enr}}$Ge-coax) and BEGe, are also treated separately in the analysis. These two types exhibit different background levels around $Q_{\beta\beta}$ and also have different energy resolutions. Another grouping is done in the run period for the $^{\text{enr}}$Ge-coax detectors while forming the data sets. The run period of approximately 30 days with a significantly higher background level (see Section 2.3.7) is considered as the *silver run period*, and the rest as the *golden run period*, accordingly. The grouping of detectors and run periods to form subsets of data with different qualities is adopted in the $0\nu\beta\beta$ decay analysis as well. It has been shown that, the best $T^{0\nu}_{1/2}$ limits are attained if data with low background index or higher energy resolution is not combined with poorer quality data, but treated separately in different data sets (Section 6.7).

Data sets together with the considered detectors, their corresponding live time and exposure are summarized in Table 4.1. The *Golden* data set contains the data from all working $^{\text{enr}}$Ge-coax detectors only in the *golden run period* and the *Silver* data set only in

Table 4.1: Data sets used for the background modeling along with the considered detectors, corresponding live time and exposure.

Data set	Detectors	Live time [days]	Exposure [kg·yr]
Golden	ANG-2, -3, -4, -5, RG-1, -2	384.8	15.4
Silver	ANG-2, -3, -4, -5, RG-1, -2	32.6	1.3
Golden-nat	GTF-112	384.8	3.1
Golden-HdM	ANG-2, -3, -4, -5	384.8	10.9
Golden-Igex	RG-1, -2	384.8	4.5
BEGe	GD-32B, -32C, -32D, -35B	228.5	1.8

the *silver* one. The *Golden-nat* data set contains the data from the $^{\text{nat}}$Ge-coax detector GTF-112 in the *golden run period*. The *silver run period* for this detector has very low statistics and is not analyzed. Data from the BEGe detectors is contained in the *BEGe* data set without a separation of silver/golden run periods due to shorter measurement period with the BEGe detectors and their lower target mass compared to the $^{\text{enr}}$Ge-coax detectors. The *Golden* data set is further split into two subsets: data from the detectors of the HdM experiment as *Golden-HdM*; and from the Igex experiment as *Golden-Igex*. This grouping is motivated by the possibility of those having small differences in their background composition due to having different histories. The individual contributions of the background components to the total B can be studied by analyzing these two data sets separately.

4.3 Experimental spectra and background components

Fig. 4.1 shows the energy spectra of the *Golden*, *Golden-nat* and *BEGe* data sets, after the data quality (Section 2.3.3), muon-veto and detector anti-coincidence cuts were applied. Some prominent structures in the spectra (indicated with a label) can be attributed to certain background sources – namely, the β spectrum of ^{39}Ar (Q_β = 565 keV), the $2\nu\beta\beta$ spectrum of ^{76}Ge ($Q_{\beta\beta}$= 2039 keV), γ-ray lines from ^{40}K at 1460.8 keV, from ^{42}K at 1524.6 keV, from ^{214}Bi at 1764.5 keV and from ^{208}Tl at 2614.5 keV. All these sources were expected due to the material in the setup, i.e. germanium, LAr, and due to contamination of the material known from the screening measurements (see Table 2.1), except ^{42}K which has been observed in an unexpectedly high count rate (see Section 3.2). Also, a peak-like structure around 5200 keV can be seen, especially in the spectrum of the *Golden* data set, which can be attributed to the α decay of ^{210}Po (E_α = 5304 keV).

The screening results also indicate ^{60}Co ($T_{1/2}$=5.3 yr) contaminations of the setup close to the detector array, i.e. in the cable suspension system. Moreover, ^{60}Co is produced cosmogenically in germanium and can still be present in the Phase I detectors (see cht:gerda:background). Both internal and external ^{60}Co contaminations can lead to ^{60}Co

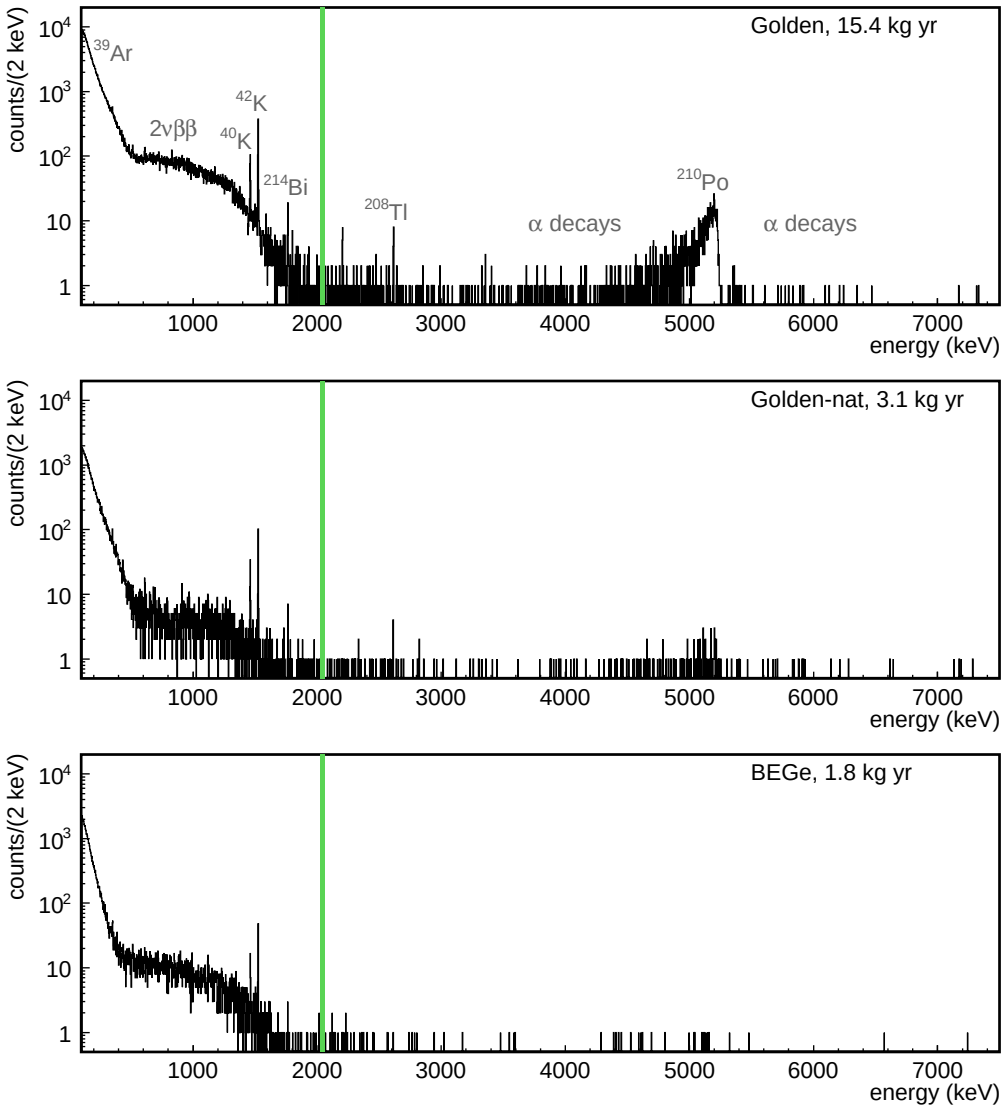

Figure 4.1: Energy spectra of the *Golden* (top), *Golden-nat* (middle) and *BEGe* (bottom) data sets. The green box indicates the $Q_{\beta\beta} \pm 20\,\text{keV}$ blinding window. The background sources with prominent structures are indicated with a label.

γ-ray lines at 1173.2 and 1332.5 keV.

Observation of the γ-ray lines of ^{214}Bi ($T_{1/2}$= 0.33 h) and ^{208}Tl ($T_{1/2}$= 183 s) in the energy spectra indicate contaminations with ^{226}Ra ($T_{1/2}$= 1600 yr) from the ^{238}U-series and with ^{228}Th ($T_{1/2}$= 1.91 yr) from the ^{232}Th-series, respectively. The ^{238}U-series, starting with ^{238}U ($T_{1/2}$= $4.5 \cdot 10^9$ yr), can be broken at ^{226}Ra ($T_{1/2}$= 1600 yr) and at ^{210}Pb ($T_{1/2}$= 22.3 yr). Similarly, the ^{232}Th-series starting with ^{232}Th ($T_{1/2}$= $1.4 \cdot 10^{10}$ yr), can be broken at ^{228}Ra ($T_{1/2}$= 5.75 yr) and at ^{228}Th ($T_{1/2}$= 1.91 yr). The parent isotope of each sub-chain can be present in the setup out of secular equilibrium, which would then reveal

itself by the observation of the γ-ray lines emitted by the radioisotopes in that sub-chain. The characteristic γ-rays in the natural decay chains are listed in Fig. A.1 and Fig. A.2.

For a more comprehensive background analysis, firstly, the count rates all the observed and/or expected γ-ray lines are determined. After that, the background components are discussed in detail.

4.3.1 Count rate of the γ-ray lines

The γ-ray lines of all the radioisotopes possibly contributing to the spectrum are indicated with a dashed line and a label in the spectrum of the *Golden* data set in Fig. 4.2. For the radioisotopes in the ^{238}U- and ^{232}Th-series, which often emit a cascade of γ-rays, only the ones above a certain intensity are considered. E.g., for ^{214}Bi all the γ-ray lines with a relative intensity greater than the one of 2447.9 keV ($I_\gamma = 1.6\%$) are considered. The γ-ray line count rates, R_S, are determined as described in Section 4.1.1.

Table 4.2 lists the energy (E_γ), the relative intensity (I_γ) and the determined R_s of the considered γ-ray lines for the three data sets: *Golden*, *Golden-nat* and *BEGe*. The count rate of some of the γ-ray lines that are in the high background level regions due to the β spectrum of ^{39}Ar or the $2\nu\beta\beta$ spectrum of ^{76}Ge, e.g. 1238 keV γ-ray line of ^{214}Bi with a similar I_γ as the 2204 keV γ-ray line, are not listed in Table 4.2. The global mode of R_s together with the 68% C.I., or an upper limit at 90% C.I. is quoted. The R_s of γ-ray lines can differ from one data set to the other, since the background sources may have different location and compositions, and also different activities for different detectors. Nevertheless, similarities are expected since the detectors experience the same external environment. Most of the γ-ray lines have indeed comparable R_s within 68% C.I.

The ^{42}K γ-ray line at 1524.7 keV is the most significant peak in all data sets. The detectors are exposed to an approximately same ^{42}K activity of the LAr surrounding them, with small deviations expected due to possible non-uniformities in the ^{42}K distribution. The R_s of the 1524.7 keV γ-ray line significantly varies between different data sets containing different detector types. The main reason is, different sizes of the detectors affects the detection efficiency for the full energy peaks (FEP). The $^{\text{nat}}$Ge-coax detector of the *Golden-nat* data set has the largest active volume and the highest R_s. While, the smaller BEGe detectors compared to the coaxial ones have the lowest R_s.

The γ-ray lines observed with high significance, i.e. $> 3\sigma$, are from ^{214}Pb and ^{214}Bi (^{226}Ra), ^{208}Tl (^{228}Th), ^{42}K (^{42}Ar) and ^{40}K, which clearly indicate the presence of these sources in the setup. The γ-ray lines of ^{228}Ac and ^{60}Co have been identified with less significance. Fewer γ-ray lines are positively identified in the energy spectrum of the *BEGe* data set compared to the others. It has the lowest exposure. Additionally, smaller active volume of the BEGe detectors reduces the detection efficiency for FEP with respect to the coaxial ones, especially for the high energy γ-ray lines.

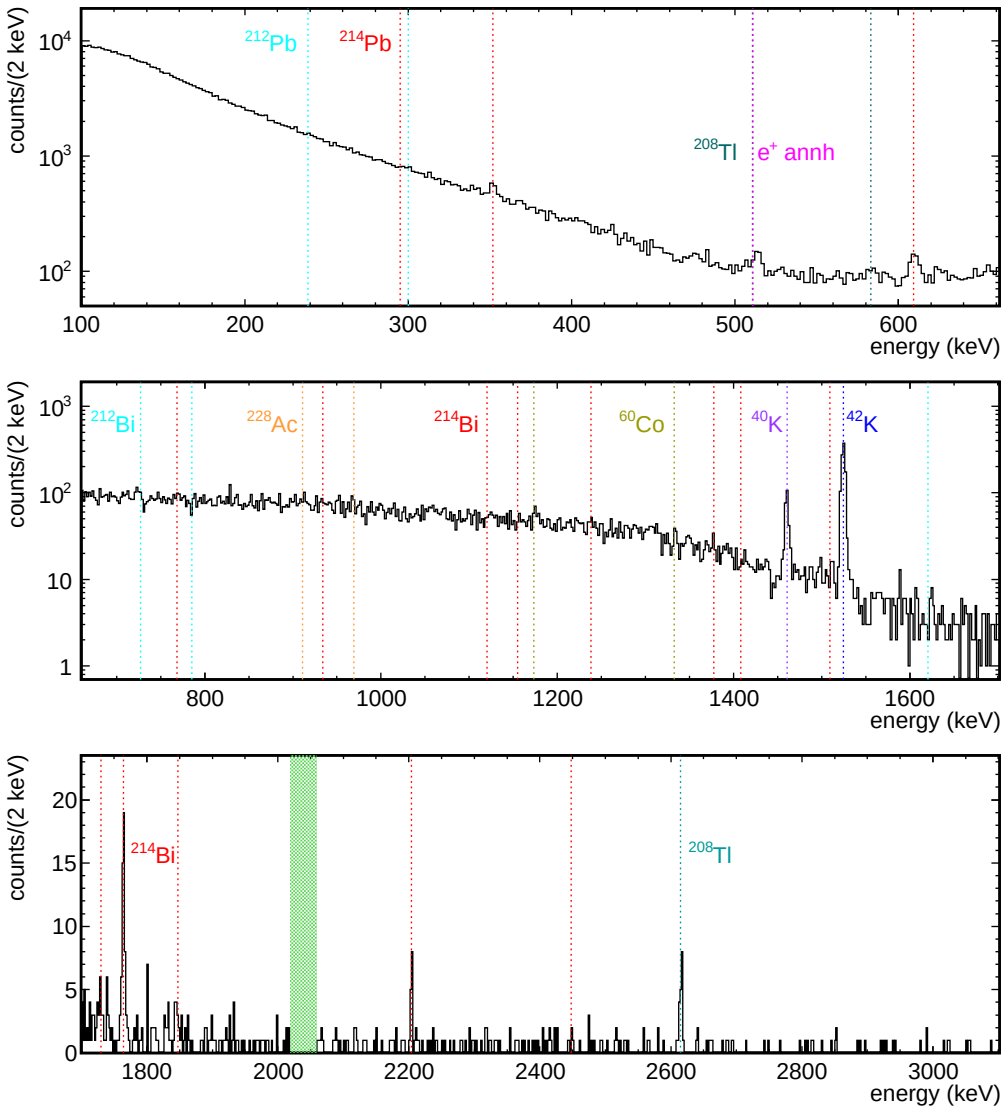

Figure 4.2: Energy spectrum of the *Golden* data set. The green box indicates the $Q_{\beta\beta} \pm 20\,\mathrm{keV}$ blinding window. The isotope and the energy of its γ-ray lines (with a relative intensity greater than a certain threshold) from the expected background sources are indicated with a label and a dashed line: cyan for ^{212}Pb and ^{212}Bi, dark cyan for ^{208}Tl, orange for ^{228}Ac, red for ^{214}Pb and ^{214}Bi, dark yellow for ^{60}Co, violet for ^{40}K and blue for ^{42}K.

Table 4.2: Energy (E_γ) and intensity (I_γ) of the γ-ray lines listed together with the determined count rates (R_S) in the energy spectra of the *Golden*, *Golden-nat* and *BEGe* data sets. I_γ is given in percentage for a decay of the parent isotope (from Ref. [144]). R_S is determined using the statistical method described in Section 4.1.1, and quoted together with the 68% C.I, or an upper limit at 90% C.I. is given. Note that R_S is the expected number of counts in the $E_\gamma \pm 3\sigma$ window, which corresponds to 8 keV for *BEGe* and 12 keV for *Golden* and *Golden-nat* data sets.

Isotope	E_γ [keV]	I_γ [%]	R_S [cts/(kg·yr)]		
			Golden (15.4 kg·yr)	*Golden-nat* (3.1 kg·yr)	*BEGe* (1.8 kg·yr)
^{214}Pb	351.9	37.6	20.4 (16.2, 24.8)	25.6 (18.1, 34.1)	27.2 (18.1, 35.4)
^{214}Bi	609.3	46.1	10.0 (8.0, 12.3)	7.6 (4.8, 11.0)	9.3 (4.4, 14.7)
	1764.5	15.4	3.1 (2.6, 3.7)	3.5 (2.4, 5.0)	1.6 (0.6, 3.0)
	1120.3	15.1	< 3.1	4.0 (1.8, 6.3)	8.5 (4.4, 12.8)
	2204.2	5.1	0.8 (0.5, 1.2)	0.8 (0.2, 1.6)	< 2.3
	1729.6	2.9	0.5 (0.2, 0.9)	0.9 (0.3, 1.8)	< 2.3
	1847.4	2.1	0.6 (0.3, 1.0)	1.2 (0.5, 2.1)	< 2.5
	2447.9	1.6	0.2 (0.1, 0.4)	< 1.8	< 2.4
^{228}Ac	911.2	25.8	3.9 (2.2, 5.6)	4.9 (2.7, 7.3)	< 9.4
	969.0	15.8	3.5 (1.8, 5.0)	4.8 (2.6, 7.4)	< 9.3
^{212}Bi	727.3	6.6	< 4.7	5.1 (2.7, 7.4)	< 6.5
^{208}Tl	2614.5	35.6	1.2 (0.9, 1.5)	1.4 (0.6, 2.3)	< 2.5
	583.2	30.4	3.9 (1.8, 5.7)	2.5 (0.4, 4.6)	< 12.1
^{60}Co	1173.2	99.97	4.2 (2.8, 5.6)	< 3.8	< 6.8
	1332.5	99.98	< 1.6	3.3 (1.6, 5.2)	2.8 (0.7, 6.0)
^{40}K	1460.8	10.7	13.6 (12.5, 15.0)	18.3 (15.7, 21.4)	14.2 (10.6, 17.8)
^{42}K	1524.7	18.0	60.3 (58.1, 62.5)	73.8 (69.1, 80.1)	43.9 (38.3, 49.5)

4.3.2 Discussion on the background components

The ^{39}Ar background from LAr dominates the low energy region of the measured spectrum due to its β decay with $Q_\beta = 565\,\text{keV}$. A dedicated analysis for determining the specific activity of ^{39}Ar with the GERDA data was presented in Section 3.4. This background component is not included in the background modeling, i.e. the observed spectrum above the endpoint energy of the ^{39}Ar β spectrum is considered in the analysis.

The expected B due to the neutron and μ fluxes at the LNGS underground laboratory have been estimated to be of the order of 10^{-5} cts/(keV·kg·yr) [145] and 10^{-4} cts/(keV·kg·yr) [146], respectively. These contributions are insignificant (see Section 2.2) with respect to the total B of GERDA Phase I, which is of the order of 10^{-2} cts/(keV·kg·yr). Hence, the background from neutron- and μ-induced events are not considered in the background modeling.

Isotopes that emit γ-rays in the $Q_{\beta\beta}\pm5\,\text{keV}$ energy region, which can possibly fake a $0\nu\beta\beta$ signal, are dangerous background sources. However, known isotopes/processes leading to γ-rays with this energy have either very short half lives, or other additional high intensity γ-ray lines that should also be observed. Some example processes are, neutron capture on ^{76}Ge [145] followed by the prompt γ-rays with 4008, 4192, 5050 and 5911 keV, inelastic neutron scattering off ^{206}Pb [147] with γ-ray lines at 898, 1705 and 3062 keV and ^{56}Co decays with γ-ray lines at 1771, 2598 and 3253 keV. There is no indication for these γ-ray lines in the energy spectrum of the GERDA Phase I.

The background sources that are identified by their γ-ray lines or other prominent structures in the energy spectrum, as well as the ones expected due to materials in the setup and contamination of the materials known from the screening measurements, are discussed below in detail. These sources are: naturally occurring radioisotopes from ^{238}U- and ^{232}Th-series as well as ^{40}K; cosmogenically produced isotopes ^{42}Ar, ^{60}Co and ^{68}Ge; and ^{76}Ge which contributes due to its $2\nu\beta\beta$ decay. The analysis for the background modeling of the GERDA Phase I energy spectrum is based on the contributions of these sources.

^{238}U- and ^{232}Th-series:

For most of the $0\nu\beta\beta$ experiments contamination of material with the radioisotopes from the ^{238}U- and ^{232}Th-series is one of the biggest concerns, since they can be found in traces almost in every material. The level of contamination can be controlled by using screened high purity materials. In GERDA Phase I, the observed γ-ray lines from ^{214}Pb and ^{214}Bi (^{226}Ra sub-chain), from ^{228}Ac (^{228}Ra sub-chain) and from ^{208}Tl (^{228}Th sub-chain) as listed in Table 4.2, clearly indicate contaminations with isotopes in the ^{238}U- and ^{232}Th-series. Only γ-ray line in the ^{210}Pb sub-chain is at 46.5 keV, which is outside the energy range where an efficient energy reconstruction of the events can be performed in GERDA Phase I.

Observed γ-ray lines with different energies for ^{214}Bi, i.e. 609.3 and 1764.5 keV, and for ^{208}Tl, i.e. 583.2 and 2614.5 keV, can give information on the distance of the source. This will be discussed later in Section 4.5. These isotopes are among the most important background sources; ^{214}Bi with its several γ-ray lines above 2039 keV, i.e. 2118.6, 2204.2,

2447.9 keV, etc., and Q_β of 3274 keV, and ^{208}Tl with its γ-ray line at 2614.5 keV are potential sources that contribute to background around $Q_{\beta\beta}$.

Another indication for the contamination of isotopes from the ^{238}U/^{232}Th-series is the large number of events observed at high energies, i.e. > 3.5 MeV, with peak like structures, which can be attributed to α decays. From the identified background sources the highest γ-ray line is 2614.5 keV (^{208}Tl) and the highest Q_β value is 3525.4 keV (^{42}K). No significant contributions from β- or γ-rays above 3.5 MeV are expected. Whereas, the energy of the emitted α particles in the natural decay series range between 4 and 9 MeV, which can result in energy depositions above 3.5 MeV. The mean range of α particles with 4–9 MeV energies is 14–41 μm in germanium and 34–113 μm in LAr [148]. Thus, α-decays have to occur at very close distances to the detectors' active volumes, i.e. within tens of μm, in order to deposit energy there. A large part of the detectors' outer surface is covered with the n^+ electrode, which forms a dead layer on the surface with a thickness of the order of millimeters Fig. 2.3. Unless the radioisotopes that originate α-decays are not deeply implanted in the thick dead layer, α-particles can not penetrate it and reach the active volume. Whereas, α-decays that take place on or close to the p^+surface, which has a dead layer thickness smaller than a μm, can result in an energy deposition in the active volume. Also, the dead layer thickness on the groove surface can be thin enough for the α-particles to penetrate. If emitted α-particles pass through material and lose part of their energy before reaching the active volume, they can result in background events around $Q_{\beta\beta}$.

Fig. 4.3 shows the energy spectra between 3.5 and 7.5 MeV for the *Golden*, *Golden-nat* and *BEGe* data sets in 50 keV binning. A large peak-like structure with a degrading tail can be seen around 5.2 MeV, especially in the *Golden* spectrum. Also, other smaller structures are visible around 4.7, 5.4 and 5.9 MeV. Such energy distributions are expected if the mono-energetic α particles decay isotropically on the p^+ surface. The ones that are emitted perpendicular to the detector surface will cross the shortest path of the dead layer, lose minimal energy there and produce a peak, while shallower emission angles will result in a distribution towards lower energies. The latter appears as a degrading tail due to the increased effect of energy loss straggling in longer paths. The position of the observed maximum will be slightly below the energy of the α particles due to the energy loss within the dead layer and will depend on the d_{dl}. Therefore, the peak-like structure around 5.2 MeV is attributed to ^{210}Po decays with $E_\alpha = 5304$ keV on the p^+ surface. The origin can be an initial ^{210}Pb or directly ^{210}Po contamination on the p^+ surface. Furthermore, the presence of events above 5.3 MeV indicates a contribution of additional source(s) with higher α energies. Given the observed structures around 4.7, 5.4 and 5.9 MeV and some events above that, the additional contribution can be attributed to the α decays in the ^{226}Ra sub-chain – namely, ^{226}Ra decay with $E_\alpha = 4784$ keV, ^{222}Rn decay with $E_\alpha = 5489$ keV, ^{218}Po decay with $E_\alpha = 6002$ keV and ^{214}Po decay with $E_\alpha = 7686$ keV. These α decays can originate from an initial ^{226}Ra contamination on the p^+ surface. Additionally, they can originate from ^{222}Rn & daughters dissolved in LAr and decay close to the p^+ surface. For a homogeneous distribution in LAr, the energy spectrum is expected to be a broad continuum without a peak structure, since α's can pass through variable amounts of material before reaching the active volume. Some amount of ^{222}Rn is expected to be present in LAr due to emanation from material with ^{226}Ra contamination.

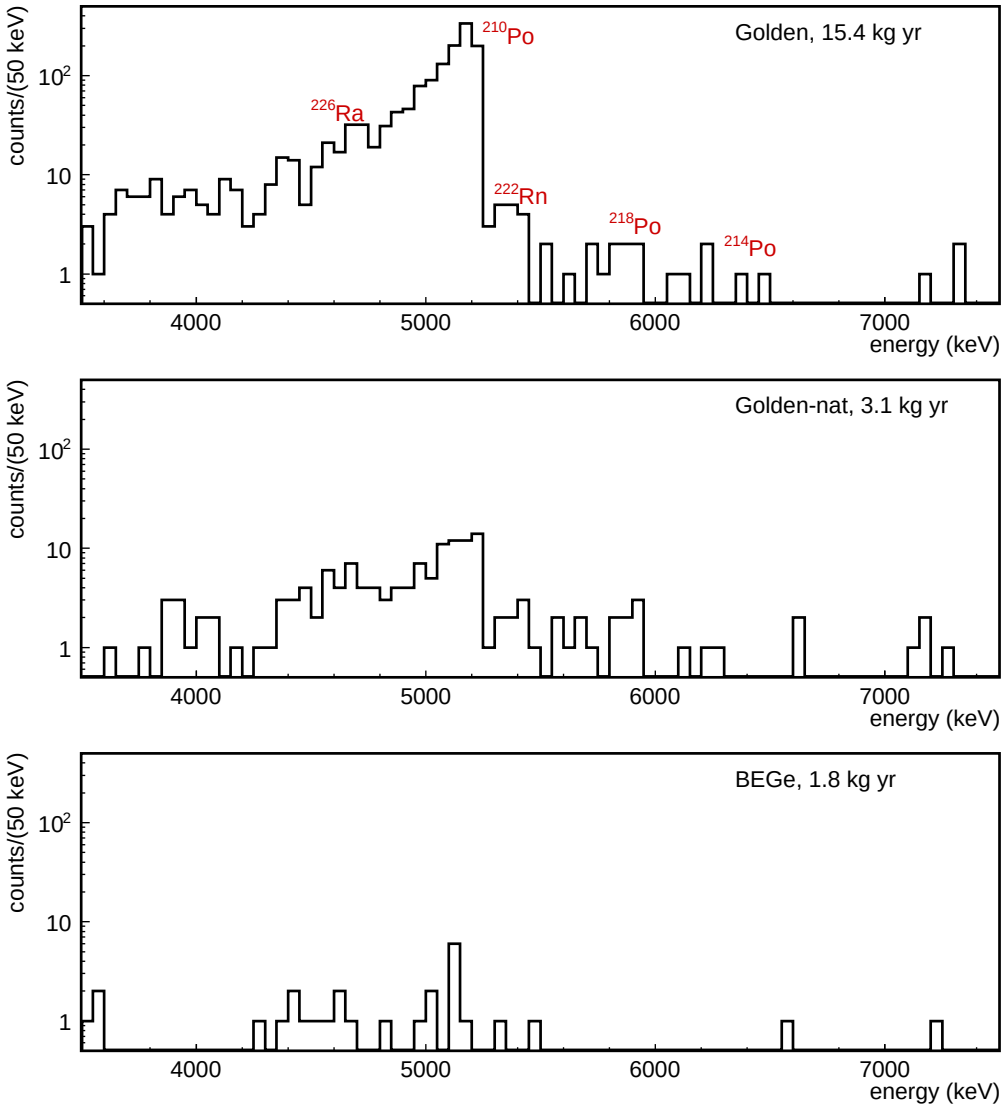

Figure 4.3: Energy spectra of the *Golden* (top), *Golden-nat* (middle) and *BEGe* (bottom) data sets at high energies. The peak-like structures attributed to the α decay of certain isotopes are indicated.

The screening measurements (Table 2.1) indicate that, many parts in the close vicinity of the detectors and also detector surfaces are contaminated with ^{226}Ra.

Another possible α-source location could be the detector volume. However, there is no indication for an internal contamination with ^{226}Ra or ^{210}Po. Decays inside the detector volume would result in a peak at E_α, which has not been observed. Also, no hints for α decays from the ^{232}Th-series can be seen in the spectra.

^{40}K:

^{40}K ($T_{1/2}$= $1.28 \cdot 10^9$ yr) is a naturally occurring radioisotope of potassium. It decays with 89.3% through β decay (Q_β = 1311.1 keV), with 10.7% through electron capture (Q_β = 1504.9 keV) followed by the emission of a single γ-ray with 1460.8 keV energy and with 0.001% through β^+ decay. Its characteristic γ-ray line at 1460.8 keV has been observed with high significance ($> 5\sigma$) in the energy spectrum of all data sets. The screening measurements (Table 2.1) indicate ^{40}K contamination in the materials close to the detectors, mainly in the detector support and array. ^{40}K background does not constitute a background at $Q_{\beta\beta}$.

^{42}Ar / ^{42}K:

^{42}Ar ($T_{1/2}$= 32.9 yr), a rare and cosmogenically or synthetically produced radioisotope of argon, has been detected in LAr of the GERDA cryostat. It decays to ^{42}K with Q_β = 599 keV. The short-lived daughter ^{42}K ($T_{1/2}$= 12.4 h) undergoes β decay with Q_β = 3525.4 keV. The 1525.6 keV γ-rays emitted with 17.6% probability in the decay of ^{42}K induce the most intensive γ-ray line in the GERDA Phase I spectrum. ^{42}K can significantly contribute to the background at $Q_{\beta\beta}$ due to its β decay with the end point energy above $Q_{\beta\beta}$. The emitted electrons first cross the dead layers on the detector surfaces before depositing energy in the active volume. The mean range of 3.5 MeV (2.0 MeV) electrons in Ge is 4.7 mm (2.6 mm) [148]. The thickness on the n^+ surface, which ranges between 0.7 and 1.0 mm for the BEGe type and between 1.4 and 2.6 mm for the ^{enr}Ge-coax type detectors, can significantly shift the β spectrum towards lower energies. While, the p^+ surface with a dead layer thickness of the order of μm practically does not degrade the energy of the electrons. Given the thinner dead layer thicknesses of the n^+ surface, the background due to ^{42}K β decays in the energy spectrum of BEGe detectors is expected to be higher compared to the ^{enr}Ge-coax detectors.

The decay product ^{42}K is in an ionic state. It can thus get a nonuniform distribution due to electric fields dispersed in LAr caused by the bias voltage of the detectors. The contribution at $Q_{\beta\beta}$ from ^{42}K decays can depend on the field lines; larger contribution at $Q_{\beta\beta}$ is expected when the ions are attracted to the detectors. This effect was verified in the GERDA commissioning phase (see Section 3.2). Consequently, a "quasi field-free configuration" was chosen for the GERDA Phase I data taking, which minimizes the drift toward detectors, hence, the ^{42}K contribution to the B at $Q_{\beta\beta}$. Moreover, each detector string was enclosed with mini-shrouds to avoid ^{42}K ions being collected from a large volume. Nevertheless, the ^{42}K distribution can still be inhomogeneous. Moreover, ^{42}K

inside the mini-shroud volume can be collected on the detector surfaces, which needs to be considered in addition to a uniform distribution in LAr.

^{60}Co and ^{68}Ge:

^{60}Co ($T_{1/2}$ = 5.3 yr), produced by cosmogenic activation in Ge, can potentially lead to background at $Q_{\beta\beta}$ of ^{76}Ge. ^{60}Co undergoes β decay (Q_β = 2823.9 keV), followed by two γ-rays with 1173.2 and 1332.5 keV and both with 100% probability. In addition to the β spectrum, the two γ-rays with a total energy of 2505.7 keV can also contribute to the background at $Q_{\beta\beta}$. Its $T_{1/2}$ allows ^{60}Co still to be present in Phase I detectors (see Section 2.2). The ^{60}Co activities of the ^{enr}Ge detectors of Phase I were calculated in [105] for a reference date of July 2009, according to the known history of exposure above ground. Using these information, the total activity for the detectors of *Golden* data set in Nov 2011, i.e. beginning of Phase I data taking, have been estimated to be 2.26 μBq. While, for the *BEGe* data set a total activity of 0.6 μBq is expected [149]. Also, an additional background contribution from ^{60}Co is expected due to contamination of materials close to the detectors (see Table 2.1).

^{68}Ge ($T_{1/2}$ = 270.8 d) is another cosmogenically produced radioisotope in Ge, which decays to ^{68}Ga ($T_{1/2}$ = 67.6 m). ^{68}Ga undergoes β decay with Q_β =2921.1 keV, thus, is a potential background source that can induce events at $Q_{\beta\beta}$. Internal ^{68}Ge contamination for the newly produced BEGe detectors is expected to be 3.7 μBq, as derived from the assumed activation rate according to [149] and the history of exposure to cosmic rays. The contribution from ^{68}Ge contamination is negligible for the semi-coaxial detectors, which have been stored underground for several years.

The expected activity for the internal contaminations are used to constrain their contributions while constructing the background model of the energy spectrum.

$2\nu\beta\beta$ decay of ^{76}Ge:

The $2\nu\beta\beta$ decay spectrum has a broad maximum at about 700 keV. The end point energy is at $Q_{\beta\beta}$ = 2039 keV. Its spectral shape can be identified in the observed spectra at energies higher than the end point energy of ^{39}Ar. The $2\nu\beta\beta$ contribution is much more pronounced e.g. in the *Golden* spectrum compared to the *Golden-nat* spectrum, due to the ^{76}Ge fraction of about 87% in the ^{enr}Ge detectors compared to the natural abundance of 7.8%. An analysis of the measured spectrum allows for a precise determination of the half life of the $2\nu\beta\beta$ process, which is described in a dedicated chapter (Chapter 5). It brings one drawback as a background component; its presence raises the background level and lessens the significance of the γ-ray lines in that region, or even hides some of the γ-ray lines that could give hints on the sources of backgrounds. Nevertheless, for the GERDA Phase I detectors with an energy resolution of about 0.1% at $Q_{\beta\beta}$, $2\nu\beta\beta$ decay is a negligible background contribution in the region of interest around $Q_{\beta\beta}$.

4.4 Monte Carlo simulation of the background components

Expected spectral shape from the decays of the background sources discussed above are obtained through Monte Carlo simulations in the MaGe framework [135] based on Geant4 [150]. The simulations for the coaxial detectors were performed as part of this work and are explained here in detail. For the BEGe detectors, the details of the simulations can be found in [21].

A detailed representation of the Gerda Phase I detectors and the setup with 4 detector strings were implemented in MaGe. The dimensions of the detectors, e.g. height, radius, dead layer thickness d_{dl} of the n^+ surface, etc., were implemented according to Table 2.2. The d_{dl} of the p^+ surface was assumed as 300 nm. A range of d_{dl} values, i.e., 100–800 nm in steps of 100 nm, was considered for the α decay simulations, considering that the effective d_{dl} can be different than the expected one. Such precision of the d_{dl} on the p^+ surface is relevant only for the simulation of α particles, which have several tens of μm range in Ge. For all other background sources, the mean free path of the emitted particles in Ge is much larger than the d_{dl} of the p^+ surface.

Different source locations are considered for the simulations: inside the Ge detectors, on the p^+ / n^+ surfaces of the detectors, in LAr, in the holders, the mini-shrouds, the Rn shroud and the heat exchanger (Chapter 2). The considered locations are representative also for materials at similar distances, given the limited statistics to distinguish their individual contributions in the measured spectrum. The α decay simulations are done on the surface of a single detector, since the spectral shape from α (also β) energy depositions is independent of the detector dimensions, but only depend on the dead layer thicknesses. Other simulations were performed by considering the whole detector array, i.e. all the detectors were simulated simultaneously, which allows for investigation of the detector anti-coincidence cut. For the simulations in LAr, different sampling volumes were considered depending on the source under study. The simulations in the holders, the mini-shrouds, the Rn shroud and the heat exchanger were performed by uniformly sampling the events within the material of these hardware components. The *G4gun* generator of Geant4 [150] was used to sample the final state of decays. The exceptional cases, where the external generator Decay0 [151] was used, is mentioned while describing the simulations of individual sources.

The energy of the events after the simulations were smeared using a Gaussian distribution, the standard deviation of which was determined from the parametrized energy resolution vs energy functions obtained for each detector using the calibration data (Section 2.3.5). The details for each simulated background source are explained below.

Simulation of the ^{238}U series

alphas: Decays of all the α-emitting isotopes in ^{226}Ra and ^{210}Pb sub-chains – namely, ^{226}Ra, ^{222}Rn, ^{218}Po, ^{214}Po and ^{210}Po were simulated on the p^+ surface. Those from ^{226}Ra sub-chain were simulated in LAr in the bore hole volume, as well. In that case, the decays were constrained in LAr inside a 1 mm thick cylindrical shell with its outer surface overlapping with the p^+ surface. Given the tens of μm range of α particles in LAr, this volume is large enough to account for the farthest α decay that can deposit energy in the detec-

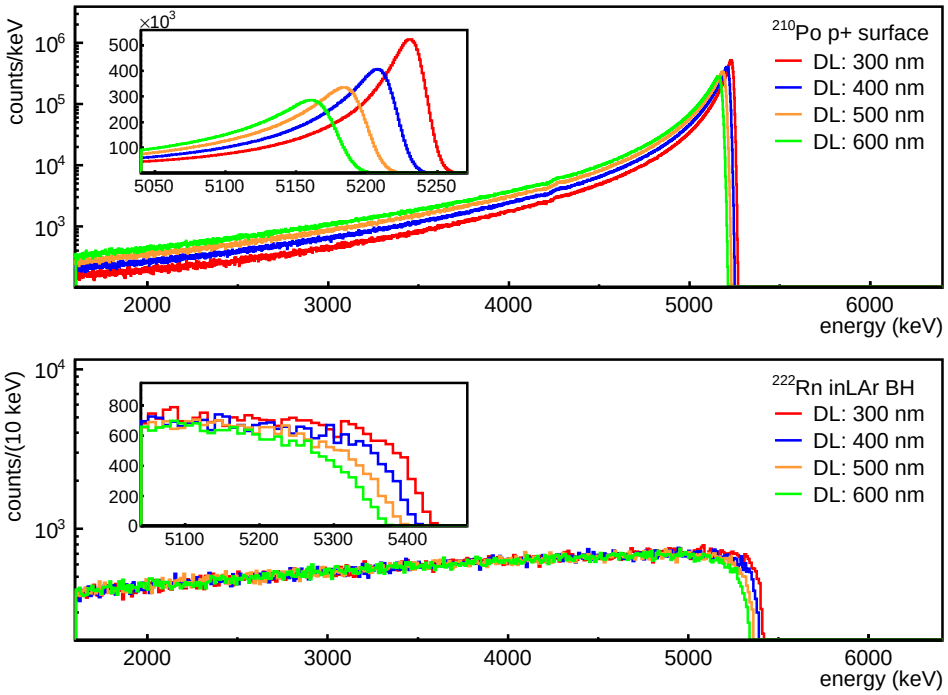

Figure 4.4: Simulated energy spectra resulting from ^{210}Po decays on the p^+ surface (top) and from ^{222}Rn decays in LAr in the bore hole volume (bottom) shown in comparison for different dead layer thicknesses and for the same number of simulated decays.

tors. Each simulation was repeated for d_{dl} of 100–800 nm in 100 nm steps. The simulated spectra of the α particles from ^{210}Po decays on the p^+ surface and from ^{222}Rn decays in LAr for d_{dl} of 300, 400, 500 and 600 nm are depicted in Fig. 4.4. While the maximum energy of the spectra depend on the energy of the emitted α particles, the spectral shape is similar for different isotopes.

^{226}Ra / ^{214}Bi: The decays of ^{214}Pb and ^{214}Bi from the ^{226}Ra sub-chain were simulated on the n^+ surface, in the holders, the mini-shrouds and the Rn shroud. The α emitting isotopes in the same sub-chain are not considered; α particles can not reach the active volume of the detectors from such distances due to their short range in the medium between the source and the active volume. Whereas, β decays with emission of γ-rays from ^{214}Pb and ^{214}Bi can contribute to the measured energy spectrum. Furthermore, ^{214}Pb and ^{214}Bi decays were simulated on the p^+ surface and in LAr volume close to the p^+ surface, as for the alphas (see above). For these isotopes, the whole bore hole volume was considered, without constraining the decays in a smaller sampling volume. The simulated energy spectra are shown in Fig. 4.5.

Simulation of the ^{232}Th-series

The sub-chains of the ^{232}Th decay chain, ^{228}Ra and ^{228}Th, do not have to be in secular

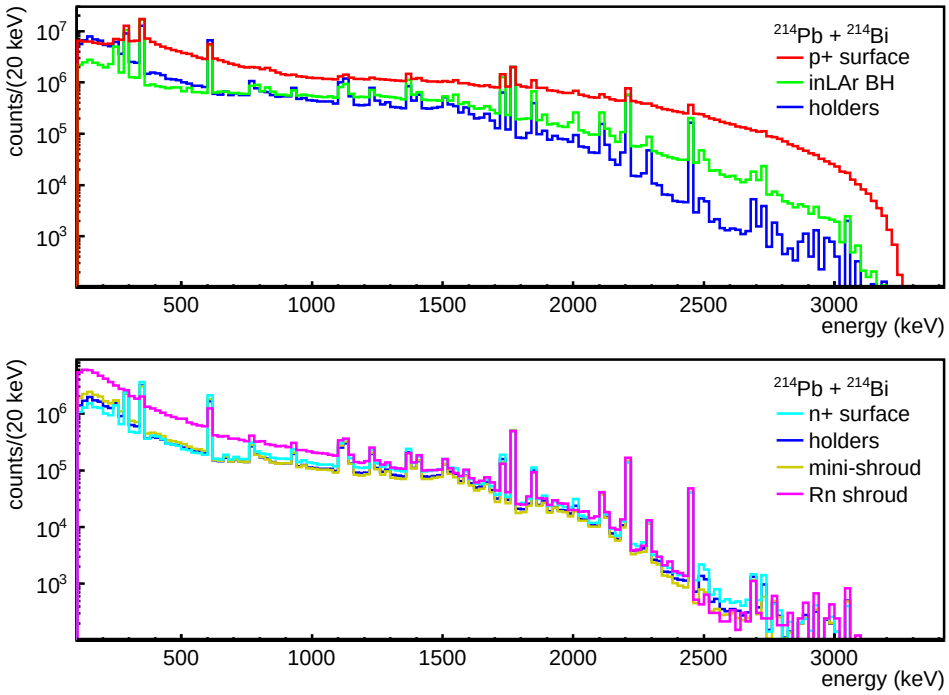

Figure 4.5: Simulated energy spectrum of ^{214}Pb and ^{214}Bi decays on the p+ surface (red), in LAr inside the bore hole volume (green), in the holders (blue), on the n+ surface (cyan), in the mini-shroud (dark yellow) and in the Rn shroud (magenta). The spectra are arbitrarily scaled to have the same 1764.5 keV γ-ray line intensity for an easy comparison of the spectral shapes.

equilibrium, and thus, were simulated separately. The α-emitting isotopes in the ^{232}Th decay chain were not simulated, given the absence of an indication for their contribution in the observed energy spectrum (Section 4.3.2).

^{228}Th / ^{208}Tl: The decays of ^{212}Bi and ^{208}Tl from the ^{228}Th sub-chain were simulated in the holders and in the Rn shroud (Fig. 4.6 top). The resulting spectra are summed by considering their different branching ratios. ^{208}Tl decays were simulated also in the heat exchanger, since they can contribute to the observed spectrum from such distance due to the high energy γ-ray line at 2614.5 keV. Also, some hints for ^{228}Th contamination of the heat exchanger were found during the commissioning runs Section 3.3.

^{228}Ra / ^{228}Ac: The decays of ^{228}Ac from ^{228}Ra sub-chain was simulated in the holders and in the Rn shroud (Fig. 4.6 bottom).

Simulation of ^{40}K

^{40}K decays were simulated in the holders and in the Rn shroud (Fig. 4.7). The main difference in the spectral shape from simulations in different locations is the ratio of peak and Compton continuum, due to a single γ-ray line with 1460.8 keV in the spectrum.

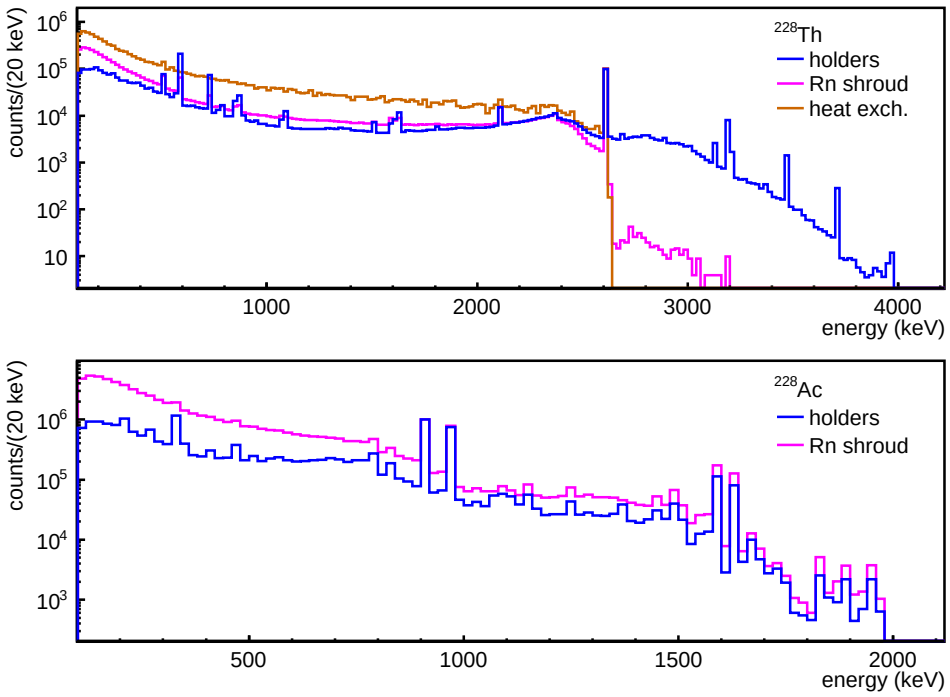

Figure 4.6: Simulated energy spectra from the decays of ^{228}Th (top) and ^{228}Ac (bottom) subchains in the holders (blue), Rn shroud (magenta) and heat exchanger (dark orange, only for ^{228}Th). The spectra are arbitrarily scaled to match the 2614.5 keV (top) and 911.2 keV (bottom) γ-ray line intensities for an easy comparison of the spectral shapes.

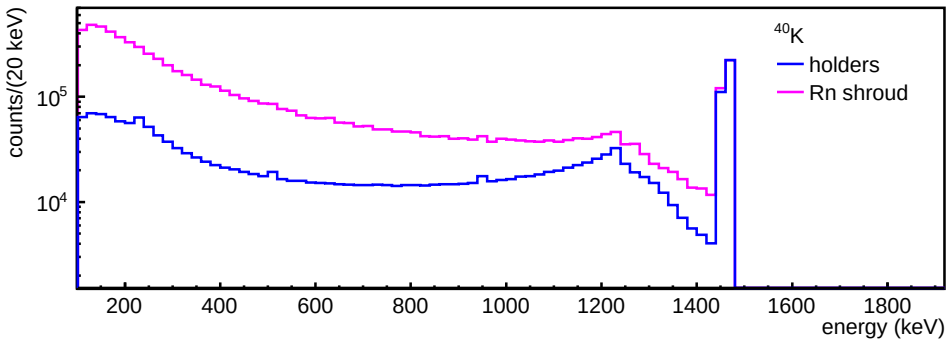

Figure 4.7: Simulated energy spectra from the decays of ^{40}K in the holders (blue) and in the Rn shroud (magenta). The spectra are arbitrarily scaled to match the 1460.8 keV γ-ray line intensities for an easy comparison of the spectral shapes.

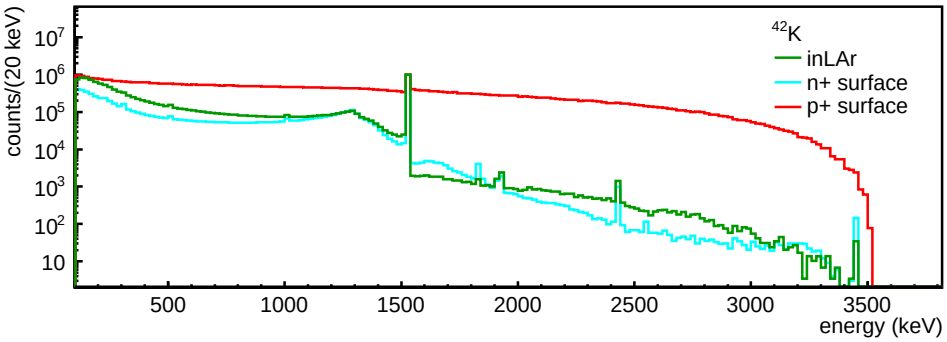

Figure 4.8: Simulated spectra of the ^{42}K decays in LAr with an homogeneous distribution (dark green), on the n+ surface (cyan) and on the p+ surface (red). The spectra are arbitrarily scaled to match the 1524.7 keV γ-ray line intensities for an easy comparison of the spectral shapes.

Simulation of ^{42}K

The decays of ^{42}K were sampled according to the generator DECAY0 [1] [151]. It produces the proper spectral shape of the ^{42}K β decay, which is not Fermi-allowed. The simulations were performed for three different source locations: in the LAr volume by assuming a uniform distribution, on the p^+ and n^+ surfaces (Fig. 4.8). For the simulation in LAr, the decays were confined to a cylindrical volume of LAr with a radius of 1.0 m and a height of 2.1 m, which is centered around the detector array.

Note that, the simulation of ^{42}K decays on the n^+ surface of the BEGe detectors, was performed with a dead layer model that assumes a zero charge collection efficiency in the first 40% fraction of the dead layer and a linearly increasing charge collection efficiency in the rest [152]. This model takes into account that the dead layer on the n^+ surface is partially active [153], which affects the detection efficiency for the surface β interactions.

Simulation of ^{60}Co

^{60}Co decays were simulated inside the Ge detectors (internal contamination) and in the holders (Fig. 4.9). For the simulation inside the Ge detectors, the same number of uniformly distributed events were simulated in the AV and in the DL of each detector separately. The total energy spectrum for one detector is then obtained by summing the resulting energy spectra from AV and DL, after scaling each with its volume fraction. The γ-ray peaks seen at 1173.2 and 1332.5 keV in the simulated spectrum of the internal contamination (labeled as inGe) are due to the decays taking place in the DL of the detectors. While in the simulated spectrum of the decays taking place in the AV no sharp peaks appear, since the total detected energy is always a sum of the energy deposition from the emitted β- and γ-rays.

[1] Note that, the energy of the 1524.7 keV γ-ray of ^{42}K is coded as 1525.0 keV in DECAY0. It can be either corrected after the simulations or fixed in the code before sampling the events.

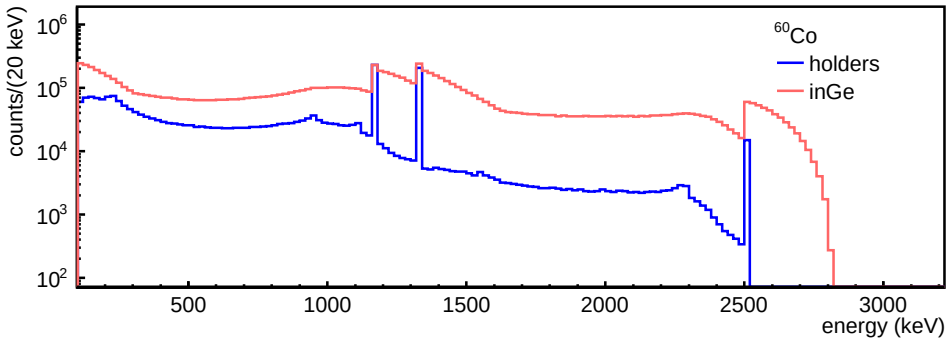

Figure 4.9: Simulated energy spectra from the decays of ^{60}Co in the holders (blue) and inside the Ge detectors (light red). The spectra are arbitrarily scaled to match the 1173.2 keV γ-ray line intensities.

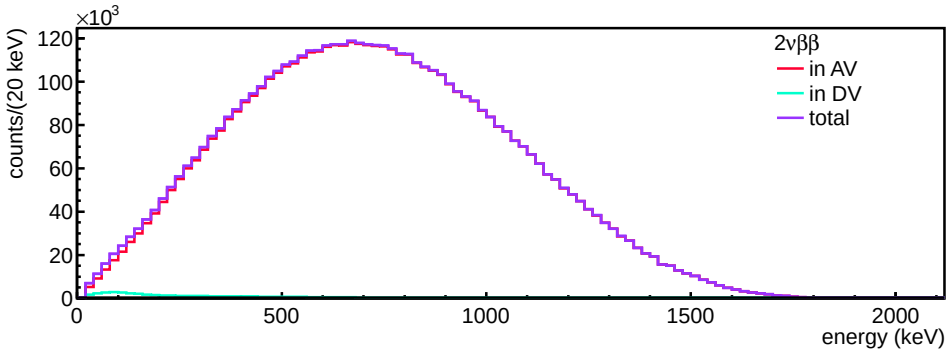

Figure 4.10: Simulated energy spectra from the ^{76}Ge $2\nu\beta\beta$ decays in the active volume (AV, light red) and in the dead layer (DV, light blue) of the Ge detectors. The total spectrum (purple) is obtained by summing the two spectra.

Simulation of $2\nu\beta\beta$ decay of ^{76}Ge

$2\nu\beta\beta$ decays of ^{76}Ge were sampled using the generator DECAY0 [151]. Same number of uniformly distributed events were simulated in the AV and in the DL of each detector separately. The total energy spectrum for one detector is obtained by summing the resulting energy spectra from AV and DL, after scaling each with its volume fraction (Table 2.2). The spectral shape resulting from the AV is very similar to the initial distribution fed into the simulation. The short range of electrons in Ge (few mm) allows for most of the energy released in the AV to be detected. The energy losses due to the escape of bremsstrahlung gammas and of electrons close to the boundaries of the AV result in a slightly softer simulated spectrum. Also for the decays that take place in the DL, large fraction of the electron energy is absorbed in the DL due to the short range of electrons. Fig. 4.10 shows the resulting energy spectra from both in AV and in DL simulations (after weighting according to AV and DL fractions), as well as the sum spectrum.

4.5 Analysis of the ^{214}Bi and ^{208}Tl backgrounds

The main source location of ^{214}Bi and ^{208}Tl backgrounds in the setup can be inferred by comparing the count rate of their γ-ray lines in the experimental spectrum to the ones in the simulated spectra at different source locations. For investigating the source location of ^{214}Bi, its γ-ray lines at 609.3, 1764.5 and 2204.2 keV and the γ-ray line from its mother isotope ^{214}Pb [2] at 351.9 keV are considered. The attenuation length of 300, 600 and 2000 keV γ-rays are 7, 10, 18 cm in LAr, respectively. This results in a significant difference in their relative count rates between close and far source locations, e.g. between holders and Rn shroud. In Table 4.3 the count rates, R_S, of the γ-ray lines in the spectrum of the *Golden* data set (as determined in Section 4.3.1) and the ones in simulated spectra are listed, together with the relative γ-ray intensities, I_γ, per decay of the mother isotope. The simulations on the p^+ and n^+ surfaces, in LAr bore hole volume, in the holders, the mini-shrouds and the Rn shroud are considered. For comparison, the γ-ray line count rates in the simulated spectra are obtained after scaling the spectra according to the intensity of the most significant γ-ray line at 1764.5 keV in the experimental spectrum. Results are given for the spectra both before and after the detector anti-coincidence cut applied. The simulations at the p^+ and n^+ surfaces and in LAr bore hole were performed with only one detector, thus, the anti-coincidence cut is not applicable to those.

The count rate of the 351.9 keV γ-ray line, denoted as $R_S(351.9\,\text{keV})$, is nearly a factor of two higher than $R_S(609.3\,\text{keV})$ in the *Golden* spectrum, while the ratio of I_γ of the two lines is 0.8. A plausible explanation is the different ranges and detection efficiencies of γ-rays with different energies. This effect can be seen if the R_S of the two lines are compared in the simulations in different source locations. For a close source location like the holders, the ratio of $R_S(351.9\,\text{keV})$ and $R_S(609.3\,\text{keV})$ is about 1.8, which decreases to 0.6 for farther locations like the Rn shroud. Another factor influencing the count rates is the complicated decay level scheme of ^{214}Bi. The decay of ^{214}Bi is followed by an emission of several photons within a few picoseconds. Detection of those photons by the neighboring detectors in coincidence with the 609.3 keV γ-ray will lead to rejection of those events if the detector anti-coincidence cut is applied. This is not expected for the 352 keV γ-ray line of ^{214}Pb. In order to investigate this effect, R_S of the γ-ray lines are determined also without the detector anti-coincidence cut applied. A decrease of about 20% in the $R_S(609.3\,\text{keV})$ after the cut can be seen both in the experimental spectrum and in the simulated spectra in close source locations, i.e. the holders and the mini-shrouds. The Rn shroud as source location is too far for the low energy photons to be detected, thus, a decrease after the cut is neither expected nor observed.

There is good agreement in the count rates of all γ-ray lines in the observed and simulated spectra in close source locations, i.e. the holders, the n^+ surface and the mini-shroud. All these locations are only few mm away from the detectors' AV. Count rates obtained from the simulation of decays in LAr BH also give compatible results. As a source location, the p^+ surface, only several 100μm away from the AV, shows a clear tension: the R_S of the γ-ray lines from simulations agree with data only within 3σ [3].

[2] ^{214}Pb and ^{214}Bi with similar half lives of less than an hour are expected to be in equilibrium

[3] The 68% C.I. is assumed as 1σ interval for easy expression

Table 4.3: Comparison of the count rates, R_S, for a selection of γ-ray lines from ^{214}Pb and ^{214}Bi in the experimental spectrum of the *Golden* data set with the ones in the simulated spectra at different source locations. The 68% C.I. for R_S is given for the γ-ray lines in the experimental spectrum (determined in Section 4.3.1), which is negligible for the simulated spectra, i.e. less than 0.1%. For comparison, R_S is determined in the simulated spectra scaled to match the intensity of the most significant γ-ray line at 1764.5 keV in the experimental spectrum. The comparison is given for the spectra both before and after the detector anti-coincidence cut applied.

Isotope	^{214}Pb	^{214}Bi	^{214}Bi	^{214}Bi
E_γ [keV]	351.9	609.3	1764.5	2204.2
I_γ [%]	37.6	46.1	15.4	5.1
after anti-coincidence cut				
R_S [cts/(kg·yr)]				
Golden data	20.4 (16.2, 24.8)	10.0 (8.0, 12.3)	3.1 (2.6, 3.7)	0.8 (0.5, 1.2)
holders	17.2	9.7	-	0.9
mini-shroud	15.4	10.2	-	0.9
Rn shroud	2.9	5.0	-	1.1
before anti-coincidence cut				
R_S [cts/(kg·yr)]				
Golden data	21.1 (16.8, 25.4)	12.7 (10.5, 15.0)	3.2 (2.7, 3.8)	0.9 (0.6, 1.3)
p^+ surface	30.4	7.8	-	0.9
n^+ surface	21.7	8.2	-	0.9
inLAr BH	27.4	13.1	-	0.9
holders	17.7	12.5	-	0.9
mini-shroud	15.7	13.6	-	0.9
Rn shroud	3.0	5.2	-	1.1

Table 4.4: Same as Table 4.3 for the γ-ray lines of ^{208}Tl. Simulated spectra are scaled to match the intensity of the 2614.5 keV γ-ray line in the experimental spectrum. The upper limits give the 90% C.I.

Isotope	^{208}Tl	^{208}Tl
E_γ [keV]	583.2	2614.5
I_γ [%]	30.4	35.6
after anti-coincidence cut		
R_S [cts/(kg·yr)]		
Golden data	3.9 (1.8, 5.7)	1.2 (0.9, 1.5)
holders	2.5	-
Rn shroud	0.5	-
heat exchanger	< 0.1	-
before anti-coincidence cut		
R_S [cts/(kg·yr)]		
Golden data	4.2 (2.4, 6.4)	1.7 (1.4, 2.1)
holders	3.4	-
Rn shroud	0.7	-
heat exchanger	< 0.1	-

The Rn shroud as a far source location, which is several tens of centimeters far away, completely disagrees: the prediction is 5σ off from the estimated $R_S(351.9\,\text{keV})$ in the experimental spectrum. Looking at these results, it can be concluded that, the major fraction of the ^{214}Bi background comes from close-by sources of the order of millimeters far away. Nevertheless, it is still possible to have minor contributions from decays on the p^+ surface and from sources at farther locations than the mini-shroud.

The same exercise is repeated for the ^{208}Tl source, considering its γ-ray lines at 583.2 and 2614.5 keV. Results are summarized in Table 4.4. The count rates of the γ-ray lines from the simulations in the holders, the Rn shroud and the heat exchanger are compared to the ones in the observed spectrum of the *Golden* data set. There is a clear preference for the holders simulation, i.e. close-by source locations. The Rn shroud simulation shows agreement only within 2σ, while for the heat exchanger simulation the tension is bigger. Therefore, only minor contributions to the observed spectrum are expected from far ^{208}Tl sources.

4.6 Analysis of the α-induced events

Possible sources and source locations that can lead to the observed events with energies higher than 3.5 MeV in the GERDA Phase I spectrum have been discussed in Section 4.3.2. The assumption that these events originate from the decays of α-emitters in the ^{226}Ra and ^{210}Pb sub-chains of the ^{238}U decay chain is verified in this section. The count rate distributions of the observed events as a function of time are compared to the expected ones given the assumptions on their origins. Also, a model describing the observed energy spectrum in the α-induced event region, i.e. 3.5–7.5 MeV, is obtained, using the simulated energy spectra of α decays on the p^+ surface and in LAr.

4.6.1 Count rate analysis

The observed peak like structure around 5.2 MeV with a degrading tail towards lower energies (Fig. 4.3) is attributed to the ^{210}Po α decays (E_α = 5.3 MeV), while the events above 5.3 MeV solely to the decays of α emitters in the ^{226}Ra sub-chain. The latter implies that, the events above 5.3 MeV should have an approximately constant count rate in time given the much longer half life of ^{226}Ra ($T_{1/2}$=1600 yr) compared to the measuring time of about 400 days. The events from ^{210}Po α decays can originate from an initial ^{210}Pb ($T_{1/2}$=22.3 yr) contamination on the p^+ surface, which would also result in an approximately constant count rate in time. They can, however, also originate from an initial ^{210}Po ($T_{1/2}$=138.4 yr) contamination. In this case, the count rate distribution is expected to decrease exponentially with the half life of ^{210}Po. The origin of these events can thus be inferred by analyzing the count rate distributions as a function of time.

The count rate distributions of the events in the 3.5–5.3 MeV and in the 5.3–7.5 MeV energy regions are obtained separately for the *Golden* data set. The models according to the assumptions discussed above are fitted to the distributions using the statistical method described in Section 4.1.2. The results of the analysis are summarized in Table 4.5.

The count rate distribution of events in the 5.3–7.5 MeV energy range is compatible with a constant rate, and thus, also with the assumption that these events originate from an initial ^{226}Ra contamination. A constant rate model fits the observed distribution well (p-value = 0.9), resulting in a constant rate of (0.09 ± 0.02) days.

The distribution of the number of events in 3.5–5.3 MeV range as a function of time shows a decreasing behavior as expected from an initial ^{210}Po contamination. For this distribution, two models are investigated: exponential rate, which assumes that all the events come from an initial ^{210}Po source; and exponential plus constant rate, which accounts also for the contributions from ^{226}Ra sub-chain and from a possible contamination with ^{210}Pb additional to the ^{210}Po, both of which would lead to events with constant rate. Fits are performed by taking the prior probability, $P_0(T_{1/2})$, as a Gaussian distribution with mean of 138.4 days and standard deviation of 0.2 days, i.e. modeling the literature value of ^{210}Po half life. Other parameters are given flat priors. Both models adequately describe the observed distribution. The fit with the exponential model resulted in a p-value of 0.1, while the one with the exponential plus constant rate model yielded a significantly better p-value of 0.9. Since the initial ^{226}Ra contamination assumed to originate the events

Table 4.5: Results of fitting an exponential and exponential plus constant count rate models to the count rate distribution of events with energies in 3.5–5.3 MeV range, and a constant rate model to the one in the 5.3–7.5 MeV range. The best fit parameters are quoted with 68% C.I.

models	C [cts/day]	N_0 [cts/day]	$T_{1/2}$ [days]	p-value
in (3.5–5.3) MeV range				
expo.		9.26 ± 0.26	138.40 ± 0.20	0.1
expo. + constant	0.57 ± 0.16	7.91 ± 0.44	138.40 ± 0.20	0.9
expo. + constant (no Gaussian prior)	0.73 ± 0.44	7.87 ± 0.44	130.40 ± 22.43	0.9
in (5.3–7.5) MeV range				
constant	0.09 ± 0.02			0.9

above 5.3 MeV (with a constant rate), contributes also in the region below (the fit region), a preference for the exponential plus constant rate model is plausible. The exponential rate model alone also describes the observed distribution well, since the constant term of (0.57 ± 0.16) cts/day is much smaller compared to the dominating exponential distribution with an initial count rate of (7.91 ± 0.44) cts/day, which corresponds to (0.18 ± 0.01) mBq. The analysis carried out by taking a flat $P_0(T_{1/2})$ results in a $T_{1/2}$ of (130.40 ± 22.43) days, which is in very good agreement with the expected (138.4 ± 0.2) days from ^{210}Po.

The count rate distribution of the events in the 3.5–5.3 MeV range together with the best fit exponential plus constant rate model (with Gaussian $P_0(T_{1/2})$) and the one in the 5.3–7.5 MeV range together with the best fit constant rate model are shown in Figs. 4.11 and 4.12, respectively. As described in Section 4.1.2, the analysis accounts for the live time fraction, i.e. the ratio of actual measuring time to the total time, which is for most of the time intervals different than 1 due to data taking interruptions. After correcting with the live time fraction, the expectations from the model are compared to the observations.

The results of the count rate analysis show excellent agreement with the assumed origin of the events. The events above 5.3 MeV have a constant count rate in time as expected from an initial ^{226}Ra contamination. The ones below 5.3 MeV come from two sources: dominantly from an initial ^{210}Po contamination, verified by the partial decrease of the count rate distribution with $T_{1/2}$ of ^{210}Po; and from an initial ^{226}Ra contamination, resulting in a small constant term. This small constant term can also partially come from an initial contamination with ^{210}Pb. A possible contribution from the ^{210}Pb contamination can be identified by the observation of the 46.5 keV γ-ray line of ^{210}Pb. However, the energy reconstruction in GERDA Phase I is not optimized for the events with such low energies. Therefore, the ^{226}Ra and a possible ^{210}Pb contributions can not be distinguished reliably.

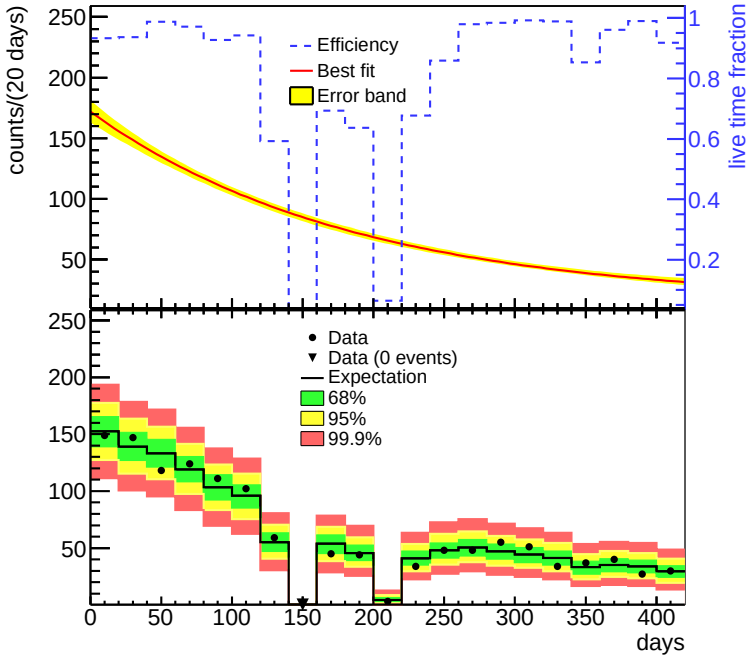

Figure 4.11: Result of fitting an exponential plus constant rate model to the count rate distribution of events with energies in the 3.5–5.3 MeV range (with Gaussian $P_0(T_{1/2})$). Upper panel: The best fit model (red line, left axis) with the 68% uncertainty band (yellow area) and the live time fraction distribution (dashed blue line, right axis). Lower panel: The observed number of events (markers) and the expected number of events (black histogram) from the best fit model that accounts for the live time fraction. The green, yellow and red regions are the smallest intervals containing 68%, 95% and 99.9% probability for the expectation, respectively.

4.6.2 Spectral analysis

The MC simulations performed to obtain the spectral shape of the background contributions from α decays are described in Section 4.4. Different dead layer thicknesses on the p^+ surface (d_{dl}) of the detectors were considered in the simulations. The maximal energy deposited in the active volume depends on d_{dl}, as demonstrated in Fig. 4.4. In order to determine d_{dl} of the detectors, firstly, the simulated spectra of ^{210}Po α decays on the p^+ surface with different d_{dl} assumptions are fitted to the energy spectrum of the *Golden* data set in the ^{210}Po peak region, i.e. 4800–5250 keV, using the statistical method described in Section 4.1.2. The fit window is dominated by ^{210}Po decays, below which ^{226}Ra ($E_\alpha = 4.8$ MeV) decays on the p^+ surface are expected to contribute as well.

Fig. 4.13 shows the results of the fits performed with different d_{dl} assumptions. The d_{dl} of 400 nm gives the most similar spectral shape compared to the others. However, none of the simulated ^{210}Po spectra with a single d_{dl} assumption adequately describes the

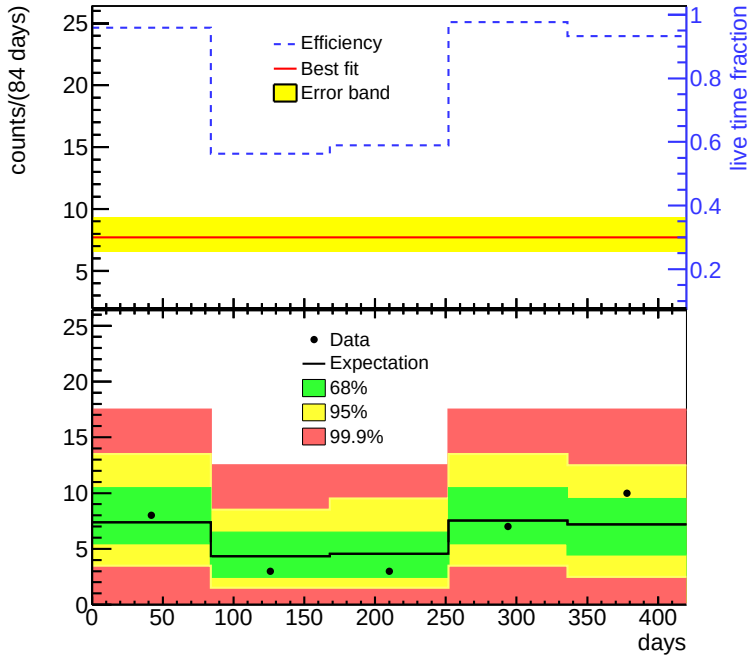

Figure 4.12: Same as Fig. 4.11 for a constant rate model fitted to the count rate distribution of events with energies in the 5.3–7.5 MeV range.

observed spectrum, i.e. all fits result in a very small p-value, i.e. < 0.001.

The dead layer thickness on the p^+ surface is expected to be around 300 nm, however, it can be non-uniform along the surface due to the B-implantation process. Moreover, the partly active transition layer between the dead layer and the active volume known to exhibit charge collection inefficiencies, resulting in an effective dead layer thickness. The energy spectrum of α events traversing a dead layer and a transition layer can be described by a superposition of spectra expected from an "idealized" dead layer without a transition layer. Thus, the simulated energy spectra with d_{dl} of 300, 400, 500 and 600 nm are used to model the effective d_{dl} that can describe the observed spectrum. The contribution of each component is kept as a free parameter in the fit. A combination of the spectra simulated for d_{dl} of 300, 400, 500 and 600 nm describes the observed peak structure very well (p-value = 0.8), with the individual contributions in the best fit model account for 66.5, 744.6, 44.3 and 302.6 counts (in the fit window), respectively. Simulated spectra with smaller (down to 100 nm) and larger (up to 800 nm) values of d_{dl} were also included in the analysis, however yielded insignificant contributions to the overall spectrum, i.e. less than 1 count.

Fig. 4.14 shows the data and the best fit model together with the individual contributions for each component with different d_{dl} assumptions. The good agreement between

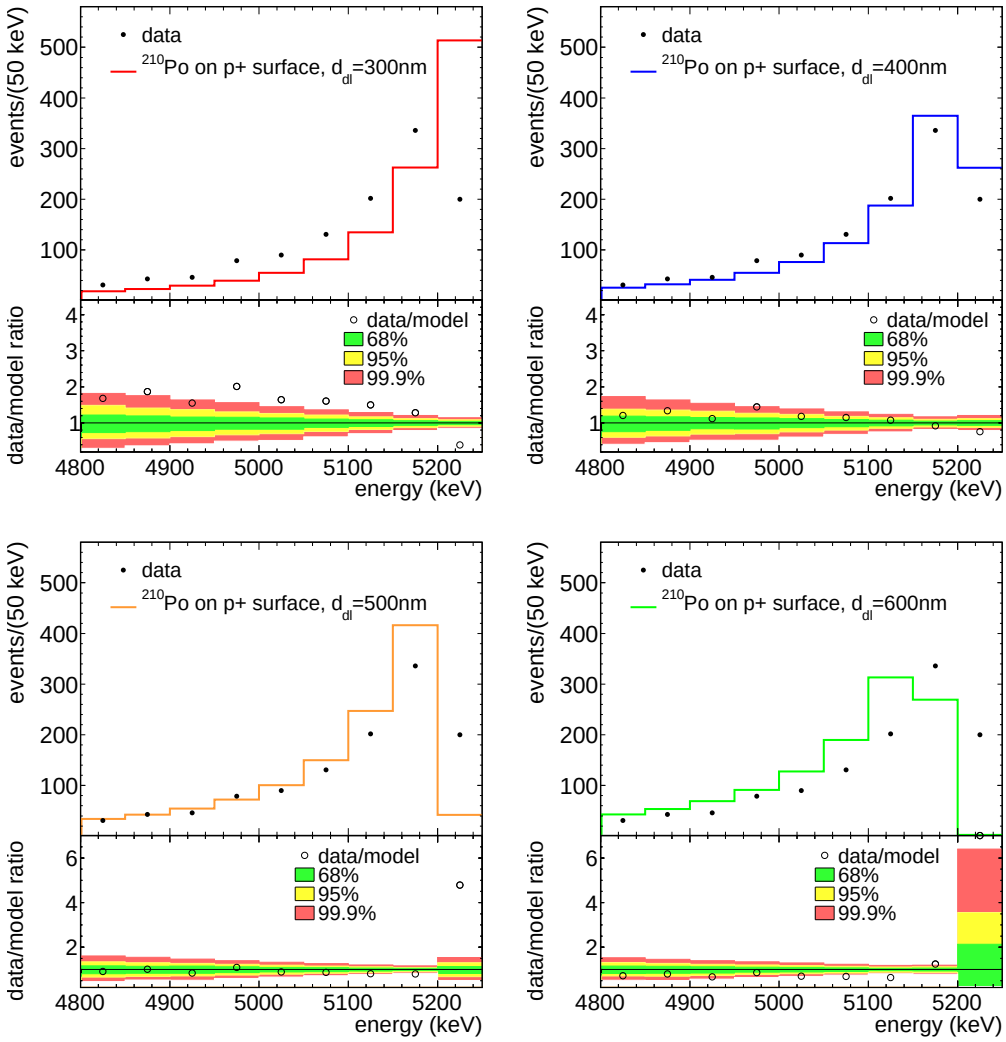

Figure 4.13: Results of fitting the simulated spectrum of ^{210}Po α decays on the p^+ surface to the energy spectrum of the *Golden* data set in the ^{210}Po peak region, i.e. 4800–5250 keV. Four fits are performed assuming d_{dl} of 300 nm (top left), 400 nm (top right), 500 nm (bottom left) and 600 nm (bottom right). Upper panels show data together with the best fit model, and lower panels data to model ratio together with the smallest intervals containing 68%, 95% and 99.9% probability for the ratio assuming the best fit parameters.

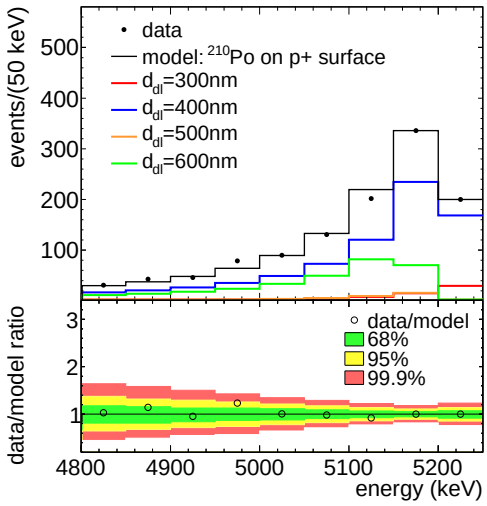

Figure 4.14: Same as Fig. 4.13. The best fit model consists of the simulated energy spectra of ^{210}Po α decays on the p^+ surface with 300, 400, 500 and 600 nm d_{dl}, individual contributions of which are shown in the upper panel.

data and the best fit model is demonstrated in the lower panel. The effective dead layer model, i.e. combination of 300, 400, 500 and 600 nm dead layer thicknesses, is used in the further analyses.

The whole energy interval above 3.5 MeV is analyzed by fitting a global α-model to the observed energy spectrum. The analysis is done for the *Golden*, *Golden-HdM*, *Golden-Igex* and *Golden-nat* data sets separately. The fit model consists of contributions from the α decays of ^{210}Po on the p^+ surface and the decays of the α-emitters in the ^{226}Ra sub-chain (^{226}Ra, ^{222}Rn, ^{218}Po and ^{214}Po) on the p^+ surface and in LAr volume close to the p^+ surface. For the contributions from p^+ surface decays, the effective dead layer model is assumed. Whereas, for the contributions of decays in LAr, the simulations with single d_{dl} of 300 nm are considered. Considering an effective dead layer model also for the latter has no influence on the results due to the lack of discriminating power of the available statistics at the maximum energy region of these components. The global fit is carried out in an energy window of 3.5–7.5 MeV divided to 50 keV wide bins, and using the statistical method described in Section 4.1.2. The scaling parameter of each model component is kept free and given a flat prior probability distribution.

The upper panels in Fig. 4.15 show the experimental spectrum together with the best fit model, as well as individual components of the α-model for the *Golden* (top) and *Golden-nat* (bottom) data sets. The α-model describes the observed spectrum above 3.5 MeV very well for both data sets, showing no indications for unidentified structures or missing background components. The contributions from the p^+ surface simulations reproduce the observed peak like structures, i.e. around 4.7 MeV (^{226}Ra), 5.3 MeV (^{222}Rn), 5.9 MeV (^{218}Po) and 5.2 MeV (^{210}Po). However, they can not account for the observed continuum below and above the peaks. Contributions from approximately flat components, like the

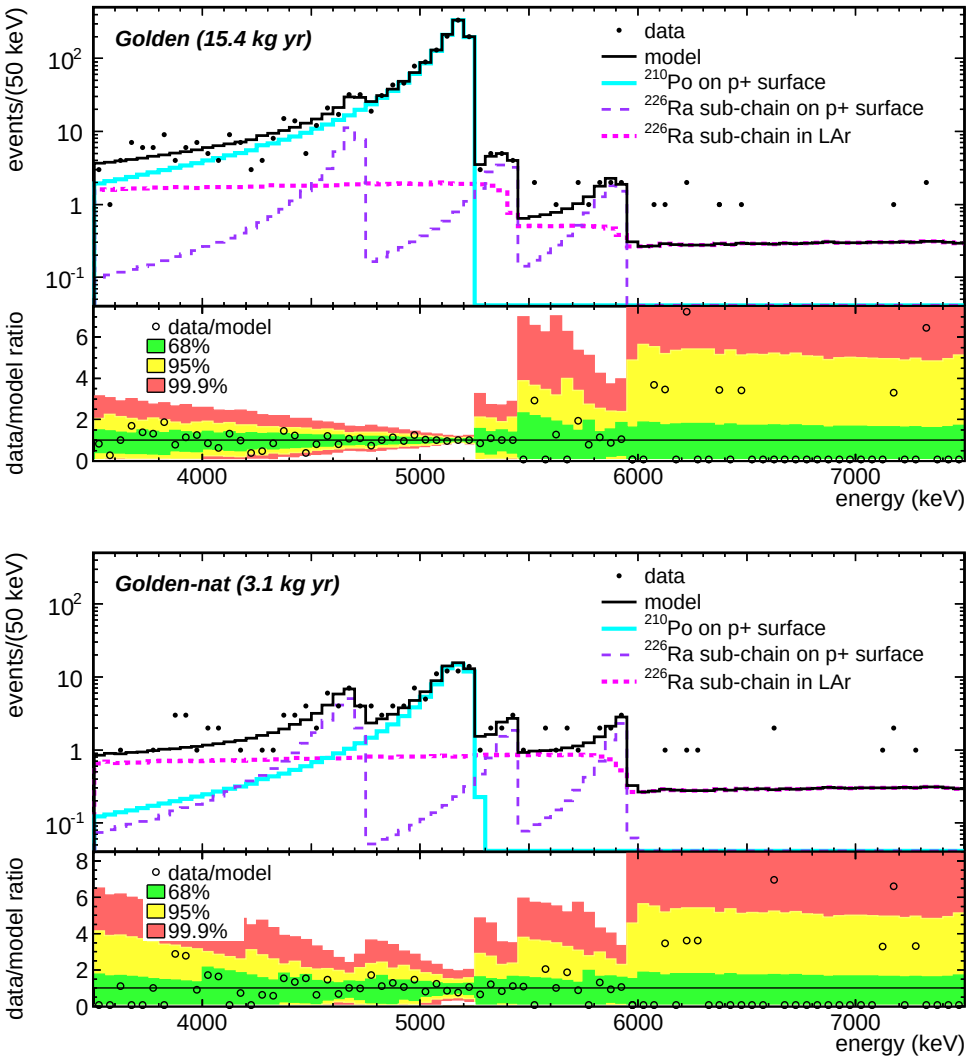

Figure 4.15: Upper panels: Experimental spectrum in the E > 3.5 MeV region (black markers) and the best fit model, together with the individual components of the best fit model for the *Golden* (top) and *Golden-nat* (bottom) data sets. Lower panels: Data to model ratio together with the smallest intervals containing 68%, 95% and 99.9% probability for the ratio assuming the best fit parameters.

energy spectra of α decays in LAr close to the p^+ surface, are necessary to describe the whole spectrum. The necessity of such flat components is more clear in the spectrum of the *Golden-nat* data set compared to the *Golden* data set: the latter is dominated by the tail of the ^{210}Po peak also in the low energy region below ~4.6 MeV (which can still not account for all the events), and thus, the contribution from LAr decays give a smaller contribution in this energy region; whereas, for the former the low energy region can clearly not be described by the p^+ surface decays alone, the contribution of which is about an order

of magnitude lower than the count rate in that energy region. The analysis is repeated also for the subsets of the *Golden* data set, namely for the *Golden-HdM* and *Golden-Igex* data sets. Their energy spectra can also be reproduced very well by the α-model. All performed α-model fits result in a p-value higher than 0.1. The considered contributions in the α-model are sufficient to describe the experimental energy spectra above 3.5 MeV.

The expected number of events from each model component in the energy spectra (0–7.5 MeV) of the analyzed data sets according to the α-models are listed in Table 4.6. The global modes with the 68% C.I. or 90% probability upper limits are quoted. The number of events from the p^+ surface decays show a systematic decrease for each subsequent isotope in the ^{226}Ra sub-chain. Such a decrease has been observed for all the analyzed data sets. The reason can be the reduced detection efficiency of the α particles emitted by the nuclei that have been recoiled away from the surface after the decay of the mother nuclei. The recoil nucleus gains about 100 keV kinetic energy after the α decay and can get detached from the p^+ surface. The detection efficiency for the α decays taking place on the p^+ surface is $\sim$50%, which is also verified by the MC simulations. Thus, in approximately half of the surface decays the daughter nuclei recoil away from the surface and the α particle it emits can escape detection due to the very small range of the α particles in LAr, i.e. few tens of μm.

The fit parameters for the spectra of α decays in LAr are strongly correlated. The spectral shapes of the decays of different isotopes in LAr are indistinguishable, i.e. all have approximately a flat energy distribution. Moreover, the number of observed events in the energy regions, where these spectra are relevant, is very small. For all the in LAr components upper limits on the parameters are derived, except for the ^{214}Po in LAr, which is the only contribution above $\sim$ 6 MeV. ^{226}Ra in LAr component does not give any contribution to the best fit α-models of the analyzed data sets. The contribution from ^{226}Ra decays in LAr was considered in the analysis to check for the possibility of ^{226}Ra on the surfaces dissolved in LAr. However, the results of the spectral analysis show no indication for ^{226}Ra in LAr, which indicates that the origin of events is ^{222}Rn in LAr.

4.6.3 ^{226}Ra activity on the p^+ surface due to the α-model

Table 4.7 lists the ^{226}Ra activities on the p^+ surface of the detectors for different data sets that are derived from the α-models, by using the expected number of events from the ^{226}Ra decays on the p^+ surface (Table 4.6) and assuming a detection efficiency of 50% [4] for the α decays on the p^+ surface. The α-model considers only the α-emitting isotopes in the ^{226}Ra sub-chain, since the model describes the energy spectrum above 3.5 MeV. When the analysis window extends below 3.5 MeV, the β/γ-emitting isotopes in the ^{226}Ra sub-chain decaying on the p^+ surface have to be taken into account as well.

[4] The detection efficiency derived from the simulations of a large sample of events is $\sim$50%, as expected in an ideal case. Note that, the uncertainty on the detection efficiency of small number of events is not accounted for in the uncertainties on the activities.

Table 4.6: Expected number of events from each α-model component in the energy spectra (0–7.5 MeV) of the analyzed data sets. The mode and the 68% C.I. or 90% probability upper limits are quoted.

Model component	Number of expected events [cts]			
	Golden (15.4 kg·yr)	*Golden-nat* (3.1 kg·yr)	*Golden-HdM* (10.9 kg·yr)	*Golden-Igex* (4.5 kg·yr)
on p^+ surface				
^{226}Ra	50.5 (36, 65)	27.5 (20, 36)	46.5 (35, 62)	8.5 (5, 13)
^{222}Rn	24.5 (18, 33)	13.5 (9, 20)	23.5 (17, 32)	6.5 (3, 10)
^{218}Po	13.5 (9, 19)	15.5 (10, 20)	13.5 (9, 19)	< 6
^{214}Po	< 10	7.5 (4, 11)	< 9	< 7
^{210}Po	1355 (1310, 1400)	76.5 (66, 88)	1258.5 (1240, 1320)	74.5 (65, 86)
in LAr BH				
^{226}Ra	< 159	< 45	< 148	< 26
^{222}Rn	< 64	< 25	< 52	< 10
^{218}Po	< 30	< 26	< 30	< 6
^{214}Po	19.5 (10, 29)	16.5 (8, 27)	14.5 (8, 25)	< 5

Table 4.7: Total ^{226}Ra activity on the p^+ surface of the detectors that are considered in the *Golden*, *Golden-HdM*, *Golden-Igex* and *Golden-nat* data sets as derived from the α-models. The 68% uncertainties are propagated from that of the expected number of events from ^{226}Ra decays on the p^+ surface (Table 4.6), which are used for deriving the activity.

data sets	^{226}Ra activity on p^+ surface [μBq]
Golden (15.4 kg·yr)	3.0 ± 0.9
Golden-HdM (10.9 kg·yr)	2.8 ± 0.8
Golden-Igex (4.5 kg·yr)	0.5 ± 0.2
Golden-nat (3.1 kg·yr)	1.6 ± 0.5

4.6.4 Contribution from α-induced events at $Q_{\beta\beta}$

The number of expected α-induced events in the energy region of interest around $Q_{\beta\beta}$ is derived from the α-model. Fig. 4.16 shows the continuum of the α-model and the individual model components in the 400 keV window around $Q_{\beta\beta}$ for the *Golden* data set. The expected total B in the 10 keV window around $Q_{\beta\beta}$ is $2.4 \cdot 10^{-3}$ cts/(keV·kg·yr) with the main contribution of $1.8 \cdot 10^{-3}$ cts/(keV·kg·yr) coming from the decays in LAr, $0.6 \cdot 10^{-3}$ cts/(keV·kg·yr) coming from ^{210}Po decays on p^+ surface and $0.3 \cdot 10^{-4}$ cts/(keV·kg·yr)

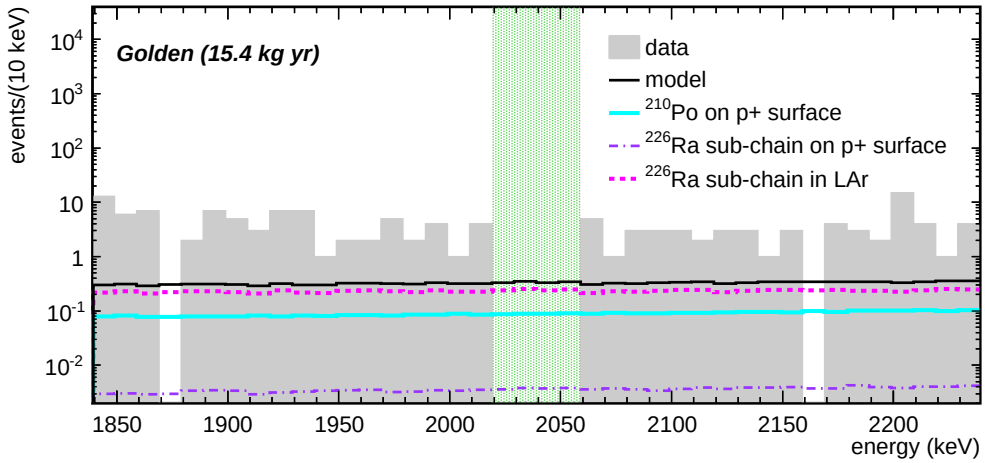

Figure 4.16: The continuum of the α-model and of the model components in the energy region of $Q_{\beta\beta}\pm200$ keV for the *Golden* data set. The green box indicates the $Q_{\beta\beta} \pm 20$ keV blinding window.

Table 4.8: Expected background index (B) in the 10 keV window around $Q_{\beta\beta}$ from the α-model and from the individual model components for *Golden*, *Golden-HdM*, *Golden-Igex* and *Golden-nat* data sets. The global mode together with the 68% C.I. is given.

components	B [10^{-3} cts/(keV·kg·yr)]			
	Golden (15.4 kg·yr)	*Golden-HdM* (10.9 kg·yr)	*Golden-Igex* (4.5 kg·yr)	*Golden-nat* (3.1 kg·yr)
^{210}Po on p^+ surface	0.63	0.84	0.15	0.20
^{226}Ra sub-chain on p^+ surface	0.03	0.03	0.01	0.09
^{226}Ra sub-chain in LAr (close to p^+ surface)	1.77	2.23	0.53	3.50
α-model	2.4 (2.3, 2.6)	3.1 (3.0, 3.3)	0.7 (0.6, 0.8)	3.8 (3.4 ,4.6)

from ^{226}Ra decays on p^+ surface for the *Golden* data set. As shown in Table 4.8, the contribution from the α-induced events around $Q_{\beta\beta}$ and also the fraction of the contribution from different components depend on the considered data set. The ^{210}Po contamination rate and hence B due to ^{210}Po is higher for the *Golden-HdM* data set compared to the *Golden-Igex* and *Golden-nat*. Whereas, the ^{226}Ra contamination rate is the highest for the *Golden-nat* data set. The IGEX detectors are the cleanest ones in terms of surface contaminations; B from the α-induced events for the *Golden-Igex* data set is nearly 3 times lower compared to other data sets. Comparison of the results from different data sets clearly indicates a correlation between B due to ^{226}Ra decays on the p^+ surface and the one in LAr. This is possibly due to the contribution from the decays of nuclei that recoil away from the p^+ surface into the LAr.

^{222}Rn is expected to be present in LAr due to emanation from the materials with ^{226}Ra contamination. The ^{222}Rn emanation rate of the cryostat in its final configuration has been measured to be (54.7±3.5) mBq. Also, the non-metallic materials used in the lock system contribute with an activity of less than 17 mBq. The B from ^{222}Rn emanated into LAr from the cryostat was estimated to be $< 0.7 \cdot 10^{-3}$ cts/(keV·kg·yr) (see Table 2.1) The B from the decays of α emitters due to ^{222}Rn in LAr close to the p^+ surface according to the α-model is higher than this estimation, i.e. $1.8 \cdot 10^{-3}$ cts/(keV·kg·yr) for the *Golden* data set. Even higher B is expected if the contribution from β- and γ-rays occurring in the decay chain are also considered. A possible explanation for this discrepancy is the ^{226}Ra contamination of materials close to the detector array, which was not accounted for in the previous estimation. The ^{226}Ra contamination of the detector surfaces (both p^+ and n^+) and the material in the close vicinity of the detectors, i.e the detector assembly, the mini-shrouds [5], etc., can result in the higher observed ^{222}Rn activity in the LAr volume close to the detectors compared to the average activity in the whole LAr volume.

4.6.5 Stability of the fit results

The stability of the α model predictions with respect to the choice of the fit window and bin width was investigated. The analysis was repeated for the bin widths of 25 keV and 100 keV, and also in a smaller fit window of 4.0–7.0 MeV for the *Golden* data set. A larger fit window was not tested, since contributions from other background sources than the ones considered in the α-model are expected to dominate the spectrum below 3.5 MeV. Also, a bin width smaller than 25 keV was not tested, since the energy calibration above 2.6 MeV is an extrapolation of the calibration curves (second order polynomial functions), and the uncertainties in the energy calibration can reach few tens of keV for these high energies (see Section 2.3.5).

The α-model shows good agreement with the observed spectrum for the tested fit window and bin widths, i.e. all fits resulting in a p-value better than 0.1. The expected B in the 10 keV window around $Q_{\beta\beta}$ from the α-model and from the individual model components are obtained for each configuration and compared to the reference fit results, which was performed in 3.5–7.5 MeV fit window with 50 keV bin width. The deviations in percentage from the reference fit results are listed in Table 4.9. Different choices of bin widths result in deviations of -0.2% and +2.2% in the expected B. Compared to the fit uncertainty of -4.2% and +8.3% on the expected B from the reference α-model, different bin widths yield stable results within the statistical uncertainty. A larger deviation of -7.6% is seen in the B obtained from the analysis in the smaller fit window of 4.0–7.0 MeV, mainly due to the ^{226}Ra sub-chain in LAr component. The contribution from this component becomes more relevant at the lower and higher energy regions of the analysis window, i.e. far from the peak like structures (see Fig. 4.15). Thus, the fit window of 4.0–7.0 MeV results in a smaller contribution of decays in LAr compared to the one in the 3.5–7.5 MeV window.

[5] The total ^{226}Ra contamination only in the three mini-shrouds is about 200 μBq as given by the screening results.

Table 4.9: Deviations in the expected B due to different fit window and bin widths compared to the reference α-model of the *Golden* data set. The reference fit was performed in 3.5–7.5 MeV fit window with 50 keV bin width. The fit window of 4.0–7.0 MeV and bin widths of 25 keV and 100 keV are tested and the deviations from the reference result are given in percentage.

	% deviation in the B		
components	3.5–7.5 MeV		4.0–7.0 MeV
	25 keV	100 keV	50 keV
^{210}Po on p^+ surface	0.4	1.0	0.1
^{226}Ra sub-chain on p^+ surface	-8.5	-6.4	4.2
^{226}Ra sub-chain in LAr (close to p^+ surface)	-0.3	2.8	-11.0
global α-model	-0.2	2.2	-7.6

4.6.6 Cross-check of the α-model

The α-model is based on the assumption that all events with energies higher than 3.5 MeV in the experimental spectra originate from α-decays taking place on or in the vicinity of the p^+ surface. This assumption has been investigated in an independent study based on pulse shape analysis (PSA) technique [20, 138]. This section summarizes the method and its results, mainly for the identification of the α-induced events.

Recognition of α-induced events using pulse shape analysis

A surface event is defined as an event that deposit energy in the active volume close to the detector surfaces, i.e. not in the bulk material. The α decays that take place on or close to the p^+ surface (possibly also the groove surface [6]) can result in energy depositions in the active volume of the detectors. Alpha particles, with a mean range of tens of μm's in Ge, have well localized energy depositions, practically point-like, and are always stopped at the surface of the detectors. Similarly, β-events have well localized energy depositions (within few millimeters). Thus, β-decays that originate from external sources, e.g. ^{214}Bi or ^{42}K, and that deposit energy in the active volume of the detectors are expected at the detector surfaces as well (including the n^+ electrode). Note that, β-events can also have secondary interaction points in the detector volume due to the emission of bremsstrahlung γ-rays produced by the electrons. Both α- and β-events are classified as *surface events* in this study. Whereas, γ-events can result in energy depositions in the whole detector volume and at single or multiple interaction positions, due to the larger penetration length of γ-rays compared to β-rays and α particles.

[6] There is no information available on the actual dead layer thickness on the groove (see Section 2.3.1). In case it is of the order of μm, the α-decays that take place on or close to the groove surface can also result in energy depositions in the active volume of the detectors. In the α-model analysis no distinction was made between the p^+ and groove surfaces. However, a possible difference in the dead layer thicknesses of the two surfaces is accounted for in the effective dead layer model, which describes the data adequately.

A mono-parametric PSA technique has been developed in [20,138] for identification of *surface events* on the p^+ electrode or groove of the semi-coaxial type Phase I detectors. The detector response as a function of the interaction location was investigated using pulse shape simulations. The electric field inside the Ge crystal and the charge transportation has been calculated for the ANG3 detector geometry. In order to study the correlation between signal shape and interaction position, the detector active volume was sampled simulating mono-energetic point-like interactions. Fig. 4.17 shows the electrode scheme, the dimensions of the crystal, the simulated electric potential and field of ANG3, as well as a representative selection of the simulated signals. Most of the detector active volume produces signals characterized by a fast leading edge at the end of the charge collection. Whereas, the volume surrounding the bore-hole (p^+ electrode) generates charge signals with a fast rising part at the beginning of the charge collection. The regions in the proximity of the groove and at the bottom of the bore-hole create signals with a steeper leading edge. In these regions, the charge collection is faster than in the rest of the crystal because of the reduced distance between the electrodes and thus the stronger electric field. The simulated signals reproduce qualitatively all the features of the observed ones in the GERDA Phase I data (see Figure 3.3 of [20]).

The rise time between 5% and 50% of the maximum pulse amplitude (rt_{5-50}) has been identified as an efficient parameter to discriminate the *surface events* on the p^+ electrode or groove from events that deposit energy elsewhere. The event classification was performed using a simple cut on this parameter. The cut was performed at a fixed value and was calibrated separately for each detector using the rt_{5-50} distribution of the ^{210}Po α-events forming the peak like structure. The cut value was defined as the rt_{5-50} value below which 95% of the events between 4.8 and 6.0 MeV are contained. Since the rise time is energy independent, as was verified using the calibration data (see Section 3.2.3 of [20]), the efficiency of the cut in identifying α-events is by definition 95%.

Fig. 4.18 shows the distribution of events as a function of rt_{5-50} and energy for the ^{enr}Ge-coax detectors considered in the *Golden* data set. The horizontal line in the plots indicates the cut value and the vertical (red) ones the γ-ray lines at 1525 keV (^{42}K) and 2614 keV (^{208}Tl) and the end-point energy of ^{42}K at 3540 keV. Also, the energy regions of $Q_{\beta\beta} \pm 100$ keV and $Q_{\beta\beta} \pm 20$ keV (blinding window) are indicated with vertical (blue) lines. The rt_{5-50} values of events in the peak-like structure from ^{210}Po decays and its continuum until 3.5 MeV, as well as in the energy region above this peak-like structure until 7.5 MeV, are in very good agreement with the expected rt_{5-50} values from α decays close to or on the p^+ and groove surfaces. A continuum of events with faster rise times, i.e. below ~ 100 ns, can be seen in the whole α-induced event region, i.e. E$>$ 3.5 MeV, which are in agreement with the expectations from decays on the p^+ surface at the bottom part of the bore hole or on the groove surfaces. The rt_{5-50} values of the events between 2.6 and 3.5 MeV are also mostly below the cut. In addition to α-decays, also contributions from β-decays, e.g. of ^{42}K and ^{214}Bi, are expected in this energy region. However, since the β events are both on the p^+ and n^+ surfaces, some events are also expected to be above the cut. A very different rt_{5-50} distribution can be seen for the events below 2.6 MeV. In this region, events are both above and below the rt_{5-50} cut, since γ-events, and also β-events both on p^+ and n^+ surfaces, are contributing to the spectrum.

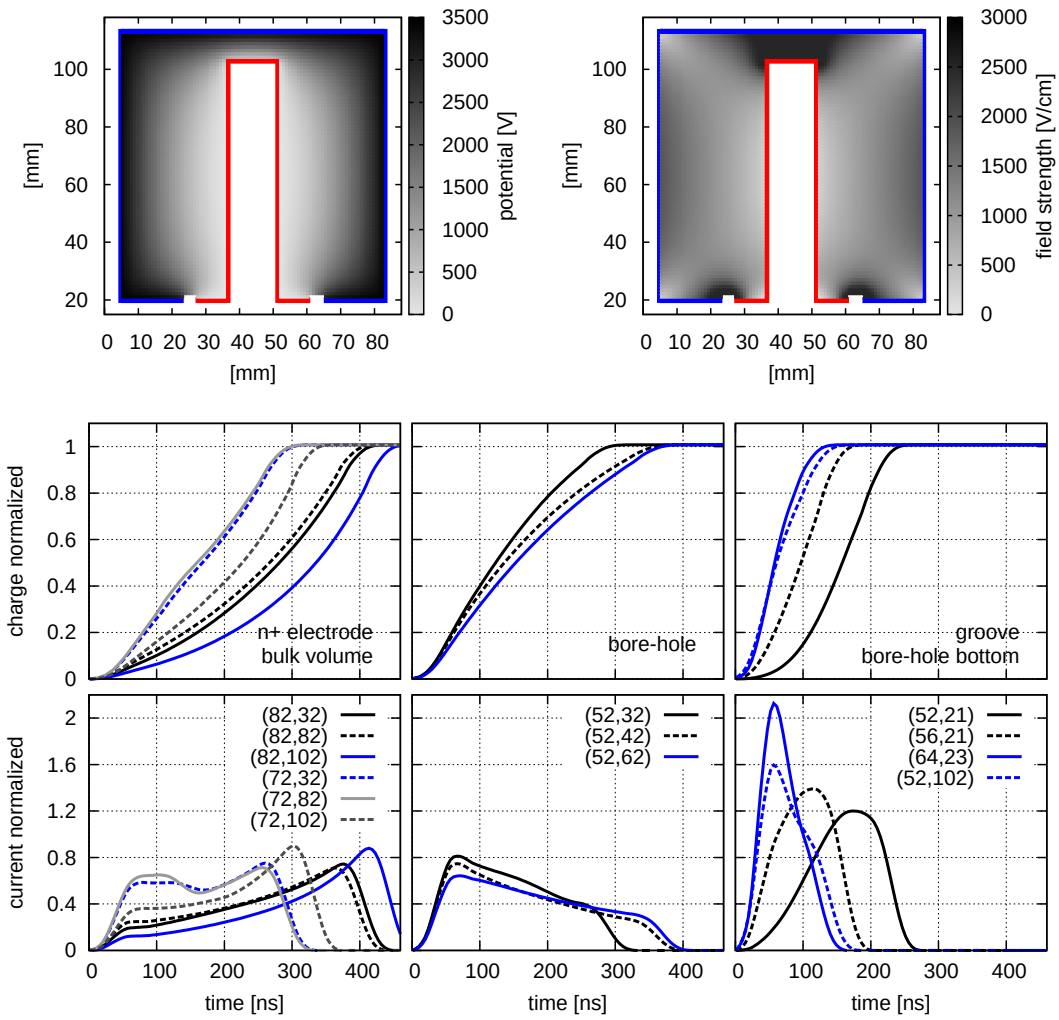

Figure 4.17: Upper plots: Simulated electrical potential (left) and field strength (right) for a vertical section of the detector passing through the symmetry axis. The n^+ and p^+ electrodes are indicated with a blue and red line, respectively. The two electrodes are divided by a groove. Lower plots: Simulated signals for point-like energy depositions occurring close to the detector surfaces or in the bulk volume. The current signals are computed by differentiating the charge signals. Taken from [20].

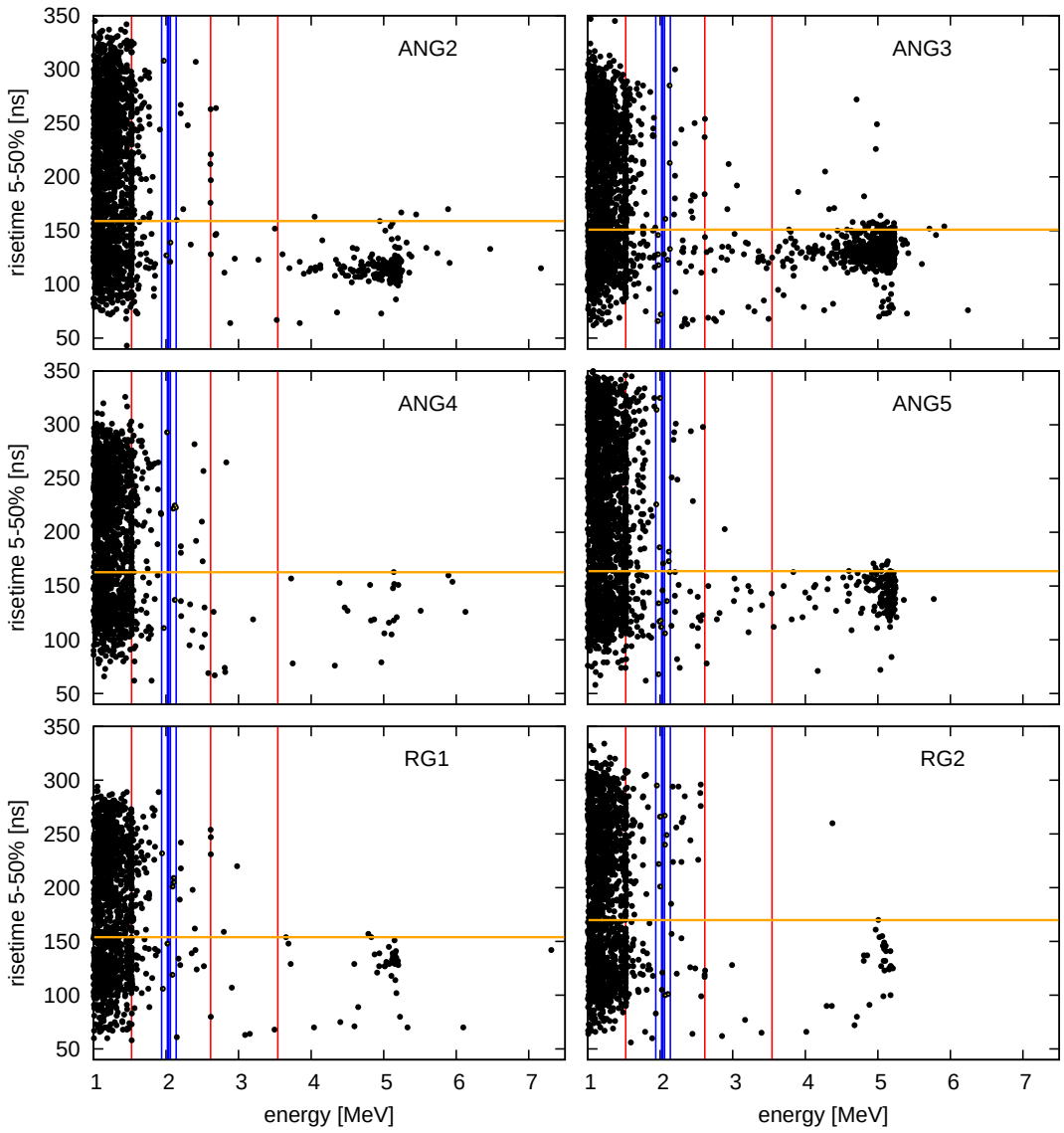

Figure 4.18: Event distribution in the rt_{5-50} vs energy space. The horizontal line shows the cut value. The following energy values have been highlighted: 1525 keV (^{42}K γ-ray line), $Q_{\beta\beta} \pm 100$ keV, $Q_{\beta\beta} \pm 20$ keV (blinded region), 2614 keV (^{208}Tl γ-ray line), 3540 keV (^{42}K end point). Update from [20].

4.7 The background model

The Phase I data sets listed in Table 4.1 are analyzed to model the entire background spectrum above the endpoint energy of ^{39}Ar, i.e. between 570 and 7500 keV. The contributions from ^{214}Bi (^{226}Ra)[7], ^{228}Th, ^{228}Ac, ^{40}K, ^{42}K, ^{60}Co, ^{68}Ge, $2\nu\beta\beta$ of ^{76}Ge and from the α-emitters – namely, the ones in the ^{226}Ra sub-chain and ^{210}Po – are considered in the background model. A detailed discussion on the background components was given in Section 4.3.2 and the MC simulations performed to obtain the spectral shape of each component assuming different source locations were described in Section 4.4. The simulated energy spectra of the background components are fitted to the observed spectra in the analysis window divided into 231 bins, each 30 keV wide, by using the method described in Section 4.1.2. In the experimental spectra, events with energies in the 2019–2059 keV range were not available for analysis due to the blinding procedure. Consistently, the number of events in this energy range of the simulated spectra were set to zero prior to the analysis.

Two different global models are defined: a minimum model, that accounts for the minimum number of background components expected to describe the observed spectrum, and a maximum model, that contains all the background components possibly giving a contribution. The assumptions on the contribution of some of the background components, according to the results of previous analyses or measurements, are modeled by the prior probability distributions of the parameters and incorporated into the analysis. These constraints are specified below. Unless otherwise specified, the parameters are kept free and given a flat prior probability distribution.

4.7.1 Minimum and maximum models for the coaxial detectors

The background components considered in the minimum model are the simulated spectra of ^{76}Ge $2\nu\beta\beta$ decays, ^{42}K decays in LAr, ^{214}Bi, ^{228}Th, ^{228}Ac, ^{40}K and ^{60}Co decays in the holders, ^{60}Co decays in Germanium, ^{214}Bi decays on the p^+ surface, and the decays of ^{210}Po and the α-emitters in the ^{226}Ra sub-chain.

The distribution of ^{42}K in LAr is assumed to be homogeneous in the minimum model as a first order approximation, since the electric fields dispersed in LAr have been minimized in the Phase I data taking configuration (Section 2.3). The possibility of higher ^{42}K densities on the p^+ or n^+ surfaces are accounted for in the maximum model. The background sources give major contributions from the contaminations in the close-by locations as shown in Tables 4.3 and 4.4 for ^{214}Bi and ^{228}Th (the same is assumed for ^{228}Ac) and as expected from the results of the screening measurements for ^{40}K and ^{60}Co. Therefore, for these background sources the contaminations in the holders are considered in the minimum model, which also represent the contaminations in *close source* locations, e.g. the n^+ surface of the detectors, the detector assembly, the mini-shroud, etc. The minimum model does not account for *medium distance* or *distant source* locations such as the Rn-shroud

[7]The contribution from ^{226}Ra sub-chain is divided into two components: from the α-emitters and from ^{214}Pb & ^{214}Bi only. Here, ^{214}Bi represents the contribution from the latter.

or the heat exchanger. Contributions from other possible source locations (even closer or farther away) are included in the maximum model.

For the contribution from the α-emitters, the α-model developed in Section 4.6.2 is considered as a single component in the minimum model. The α-model describes the whole observed spectrum in the 3.5–7.5 MeV energy range very well. Its continuum towards lower energies is approximately flat without any structures. Therefore, no significant difference in the results is expected when the pre-obtained α-model is used instead of considering each individual component of the α-model in the global fit. The ^{226}Ra activity on the p^+ surface of the detectors was derived from the α-model in Section 4.6.3. The α-model accounts for the contribution of only the α-emitters in the ^{226}Ra sub-chain, due to the analysis energy window considered in the α-induced events. In the global background model, the contribution from ^{214}Bi decays on the p^+ surface given the ^{226}Ra activity listed in Table 4.7 is taken into account as well. The parameter of this component is given a Gaussian prior probability distribution that models the expected ^{226}Ra activity on the p^+ surface.

The contribution from ^{60}Co decays in ^{enr}Ge-coax detectors is constrained according to the expected initial ^{60}Co activity in the beginning of Phase I data taking; in total 2.3 μBq for the detectors of the *Golden* data set, with 1.3 μBq coming from the HdM and 1.0 μBq from the Igex detectors (see Section 2.2). The parameter for this background component is given a range between zero and the value that corresponds to the ^{60}Co activity, and a flat prior in that range. Such information is not available for the ^{nat}Ge-coax detectors. Thus, the parameter of ^{60}Co in Ge component is kept free for the analysis of the *Golden-nat* data set.

The maximum model contains the contributions from ^{42}K decays on the p^+ and n^+ surfaces, ^{214}Bi decays in the Rn shroud and in LAr in the bore hole volume with an homogeneous distribution, ^{228}Th and ^{228}Ac decays in the Rn shroud and ^{228}Th decays in the heat exchanger, in addition to the minimum model components. The additional components in the maximum model account for the possibility that, the background sources in different locations than the ones assumed in the minimum model can also give significant contributions to the observed spectrum. These different locations are detector surfaces, medium distances (represented by the Rn shroud) and distant locations (represented by the heat exchanger). Both minimum and maximum models describe the experimental spectra of the *Golden* and *Golden-nat* data sets equally well, i.e. p-values > 0.1 and similar. However, the minimum model has 10 parameters, whereas the maximum model has 17. Figs. 4.19 to 4.21 show the results of the minimum and maximum model fit to the *Golden* spectrum, and the minimum model fit to the *Golden-nat* spectrum. The experimental spectra and the best fit models are shown together with the individual model components in the energy range of 570–3630 keV. The only contribution above 3500 keV comes from the α-model, which was shown in Fig. 4.15 for both *Golden* and *Golden-nat* data sets. Note that the overall scaling of the α-models did not change in the global fits performed here. The lower panels in Figs. 4.19 to 4.21 show the good agreement between the observations and the expectations from the global background model. The energy spectra of the *Golden-HdM* and *Golden-Igex* data sets can also be described by the minimum model very well.

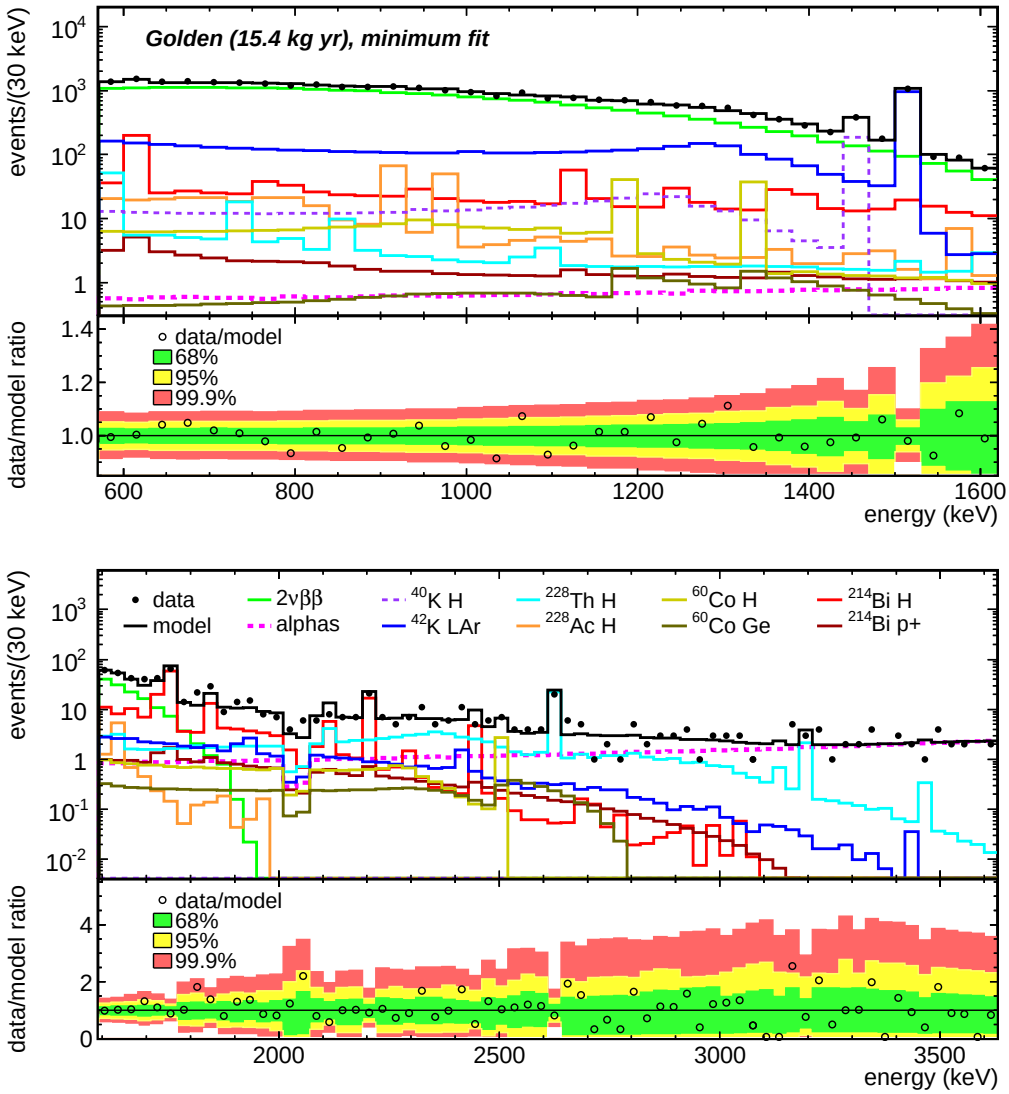

Figure 4.19: Background model and decomposition obtained from fitting the minimum model to the energy spectrum of the *Golden* data set. The experimental spectrum and the best fit model together with the individual model components are shown from 570 to 3630 keV in the upper panels. See Fig. 4.15 for the 3500–7500 keV energy range. The lower panels show the ratio of data and model predictions together with the smallest intervals containing 68% (green band), 95% (yellow band) and 99.9% (red band) probability for the ratio assuming the best fit parameters.

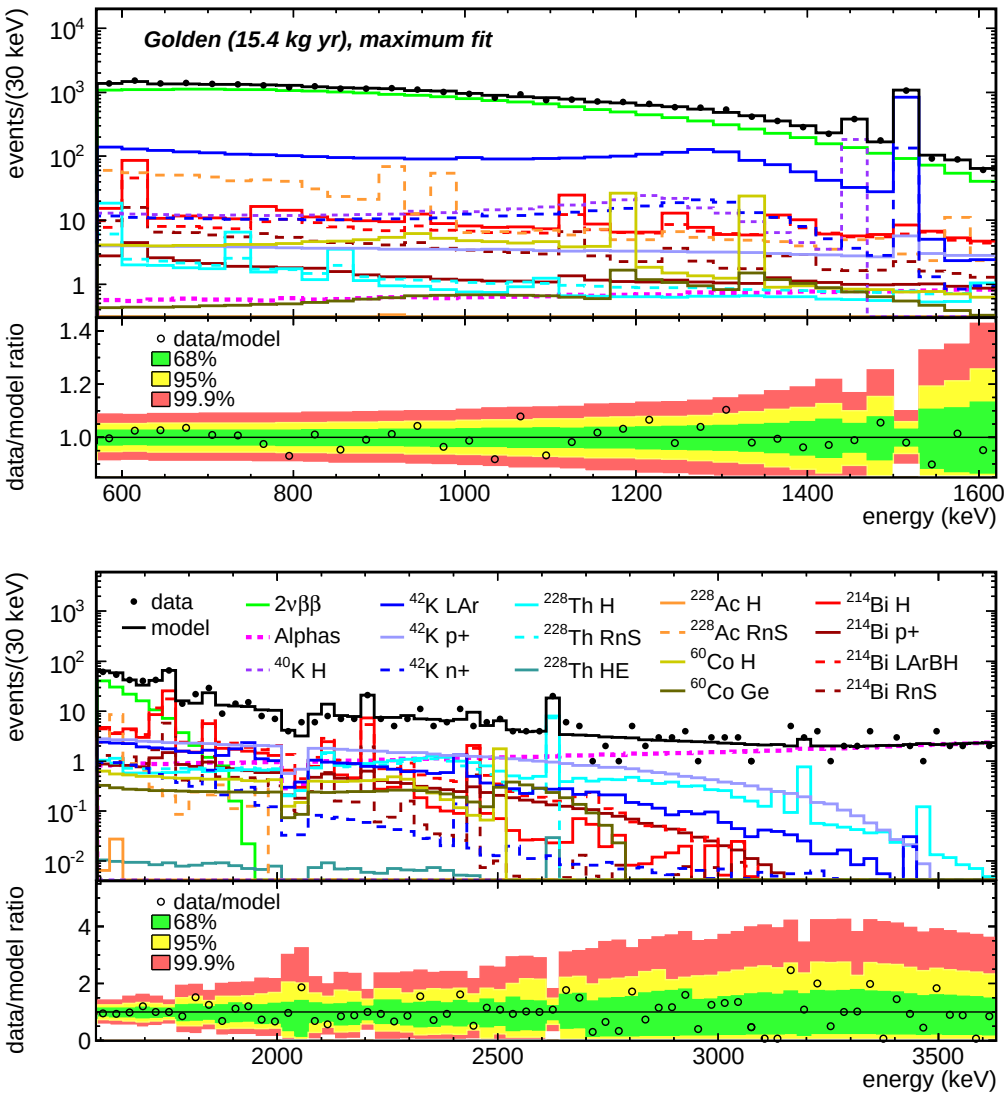

Figure 4.20: Same as Fig. 4.19 for the maximum model of the *Golden* data set.

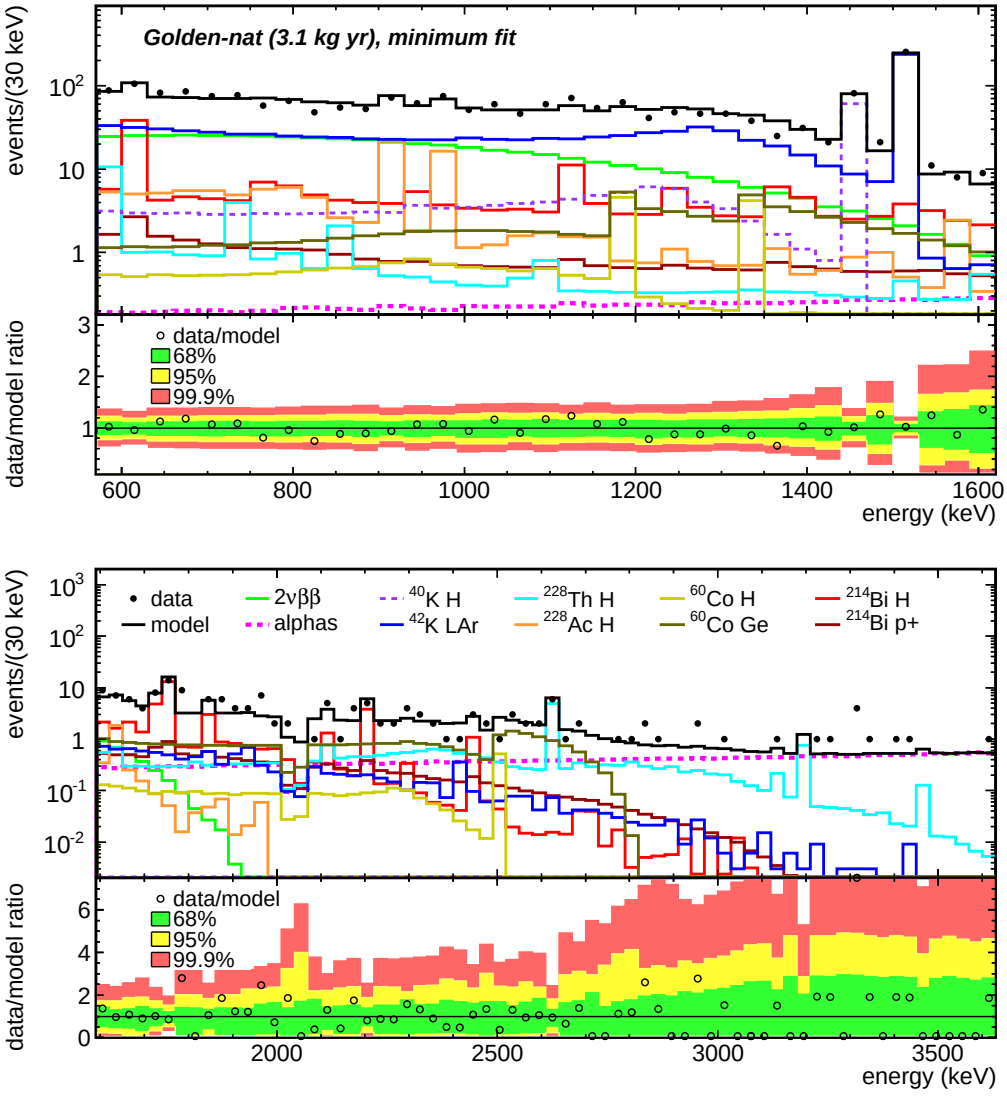

Figure 4.21: Same as Fig. 4.19 for the minimum model of the *Golden-nat* data set.

4.7.2 Extended minimum model for the *Silver* data set

The *Silver* data set contains the data from the same set of detectors as the *Golden* data set, however, in the *silver run period*, i.e. $\sim$ 30 days of data taking that are not included in the *golden run period* (see Section 4.2). The energy spectrum of the *Silver* data set can not be described well with the minimum model of the *Golden* data set. The minimum model parameters are given Gaussian priors that model the results of the minimum fit to the *Golden* data set and fitted to the spectrum of the *Silver* data set, which resulted in a p-value of < 0.01. The observed background rate is significantly higher in the *silver run period* compared to other run periods (see Section 2.3.6), indicating the presence of additional background sources. These can be the increased rate of ^{42}K and/or ^{214}Bi (^{222}Rn) decays on and close to the detector surfaces due to an altered distribution of these isotopes in LAr, which is expected due to the alterations in the experimental surrounding during the detector array modifications. The global fit was repeated with the minimum model components by keeping all parameters free. However, the rate of the background components that are expected to be stable, i.e. in the holders or in Ge, changed significantly compared to the minimum model of the *Golden* data set, which is not plausible.

An extended minimum model is defined by including the possible extra background contributions – namely, ^{42}K decays on the p^+ and n^+ surfaces, and ^{214}Bi decays on the n^+ surface and in LAr close to the p^+ surface – in the minimum model components. The contributions from ^{214}Bi, ^{228}Th, ^{228}Ac, ^{40}K and ^{60}Co decays in the holders and from ^{60}Co decays in Ge are assumed to be stable during the whole run period. Therefore, the parameter of these background components were constrained by Gaussian priors that model the minimum model results of the *Golden* data set. The parameters of the extra background components, and also the one of the $2\nu\beta\beta$ decay component for consistency check, were kept free. The extended minimum model describes the energy spectrum of the *Silver* data set very well (p-value = 0.4). The background contributions, especially from the extra components that account for the increased B is the *silver run period*, are discussed in Section 4.7.7.

4.7.3 Extended minimum model for the *BEGe* data set

The energy spectrum of the BEGe detectors has been analyzed in a separate work [21] using an equivalent procedure as for the coaxial detectors described above and the same statistical method as in Section 4.1.2. An extended minimum model was fitted to the observed energy spectrum. The model contains two more background components in addition to the minimum model components of the coaxial detectors: ^{68}Ge decays in Ge and ^{42}K decays on the n^+ surface. For the BEGe detectors, a contribution from the internal ^{68}Ge ($T_{1/2} = 271\,\mathrm{d}$) contamination is expected as discussed in Section 4.3.2. The contributions from the internal contaminations with ^{68}Ge and ^{60}Co are constrained by defining an upper bound for the parameter ranges according to activities of 3.7 and $0.6\,\mu$Bq, respectively. The upper bounds were derived from the known history of exposure to cosmic rays for the individual detectors and according to [149]. The ^{42}K decays on the

n^+ surface component was added to the model due to the enhanced contribution expected for the BEGe detectors with respect to the coaxial detectors, given the smaller d_{dl} of the n^+ surface of BEGe detectors. The extended minimum model adequately describes the spectrum of the *BEGe* data set (p-value = 0.5). The total B and the contributions from the individual model components are discussed in Section 4.7.7.

4.7.4 Comparison of the γ-ray line count rates

An important verification of the global background model is to compare the γ-ray line count rates, R_s, in the experimental spectrum to the ones predicted by the model. This is especially important, as the global fit was performed using a bin width much larger than the energy resolution of the detectors. Moreover, the global model gives a prediction for R_s of the 351.9 keV γ-ray line of ^{214}Pb, which is outside the fit window. The intensity of this γ-ray line strongly depends on the source location mainly due to its low energy; the closer the source position, the higher is the expected intensity (see Table 4.3 for the quantification through MC simulations). The predicted R_s of the 351.9 keV γ-ray line should agree with the observed one for an accurate global model.

The R_s of the γ-ray lines determined in the experimental spectra in Section 4.3.1 and the ones predicted by the global model components given the best fit parameters are listed for the *Golden* and *Golden-nat* data sets in Tables 4.10 and 4.11, respectively. The uncertainties on the predicted R_s by the global models are due to the fit uncertainty on the parameters of the model components that give contribution to the γ-ray line. The statistical uncertainty due to the simulated number of events is less than 0.1%, which is negligible compared to the fit uncertainty. The R_s of the γ-ray lines in the *Golden* data set, including the 351.9 keV line, are in very good agreement with the predictions from both minimum and maximum models, i.e. within the 68% uncertainty intervals. For the *Golden-nat* data set, the minimum model predictions show very good agreement with data for all the γ-ray lines. Whereas, the maximum model predictions for the 351.9 keV (^{214}Pb) and 727.3 keV (^{212}Bi) γ-ray lines show significant disagreement, i.e. outside the 95% uncertainty interval. The spectrum of the *Golden-nat* data set, with a factor of five less statistics compared to the *Golden* data set, could be consistently described with the maximum model if some of the free parameters were constrained. Such necessary constraints might be coming from the higher statistics, and consequently, more significant structures in the energy spectrum of the *Golden* data set, which can explain why it is consistently decomposed by the maximum model without any additional constraints on the parameters.

4.7.5 Source activities

The global model provides a full decomposition of the background spectrum into the individual components with their expected contributions. The source activities of the background components are derived using the number of simulated events and the results of the scaling parameters from the global fit. Table 4.12 summarizes the source activities for the considered background components in the minimum and maximum models of the

Table 4.10: Comparison of the observed γ-ray line count rates, R_s, and the predicted ones from the minimum and maximum models given the best fit parameters for the *Golden* data set. The 68% C.I. of R_s (or 95% probability upper limit) predicted by the global models are propagated from the uncertainties or limits on the fit parameters. The statistical uncertainty due to the simulated number of events is less than 0.1% and negligible compared to the fit uncertainty.

Isotope	E_γ [keV]	R_S [cts/(kg·yr)]		
		minimum model	maximum model	data (*Golden*)
^{214}Pb	351.9	20.1 (17.9, 22.7)	17.5 (4.2, 24.5)	20.4 (16.2, 24.8)
^{214}Bi	609.3	11.2 (10.0, 12.6)	8.0 (2.0, 11.2)	10.0 (8.0, 12.3)
	1764.5	3.6 (3.2, 4.1)	2.7 (0.7, 3.8)	3.1 (2.6, 3.7)
	1120.3	2.6 (2.3, 2.9)	1.8 (0.4, 2.5)	< 3.1
	2204.2	1.0 (0.9, 1.1)	0.8 (0.2, 1.1)	0.8 (0.5, 1.2)
	1729.6	1.0 (0.9, 1.1)	1.0 (0.2, 1.4)	0.5 (0.2, 0.9)
	1847.4	0.6 (0.5, 0.7)	0.6 (0.1, 0.8)	0.6 (0.3, 1.0)
	2447.9	0.3 (0.27, 0.34)	0.2 (0.05, 0.3)	0.2 (0.1, 0.4)
^{228}Ac	911.2	3.8 (2.2, 5.8)	3.4 (1.0, 3.6)	3.9 (2.2, 5.6)
	969.0	2.7 (1.5, 4.1)	2.6 (0.8, 2.8)	3.5 (1.8, 5.0)
^{212}Bi	727.3	0.9 (0.8, 1.1)	0.4 (0.1, 0.6)	< 4.7
^{208}Tl	2614.5	1.4 (1.2, 1.7)	1.0 (0.2, 1.5)	1.2 (0.9, 1.5)
	583.2	2.9 (2.5, 3.5)	1.3 (0.3, 2.0)	3.9 (1.8, 5.7)
^{60}Co	1173.2	2.5 (1.6, 3.7)	1.6 (0.6, 2.9)	4.2 (2.8, 5.6)
	1332.5	2.3 (1.4, 3.4)	1.5 (0.5, 2.6)	< 1.6
^{40}K	1460.8	11.8 (10.6, 13.6)	11.8 (10.6, 13.6)	13.6 (12.5, 15.0)
^{42}K	1524.7	61.2 (59.3, 63.8)	61.4 (48.5, 66.2)	60.3 (58.1, 62.5)

Table 4.11: Same as Table 4.11 for the *Golden-nat* data set.

Isotope	E_γ [keV]	R_S [cts/(kg·yr)]		
		minimum model	maximum model	data (*Golden-nat*)
^{214}Pb	351.9	22.1 (17.7, 27.3)	4.6 (3.1, 6.0)	25.6 (18.1, 34.1)
^{214}Bi	609.3	11.2 (9.0, 13.8)	6.5 (4.4, 8.6)	7.6 (4.8, 11.0)
	1764.5	4.1 (3.3, 5.1)	3.7 (2.5, 4.9)	3.5 (2.4, 5.0)
	1120.3	2.6 (2.1, 3.2)	3.0 (2.1, 3.9)	4.0 (1.8, 6.3)
	2204.2	1.2 (1.0, 1.5)	1.3 (0.9, 1.7)	0.8 (0.2, 1.6)
	1729.6	1.3 (1.0, 1.6)	0.8 (0.5, 1.1)	0.9 (0.3, 1.8)
	1847.4	0.7 (0.6, 0.9)	0.5 (0.3, 0.6)	1.2 (0.5, 2.1)
	2447.9	0.3 (0.2, 0.4)	0.4 (0.3, 0.5)	< 1.8
^{228}Ac	911.2	6.1 (3.9, 8.6)	5.4 (0.5, 9.8)	4.9 (2.7, 7.3)
	969.0	4.4 (2.8, 6.2)	3.9 (0.4, 7.1)	4.8 (2.6, 7.4)
^{212}Bi	727.3	1.0 (0.6, 1.6)	0.05 (< 0.2)	5.1 (2.7, 7.4)
^{208}Tl	2614.5	1.5 (0.9, 2.4)	1.5 (< 6.7)	1.4 (0.6, 2.3)
	583.2	3.0 (1.8, 4.7)	0.2 (< 0.9)	2.5 (0.4, 4.6)
^{60}Co	1173.2	2.0 (0.1, 4.6)	1.9 (0.1, 3.2)	< 3.8
	1332.5	1.9 (0.1, 4.4)	1.7 (0.1, 2.8)	3.3 (1.6, 5.2)
^{40}K	1460.8	19.4 (16.7, 23.0)	19.8 (16.7, 23.1)	18.3 (15.7, 21.4)
^{42}K	1524.7	75.0 (70.2, 82.4)	75.6 (49.1, 78.3)	73.8 (69.1, 80.1)

Golden data set and the minimum model of the *Golden-nat* data set. The results from the maximum model of the latter will not be considered, due to the inconsistencies in the γ-ray line count rates between the model prediction and data (Section 4.7.4).

The scaling parameter of ^{214}Bi on p^+ surface component was given a Gaussian prior that models the estimated ^{226}Ra activity on the p^+ surface according to the α-model. Its posterior probability distribution is practically the same as the given prior, showing that the assumed ^{226}Ra activity does not contradict with the rest of energy spectrum, i.e. below 3.5 MeV. The parameter of ^{60}Co in Ge component for the *Golden* data set was constrained to an upper bound due to the expected ^{60}Co activity from the activation history. The best fit parameter value gives the upper bound, thus, a lower limit is derived for this component. The parameter of all other components, and thus also the activity of the sources, were kept free in the fit.

Table 4.12: Source activities derived from the global models given the best fit parameters and the 68% C.I. or the 90% probability upper/lower limits. See text for details.

Source	Location	Units	Activity		
			Golden (15.4 kg·yr)		*Golden-nat* (3.1 kg·yr)
			Min. model	Max. model	Min. model
^{214}Bi	p$^+$ sur.	μBq	3.0 (2.3, 3.9)*	3.0 (2.1, 4.0)*	1.6 (1.2, 2.1)*
^{214}Bi	holders	μBq/det	34.9 (31.1, 39.4)	15.0 (3.7, 21.0)	34.1 (27.2, 40.7)
^{214}Bi	LAr BH	μBq/kg		196.1 ($<$ 299.5)	
^{214}Bi	Rn shr.	mBq		10.0 ($<$ 49.9)	
^{228}Th	holders	μBq/det	15.1 (13.1, 18.3)	5.5 (1.3, 8.3)	15.7 (9.7, 24.9)
^{228}Th	Rn shr.	mBq		6.0 ($<$ 10.1)	
^{228}Th	Heat E.	mBq		16.2 ($<$ 4122)	
^{228}Ac	holders	μBq/det	17.6 (10.0, 26.8)	0.08 ($<$ 15.7)	25.9 (16.7, 36.7)
^{228}Ac	Rn shr.	mBq		91.5 (27.7, 97.1)	
^{40}K	holders	μBq/det	151.6 (136.0, 173.9)	151.1 (136.0, 174.0)	218.5 (187.7, 259.5)
^{60}Co	holders	μBq/det	4.9 (3.1, 7.3)	3.2 (1.2, 5.2)	2.6 (0, 5.9)
^{60}Co	Ge	μBq	2.3 ($>$ 0.4)†	2.3 ($>$ 0.2)†	6.0 (3.0, 8.4)
^{42}K	LAr	μBq/kg	106.2 (102.9, 110.7)	91.4 (72.2, 98.7)	98.3 (92.1, 108.1)
^{42}K	p$^+$ sur.	μBq		11.6 (3.1, 18.3)	
^{42}K	n$^+$ sur.	μBq		4.1 (1.2, 8.5)	

* Gaussian prior on the parameter due to α-model.
† Strict parameter range due to activation history.

Minimum model results:

The source activities derived from the minimum model of the *Golden* and *Golden-nat* data sets are consistent with each other. Since the detectors of both data sets experience the same environment, an agreement in the external contamination rates is, to some extent, expected. For ^{214}Bi, ^{228}Th, ^{228}Ac and ^{60}Co in the holders and ^{42}K in LAr components, the results from the two separate data sets agree within the 68% C.I. and for the ^{40}K in the holders component within the 95% C.I. The agreement demonstrates that the minimum model consistently describes the energy spectra of *Golden* and *Golden-nat* data sets. Another interesting comparison is between the resulting activities of ^{228}Ac and ^{228}Th in holders. These two isotopes were not assumed to be in equilibrium in the global model, considering the possibility that the secular equilibrium between ^{228}Ra and ^{228}Th sub-chains can be broken. However, the activities derived from the minimum model are in agreement with each other, indicating a secular equilibrium between the two sub-chains.

Maximum model results:

The maximum model for the *Golden* data set contains the same background sources as the minimum model, however, gives an alternative decomposition of the source location. The contribution from ^{214}Bi does not come only from the holders, but is shared between the holders, LAr BH and the Rn shroud. However, the spectral shape due to the ^{214}Bi decays in LAr BH or in the Rn shroud is not very different than the one in the holders (see Fig. 4.5); the former differs (less than an order of magnitude) in the energy region above ~ 2 MeV and the latter below ~ 1.5 MeV. Therefore, it is not possible to disentangle these different source locations by spectral analysis with the available statistics. Due to the same reason the parameters of these components turn out to be strongly correlated as shown in Fig. 4.22. A distinct spectral shape results from the p^+ surface decays, the contribution of which was constrained with a Gaussian prior. The contributions from ^{228}Th and ^{228}Ac sources come from the holders, Rn shroud and heat exchanger (only for ^{228}Th) in the maximum model. The correlation is mainly between the scaling parameters for the holders and Rn shroud for these sources. For the ^{42}K contribution, in LAr and on n^+ surface components are strongly correlated, again due to marginal differences in their spectral shapes. Although the maximum model gives a consistent description of the energy spectrum of *Golden* data set, decomposition of the source locations according to the model are more or less random for the components with highly correlated parameters (with similar spectral shapes), and can not be interpreted as an indicative outcome of the global model.

Comparison with the screening measurement results:

All the radioactive contaminations expected due to the material screening are observed in the experimental spectrum and considered in the global background models. The source activities derived from the global background models can be compared to the expectations from the screening measurements summarized in Table 2.1. The total ^{214}Bi activity expected due to the screening measurements from close-by sources is about (23 ± 7) μBq/det and additional contributions are expected from medium distance or distant sources. This expectation is in good agreement with the minimum model result, i.e. ~ 35 μBq/det. The ^{228}Th activity in the close source locations due to the screening is lower than the one derived by the minimum model, indicating unidentified ^{228}Th contaminations. The ^{228}Th activity in the heat exchanger material was estimated to be maximum (33 ± 6) mBq/kg or (519 ± 94) mBq using the commissioning data (see Section 3.3). The contribution from the heat exchanger is 16.2 mBq (< 4122 mBq) as derived from the maximum model, which is not in contradiction with the commissioning data analysis result. For the ^{40}K and ^{60}Co sources the overall activity from the model predictions and from the screening results are comparable, if all source locations are taken into account.

The expectations from the screening measurements are not completely sufficient to account for the observed background in GERDA Phase I. However, in most cases the results are not directly comparable because the contaminations exist in many hardware components in different locations, whereas the simulations are performed at well defined representative locations.

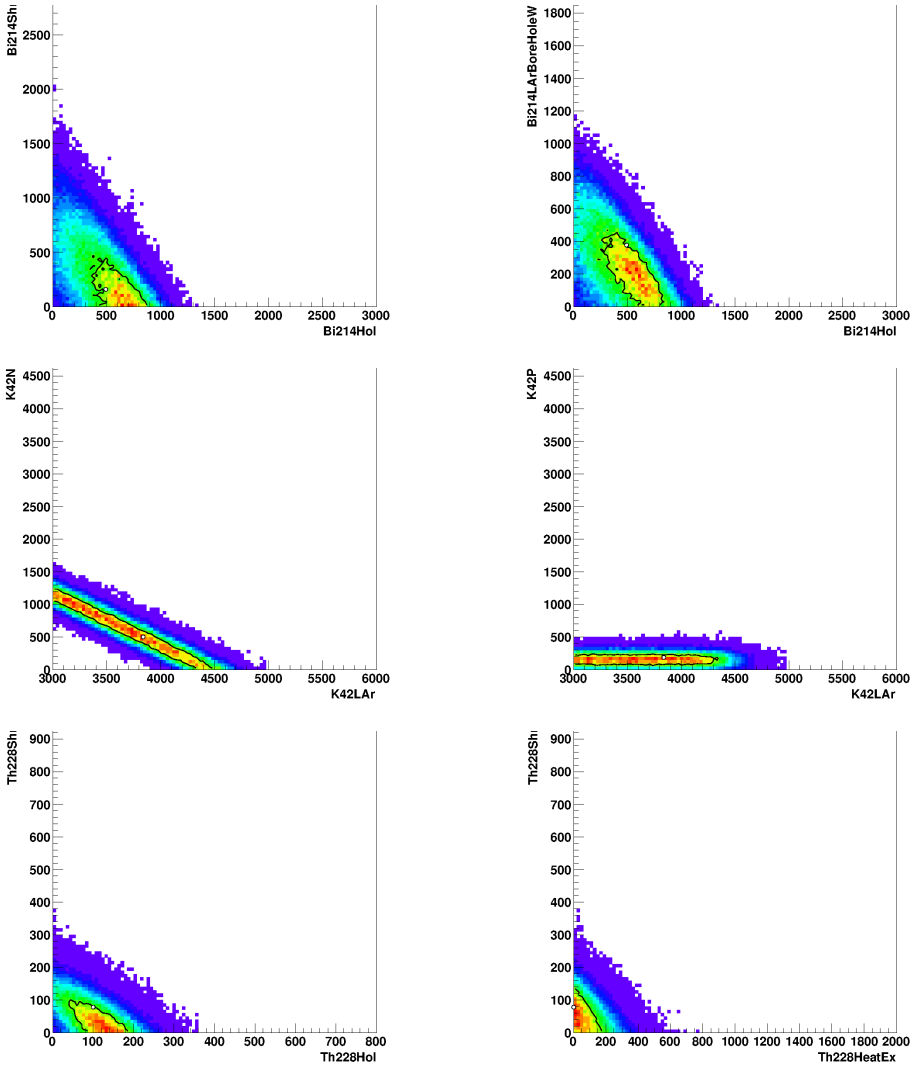

Figure 4.22: The correlation between the parameters of the maximum model of *Golden* data set. Upper left: ^{214}Bi holders vs Rn shroud. Upper right: ^{214}Bi holders vs LAr BH. Middle left: ^{42}K LAr vs n^+ surface. Middle right: ^{42}K LAr vs p^+ surface. Lower left: ^{228}Th holders vs Rn shroud. Lower right: ^{228}Th heat exchanger vs Rn shroud.

The contribution of the $2\nu\beta\beta$ decay to the observed spectrum predicted by global models allows for deriving the half life of the process, which is one of the important physics results of GERDA Phase I and is discussed in detail in Chapter 5.

The ^{42}K activity derived from the global model component for uniform ^{42}K distribution in LAr gives also the specific activity of ^{42}Ar in natural argon. This important result along with the systematic uncertainties is discussed in the following section.

4.7.6 Specific activity of ^{42}K (^{42}Ar)

The global background model component for the uniform ^{42}K distribution in LAr yields a specific activity of $\left(106.2^{+4.5}_{-3.3}\right)$ μBq/kg from the minimum and $\left(91.4^{+7.3}_{-19.2}\right)$ μBq/kg from the maximum model of the *Golden* data set, and $\left(98.3^{+9.8}_{-6.2}\right)$ μBq/kg from the minimum model of the *Golden-nat* data set (Table 4.12). The results of the minimum models for two data sets, which contain different detectors, agree within 68% C.I., and the maximum model result, which accounts additionally for two alternative contributions of ^{42}K (on the n^+ and p^+ surfaces), also agree with the minimum model results within 95% C.I.

The systematic uncertainty arising from the global model assumptions is evaluated for the ^{42}K specific activity derived from the minimum model of the *Golden* data set. The maximum model already gives a different decomposition of the ^{42}K source location, i.e. a non-uniform distribution that accounts for the possibility of ^{42}K ions attracted to detectors surfaces. Other differences in the minimum model components, that can influence the fit result for ^{42}K specific activity in LAr, are considered. Single modifications are introduced to the minimum model:

- ^{214}Bi in LAr BH added,
- ^{214}Bi on the p^+ surface removed,
- ^{228}Th & ^{228}Ac in the holders removed and ^{228}Th & ^{228}Ac in the Rn shroud added instead,
- ^{60}Co in Ge removed,
- ^{60}Co in the holders removed,
- ^{42}K on the p^+ surface added.

The ^{42}K specific activity, A, is derived for each alternative global model and listed in Table 4.13, along with the minimum and maximum model results. The maximum model accounts for the ^{42}K decays on the n^+ surface, the spectral shape of which is only marginally different than the one of the ^{42}K in LAr component (Fig. 4.8), and hence the parameters of the two are strongly correlated (Fig. 4.22). Thus, the largest difference to the minimum model best fit result, i.e. -13.9%, occurs for the maximum model. The largest positive deviation is +0.4% if the model component of ^{228}Th & ^{228}Ac decays in the Rn shroud is included, and is negligible compared to the fit uncertainties. Modifications of single model components do not result in large deviations in A. This is mainly because of the

Table 4.13: The specific activity of ^{42}K, A, as derived from the global background models. The best fit model predictions are given together with the 68% C.I. (fit uncertainty only). In the alternative global models a single modification to the minimum model components is introduced: the added or removed model component is denoted with '+' and '−' sign, respectively.

Global model	A [μBq/kg]
Minimum model	$106.2^{+4.5}_{-3.3}$
+ ^{214}Bi LAr BH	$106.0^{+3.5}_{-3.3}$
− ^{214}Bi p$^+$ surface	$106.2^{+4.6}_{-3.4}$
− ^{228}Th & ^{228}Ac holders + Rn shroud	$106.6^{+4.0}_{-3.3}$
− ^{60}Co Ge	$106.3^{+4.2}_{-3.5}$
− ^{60}Co holders	$107.1^{+3.9}_{-3.4}$
+ ^{42}K p$^+$ surface	$105.5^{+4.5}_{-3.3}$
Maximum model	$91.4^{+7.3}_{-19.2}$

1524.7 keV γ-ray line of ^{42}K measured with very high intensity (Table 4.2), which strongly determines A in the global fit.

Other systematic uncertainties, as evaluated in [154], are due to: active mass of the detectors (2.1%); dimensions of the detectors as implemented in MaGe (0.6%); other geometry details due to MC implementation (1.5%); density of LAr (0.5%); ^{42}K decays outside the sampling volume (0.5%); non-uniformity of the decay distribution (10.0%); cross sections and Geant4 physics (4%); resulting in a total uncertainty of 11.1%. The systematic uncertainty is dominated by the assumption of a homogeneous ^{42}K distribution in LAr, which is not necessarily the case due to the drift of ^{42}K ions in the electric field dispersed in LAr. Since the activity derived from the fit is practically determined by the intensity of the 1525 keV γ-ray line and not by the continuum, the assumption on the position of decays might have as large uncertainty as 10%. This item determines the systematic uncertainty of the measurement.

Taking the ^{42}K (^{42}Ar) specific activity derived from the minimum model of the *Golden* data set as the reference value, and summing systematic uncertainty contributions that are accounted for in quadrature, yields

$$A = \left[106.2\,^{+4.5}_{-3.3}\,(\text{stat})\,^{+11.9}_{-18.9}\,(\text{syst})\right]\ \mu\text{Bq/kg} = \left(106.2\,^{+12.7}_{-19.2}\right)\ \mu\text{Bq/kg}\ . \tag{4.18}$$

The positive measurement of ^{42}K in the LAr of Gerda allows for the determination of the specific activity of ^{42}K, and thus also the ^{42}Ar concentration in natural argon. The measurements reported in literature only provide upper limits for ^{42}Ar concentration in natural argon, e.g. 30.0 μBq/kg [88] and 42.9 μBq/kg [87] at 90% C.L., which are in tension with the Gerda result.

Table 4.14: Total B and the contributions from the individual background components in the 10 keV (8 keV for *BEGe*) window around $Q_{\beta\beta}$ derived from the global background models of the *Golden*, *Silver* and *BEGe* data sets. Note that, the spectra from ^{40}K, ^{228}Ac and ^{76}Ge $2\nu\beta\beta$ decay do not contribute in this energy window. The best fit results (global modes) are quoted together with the 68% C.I. or the 90% probability upper/lower limits.

Source	Location	B [10^{-3} cts/(keV·kg·yr)]			
		Golden (15.4 kg·yr)		*Silver* (1.3 kg·yr)	*BEGe* (1.8 kg·yr)
		Min. model	Max. model	Ext. min. model	Ext. min. model
alphas		2.4 (2.4, 2.5)	2.4 (2.3, 2.5)	2.3 (2.2, 2.4)	1.5 (1.2, 1.8)
^{214}Bi	p^+ sur.	1.4 (1.0, 1.8)*	1.3 (0.9, 1.8)*	19.7 (0.5, 19.8)	0.7 (0.1, 1.3)*
^{214}Bi	n^+ sur.			0.0 ($<$ 1.1)	
^{214}Bi	holders	5.2 (4.7, 5.9)	2.2 (0.5, 3.1)	5.1 (4.3, 5.5)	5.1 (3.1,6.9)
^{214}Bi	LAr BH		3.1 ($<$ 4.7)	0.0 ($<$ 2.2)	
^{214}Bi	Rn shr.		0.7 ($<$ 3.5)		
^{228}Th	holders	4.5 (3.9, 5.4)	1.6 (0.4, 2.5)	4.5 (3.7, 5.3)	4.2 (1.8, 8.4)
^{228}Th	Rn shr.		1.7 ($<$ 2.9)		
^{228}Th	Heat ex.		0.015 ($<$ 3.8)		
^{60}Co	holders	1.4 (0.9, 2.1)	0.9 (0.3, 1.4)	1.1 (0.5, 1.7)	($<$ 4.7)
^{60}Co	Ge	0.6 ($>$ 0.1)†	0.6 ($>$ 0.1)†	0.0 ($>$ 0.1)†	1.0 (0.3, 1.0)†
^{68}Ge	Ge				1.5 ($>$ 6.7)†
^{42}K	LAr	3.0 (2.9, 3.1)	2.6 (2.0, 2.8)	3.5 (1.0, 3.3)‡	2.0 (1.8, 2.3)
^{42}K	p^+ surf.		4.6 (1.2, 7.4)	8.3 (0.4, 17.2)	
^{42}K	n^+ surf.		0.2 (0.1, 0.4)	0.0 ($<$ 1.0)	20.8 (6.8, 23.7)
Global model		18.5 (17.6, 19.3)	21.9 (20.9, 23.9)	44.5 (35.8, 54.5)	38.1 (32.2, 43.3)

* Gaussian prior on the parameter due to α-model.
† Strict parameter range due to the activation history.
‡ Mode of the marginalized posterior probability distribution is 3.0.

4.7.7 Background in the energy region of interest around $Q_{\beta\beta}$

The expected total background index (B) from the global background models, along with the contribution from the individual model components, in the 10 keV window around $Q_{\beta\beta}$ are listed in Tables 4.14 and 4.15 for all the analyzed data sets. The best fit model predictions are quoted together with the 68% C.I. or 90% probability limits. The uncertainty on the total B is obtained by propagating the uncertainties on the model parameters as described in Section 4.1. The probability distributions for the total B are shown in Fig. 4.23 for the minimum and maximum models of the *Golden* data set.

Significant background contributions at $Q_{\beta\beta}$ are coming from the decays of ^{214}Bi, ^{228}Th, ^{60}Co, ^{68}Ge (only for BEGes), ^{42}K and the α-emitting isotopes, i.e ^{210}Po and the

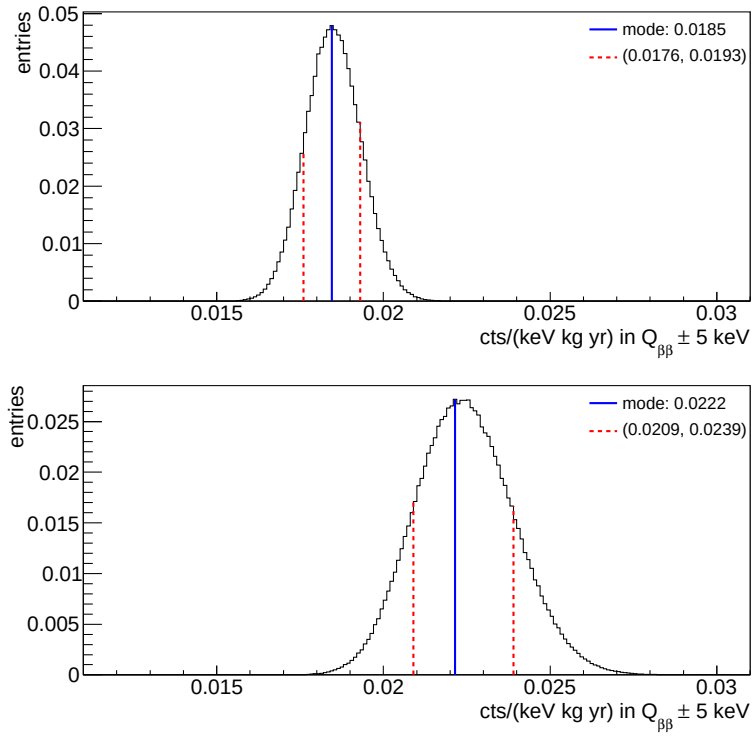

Figure 4.23: Probability distributions of the total B from the minimum (top) and maximum (bottom) models of the *Golden* data set. The distributions are obtained using the sampling of the model parameters according to the full posterior probability distribution (see Section 4.1). The vertical blue line marks the mode of the distributions, while the red ones show the boundaries of the smallest intervals that contain the 68% probability.

ones in the ^{226}Ra sub-chain, according to the global background models. Comparison of the minimum and maximum models of the *Golden* data set (Table 4.14) shows that, the contribution from the assumed source locations depend on the model. However, except for the ^{42}K contribution, the overall B of the individual background sources do not differ significantly from minimum to maximum model. For example, the total B from the external ^{214}Bi sources is about $5 \cdot 10^{-3}$ cts/(keV·kg·yr) according to both minimum and maximum models. The higher total B expected from the maximum model compared to the minimum one is mainly due to the contribution of ^{42}K decays on the p^+ surface. An important difference between the predictions of the two models is, the contribution from the decays on or close to the p^+ surface. It is only $\sim 20\%$ of the total B for the minimum model due to the contributions from alphas and ^{214}Bi on the p^+ surface, and increases to $\sim 50\%$ for the maximum model due to the additional contributions of ^{42}K decays on the p^+ surface and ^{214}Bi decays in LAr bore hole (vicinity of the p^+ surface).

According to the extended minimum model of the *Silver* data set, the increase in the total B during the *silver run period* is due to the ^{214}Bi and/or ^{42}K decays on the detector surfaces. According to this model, the biggest contribution comes from decays on the

Table 4.15: Same as Table 4.14 for the minimum models of the *Golden-HdM*, *Golden-Igex* and *Golden-nat* data sets, shown in comparison to the one of the *Golden* data set.

Source	Location	B [10^{-3} cts/(keV·kg·yr)]			
		Golden (15.4 kg·yr)	*Golden-HdM* (10.9 kg·yr)	*Golden-Igex* (4.5 kg·yr)	*Golden-nat* (3.1 kg·yr)
alphas		2.4 (2.4, 2.5)	3.1 (3.0, 3.2)	0.7 (0.6, 0.8)	3.8 (3.5, 4.2)
^{214}Bi	p^+ sur.	1.4 (1.0, 1.8)*	1.9 (1.4, 2.4)*	0.7 (0.4, 1.0)*	3.7 (2.7, 4.8)*
^{214}Bi	holders	5.2 (4.7, 5.9)	5.4 (4.8, 6.1)	4.5 (4.0, 5.5)	4.9 (3.9, 6.1)
^{228}Th	holders	4.5 (3.9, 5.4)	4.4 (3.7, 5.6)	4.7 (3.6, 6.3)	4.0 (2.5, 6.3)
^{60}Co	holders	1.4 (0.9, 2.1)	0.7 (0.2, 1.2)	3.4 (2.2, 4.8)	1.1 (0.0, 2.4)
^{60}Co	Ge	0.6 (> 0.1)†	0.5 (> 0.1)†	0.8 (> 0.1)†	9.2 (4.5, 12.9)
^{42}K	LAr	3.0 (2.9, 3.1)	3.0 (2.9, 3.2)	2.9 (2.7, 3.1)	2.9 (2.7, 3.2)
Global model		18.5 (17.6, 19.3)	18.9 (18.0, 20.0)	17.8 (16.4, 19.5)	29.6 (27.1, 32.7)

* Gaussian prior on the parameter due to α-model.
† Strict parameter range due to the activation history.

p^+ surface, the dead layer of which is thinner than a μm, and hence, has a much higher detection efficiency for β-rays from ^{214}Bi and ^{42}K compared to the n^+ surface. The other background components – namely, ^{214}Bi, ^{228}Th, ^{60}Co in the holders and ^{60}Co in Ge – result in B contributions comparable to the ones from the minimum model of the *Golden* data set, i.e. in agreement with the given prior probabilities.

The extended minimum model of the *BEGe* data set is also in agreement with the minimum model of the *Golden* data set in terms of the background contributions in the holders. An additional background contribution at $Q_{\beta\beta}$ comes from the internal ^{68}Ge contamination. According to the model, the highest B contribution, i.e. nearly half of the total B, comes from the ^{42}K decays on the n^+ surface of the BEGe detectors. This is plausible due to the increased detection efficiency for β-rays on the n^+ surface of the BEGe detectors with thinner dead layer thickness compared to the coaxial ones. It is also consistent with the results of background decomposition through pulse shape discrimination method applied to the GERDA Phase I data [97].

Comparison of the background decomposition according to the minimum models of the *Golden-HdM*, *Golden-Igex* and *Golden-nat* data sets to the one of the *Golden* data set (see Table 4.15) shows that, the minimum model can describe different data sets coherently. The B contributions of the background sources in the holders and also of the ^{42}K in LAr from the minimum models of different data sets are consistent with each other. The internal and detector surface contaminations are detector dependent, thus, no consistency is expected in the B contributions from alphas, ^{214}Bi on the p^+ surface and ^{60}Co in Ge.

Table 4.16: Total B in the 10 keV window around $Q_{\beta\beta}$ for the *Golden* data set, as derived from the global background models given the best fit parameters. In the alternative global models a single modification to the minimum model components is introduced: the added or removed model component is denoted with '+' and '−' sign, respectively. The results of the minimum and maximum models are also listed for completeness.

Global model	B [10^{-3} cts/(keV·kg·yr)]
Minimum model	18.5 (17.6, 19.3)
+ ^{214}Bi LAr BH	19.8
− ^{214}Bi p^+ surface	17.8
− ^{228}Th & ^{228}Ac holders + Rn shroud	19.3
− ^{60}Co Ge	18.3
− ^{60}Co holders	20.1
+ ^{42}K p^+ surface	21.6
Maximum model	21.9 (20.9, 23.9)

Systematic uncertainty due to background model assumptions

The minimum model contains only well-motivated, significant background components and incorporates all the available prior knowledge, while the maximum model increases the number of parameters by accounting for the further possible background components that can give contributions to B. In order to investigate the influence of the choice of model components on the obtained results, single modifications are introduced to the set of components in the minimum model of the *Golden* data set, as in Section 4.7.6. Table 4.16 lists the resulting total B for all the alternative global models that fit the observed spectrum reasonably well, i.e. p-value > 0.1, and for the minimum and maximum models. The largest systematic uncertainties on the minimum model result due to model assumptions are -4% (due to "minimum model − ^{214}Bi p^+ surface") and +18.4% (due to the maximum model).

4.7.8 Determination of the background index evaluation window

Fig. 4.24 shows the experimental spectrum of the *Golden* data set together with the best fit global model around $Q_{\beta\beta}$, for both minimum and maximum model fits. The global fits were performed on the experimental spectra with the $Q_{\beta\beta} \pm 20$ keV blinding window. After the energy calibration and the background models were finalized, the blinding energy window was reduced to $Q_{\beta\beta} \pm 5$ keV ($Q_{\beta\beta} \pm 4$ keV for the BEGe detectors) in May 2013. Observed events in the 30 keV energy window of the *Golden* data set, i.e. in 2019–2034 keV plus 2044–2059 keV windows, which were not considered in the background analysis, are shown with light gray histograms in Fig. 4.24. The predictions from the global background models can be tested using these events. The background expectation in this 30 keV energy window is 8.6 events from the minimum and 10.1 events from the maximum

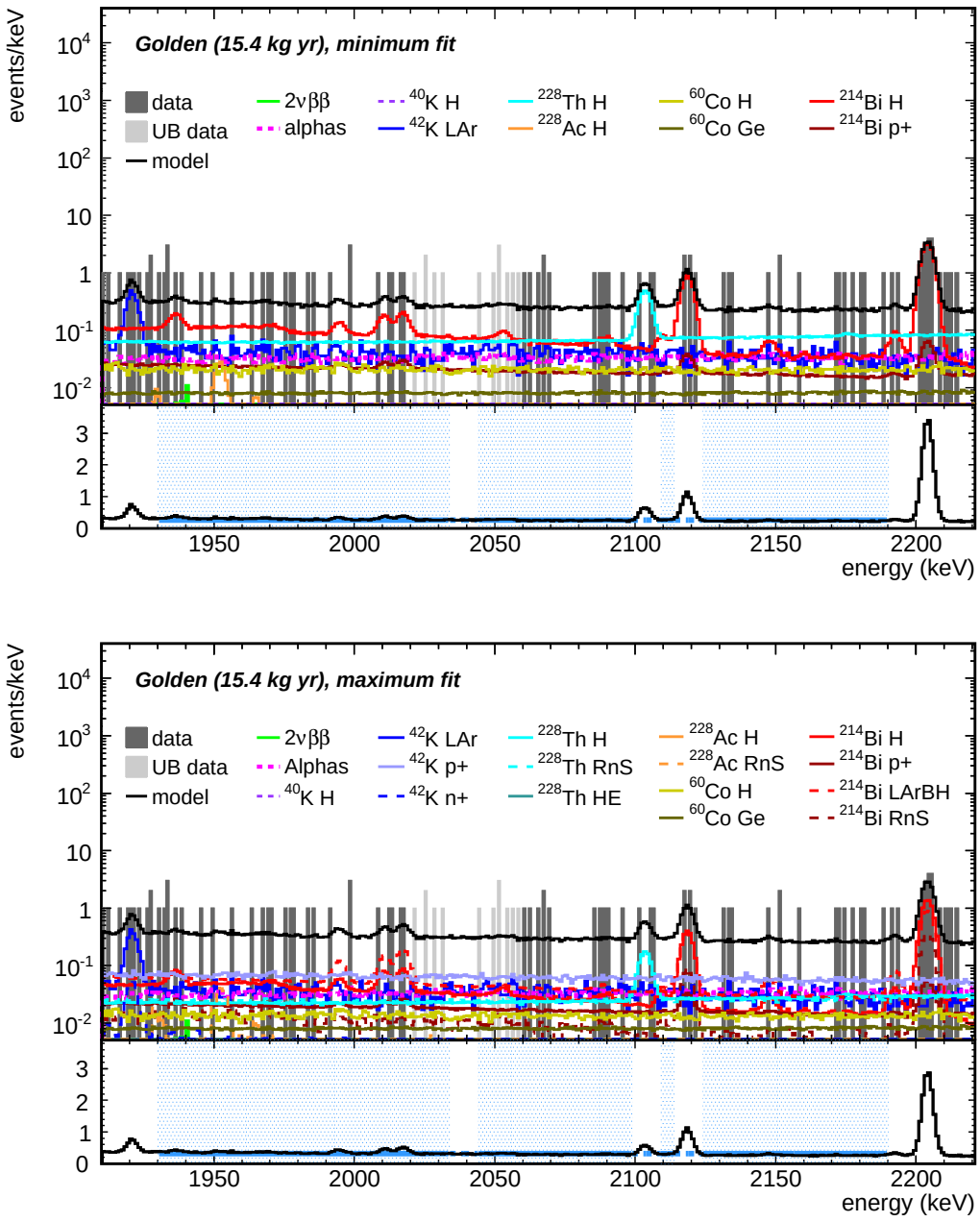

Figure 4.24: Upper panels: The experimental spectrum of the *Golden* data set (data) around $Q_{\beta\beta} = 2039\,\text{keV}$ together with the minimum (top) and maximum (bottom) models and the individual model components given the best fit parameters. The light gray histogram shows the observed events after the partial unblinding (UB data) in the 30 keV window, i.e. 2019–2034 keV plus 2044–2059 keV intervals, which were not considered in the global fits. Lower panels: Best fit global model (black histogram) in linear scale together with the flat background model (blue line), which is a flat distribution fitted to data in the B evaluation window (blue shaded areas): the energy interval between 1930 and 2190 keV, excluding the $Q_{\beta\beta} \pm 5\,\text{keV}$ blinding window and the γ-ray line regions of $(2104 \pm 5)\,\text{keV}$ and $(2119 \pm 5)\,\text{keV}$.

Table 4.17: Total B in the $Q_{\beta\beta} \pm 5\,\text{keV}$ window ($\pm 4\,\text{keV}$ for the *BEGe* data set) according to the global background model and the flat background model. In the latter, B is determined from the number of observed events in the B evaluation window according to the flat distribution assumption. See text for details.

data sets	B [10^{-3} cts/(keV·kg·yr)]	
	Global background model	Flat background model
Golden (15.4 kg·yr)	18.5 (17.6, 19.3)	18.9 (16.7, 21.3)
Golden-HdM (10.9 kg·yr)	18.9 (18.0, 20.0)	17.2 (14.7, 20.1)
Golden-Igex (4.5 kg·yr)	17.8 (16.4, 19.5)	23.2 (17.8, 28.4)
Golden-nat (3.1 kg·yr)	29.6 (27.1, 32.7)	32.2 (26.1, 39.4)
Silver (1.3 kg·yr)	44.5 (35.8, 54.5)	65.8 (52.8, 83.2)
BEGe (1.8 kg·yr)	38.1 (32.2, 43.3)	36.1 (27.4, 46.2)

model, according to the total B predictions for the *Golden* data set listed in Table 4.14. In total 13 events are observed in the same window, which show good agreement with the expectations: the probability to observe 13 events or more is 10% given the minimum and 22% given the maximum model predictions. In the *Golden-nat* data set 5 events are observed in the 40 keV window. The probability to observe 5 events or more given the minimum model prediction of 3.7 events is 31%. Thus, the global background model of the *Golden-nat* data set is also in good agreement with the observations.

The global background models predict an approximately flat distribution in a wide energy range around $Q_{\beta\beta}$, if the expected γ-ray lines are excluded. Total B can also be determined using the number of observed events in this flat energy window around $Q_{\beta\beta}$. The B evaluation window is defined as the energy interval from 1930 keV to 2190 keV, excluding the (2104 ± 5) keV and (2119 ± 5) keV intervals. The excluded intervals are the 10 keV windows around the γ-ray peaks at 2104 keV (SEP of ^{208}Tl) and 2119 keV (^{214}Bi), respectively. The upper bound of the B evaluation window is right above the 1922 keV γ-ray line of ^{42}K and the lower bound is right below the 2204 keV γ-ray line of ^{214}Bi. The total B evaluation window is 230 keV wide, indicated with shaded blue areas in the lower panels of Fig. 4.24. A fit with a flat distribution performed in this energy window results in a very good agreement with the experimental spectrum, shown also in the lower panels of Fig. 4.24 with blue lines. The difference in the best fit B value is less than 1% if a linear instead of a flat distribution is assumed, which is negligible compared to the statistical uncertainty on B.

Table 4.17 shows the total B determined from the number of observed events in the B evaluation window according to the flat distribution assumption, referred to as flat background model, and the predictions from the global background models for all the analyzed Phase I data sets. There is very good agreement between the global model and flat background model results. Note that, the size of the B evaluation window is 230 keV for the *Golden*, *Golden-HdM*, *Golden-Igex* and *Silver*, 240 keV for the *Golden-nat* and

Table 4.18: The expected total B in 10 keV window around $Q_{\beta\beta}$ and the contribution from the individual background components according to the global background models of the *Golden* data set with 15.4 and 17.9 kg·yr exposures. The global mode and the 68% C.I. or the lower limit at 90% C.I. are quoted.

Source	Location	B [10^{-3} cts/(keV·kg·yr)]	
		Golden (15.4 kg·yr)	*Golden* (17.9 kg·yr)
alphas		2.4 (2.4, 2.5)	2.3 (2.2, 2.4)
^{214}Bi	p^+ sur.	1.4 (1.0, 1.8)*	1.5 (1.1, 1.9)*
^{214}Bi	holders	5.2 (4.7, 5.9)	5.0 (4.6, 5.6)
^{228}Th	holders	4.5 (3.9, 5.4)	4.8 (4.2, 5.6)
^{60}Co	holders	1.4 (0.9, 2.1)	1.5 (1.0, 2.1)
^{60}Co	Ge	0.6 (> 0.1)†	0.6 (> 0.1)†
^{42}K	LAr	3.0 (2.9, 3.1)	2.9 (2.8, 3.0)
Global model		18.5 (17.6, 19.3)	18.7 (17.9, 19.5)

* Gaussian prior on the parameter due to α-model.
† Strict parameter range due to the activation history.

232 keV for the *BEGe* data sets. Whereas, the global fit window is 6890 keV wide, i.e. between 570 and 7500 keV, excluding $Q_{\beta\beta} \pm 20$ keV. Since the considered energy range for the global models is much larger compared to the B evaluation window, the uncertainties on B from the global models are smaller. However, if the systematic uncertainties on the results from the global models due to the choice of the model components (Table 4.15) are taken into account, the size of the total uncertainty becomes comparable to the statistical uncertainty on the flat background model result.

4.7.9 Validity of the background model for the complete Phase I data set

The whole study for background characterization and modeling of the Phase I energy spectrum described in this chapter has been performed using the data recorded until March 3rd, 2013. The data set that has been considered in the $0\nu\beta\beta$ decay analysis reported in [18] and Chapter 7, however, contains the Phase I data recorded until May 21st, 2013, i.e. includes an additional $\sim$ 3 months exposure. The *Golden* data set exposure has increased from 15.4 to 17.9 kg·yr with this additional data. The background assumptions in the $0\nu\beta\beta$ decay analysis are based on the predictions of the background model described here. Therefore, the validity of the background model for the data set considered in the $0\nu\beta\beta$ analysis is demonstrated in this section.

The minimum model, defined in Section 4.7.1, is fitted to the energy spectrum of the *Golden* data set with 17.9 kg·yr exposure. Table 4.18 shows the total B and the contribution from the individual model components in the $Q_{\beta\beta} \pm 5$ keV window according to the global model for the *Golden* data set with 17.9 kg·yr exposure, in comparison to

the one with 15.4 kg·yr exposure. The model predictions for the two data sets show very good agreement within 68% C.I., which confirms the validity of the background model for the complete Phase I data set and also demonstrates the stable data taking conditions.

In Figs. 4.25 to 4.28 the energy spectrum of the *Golden* (17.9 kg·yr) data set and the global background model together with the individual model components are shown in the full analysis window of 570–7500 keV. The bin width used for the global fit was 30 keV. For the representation of the results, different binning in different regions are used: 2 keV for the 570–2070 keV region, 5 keV for the 2070–2820 keV region, and larger bin widths above that due to the lower count rates in the higher energy regions. The bin width is chosen fine enough, i.e. given the energy resolution of $\sim$ 2 keV, in the regions with high event rate, to check whether the fluctuations hint any unidentified structures such as γ-ray lines. There is no indication for significant deviations from the global model expectations.

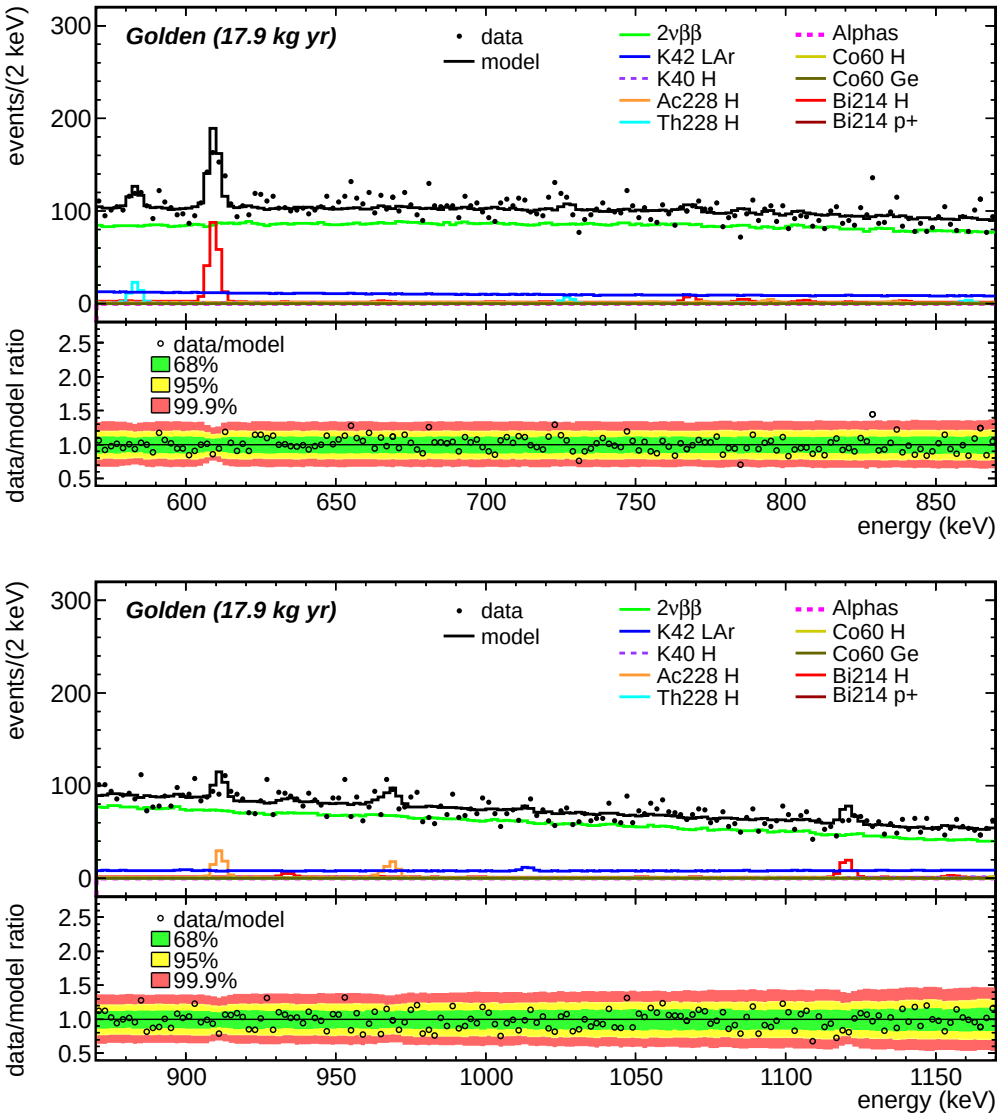

Figure 4.25: The energy spectrum of the *Golden* (17.9 kg·yr) data set and the global background model together with the individual model components in the 570–870 keV (top) and 870–1170 keV (bottom) energy windows. The lower panels show the ratio of data and the best fit model predictions together with the smallest intervals containing minimum 68% (green band), 95% (yellow band) and 99.9% (red band) probability for the ratio assuming the best fit parameters. In total 70% of the data points are in the green, 95% in the yellow and 99.7% in the red bands.

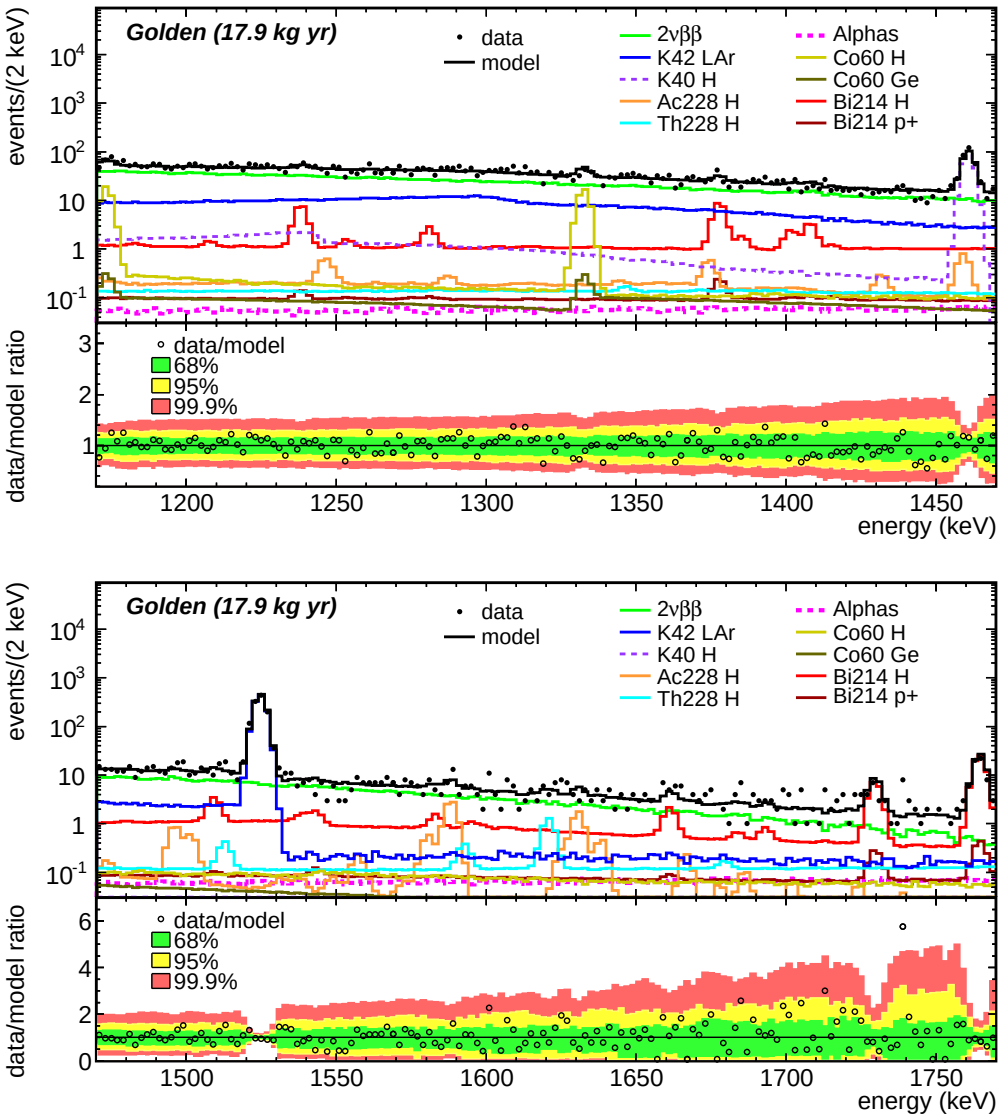

Figure 4.26: Same as Fig. 4.25 in the 1170–1470 keV (top) and 1470–1770 keV (bottom) energy windows. In total 74% of the data points are in the green, 97% in the yellow and 99.7% in the red bands.

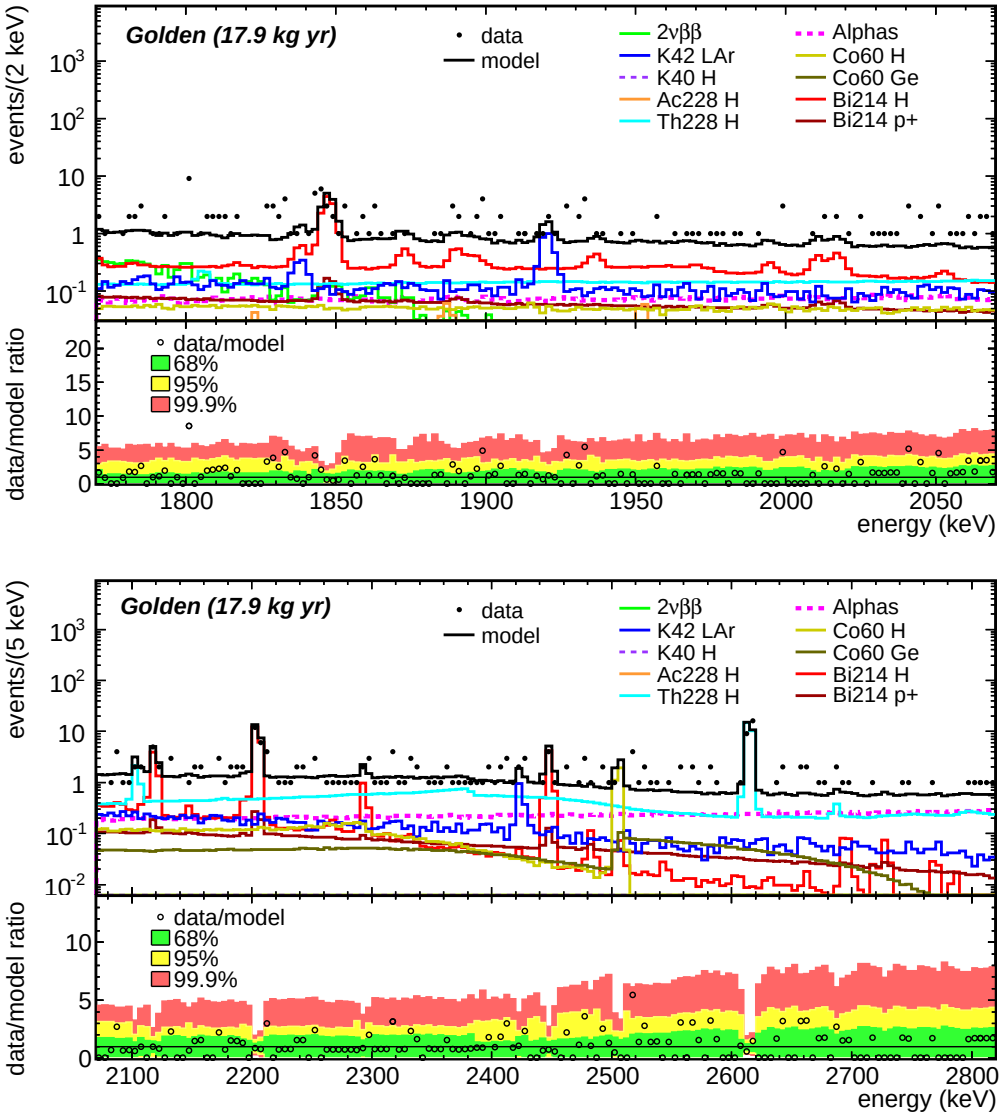

Figure 4.27: Same as Fig. 4.25 in the 1770–2070 keV (top) and 2070–2820 keV (bottom) energy windows. In total 77% of the data points are in the green, 96% in the yellow and 99.7% in the red bands.

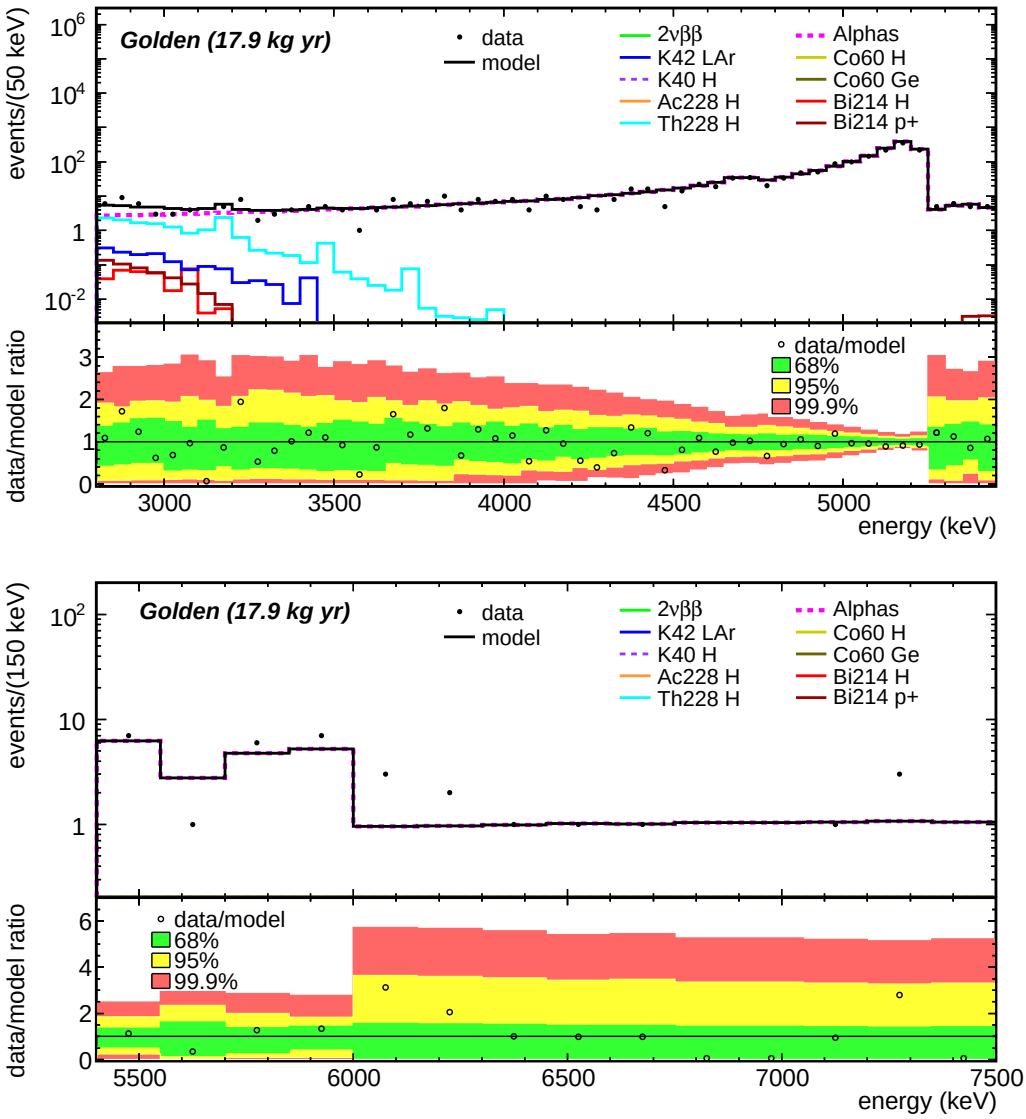

Figure 4.28: Same as Fig. 4.25 in the 2800–5450 keV (top) and 5400–7500 keV (bottom) energy windows. In total 71% of the data points are in the green, 97% in the yellow and 100% in the red bands.

Chapter 5

Results on the half life of the ^{76}Ge $2\nu\beta\beta$ decay

The half life of the $2\nu\beta\beta$ decay of ^{76}Ge has been determined using the *Golden* data set of GERDA Phase I, corresponding to 17.9 kg·yr exposure. Also, $T^{2\nu}_{1/2}$ extracted from other Phase I data sets (Table 4.1) with lower exposures are presented. The measured energy spectra consist of contributions from $2\nu\beta\beta$ decays of ^{76}Ge together with those from several different background sources. The background characterization and decomposition of the observed energy spectra into their individual components through global fits were described in Chapter 4. The $2\nu\beta\beta$ decay contribution to the measured spectra determined from the global background models is used for deriving $T^{2\nu}_{1/2}$.

Firstly, a summary of the previous analysis performed to determine $T^{2\nu}_{1/2}$ with the first 5 kg·yr of data collected in GERDA Phase I is given. Then, the analysis performed with 17.9 kg·yr of data is described. The results from the two analyses are consistent and demonstrate the significant reduction of some of the contributions to the uncertainty on $T^{2\nu}_{1/2}$ due to the increased exposure and better understanding of the background. The $T^{2\nu}_{1/2}$ results from earlier ^{76}Ge experiments are also presented for comparison.

5.1 Determination of $T^{2\nu}_{1/2}$ using early data

Data collected between 9 November 2011 and 21 March 2012 during GERDA Phase I, corresponding to 5.0 kg·yr exposure, have been analyzed to determine the $T^{2\nu}_{1/2}$ [23, 155]. The considered data are part of the *Golden* data set, i.e. about the first quarter of the final exposure. The analysis was carried out on the sum spectrum of the six $^{\text{enr}}$Ge-coax detectors by performing a spectral fit in the energy range of 600–1800 keV and using the method described in Section 4.1.2. The $2\nu\beta\beta$ decay of ^{76}Ge is the major contribution in the fit window. In the energy interval below 600 keV, where the fraction of the $2\nu\beta\beta$ spectrum is about 37%, the ^{39}Ar β decay with $Q_\beta = 565$ keV dominates the observed spectrum (see Fig. 4.1). The γ-ray line of ^{214}Bi at 1765 keV measured with high significance (Table 4.2) is included in the analysis energy window, in order to better constrain the contribution

from this source. The energy range above 1800 keV is practically insensitive to the $2\nu\beta\beta$ decay signal; the probability for a $2\nu\beta\beta$ decay to deposit energy above 1800 keV is $< 0.02\%$ with detector related effects taken into account through a MC simulation. Thus, the fit window is well suited for the study of $2\nu\beta\beta$ decay signal.

The model fitted to the measured energy spectrum contains the $2\nu\beta\beta$ decay of ^{76}Ge and three background contributions relevant in the fit window – namely, ^{42}K, ^{40}K and ^{214}Bi – the presence of which is established by their characteristic γ-ray lines (see Table 4.2). Other potential background components like ^{228}Ac and ^{208}Tl from ^{232}Th decay series, and ^{60}Co are not considered in the reference analysis. The characteristic γ-ray lines of these sources had poor statistical significance ($< 2\sigma$) in the considered 5 kg·yr of data. However, their possible contributions are taken into account in the systematic uncertainty evaluation. The expected spectral shapes of the model components were obtained through MC simulations for each detector individually, as described in Section 4.4. The ^{42}K activity is assumed to be uniformly distributed in the LAr volume. The ^{40}K and ^{214}Bi components are assumed to contribute only from the *close source* locations, i.e. only the simulated spectra of the decays in the holders are considered. The ratio of the ^{214}Bi γ-ray line intensities observed in the experimental spectrum is consistent with this assumption [137]. The expectation from the $2\nu\beta\beta$ decay component – namely, the contribution of the signal in this analysis – in the ΔE_i wide i-th bin of a single detector spectrum is written as

$$\lambda_{i,2\nu} = k_0 t \frac{f_{76}}{T^{2\nu}_{1/2}} M \left[f_{AV} \varepsilon^{fit}_{AV} \int_{\Delta E_i} \phi_{AV}(E) dE + (1 - f_{AV}) \varepsilon^{fit}_{DL} \int_{\Delta E_i} \phi_{DL}(E) dE \right], \quad (5.1)$$

where $k_0 = 15.06$ cts/(kg·yr), which corresponds to the decay rate of 1 kg of $^{\text{enr}}$Ge with 100% enrichment and normalized half life of 10^{21} years. The considered live time, t, is 125.9 days. The total mass, M, enrichment and active volume fractions, f_{76} and f_{AV}, of the individual detectors are listed in Table 2.2. ϕ_{AV} and ϕ_{DL} are the normalized energy spectra of the simulated $2\nu\beta\beta$ decays taking place in the active volume and dead layer of the detectors, respectively (Section 4.4). The detection efficiency, ε^{fit}_{AV} (ε^{fit}_{DL}), corresponds to the probability that a $2\nu\beta\beta$ decay taking place in the active volume (dead layer) of a detector releases energy in the fit window, i.e. between 600 and 1800 keV, which is determined for each detector using the corresponding ϕ_{AV} (ϕ_{DL}). f_{AV} and f_{76} are treated as nuisance parameters in the fit for each detector individually, thus, the systematic uncertainties due to these parameters are folded into the analysis. The prior probabilities for the f_{AV} and f_{76} are modeled as a Gaussian distribution, having mean value and standard deviation according to the parameter values given in Table 2.2. The correlated term in the uncertainties on f_{AV} is taken into account. The prior probability for $T^{2\nu}_{1/2}$ is taken as a flat distribution.

The fit model has 32 parameters: the individual scaling parameters of the three background components for the six detectors; f_{AV} and f_{76} of each detector; a common term that describes the correlated uncertainty on f_{AV}; and $T^{2\nu}_{1/2}$ common for all the detectors. The model describes the observed spectrum very well (p-value = 0.8). The signal-to-background (s/b) ratio in the analysis energy window of 600–1800 keV is about 4:1. Individual contributions of the model components according to the best fit model are: 79.9% from the $2\nu\beta\beta$ decay, 14.1% from ^{42}K, 3.8% from ^{214}Bi, and 2.1% from ^{40}K.

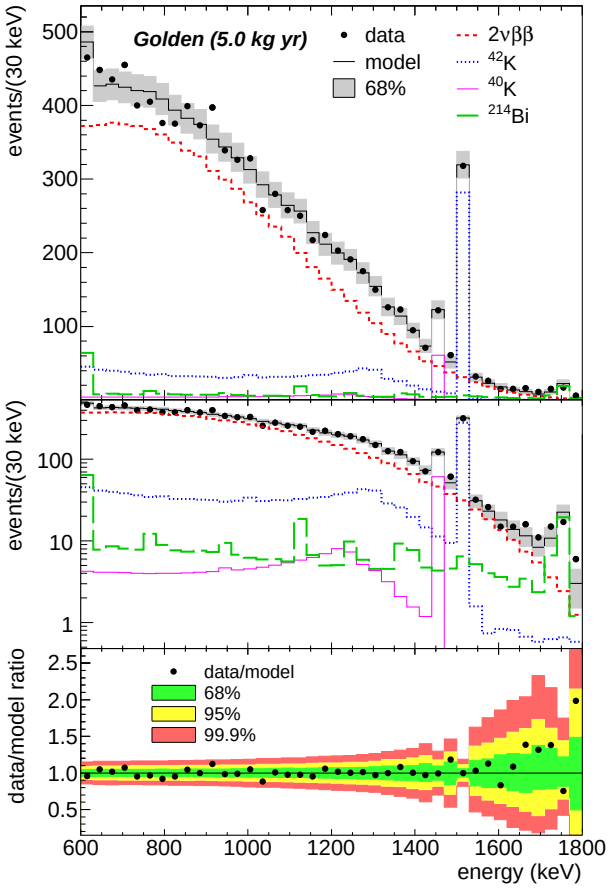

Figure 5.1: Upper and middle panels show the sum energy spectrum of the six $^{\text{enr}}$Ge-coax detectors (markers) contained in the *Golden* (5.0 kg·yr) data set together with the best fit model (black histogram) in linear and logarithmic scales, respectively. Individual contributions from $2\nu\beta\beta$ decay (red), ^{42}K (blue), ^{40}K (purple) and ^{214}Bi (green) are shown separately. The gray band covers the 68% probability interval calculated from the expected number of events due to the best fit model. The lower panel shows the ratio between data and best fit model prediction together with the smallest intervals containing 68% (green band), 95% (yellow band) and 99.9% (red band) probability for the ratio assuming the best fit parameters [23].

Fig. 5.1 shows the experimental spectrum and the best fit model together with the individual contributions from the model components. The lower panel shows the good agreement between data and the best fit model [143]. The probability distribution for $T^{2\nu}_{1/2}$, $P(T^{2\nu}_{1/2})$, is derived from the full posterior probability distribution by integrating over all 31 nuisance parameters. The best estimate of $T^{2\nu}_{1/2}$ together with the 68% C.I. is $(1.84^{+0.09}_{-0.08})\cdot 10^{21}$ yr. The uncertainty is derived as the smallest interval containing 68% probability in the $P(T^{2\nu}_{1/2})$ distribution. It includes the systematic uncertainty on $T^{2\nu}_{1/2}$ due to the nuisance parameters f_{AV} and f_{76}. The same analysis repeated with fixed f_{AV} and f_{76} values, i.e. by taking the central value of the parameters without considering their uncertainties, yields a fit uncertainty of $0.03 \cdot 10^{21}$ yr. Thus, given 1.6% of statistical uncertainty, the systematic uncertainty arising from the uncertainties on f_{AV} and f_{76} corresponds to about 4%.

Systematic uncertainties that were not included in the fitting procedure are evaluated and accounted for in the final $T^{2\nu}_{1/2}$ result. The largest contribution to the uncertainty is +5.3%, coming from additional background components that are not included in the reference fit model. It is estimated by re-running the fit with the contributions from ^{60}Co, ^{228}Ac and ^{228}Th (approximated to be a flat background) added to the model. Since any additional background component leads to a longer $T^{2\nu}_{1/2}$, this uncertainty is asymmetric. The uncertainty due to the assumptions on the spectral shape of the background components is estimated to be 2.1%. It was evaluated by repeating the analysis with different assumptions on the position and distribution of the sources and with artificial variations of the ratio between the full energy peaks and the Compton continua. The initial $2\nu\beta\beta$ decay spectrum was sampled according to the distribution of [156] (with the Primakoff–Rosen approximation removed) that is implemented in DECAY0 [151]. The uncertainty arising from the shape of the initial $2\nu\beta\beta$ decay spectrum is evaluated by comparing the spectrum generated by DECAY0 to the one derived by the Primakoff–Rosen approximation, which was used in earlier works, e.g. in [157]. The analysis repeated by using the formula of [157] yielded a deviation of 1% from the $T^{2\nu}_{1/2}$ result of the reference analysis [1]. Other systematic uncertainties are estimated to be 2.2% due to the MC simulation regarding the precision of the geometry model and the accuracy of the tracking of particles, and 0.5% due to data acquisition and handling.

The $T^{2\nu}_{1/2}$ determined with the first 5.0 kg·yr of the *Golden* data set is

$$T^{2\nu}_{1/2} = (1.84^{+0.14}_{-0.10}) \cdot 10^{21}\,\text{yr}\ , \tag{5.2}$$

with the fit and systematic uncertainties combined in quadrature.

[1] It was later realized that, the unexpectedly large deviation is due to one of the wrong coefficients in the used formula. When it is corrected, the uncertainty from this item is negligible compared to the others.

5.2 Determination of $T_{1/2}^{2\nu}$ with the complete Phase I data

The global models developed in Section 4.7 describe the energy spectra of the Phase I data sets in the analysis window of 570–7500 keV. The contribution of the $2\nu\beta\beta$ decay to the measured energy spectrum according to the global models is used for determining $T_{1/2}^{2\nu}$. The minimum and the extended minimum global models which contain only the dominant background contributions are treated as the reference models. The results of alternative global models with different set of background components are used to evaluate the systematic uncertainties arising from the model assumptions.

The scaling parameter of the $2\nu\beta\beta$ decay spectrum, $N_{2\nu}^{fit}$, resulting from the global fit, i.e. the number of events under the $2\nu\beta\beta$ decay spectrum in the 570–2039 keV interval, is used for the calculation. The initial spectrum of the two electrons emitted in the $2\nu\beta\beta$ decay of ^{76}Ge was sampled using DECAY0 [151]. The $2\nu\beta\beta$ decays were then simulated separately in the active volume (AV) and in the dead layer (DL) of each detector (Section 4.4). The total $2\nu\beta\beta$ decay spectrum of a detector was obtained by summing the resulting AV and DL spectra after scaling each with their volume ratio. The $2\nu\beta\beta$ decay component included in the global fit is the sum of the total $2\nu\beta\beta$ decay spectra of the detectors contained in that data set. $T_{1/2}^{2\nu}$ is calculated given the best fit $N_{2\nu}^{fit}$ parameter after taking into account the detection efficiency for $2\nu\beta\beta$ decays in the fit window. Since the detection efficiencies are very different for the decays taking place in the AV and in the DL, and also both differ, albeit slightly, from detector to detector, $T_{1/2}^{2\nu}$ is written in terms of all detector specific parameters as

$$T_{1/2}^{2\nu} = \frac{(\ln 2)\ N_A}{M_A\, N_{2\nu}^{fit}} \sum_i M_i\, t_i\, f_{76,i} \left[f_{AV,i}\, \varepsilon_{AV,i}^{fit} + (1 - f_{AV,i})\, \varepsilon_{DL,i}^{fit} \right], \tag{5.3}$$

with N_A being Avogadro's constant and M_A the molar mass of the detector material, i.e. 72.6 g for the ^{nat}Ge and 75.6 g for the ^{enr}Ge detectors. The summation runs over all detectors contained in the analyzed data set. The considered live time (t), the total detector mass (M), the fraction of ^{76}Ge atoms (f_{76}), the active volume fraction (f_{AV}), the detection efficiency in the active volume (ε_{AV}^{fit}) and in the dead layer (ε_{DL}^{fit}) of the individual detectors are taken into account separately. The parameters M, t, f_{76} and f_{AV} are listed in Table 2.2 and Table 2.3 for all Phase I detectors. The systematic uncertainty on $T_{1/2}^{2\nu}$ related to the uncertainties on these parameters is discussed in Section 5.3.1. The detection efficiency, ε_{AV}^{fit} (ε_{DL}^{fit}), corresponds to the probability that a $2\nu\beta\beta$ decay taking place in the active volume (dead layer) of a detector releases energy in the fit window, i.e. 570–7500 keV. The ε_{AV}^{fit} and ε_{DL}^{fit} are obtained through dedicated MC simulations (Section 4.4) and are listed in Table 5.1 for the individual detectors. The average ε_{AV}^{fit} slightly varies between different detector types, i.e. 0.668 for the ^{nat}Ge-coax, 0.667 for the ^{enr}Ge-coax and 0.666 for the BEGe detectors, depending on their surface-to-volume ratios. The electrons emitted in a $2\nu\beta\beta$ decay that takes place in the AV usually deposit their full kinetic energy within the AV, apart from small energy losses due to the escape of Bremsstrahlung or fluorescence photons. In fact, if the entire energy range instead of the fit window is considered, the average ε_{AV}^{fit} is 0.998. Due to the same reason, the detection

Table 5.1: Detection efficiencies of the individual detectors, ε_{AV}^{fit} and ε_{DL}^{fit}, defined as the probability for a $2\nu\beta\beta$ decay taking place, respectively, in the active volume and in the dead layer of a detector to produce an energy deposition above 570 keV (fit window). The estimates are based on the MC simulations of $2\nu\beta\beta$ decays in the GERDA Phase I detectors described in Section 4.4. Statistical uncertainty due to the number of simulated events is of the order of 0.1%.

Detector	ε_{AV}^{fit} [%]	ε_{DL}^{fit} [%]
ANG2	0.667	0.009
ANG3	0.667	0.011
ANG4	0.667	0.015
ANG5	0.667	0.008
RG1	0.666	0.011
RG2	0.667	0.011
GTF112	0.668	0.026
GD32B	0.666	0.020
GD32C	0.666	0.025
GD32D	0.665	0.030
GD35B	0.666	0.026

Table 5.2: The scaling parameter, $N_{2\nu}^{fit}$, of the $2\nu\beta\beta$ decay spectrum in the global fits and the corresponding $T_{1/2}^{2\nu}$ determined according to Eq. (5.3). Best fit results are given together with the 68% C.I. (fit uncertainty only) also quoted in percentage in the last column.

Data set	$N_{2\nu}^{fit}$ [cts]	$T_{1/2}^{2\nu}$ [10^{21} yr]	68% uncert. [%]
Golden (17.9 kg·yr)	25690 (25360, 26000)	1.926 (1.903, 1.951)	$^{+1.3}_{-1.2}$
Golden (15.4 kg·yr)	22080 (21780, 22380)	1.925 (1.899, 1.951)	± 1.4
Golden-HdM (10.9 kg·yr)	15725 (15440, 16000)	1.919 (1.886, 1.955)	$^{+1.9}_{-1.7}$
Golden-Igex (4.5 kg·yr)	6340 (6160, 6520)	1.943 (1.889, 1.999)	$^{+2.9}_{-2.8}$
Golden-nat (3.1 kg·yr)	500 (410, 580)	1.817 (1.566, 2.216)	$^{+22.0}_{-13.8}$
Silver (1.3 kg·yr)	1816 (1764, 1920)	1.984 (1.876, 2.042)	$^{+2.9}_{-5.4}$
BEGe (1.8 kg·yr)	2650 (2490, 2714)	1.999 (1.952, 2.128)	$^{+6.5}_{-2.4}$

efficiency for the decays in the DL is very low; ε_{DL}^{fit} is on average 0.026 for the ^{nat}Ge-coax, 0.011 for the ^{enr}Ge-coax and 0.025 for the BEGe detectors. The surface-to-volume ratio of the dead volume has the opposite effect; a larger ratio leads to higher ε_{DL}^{fit}. Since ^{enr}Ge-coax detectors have the thickest DL on the n^+ surface, they have the lowest ε_{DL}^{fit} of 0.011.

The first 15.4 kg·yr of the *Golden* data set contains all six ^{enr}Ge-coax detectors. However, data from RG2 were not included in the last 2.5 kg·yr of exposure (see Section 2.3.6).

The *BEGe* (1.8 kg·yr) data set contains data from four BEGe detectors. Some of them were excluded from data set only for some runs, i.e. GD32B in Run 37 with 23.46 days and GD32D in Run 38 with 13.88 days exposure (Section 2.3.6). These different detector sets with different M and t are accounted for in the calculations.

Table 5.2 lists $T^{2\nu}_{1/2}$ determined according to Eq. (5.3) for all the data sets, given the best fit $N^{fit}_{2\nu}$ values. Uncertainty intervals correspond to 68% C.I. of the parameter $N^{fit}_{2\nu}$ propagated to $T^{2\nu}_{1/2}$. The results from different data sets show very good agreement with each other within 68% uncertainties. Even the *Golden-nat* data set result agrees well with the results obtained from the $^{\text{enr}}$Ge detectors, despite the much smaller target mass of the $^{\text{nat}}$Ge detector.

5.3 Systematic uncertainties

The systematic uncertainties on $T^{2\nu}_{1/2}$ related to the fit model, MC simulations and data acquisition and selection are evaluated. Table 5.3 summarizes the contribution from each item for the $T^{2\nu}_{1/2}$ determined with the *Golden* (17.9 kg·yr) data set. The total systematic uncertainty is ±4.7%, corresponding to $\pm 0.091 \cdot 10^{21}$ yr. The largest contribution (85%) comes from the uncertainty on the active ^{76}Ge exposure which is mainly driven by the uncertainties on f_{76} and f_{AV} of the detectors, i.e. 4%. This uncertainty can be reduced only by performing a new and more precise measurement of the active mass of the $^{\text{enr}}$Ge-coax detectors. The systematic uncertainty due to the fit model has improved significantly for the *Golden* (17.9 kg·yr) data set with respect to the *Golden* (5.0 kg·yr) presented in Section 5.1, i.e. $^{+1.3\%}_{-1.2\%}$ vs $^{+5.7\%}_{-2.1\%}$. It demonstrates the higher accuracy of the background model achieved with the increased exposure, thus, with the increased significance of the γ-ray lines and other structures in the energy spectrum. The uncertainties due to the shape of the initial $2\nu\beta\beta$ decay spectrum and due to data selection are negligible with respect to the other items. The evaluation of the uncertainty contributions listed in Table 5.3 is described in the following sections.

The full systematic uncertainty has not been evaluated for the other data sets. $T^{2\nu}_{1/2}$ derived from the *Golden-HdM* and *Golden-Igex* data sets were presented mainly for cross-check of the global models developed for the separate data sets containing the HDM and IGEX detectors. The systematic uncertainty on the *Golden-nat* result is expected to be negligible with respect to its large statistical uncertainty. The *Silver* data set result has a larger fit uncertainty compared to the *Golden* data set due to its smaller exposure. Also, a larger systematic uncertainty related to the background model assumptions is expected. Other systematic uncertainty contributions are expected to be of the same order, since the two data sets contain data from the same detectors acquired in different measuring periods (Table 4.1). For the *BEGe* data set result, the systematic uncertainty due active ^{76}Ge exposure is 2%, which is twice smaller than the one for the *Golden* data set (see Section 5.3.1). Nevertheless, given the much smaller exposure of 1.8 kg·yr acquired with the BEGe detectors, the systematic uncertainty related to the background model assumptions is expected to be much larger for the *BEGe* data set.

Table 5.3: Systematic uncertainties on $T^{2\nu}_{1/2}$ determined with the *Golden* (17.9 kg·yr) data set. Total systematic uncertainty is obtained as combination of individual contributions in quadrature.

Item	Uncertainty on $T^{2\nu}_{1/2}$ [%]	
Shape of the initial $2\nu\beta\beta$ decay spectrum	< 0.1	
Global model components	$^{+1.4}_{-1.2}$	
Active ^{76}Ge exposure	± 4	
Subtotal fit model		± 4.2
Precision of the Monte Carlo geometry model	± 1	
Accuracy of the Monte Carlo tracking	± 2	
Subtotal Monte Carlo simulation		± 2.2
Data acquisition and handling		< 0.1
Total		± 4.7

5.3.1 Fit model

The uncertainties related to the fit model are considered to be due to the initial shape of $2\nu\beta\beta$ decay spectrum given as input to the MC simulations, the choice of the background model components in the global fit and the uncertainty on the active ^{76}Ge exposure.

Shape of the initial $2\nu\beta\beta$ decay spectrum

The primary spectrum of the two electrons emitted in the $2\nu\beta\beta$ decay of ^{76}Ge is sampled according to the distribution of [156] (with the Primakoff–Rosen approximation removed) implemented in DECAY0 [151]. In order to obtain the energy spectra of the individual detectors including the detector-related effects, the initial states were fed into MC simulation as described in Section 4.4. The resulting energy spectra were used in the reference analysis. The statistical analysis is repeated by using directly the initial $2\nu\beta\beta$ decay spectrum as generated by DECAY0 in the global fit, i.e. the MC simulation step is omitted. All detector-related effects such as energy losses from the active volumes and finite energy resolution are hence neglected. The best $T^{2\nu}_{1/2}$ estimate resulting from the global fit, $1.915 \cdot 10^{21}$ yr, deviates -0.6% from the reference result. This deviation is mainly due to the energy escaping the boundaries of the active volume of the detectors, which is accounted for through MC simulation in the reference analysis. The difference in the $T^{2\nu}_{1/2}$ result is also comparable to the difference in the shape of the two spectra; the fraction of events in the analysis window, i.e. above 570 keV, is 67.1% in the initial $2\nu\beta\beta$ decay spectrum, which reduces to 66.4% after the MC simulation.

The systematic uncertainty due to the initial $2\nu\beta\beta$ decay spectrum is evaluated by comparing the spectrum generated by DECAY0 to the one of [29], referred to as Kotila-Iachello spectrum in the following. The Kotila-Iachello spectrum and the spectrum generated by DECAY0 both before (preMC) and after the MC simulations (postMC) are shown

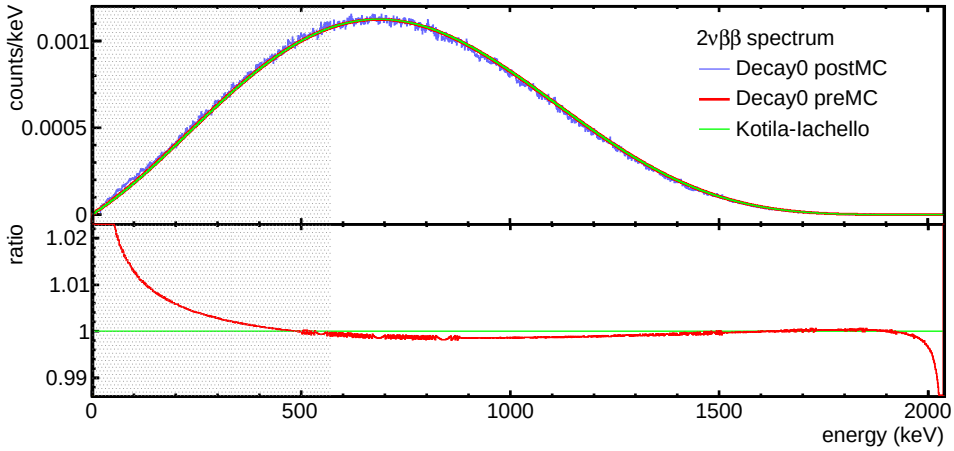

Figure 5.2: Upper panel: $2\nu\beta\beta$ decay spectra according to Kotila-Iachello [29] (green histogram) and DECAY0 [151] before (preMC, red histogram) and after the MC simulation (postMC, blue histogram). Lower panel: The ratio of the DECAY0 (preMC) and Kotila-Iachello spectra.

in Fig. 5.2. The lower panel of the figure shows the ratio of the DECAY0 (preMC) and Kotila-Iachello spectra. In the analysis window chosen for this work (not shaded area), the maximum deviation from Kotila-Iachello spectrum is about 0.2% and the total deviation, i.e. integral of the spectrum in the 570–2039 keV interval, is 0.1%. When the global fit is repeated using the Kotila-Iachello spectrum instead of the one generated by DECAY0 the difference in the $T^{2\nu}_{1/2}$ result is less than 0.1%.

Global model components:

The systematic uncertainty related to the global background model assumptions is evaluated from the results of alternative global models that also describe the energy spectrum of the *Golden* (17.9 kg·yr) data set well. For each alternative model a single modification is introduced to the set of model components of the reference model (minimum model) which either alters the assumption of the source location for a given background source, or excludes its contribution from the global model. Table 5.4 lists the best fit $N^{fit}_{2\nu}$ parameter for the alternative global models and the corresponding $T^{2\nu}_{1/2}$ determined according to Eq. (5.3). The variations are denoted with "+" and "−" for the added and removed components, e.g. "^{40}K, + Rn shroud" stands for the alternative model that additionally accounts for the ^{40}K decays in the Rn shroud, which was considered only in the holders. The alternative global models account for different source location compositions for all the background sources considered in the reference global model. Thus, different spectral shapes depending on the distance of the source from detectors are taken into account in the evaluated uncertainty. The models that completely exclude the contribution from ^{228}Ac or from ^{60}Co decays, or that exclude the contribution of ^{60}Co decays in the holders, and that account for ^{228}Th & ^{228}Ac contributions in the Rn shroud instead of the holders, do not describe the data adequately (p-value < 0.01) and, thus, are not considered.

Table 5.4: The scaling parameter, $N_{2\nu}^{fit}$, of the $2\nu\beta\beta$ decay spectrum in the global fits and the corresponding $T_{1/2}^{2\nu}$ determined according to Eq. (5.3). The best fit model predictions are given together with 68% C.I. The results according to the reference model (minimum model) and to the alternative global models obtained by introducing single modifications to the set of the minimum model components are listed. The modifications are denoted with "+" and "−" for added or removed model components. The deviations in percentage from the minimum model best fit $T_{1/2}^{2\nu}$ result, $\Delta T_{1/2}^{2\nu}$, are given as well.

global model	$N_{2\nu}^{fit}$ [cts]	$T_{1/2}^{2\nu}$ [10^{21} yr]	$\Delta T_{1/2}^{2\nu}$ [%]
Minimum model	25690 (25360, 26000)	1.926 (1.903, 1.951)	-
^{214}Bi, − p^+ surface	25660 (25330, 25980)	1.929 (1.905, 1.954)	+0.2
^{214}Bi, + LAr BH	25960 (25550, 26210)	1.906 (1.888, 1.937)	−1.0
^{214}Bi, + Rn shroud	25510 (25090, 25810)	1.940 (1.917, 1.972)	+0.7
^{228}Th & ^{228}Ac, + Rn shroud	25340 (24990, 25760)	1.953 (1.921, 1.980)	+1.4
^{40}K, + Rn shroud	25340 (24910, 25710)	1.953 (1.925, 1.987)	+1.4
^{42}K, + n^+ surface	26000 (25520, 26190)	1.903 (1.890, 1.939)	−1.2
^{42}K, + p^+ surface	25860 (25520, 26180)	1.914 (1.890, 1.939)	−0.6
^{60}Co, − in Ge	25680 (25340, 26000)	1.927 (1.903, 1.953)	+0.1

The largest deviations from the reference $T_{1/2}^{2\nu}$ result are -1.2% and +1.4%, which are comparable to the fit uncertainties, i.e. -1.2% and +1.3%. The alternative models that result in 1.4% longer $T_{1/2}^{2\nu}$ accounts for ^{228}Th & ^{228}Ac or ^{40}K decays contributing also from the distant source locations like Rn shroud instead of assuming only close source locations like holders; both models yield $T_{1/2}^{2\nu}$ of $1.953 \cdot 10^{21}$ yr. The alternative model including the contribution from ^{214}Bi decays in the Rn shroud in addition to the p^+ surface and holders yields longer $T_{1/2}^{2\nu}$ of $1.940 \cdot 10^{21}$ yr as well. Also, a smaller increase in $T_{1/2}^{2\nu}$ has been observed for the models that exclude contributions from very close source locations, like "^{214}Bi, – p^+ surface" and "^{60}Co, – in Ge". In this case, the contributions of these model components are compensated by others, i.e. ^{214}Bi and ^{60}Co decays in the holders, respectively, which also slightly changes the source location assumptions to a farther one. Given these modifications in the global model assumptions, an increase in the $T_{1/2}^{2\nu}$ estimation is expected. The peak-to-Compton ratio of the γ-rays decreases for farther source locations (Figs. 4.5 to 4.7) which results in higher contributions from the background sources in the $2\nu\beta\beta$ spectrum region. E.g., the ratio of the number of counts in the 10 keV interval around 911 keV γ-ray line and the counts in the 570–2039 keV interval is 0.15 in the simulated spectrum of ^{228}Ac contamination in the holders, which decrease to 0.08 for the simulation of that in the Rn shroud; for the 1460.8 keV γ-ray line of ^{40}K the ratio is 0.32 (holders) versus 0.16 (Rn shroud). The models that include additional contributions from close source locations, like ^{214}Bi decays in LAr in the bore hole volume (vicinity of the p^+ surface) or ^{42}K decays on the n^+ and p^+ surfaces, result in a decrease in the $T_{1/2}^{2\nu}$ value. The largest deviation of −1.2% results from the "^{42}K, + n^+ surface".

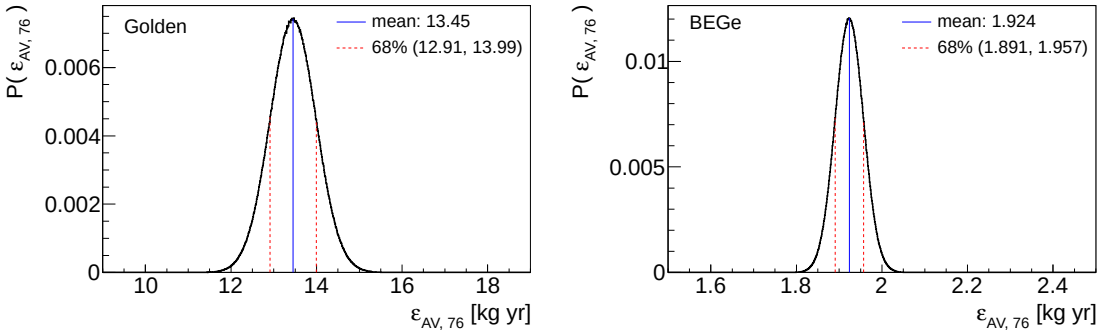

Figure 5.3: Probability distributions of $\mathcal{E}_{AV,76}$ for the *Golden* (left) and *BEGe* (right) data sets.

Active ^{76}Ge exposure

The uncertainties on M, t, f_{AV} and f_{76} were not accounted for in the determination of $T^{2\nu}_{1/2}$ in Eq. (5.3). The product of these parameters gives the exposure in terms of the ^{76}Ge active mass, $\mathcal{E}_{AV,76}$. The total uncertainty on $\mathcal{E}_{AV,76}$ is calculated using MC approach. The total detector masses are known with good accuracy. The uncertainty on f_{76} of the $^{\text{enr}}$Ge-coax (BEGe) detectors is on average 2.1% (1.5%) and on f_{AV} is on average 6.2% (3.1%). The latter has also correlated uncertainties for the $^{\text{enr}}$Ge-coax detectors. The uncertainty on t is 0.3% as discussed in Section 2.3.7. The $\mathcal{E}_{AV,76}$ of the Phase I data sets is calculated as

$$\mathcal{E}_{AV,76} = \sum_i M_i t_i f_{AV,i} f_{76,i} \ , \tag{5.4}$$

where the sum runs over the detectors considered in the data set and t_i, $f_{AV,i}$ and $f_{76,i}$ are randomly sampled according to their own distributions, i.e. modeled as Gaussian distributions with mean values and standard deviations according to parameter values given in Table 2.2. The correlations between $f_{AV,i}$ of the detectors are also taken into account. The calculations yield $\mathcal{E}_{AV,76}$ of $(13.45 \pm 0.54)\,\text{kg}_{AV,76}\,\text{yr}$ for the *Golden*, $(0.978 \pm 0.039)\,\text{kg}_{AV,76}\,\text{yr}$ for the *Silver* and $(1.923 \pm 0.033)\,\text{kg}_{AV,76}\,\text{yr}$ for the *BEGe* data set, which correspond to an uncertainty of 4%, 4% and 2%, respectively. The uncertainty on $\mathcal{E}_{AV,76}$ is mainly driven by the uncertainties on f_{AV} and f_{76}. The obtained probability distributions of the $\mathcal{E}_{AV,76}$ for the *Golden* and *BEGe* data sets are shown in Fig. 5.3. Note that the uncertainties on the $\mathcal{E}_{AV,76}$ of the *Golden* and *Silver* data sets are equal, since data from the same detectors in different measuring periods are considered for the two sets (see Section 2.3.6).

The uncertainties on the f_{AV} and f_{76} mainly affect the number of ^{76}Ge nuclei in the active volume of the detectors, with a relatively smaller impact on the detection efficiency for the background sources which is neglected.

5.3.2 Monte Carlo simulation

The uncertainty on $T^{2\nu}_{1/2}$ related to the MC simulation is considered to be arising from the precision of the geometry model implemented in MaGe and from the accuracy of

particle tracking. The latter is performed by GEANT4 and related to the physics model employed for particle tracking, thus, is independent from the former.

Precision of the Monte Carlo geometry model

Systematic uncertainty related to the details of the experimental geometry implemented in MAGE is considered separately for the detector dimensions and for the dimensions of the other volumes surrounding the detectors [155]. The Monte Carlo geometry model fails in reproducing some small details of the detector geometries such as rounded corners, which results in a difference of 0.6% on average in the total detector mass with respect to the reference values summarized in Table 2.2. The uncertainty on the detector mass is expected to show up linearly on the $T^{2\nu}_{1/2}$ estimation. The uncertainty on the dimensions of other volumes such as holders, electronics, etc., have an impact on the simulations of the external background sources, since particles or γ-rays originating from decays can deposit energy in the surrounding material before detection. This contribution was evaluated to be 1.5% in the study for determination of the ^{42}K specific activity [154]. A smaller contribution, i.e. 0.8%, is assumed in this work, since only the uncertainty due to the spectral shapes, and not the absolute efficiency for ^{42}K, matters for the $T^{2\nu}_{1/2}$ determination. The total uncertainty due to the MC geometry model is 1% with the two separate contributions summed in quadrature.

Accuracy of the Monte Carlo tracking

The uncertainty due to MC tracking comes from the propagation of photons and particles in the MAGE setup and from the interaction cross sections of γ-rays. The electromagnetic physics processes provided by GEANT4 for γ-rays and $e^{\pm}$ have been systematically validated at the few-percent level in the energy range which is relevant for γ-ray spectroscopy [158]. A contribution of 2% is estimated for this component [155], which is mainly due to the propagation of the external γ-rays. A smaller contribution comes from the propagation of the $2\nu\beta\beta$ decay electrons, since they mostly deposit their entire kinetic energy within the detectors.

5.3.3 Data acquisition and handling

The trigger and reconstruction efficiencies for physical events are practically 100% above 200 keV, which is assessed by the comparison of the two independent energy reconstruction algorithms. The performance of the quality cuts applied to the Ge detector signals of the Phase I data set has been investigated through a visual analysis [159]. According to that analysis, the fraction of anomalous pulses accepted by the muon-veto, detector anti-coincidence and the quality cuts is 0.04%, while, the fraction of valid events rejected by the quality cuts is 0.02%. The total uncertainty on $T^{2\nu}_{1/2}$ related to energy reconstruction and event selection is, thus, $< 0.1\%$ (for details see Section 2.3.2).

5.4 Results and conclusions

The half life of the $2\nu\beta\beta$ decay of ^{76}Ge has been determined with the *Golden* data set of GERDA Phase I, corresponding to an exposure of 17.9 kg·yr. The global model (Section 4.7) that describes the observed energy spectrum of the $^{\text{enr}}$Ge-coax detectors in the 570–7500 keV interval was used to derive $T^{2\nu}_{1/2}$. The determined $T^{2\nu}_{1/2}$ together with the statistical (fit) and systematic uncertainties is

$$T^{2\nu}_{1/2} = (1.926^{+0.025}_{-0.022}\,\text{stat} \ \pm 0.091\,\text{syst}) \cdot 10^{21}\,\text{yr} = (1.926 \pm 0.094) \cdot 10^{21}\,\text{yr}. \tag{5.5}$$

The total uncertainty (4.9%) is the combination of statistical ($\sim$ 1.2%) and systematic (4.7%) uncertainties in quadrature. The systematic uncertainty is dominated by the uncertainties on the active volume and enrichment fractions of the $^{\text{enr}}$Ge-coax detectors, that result in a contribution of 4%. Other relevant contributions to the systematic uncertainty are related to Monte Carlo simulation (2.2%) and to the fit model ($\sim$ 1%).

The $T^{2\nu}_{1/2}$ result of the *Golden* data set is consistent with the one derived from the first 5 kg·yr exposure of the same data set within 68% uncertainty. The enhanced precision of the $T^{2\nu}_{1/2}$ result obtained with higher exposure is mainly due to a better understanding of the background and thus more accurate background modeling. A significant reduction of the systematic uncertainty arising from background model assumptions compared to the previous result has been attained, i.e. from $^{+5.7\%}_{-2.1\%}$ to $^{+1.4\%}_{-1.2\%}$. The larger positive uncertainty on the previous result is due to the background contributions, such as ^{60}Co, ^{228}Ac, ^{228}Th, etc., that were not included in the reference model but accounted for in the systematic uncertainty. The characteristic γ-ray lines of these background sources became more significant with the increased exposure. Thus, they are included in the reference global model, which also resulted in a slight increase in the best $T^{2\nu}_{1/2}$ estimate. Moreover, the background components are better characterized and constrained with the larger data set, which resulted in a further reduction of the uncertainty due to the background model.

Fig. 5.4 shows $T^{2\nu}_{1/2}$ of ^{76}Ge reported from earlier experiments between 1990 and 2005, two weighted averages and the GERDA Phase I results obtained with 5.0 and 17.9 kg·yr of data. The $T^{2\nu}_{1/2}$ result of more recent experiments are systematically longer. Most probable reason is the improved s/b in recent experiments that achieved lower background levels, which lessens the importance of background subtraction in the analysis. In the energy spectrum of the *Golden* (17.9 kg·yr) data set of GERDA Phase I, s/b in the 570–2039 keV interval is about 3:1 according to the best fit model. It is better than the result of any previous experiment; the best s/b achieved earlier for ^{76}Ge was about 1:1 by HDM [77]. The $T^{2\nu}_{1/2}$ results of GERDA are in better agreement with the two most recent results that are based on the re-analysis of the HDM data [157, 160], and also have comparable uncertainties to those in spite of the smaller exposure of GERDA Phase I, owing to the superior s/b achieved.

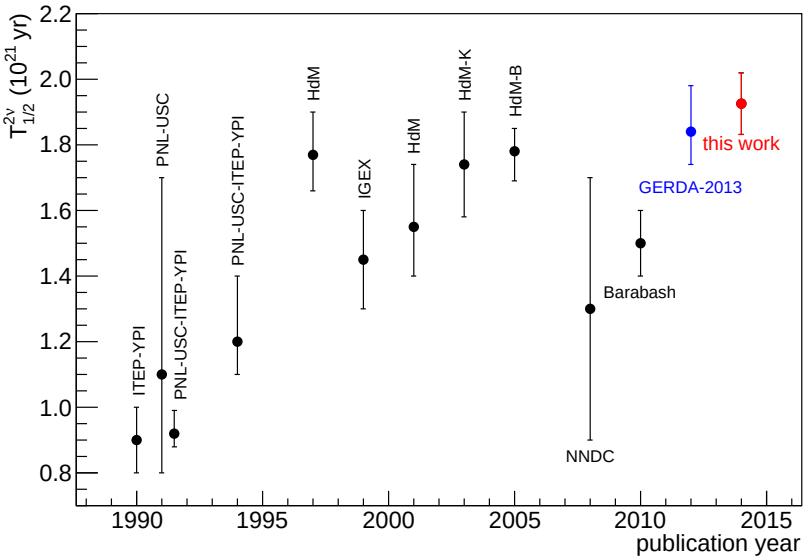

Figure 5.4: Experimental results for $T^{2\nu}_{1/2}$ of ^{76}Ge versus publication year. It includes results from the experiments ITEP-YPI [161], PNL-USC ($^{\text{nat}}$Ge) [162], PNL-USC-ITEP-YPI [163, 164], Heidelberg-Moscow (HDM) [77, 113] and IGEX [114, 165], as well as the re-analysis of the HDM data by Klapdor-Kleingrothaus *et al.* [157] (HdM-K) and by Bakalyarov *et al.* [160] (HdM-B). The NNDC-recommended value [166] and the global weighted average evaluated by Barabash [167] are also shown. The last two results are from the Phase I of the GERDA experiment; $(1.84^{+0.14}_{-0.10})\cdot10^{21}$ yr determined with the first 5.0 kg·yr of data [23] and $(1.926 \pm 0.094)\cdot10^{21}$ yr with 17.9 kg·yr of data (this work). Modified from the Fig. 4. of [23].

Chapter 6

Studies for the ^{76}Ge $0\nu\beta\beta$ signal search

The analysis for evaluating the probability of a $0\nu\beta\beta$ signal presence given the expected background in GERDA Phase I data is performed using Bayesian inference. Description of the analysis parameters and the analysis method are given in Sections 6.1 and 6.2. Data considered for the analysis and grouping of data into subsets with similar characteristics, like background level or energy resolution, are presented in Section 6.3. All studies concerning the analysis, such as determination of the background level around $Q_{\beta\beta}$ (Section 6.4), evaluation of the $0\nu\beta\beta$ signal acceptance and detection efficiency (Section 6.5), and optimization of the analysis energy window width (Section 6.6), were performed prior to opening the blinding window, i.e. before the events in the $Q_{\beta\beta} \pm 5\,\mathrm{keV}$ window were processed. Section 6.7 gives the sensitivity of GERDA Phase I, evaluated with the determined analysis parameters and by using the available data in different ways of grouping. It demonstrates the best way of treating data in the analysis for attaining the highest sensitivity, i.e. best limit on the half life of $0\nu\beta\beta$ decay ($T^{0\nu}_{1/2}$).

6.1 Analysis parameters

The half life of the $0\nu\beta\beta$ process is related to the number of measured $0\nu\beta\beta$ decay events as given in Eq. (1.16). In the case of observing a number of events, n, due to both $0\nu\beta\beta$ decay (signal) and background processes, the signal strength (or corresponding limit), ν, can be inferred from data, given that the expected number of background events, λ, is known. The latter is expressed in terms of the background index, B, which is defined as

$$B = \frac{\lambda}{M \cdot t \cdot \Delta E} \ , \tag{6.1}$$

where M is the total detector mass, t the measurement time and ΔE the width of the energy window considered for counting events. The product of M and t is also referred to as exposure, and denoted with $\mathcal{E}$. Since B is normalized in terms of $\mathcal{E}$ and ΔE, it is a measure of background counts that is comparable between different detectors or data

sets, and is given in units of cts/(keV·kg·yr). The half life of the $0\nu\beta\beta$ process is the parameter reported as the result of the analysis. Using ν inferred from data analysis, $T^{0\nu}_{1/2}$ is calculated as

$$T^{0\nu}_{1/2} = \frac{(\ln 2) N_A}{M_A\, \nu}\, \mathcal{E}\, \epsilon \ , \tag{6.2}$$

where N_A is Avogadro's constant, $M_A = 0.0756\,\mathrm{kg}$ the molar mass of the enriched material and ϵ the signal detection efficiency. The latter accounts for the enrichment fraction (f_{76}) and the active volume fraction (f_{AV}) of the detectors, the efficiency for detecting the full energy peak (ε_{FEP}), and, if pulse shape discrimination (PSD) selection is applied to data, the signal acceptance of PSD cuts (ε_{PSD}). The analysis method using Bayesian approach, for estimation of ν, thus of $T^{0\nu}_{1/2}$ through Eq. (6.2), is described in the following.

6.2 Bayesian formulation

The formulation for a Bayesian analysis of $0\nu\beta\beta$ signal is adopted from [63, 168]. Two hypotheses, H and $\bar{H}$, are defined to explain the observed events (data): in H, the measured energy spectrum is due to background processes only; and in $\bar{H}$, the $0\nu\beta\beta$ signal contributes to the spectrum in addition to background processes. The conditional probabilities for the hypotheses H or $\bar{H}$ to be true given data D are labeled as $P(H|D)$ and $P(\bar{H}|D)$, respectively, and they obey the relation:

$$P(H|D) + P(\bar{H}|D) = 1 \ . \tag{6.3}$$

$P(\bar{H}|D)$ can be calculated using Bayes' theorem:

$$P(\bar{H}|D) = \frac{P(D|\bar{H}) P_0(\bar{H})}{P(D)} \ , \tag{6.4}$$

where the probability of data is:

$$P(D) = P(D|\bar{H}) P_0(\bar{H}) + P(D|H) P_0(H) \ . \tag{6.5}$$

The values of the prior probabilities for H and $\bar{H}$, denoted with $P_0(H)$ and $P_0(\bar{H})$, are chosen depending on the knowledge from previous experiments or model predictions. If such information is not available, or not intended to be included in the analysis, equal probabilities of 0.5 can be assigned to the hypotheses.

The conditional probabilities for observing D given that the hypothesis H is true or not true, $P(D|H)$ and $P(D|\bar{H})$, respectively, can be written as

$$P(D|H) = \int P(D|\vec{B}, H) P_0(\vec{B}) d\vec{B} \ , \tag{6.6}$$

$$P(D|\bar{H}) = \int \left[\int P(D|\vec{B}, 1/T^{0\nu}_{1/2}, \bar{H}) P_0(\vec{B}) d\vec{B} \right] P_0(1/T^{0\nu}_{1/2}) d(1/T^{0\nu}_{1/2}) \ , \tag{6.7}$$

where $\vec{B}$ represents the background indices of the considered data sets and $1/T^{0\nu}_{1/2}$ a common parameter, if multiple data sets are analyzed together. The prior probabilities

for $\vec{B}$ and $1/T^{0\nu}_{1/2}$ are denoted as $P_0(\vec{B})$ and $P_0(1/T^{0\nu}_{1/2})$, respectively. Since the parameters B are not precisely known, the uncertainties are accounted for in the analysis by giving a distribution of their possible values modeled by $P_0(\vec{B})$. In stead of $T^{0\nu}_{1/2}$, its inverse is used in the formulation, since ν is the parameter inferrable from data and is linearly proportional to $1/T^{0\nu}_{1/2}$ (Eq. (6.2)). In this way, the uncertainties on ν are correctly propagated to the parameter $T^{0\nu}_{1/2}$. The probability $P_0(1/T^{0\nu}_{1/2})$ can be modeled considering the present knowledge, e.g. from previous experiments, or a flat probability distribution in the allowed region can be assigned, which implies equal probabilities for different signal rates ν.

The value of $P(\bar{H}|D)$ is the best statement concerning the possibility of having observed a $0\nu\beta\beta$ signal. If $P(\bar{H}|D)$, or alternatively the Bayes Factor,

$$K = \frac{P(\bar{H}|D)}{P(H|D)}, \tag{6.8}$$

exceeds the predefined threshold for evidence or discovery, the best (most probable) value for $T^{0\nu}_{1/2}$, as well as the uncertainties, can be extracted from the probability distribution:

$$\begin{aligned} P(1/T^{0\nu}_{1/2}|D,\bar{H}) &= \frac{P(D|1/T^{0\nu}_{1/2},\bar{H})P_0(1/T^{0\nu}_{1/2}|\bar{H})}{P(D|\bar{H})} \\ &= \frac{P(D|1/T^{0\nu}_{1/2},\bar{H})P_0(1/T^{0\nu}_{1/2}|\bar{H})}{\int P(D|1/T^{0\nu}_{1/2},\bar{H})P_0(1/T^{0\nu}_{1/2})d(1/T^{0\nu}_{1/2})} \\ &= \frac{\left[\int P(D|\vec{B},1/T^{0\nu}_{1/2},\bar{H})P_0(\vec{B})d\vec{B}\right] P_0(1/T^{0\nu}_{1/2}|\bar{H})}{\int \left[\int P(D|\vec{B},1/T^{0\nu}_{1/2},\bar{H})P_0(\vec{B})d\vec{B}\right] P_0(1/T^{0\nu}_{1/2}|\bar{H})d(1/T^{0\nu}_{1/2})}. \end{aligned} \tag{6.9}$$

If the requirement for evidence is not fulfilled, $P(1/T^{0\nu}_{1/2}|D,\bar{H})$ can be used to set limits on $T^{0\nu}_{1/2}$, under the assumption that $\bar{H}$ is true but the $0\nu\beta\beta$ signal is too weak to contribute to the measured spectrum. For example, a 90% probability lower limit (T_{90}) can be found by requiring

$$\int_0^{1/T_{90}} P(1/T^{0\nu}_{1/2}|D,\bar{H})d(1/T^{0\nu}_{1/2}) = 0.90\ . \tag{6.10}$$

The probability distributions $P(D|\vec{B},H)$ and $P(D|\vec{B},1/T^{0\nu}_{1/2},\bar{H})$, also called the *likelihood*, can be defined differently depending on the analysis, as described in Sections 6.2.1 and 6.2.2. The definition of the likelihood is general, i.e. not part of the adopted Bayesian approach.

6.2.1 Counting method

The number of events within an energy interval ΔE around $Q_{\beta\beta}$ can be used to determine (or set a limit on) $T^{0\nu}_{1/2}$. If different data sets (denoted by i) are analyzed together, the probability of observing D over all data sets given the hypothesis H can be written as

$$P(D|\vec{B},H) = \prod_i \frac{e^{-\lambda_i}\lambda_i^{n_i}}{n_i!}\ , \tag{6.11}$$

and given the hypothesis $\bar{H}$ as

$$P(D|\vec{B}, 1/T^{0\nu}_{1/2}, \bar{H}) = \prod_i \frac{e^{-(\lambda_i+\nu_i)}(\nu_i+\lambda_i)^{n_i}}{n_i!} \ , \tag{6.12}$$

where n_i is the number of observed events within ΔE_i, and λ_i and ν_i (as the relations given in Eqs. (6.1) and (6.2)) are expressed as

$$\lambda_i = B_i \cdot M_i \cdot t_i \cdot \Delta E_i \ , \tag{6.13}$$

and

$$\nu_i = \frac{(\ln 2) N_A}{M_A \, T^{0\nu}_{1/2}} \, \mathcal{E}_i \, \epsilon_i \, \varepsilon_{res,i} \ . \tag{6.14}$$

The parameter $\varepsilon_{res,i}$ is the fraction of the Gaussian signal within ΔE_i, which can be different than 1. It depends on the energy resolution at $Q_{\beta\beta}$ and on the width of ΔE, and can be calculated according to Eq. (1.23). The width of ΔE can be optimized for a discovery or for setting the best limit on $T^{0\nu}_{1/2}$, as exemplified in Section 1.3.2. While ε_{res} will worsen for a smaller window size due to finite energy resolution, the signal-to-background ratio (s/b) will increase, such that, the optimum width of ΔE will be a trade-off between the two parameters. The optimum ΔE depends both on the background level and on the energy resolution, which are different for different data sets. Thus, an individual ΔE can be chosen for each data set.

6.2.2 Binned spectral fit

The analysis for the estimation of $T^{0\nu}_{1/2}$ can also be performed by fitting a model spectrum containing the signal and background contributions to the observed one, assuming that the spectral shapes of the signal and background processes are known. In this case, the spectrum is confined to a certain energy window and divided into bins. The number of events in each bin follows a Poisson distribution. Again analyzing different data sets (denoted by i) together, and having observed n_{ij} events in the j-th bin of the energy spectrum of data set i, the probability to observe the measured spectrum given $\vec{B}$ (in case H is true) can be written as

$$P(D|\vec{B}, H) = \prod_i \prod_j \frac{e^{-\lambda_{ij}} \lambda_{ij}^{n_{ij}}}{n_{ij}!} \ , \tag{6.15}$$

and given $\vec{B}$ and $1/T^{0\nu}_{1/2}$ (in case $\bar{H}$ is true) as

$$P(D|\vec{B}, 1/T^{0\nu}_{1/2}, \bar{H}) = \prod_i \prod_j \frac{e^{-(\lambda_{ij}+\nu_{ij})}(\nu_{ij}+\lambda_{ij})^{n_{ij}}}{n_{ij}!} \ . \tag{6.16}$$

Here, the number of expected events in the j-th bin of the spectrum of data set i due to background (λ_{ij}) and signal (ν_{ij}) contributions are defined as

$$\lambda_{ij} = \lambda_i \int_{\Delta E_j} f_B(E) dE \ , \qquad \nu_{ij} = \nu_i \int_{\Delta E_j} f_S(E) dE \ , \tag{6.17}$$

where ΔE_j is the width of the j-th bin, $f_B(E)$ and $f_S(E)$ are the normalized energy spectra from background and signal processes, respectively.

6.3 Data sets

The measurement period between November 2011 and May 2013 is considered for this analysis. Data taking runs and detector configurations in this period were described in Section 2.3.6. The valid measurement time (live time) and exposure of individual detectors are listed in Table 2.3. Data are grouped into three subsets with similar characteristics, as for the background modeling presented in Chapter 4. All data from the BEGe detectors, which have higher energy resolution compared to the $^{\text{enr}}$Ge-coax detectors, form the *BEGe* data set. The $^{\text{enr}}$Ge-coax detector data are split into two subsets. The *Silver* data set contains data taken within a period of about a month, during which some changes in the detector array were introduced, i.e. BEGe detectors were inserted into the setup, and a higher background level was observed. The *Golden* data set covers the rest of the measurement period, which is the major part of the $^{\text{enr}}$Ge-coax data. According to the numbering convention given in Section 2.3.6, Runs 35–46 are considered in the *BEGe*, Runs 34 & 35 in the *Silver* and Runs 25–46 (excl. 34 & 35) in the *Golden* data sets. The exposure-weighted average FWHM at $Q_{\beta\beta}$ is (4.8±0.2), (4.8±0.2) and (3.2±0.2) keV, and the total exposure ($\mathcal{E}$= diode mass × live time) is 17.9, 1.3 and 2.4 kg·yr, respectively for the *Golden*, *Silver* and *BEGe* data sets. All data sets combined yield an exposure-weighted average FWHM of (4.6 ± 0.2) keV and a total exposure of 21.6 kg·yr.

6.4 Background in the region of interest around $Q_{\beta\beta}$

The energy spectrum produced by background processes can be described by the global background model developed in Section 4.7. The background model predicts approximately a flat energy distribution in a 240 keV wide energy window between 1930 and 2190 keV, after excluding the energy intervals of (2104 ± 5) keV and (2119 ± 5) keV that contain the γ-ray peaks from ^{208}Tl and ^{214}Bi, respectively (see Fig. 4.24). The expected background index at $Q_{\beta\beta}$ (B) for the individual GERDA data sets is evaluated from the observed number of events in this energy window minus the ($Q_{\beta\beta}$±5) keV blinding window, and under the assumption of a constant background as a function of energy. The net width of the B evaluation window is hence 230 keV. In total 77 [1] events in the *Golden* (17.9 kg·yr), 19 events in the *Silver* (1.3 kg·yr) and 23 events in the *BEGe* (2.4 kg·yr) data set are observed within this energy window, corresponding to B of $(19 \pm 2) \cdot 10^{-3}$, $(64^{+16}_{-14}) \cdot 10^{-3}$ and $(42^{+10}_{-8}) \cdot 10^{-3}$ cts/(keV·kg·yr), respectively.

Pulse shape discrimination (PSD) methods are applied to data, in order to improve

[1] The number of counts before unblinding were 76 in total. After the events in the $Q_{\beta\beta} \pm 5$ keV window were processed, one event with 2044.3 keV from ANG4 appeared outside the 10 keV window, which increased the number of events from 76 to 77 in the 230 keV wide B evaluation window. This event is considered in all the calculations reported in the official GERDA paper, although the number is mistakenly quoted as 76 in stead of 77 in Table 1 of [18].

the sensitivity to $0\nu\beta\beta$ signal by rejecting background-like events. The PSD methods and their efficiencies are described in Section 6.5.2. After applying PSD cuts, the expected background in the 230 keV window decreases to 45 events in the *Golden*, 9 events in the *Silver* and 3 events in the *BEGe* data set, corresponding to B of $(11 \pm 2) \cdot 10^{-3}$, $(30^{+12}_{-9}) \cdot 10^{-3}$ and $(5^{+4}_{-3}) \cdot 10^{-3}$ cts/(keV·kg·yr), respectively. Considering all data sets with a total exposure of 21.6 kg·yr results in a B of $(24 \pm 2) \cdot 10^{-3}$ cts/(keV·kg·yr) without PSD and $(11^{+2}_{-1}) \cdot 10^{-3}$ cts/(keV·kg·yr) with PSD cuts. It is important to mention that, using PSD selection do not only reject background-like events, but also, to some degree, signal-like events. This is accommodated in the signal acceptance in the following analysis. [2]

6.5 Detection efficiency and acceptance of $0\nu\beta\beta$ signal

The signal efficiency, ϵ, for each GERDA data set is calculated as

$$\epsilon = \frac{\sum_i f_{76,i}\, f_{AV,i}\, M_i\, t_i\, \varepsilon_{FEP,i}}{\mathcal{E}} \cdot \varepsilon_{PSD} \ , \tag{6.18}$$

where the index i runs over the detectors considered in that data set. Since individual detectors have different exposures (see Table 2.3), ϵ is determined as an exposure ($\mathcal{E} = \sum_i M_i\, t_i$) weighted average value. The parameter $\varepsilon_{FEP,i}$ was evaluated through MC simulations, separately for all the detectors, as described in Section 6.5.1. The parameter ε_{PSD} was determined for each data set, which is presented in Section 6.5.2. If no PSD selection is applied to data, $\varepsilon_{PSD} = 1$. The uncertainty on ϵ (without PSD) is calculated from its probability distribution, $P(\epsilon)$, that is obtained through a MC approach. The values of $f_{76,i}$, $f_{AV,i}$, $\varepsilon_{FEP,i}$ and t_i are randomly sampled according to their individual probability distributions, modeled as Gaussian distributions with mean values and standard deviations given according to the known parameter values: $f_{76,i}$ and $f_{AV,i}$ listed in Table 2.2; $\varepsilon_{FEP,i}$ in Table 6.1; and t_i in Table 2.3 with 0.3% uncertainty. The correlated and uncorrelated uncertainties on $f_{AV,i}$ are properly taken into account. The uncertainties on $\varepsilon_{FEP,i}$ are considered to be completely correlated, since they are due to systematic uncertainties arising from MC simulation. Fig. 6.1 shows the resulting $P(\epsilon)$ distributions for the *Golden* and *Silver* data sets [3] (left plot) and for the *BEGe* data set (right plot), which yield ϵ (without PSD) of 0.688 ± 0.031 and 0.720 ± 0.019, respectively.

When PSD selection cuts are applied to data, ϵ reduces further due to the acceptance of $0\nu\beta\beta$ events by the PSD cuts being different than 1. The parameter ε_{PSD} is estimated to be $0.90^{+0.05}_{-0.09}$ for the *Golden* and *Silver*, and 0.92 ± 0.02 for the *BEGe* data sets (see Section 6.5.2), resulting in a reduced ϵ of 0.663 ± 0.022 and $0.619^{+0.044}_{-0.068}$, respectively.

Considering all data sets together gives an ϵ of 0.692 ± 0.028 without PSD and $0.624^{+0.039}_{-0.060}$ with PSD cuts.

[2] Otherwise, B must have been scaled for the reduced exposure, which would result in a higher value than what is quoted here.

[3] These two data sets contain the same detectors in different measurement periods (see Section 6.3), and thus, have the same $P(\epsilon)$ distribution.

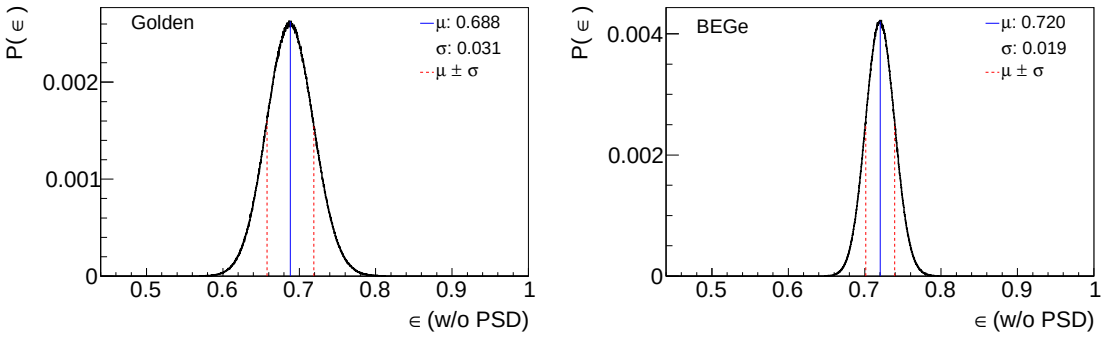

Figure 6.1: The probability distributions of ϵ without PSD, $P(\epsilon)$, for the *Golden* and *Silver* (left) and for the *BEGe* (right) data sets. The mean value (μ) and the standard deviation (σ) of the distributions are given in the legends. μ and $\mu \pm \sigma$ are labeled with solid blue and dashed red lines, respectively.

6.5.1 Efficiency for detecting the full energy peak

The efficiency for detecting the full energy $0\nu\beta\beta$ peak, ε_{FEP}, is defined as the probability that a $0\nu\beta\beta$ decay taking place in the active volume of a detector releases its entire energy in it. Energy losses can occur due to bremsstrahlung photons, fluorescence x-rays, or electrons escaping the active volume of the detectors. The parameter ε_{FEP} is obtained for the individual Phase I detectors through MC simulations in MaGe [135]. The primary spectrum of the $0\nu\beta\beta$ decays is generated using Decay0 [151]. For the $^{\text{enr}}$Ge-coax detectors, the decays are sampled within the active volume of each detector separately. A realistic implementation of the detectors in MaGe, with the dimensions and dead layer thicknesses given according to Table 2.2, is used for the simulation. Whereas, for the BEGe detectors, ε_{FEP} is determined with the Dead Layer Post Processing (DLPP) approach [152]. The detector is simulated as a single Geant4 physical volume that does not include a dead layer and a posterior volume cut is used to determine the spectrum in the active volume. After obtaining the simulated energy spectra of $0\nu\beta\beta$ decays that include detector related effects (except energy resolution), ε_{FEP} is determined as the ratio of the number of events with an energy deposition at $Q_{\beta\beta}$, i.e. (2039 ± 0.5) keV, to the total number of events sampled in the active volume of the detectors. Since ε_{FEP} is normalized to the number of decays taking place in the active volume, the uncertainty on the determined ε_{FEP} and the uncertainties on the f_{AV}, which has been considered separately in Eq. (6.18), are practically decoupled. The statistical uncertainty on ε_{FEP} due to limited number of simulated events is of the order of 0.1%. The systematic uncertainty due to the MaGe MC simulation is estimated to be 2% and arises from the uncertainties on the knowledge of the $0\nu\beta\beta$ spectrum, accuracy of the MC tracking and precision of the MC geometry model (Section 5.3.2). The results for individual detectors are listed in Table 6.1. The average ε_{FEP} is 0.92 ± 0.02 for the $^{\text{enr}}$Ge-coax detectors considered in the *Golden* and *Silver* data sets and 0.90 ± 0.02 for the BEGe detectors contained in the *BEGe* data set.

Table 6.1: Efficiency for detecting the full energy peak, ε_{FEP}, of $0\nu\beta\beta$ decays for the ^{enr}Ge detectors of Phase I. Note that ε_{FEP} is normalized to the number of decays sampled in the active volume. $\Delta\varepsilon_{FEP}$ is the systematic uncertainty arising from the MaGe MC simulation. Statistical uncertainties due to the limited number of simulated events are of the order of 0.1%.

Detector	$\varepsilon_{FEP} \pm \Delta\varepsilon_{FEP}$
ANG1 *	0.89 ± 0.02
ANG2, ANG3, ANG4, ANG5, RG1	0.92 ± 0.02
RG2, RG3 *	0.91 ± 0.02
GD32B, GD32C, GD32D, GD35B	0.90 ± 0.02
GD35C *	0.89 ± 0.02

* Not considered in the analysis (see Section 2.3.6).

6.5.2 Pulse shape discrimination methods and efficiencies

Pulse shape discrimination methods are applied to Gerda Phase I data, which improve the experimental sensitivity by rejecting background-like events, while keeping signal-like events with high efficiency, using their different topology. The energy deposited by the two electrons in $0\nu\beta\beta$ decay events is mostly ($\sim$ 90%) localized within few mm^3 in the detector volume. The signal events are categorized as single-site events (SSE). Whereas, most background events, e.g. multiple Compton scattered γ-rays, deposit energy in several locations, well separated by few cm in the detector, and thus, are classified as multi-site events (MSE). The pulse shapes are in general different for SSE and MSE (see Fig. 1.8). Also, background events from β or α decays near or at the detector surfaces, which are mostly SSE, exhibit characteristic pulse shapes, which allow them to be recognized efficiently. PSD methods use these features to distinguish between background- and signal-like events. The PSD selection cuts applied to Gerda Phase I data are optimized to yield the best sensitivity for a $T^{0\nu}_{1/2}$ limit. The methods, selection cuts and efficiencies are reported in detail in [97], and briefly described below.

For the BEGe detectors, the method is based on a single pulse shape parameter A/E, i.e. the ratio of the maximum of the current pulse (A) and the energy (E), and allows for a simple and effective PSD selection [97–99]. The A/E cut efficiency is determined from Gerda calibration data, using events in the double escape peak (DEP, 1593 keV) of the 2615 keV γ-ray from ^{208}Tl. These events are created when the γ-rays interact through pair-production and the annihilation γ's escape the detector. Thus, their pulse shapes represent those of $0\nu\beta\beta$ decay events. The acceptance of signal-like events after the selection cut is $\varepsilon_{PSD} = 0.921 \pm 0.019$, while only 20% of the background events around $Q_{\beta\beta}$ survive. The signal efficiency, ε_{PSD}, is cross-checked with $2\nu\beta\beta$ decays of ^{76}Ge in the 1.0–1.4 MeV interval, which give a consistent result.

For the ^{enr}Ge-coax detectors, a PSD method based on an artificial neural network (ANN) is used. For the training of ANN, the DEP events at 1593 keV are used as signal-like sample and the γ-ray events in the full energy absorption peak (FEP) at 1621 keV from ^{212}Bi decays as the background-like sample. The cut on the classifier output of the

neural network is chosen to retain 90% of the DEP events. The signal acceptance is, thus, $\varepsilon_{PSD} = 0.90^{+0.05}_{-0.09}$, with the uncertainty derived from the $2\nu\beta\beta$ decays and from Compton edge events. About 55% of the background events around $Q_{\beta\beta}$ are classified as SSE-like and considered for the analysis. Two alternative PSD methods were developed and used for cross-checks: one based on a likelihood approach trained on Compton edge events; and the other uses a combination of A/E and the asymmetry of the current pulse. The three PSD methods use different training samples and selection criteria. Their results show good agreement, i.e. about 90% of the events rejected by ANN are also rejected by the two alternative methods.

6.6 Optimum width of the analysis window for limit setting

In the counting method described in Section 6.2.1, the number of events that fall within an energy window ΔE around $Q_{\beta\beta}$ are analyzed. The parameter ε_{res}, that is the fraction of the Gaussian signal within ΔE, depends on the energy resolution, σ_E, and the width of ΔE, as given in Eq. (1.23). Although, narrowing ΔE reduces ε_{res}, it increases the s/b ratio in the analysis window, and thus, can yield a higher sensitivity to $0\nu\beta\beta$ decay process. The procedure for finding the optimal width of ΔE for the best expected average limit on $T^{0\nu}_{1/2}$ was given in Section 1.3.2. The optimum window, ΔE_{opt}, for the individual Phase I data sets is determined following the same procedure. Fig. 6.2 shows the average 90% probability lower limit on $T^{0\nu}_{1/2}$ as a function of ΔE, given the determined analysis parameters: $\mathcal{E}$ and FWHM (Section 6.3), B (Section 6.4)and ϵ (Section 6.5) both without PSD (top plot) and with PSD (bottom plot). The resulting ΔE_{opt} is 7.5, 9.0 and 6.0 keV without PSD, and increases to 8.0, 9.5, and 8.0 keV in the case of using PSD; and the parameter ε_{res} for the given ΔE_{opt} is 0.934, 0.973 and 0.973 without PSD, and 0.950, 0.980 and 0.997 with PSD, for the *Golden*, *Silver* and *BEGe* data sets, respectively. Although B of the *Silver* data set is higher than that of the *Golden* data set, its optimum window is larger (both have the same FWHM). This is due to the low enough $\mathcal{E}$, and hence, small enough expected background counts for the *Silver* data set, such that having zero events is very likely even with large window sizes. Thus, it is optimal to have wide ΔE with high ε_{res} for this data set. The *BEGe* data set has a narrower ΔE_{opt} compared to the others, owing to its superior energy resolution. The application of PSD methods to data reduces B and hence results in a wider ΔE_{opt} for all the data sets.

6.7 Experimental sensitivity of GERDA Phase I

The sensitivity of GERDA Phase I to $0\nu\beta\beta$ signal is evaluated using the analysis parameters, $\mathcal{E}$, FWHM, B, ϵ, ΔE_{opt} and ε_{res} given above. Monte Carlo techniques are used to generate possible energy spectra from the same starting conditions. In total 10^4 MC realizations of GERDA Phase I are generated. For each realization, the expected number of signal and background events, ν and λ, are fixed and the number of measured events are generated as random numbers according to Poisson distributions with means ν and λ. The $0\nu\beta\beta$ decay spectrum is sampled from a Gaussian distribution with mean value at

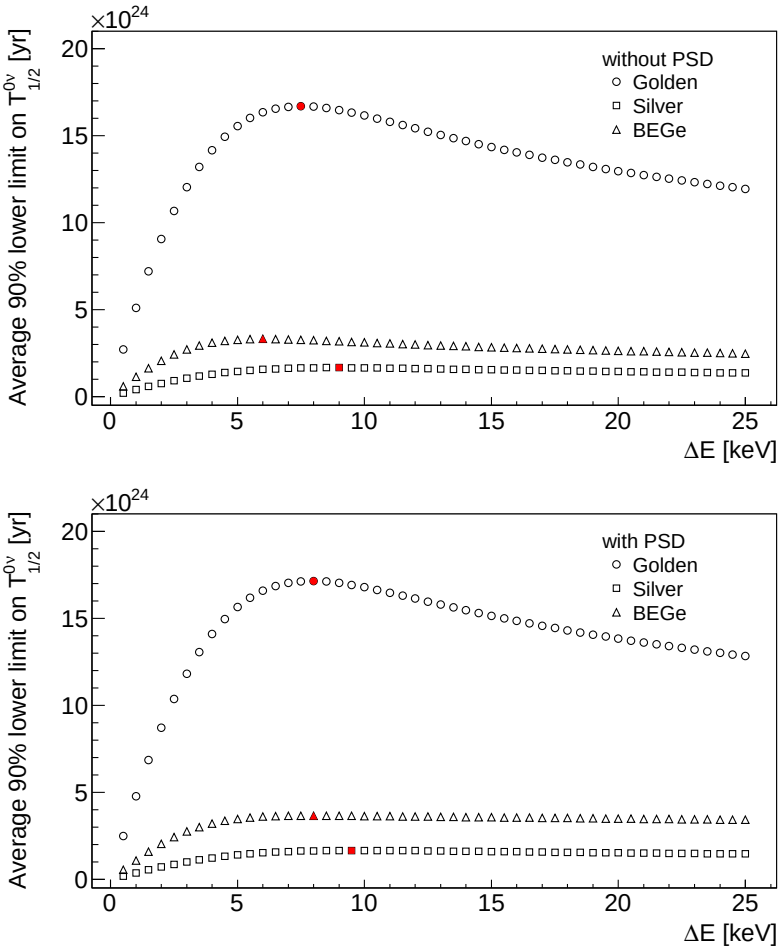

Figure 6.2: The average 90% probability lower limit on $T^{0\nu}_{1/2}$ as a function of the width of the analysis window ΔE, both without PSD (top plot) and with PSD (bottom plot) selection applied to data. The parameters for $\{$*Golden*, *Silver*, *BEGe*$\}$ data sets are given as: $\mathcal{E} = \{17.9, 1.3, 2.4\}$ kg·yr, FWHM $= \{4.8, 4.8, 3.2\}$ keV, $\epsilon = \{0.688, 0.688, 0.720\}$ (w/o PSD) and $\{0.619, 0.619, 0.663\}$ (with PSD), $BI = \{0.019, 0.064, 0.042\}$ cts/(keV·kg·yr) (w/o PSD) and $\{0.011, 0.030, 0.005\}$ cts/(keV·kg·yr) (with PSD), resulting in $\Delta E_{opt} = \{7.5, 9.0, 6.0\}$ keV (w/o PSD) and $\{8.0, 9.5, 8.0\}$ keV (with PSD) for achieving the best $T^{0\nu}_{1/2}$ limit, indicated with filled red markers.

$Q_{\beta\beta} = 2039\,\text{keV}$ and standard deviation according to FWHM at $Q_{\beta\beta}$. The $0\nu\beta\beta$ signal contribution is defined as given in Eq. (6.14). In order to asses the limit setting sensitivity, the signal is assumed to be too weak to contribute to the measured energy spectrum. The background spectrum for each realization is sampled from a flat distribution in the 240 keV energy window, where a constant rate was predicted by the background model (Section 6.4). The number of background events in this window is allowed to fluctuate according to a Poisson distribution with mean λ, which is determined from the parameter B of the data set under consideration according to Eq. (6.13).

The Bayesian analysis described in Section 6.2 is performed on each sampled energy spectrum (MC data). For the background contribution, $P_0(\vec{B})$, is modeled as a Poisson distribution with mean according to the number of events observed in the 230 keV wide B evaluation window (Section 6.4). $P_0(1/T^{0\nu}_{1/2})$ is taken as a flat distribution between 0 and $10^{-24}\,\text{yr}^{-1}$. When using the counting method (Section 6.2.1), the number of events that fall within ΔE_{opt} are considered as the number of observed events n in Eq. (6.12). In the spectral analysis (Section 6.2.2), a Gaussian signal plus flat background model is fitted to the sampled energy spectra using 1 keV binning and in the 240 keV window: with the signal shape, $f_S(E)$, assumed as a Gaussian distribution with mean value at $Q_{\beta\beta} = 2039\,\text{keV}$ and the corresponding standard deviation at $Q_{\beta\beta}$; and the background shape, $f_B(E)$, as a flat distribution in the fit window. The computation is done using Markov Chain Monte Carlo within the analysis toolkit BAT [141]. For each sampled spectrum, a 90% probability lower limit on $T^{0\nu}_{1/2}$ is calculated from the obtained $P(1/T^{0\nu}_{1/2}|D,\bar{H})$ distribution (Eqs. (6.9) and (6.10)).

A possible gain in sensitivity due to grouping of data is investigated by repeating the analysis for three different options of using the available data:

- Only the *Golden* ($\mathcal{E} = 17.9\,\text{kg·yr}$) data set;
- *Combined:* The data sets *Golden* ($\mathcal{E} = 17.9\,\text{kg·yr}$), *Silver* ($\mathcal{E} = 1.3\,\text{kg·yr}$) and *BEGe* ($\mathcal{E} = 2.4\,\text{kg·yr}$) combined into one set, with a total exposure of 21.6 kg·yr;
- *All:* All data sets analyzed together but treated separately in the likelihood functions.

For each option MC data are generated and analyzed as described above. The 90% probability lower limit on $1/T^{0\nu}_{1/2}$ is derived for all MC realizations, and the normalized distribution of the resulting limits is treated as a probability distribution. The limit setting sensitivity is then determined as the median of this distribution. Fig. 6.3 shows the normalized distribution of $1/T^{0\nu}_{1/2}$ limits at 90% C.I., in the case of performing a binned spectral fit for the option *All* and using PSD selection cuts. The median of the distribution is $0.49 \cdot 10^{-25}\,\text{yr}^{-1}$, which corresponds $T^{0\nu}_{1/2}$ of $2.04 \cdot 10^{25}\,\text{yr}$.

Table 6.2 lists the median sensitivity for the 90% probability limit on $T^{0\nu}_{1/2}$ for three options of using data, *Golden*, *Combined* and *All*, both with and without PSD, and for the analyses performed using both the counting method and the binned spectral fit. The best sensitivity is attained when all data is used in subsets with similar characteristics by treating each separately in the analysis (*All*), instead of combining all data into one set (*Combined*). Applying PSD selection to data, which leads to a significant improvement

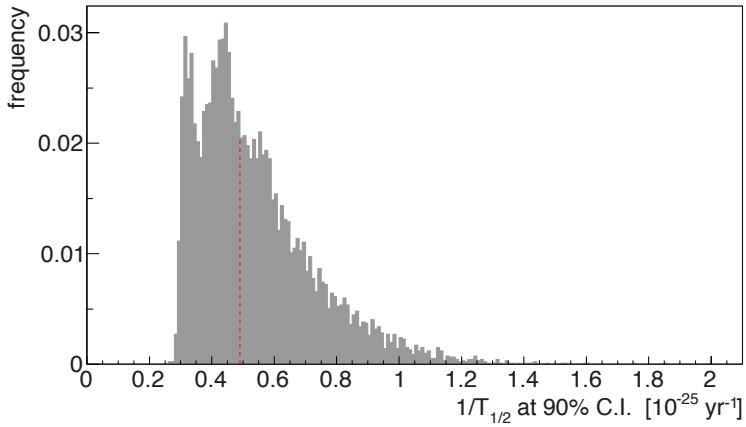

Figure 6.3: Normalized distribution of $1/T^{0\nu}_{1/2}$ limits at 90% C.I. derived from 10^4 MC realizations of the GERDA experiment. MC data were generated for individual data sets given the analysis parameters determined for Phase I after PSD selection cuts. A binned spectral fit was performed on each sampled energy spectrum, by treating the subsets of data separately in the likelihood function, i.e. option *All* in Table 6.2. The median of the distribution is $0.46 \cdot 10^{-25}\,\mathrm{yr}^{-1}$, which corresponds to $T^{0\nu}_{1/2}$ of $2.04 \cdot 10^{25}\,\mathrm{yr}$.

in the background levels in cost of a small decrease in the signal efficiencies, improves the sensitivity as expected. Moreover, the results show that, the spectral fit yields a better sensitivity compared to the counting method. In the spectral analysis, additional information like the spectral shape of the signal and background processes, are taken into account as well, which can improve the results.

Table 6.2: The median sensitivity for the 90% probability lower limit on $T^{0\nu}_{1/2}$ evaluated with Bayesian analysis using the counting method and the binned spectral fit for three different options of using the available data: only *Golden* data set; all data combined into one set (*Combined*); and individual data sets analyzed together but treated separately in the likelihood function (*All*). Results are given for both with and without the PSD selection cuts.

Data set	Median sensitivity for the 90% prob. limit [10^{25} yr]			
	Counting method		Binned spectral fit	
	w/o PSD	with PSD	w/o PSD	with PSD
Golden	1.67	1.72	1.67	1.74
Combined	1.71	1.82	1.79	1.98
All	1.71	1.94	1.83	2.04

Chapter 7

Results on ^{76}Ge $0\nu\beta\beta$ signal search

GERDA Phase I data is analyzed for estimating (or setting a limit on) the $0\nu\beta\beta$ signal rate using Bayesian approach. The energy spectrum after opening the blinding window is presented in Section 7.1, and the results of the analysis in Section 7.2. An extended analysis that includes the energy spectra from the two previous ^{76}Ge experiments, HDM and IGEX, is described in Section 7.3. The analysis presented in this chapter is carried out consistently with the one performed by the GERDA analysis team that is reported in [18]. An alternative analysis of both GERDA Phase I and combined ^{76}Ge data using Frequentist approach, reported in [18] as well, is described here for completeness.

7.1 Unblinding

The blinding energy window of $Q_{\beta\beta} \pm 5\,\text{keV}$ was opened in June 2013, after the data selection cuts and the analysis parameters were determined. In total 7 events are observed within this 10 keV window: 5 in the *Golden* (2 after PSD); 1 in the *Silver* (1 after PSD); and 1 in the *BEGe* (0 after PSD) data set. Table 7.1 gives the details of the events, listing the data set, detector, energy and date for each one of them, including whether or not they passed the PSD selection cut. Fig. 7.1 shows the energy spectrum of the individual data sets in 1 keV binning. The shaded region indicates the B evaluation window between 1930 and 2190 keV, excluding $Q_{\beta\beta} \pm 5\,\text{keV}$ and the two energy intervals, 2099–2109 keV and 2114–2124 keV, where a substantial contribution from γ-ray lines due to background sources are expected. The global background model predicts a flat distribution in this energy window, including the 10 keV interval around $Q_{\beta\beta}$ (Fig. 4.24). Table 7.2 lists the relevant analysis parameters described in Chapter 6, along with the number of expected background counts (λ) and observed events (n) in the 10 keV window, for the subsets *Golden*, *Silver* and *BEGe*, and for the *Combined* data set, both with and without PSD selection. In all cases, n is consistent with λ. In fact, considering the *Combined* data set, the probability to observe n or more events given λ is $P(n \geq 7|5.2) = 0.27$ without PSD and $P(n \geq 3|2.4) = 0.43$ with PSD selection. In both cases, the probability to observe the measured events given the expected background is high. Thus, GERDA Phase I data show no indication of a $0\nu\beta\beta$ signal.

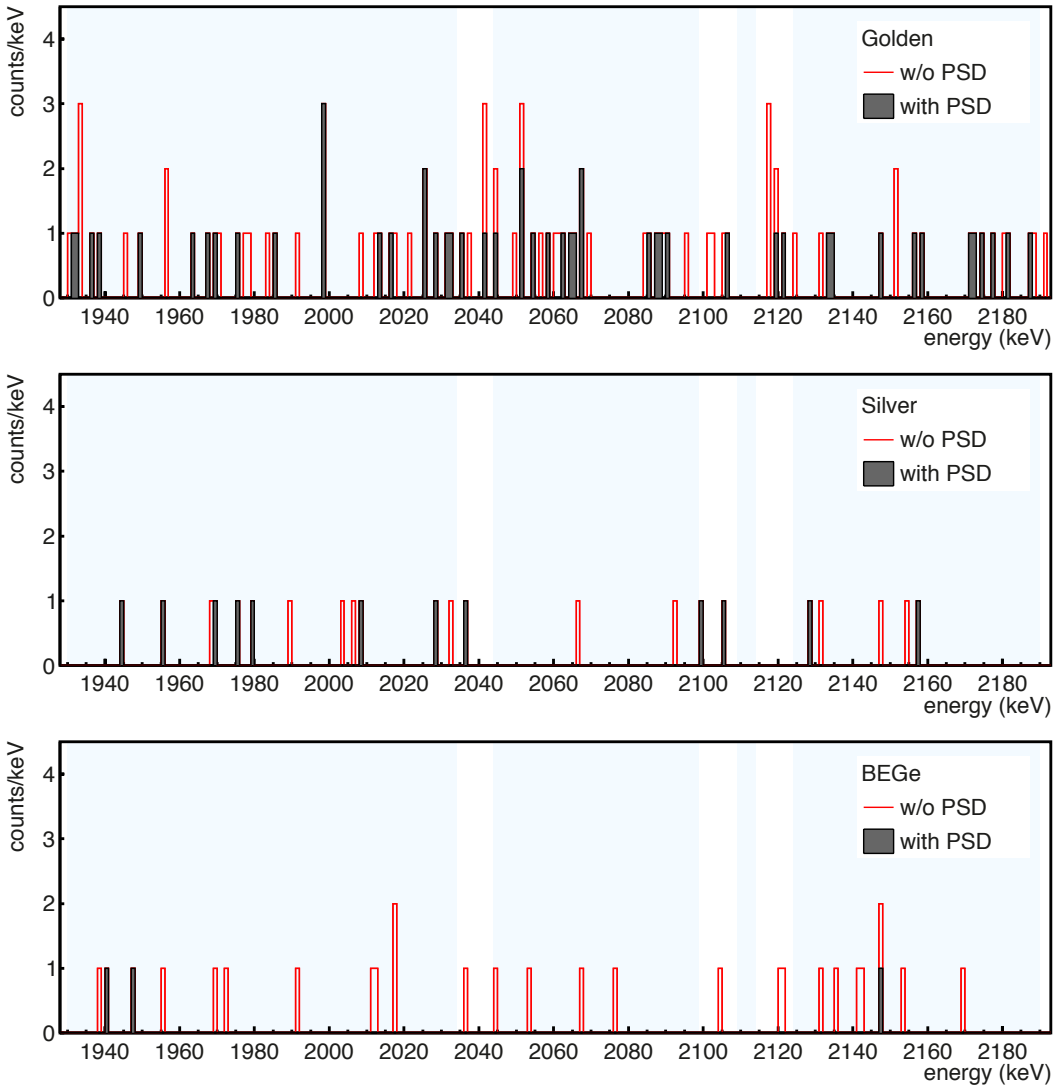

Figure 7.1: Energy spectra of the *Golden* (top), *Silver* (middle) and *BEGe* (bottom) data sets before (empty) and after (filled histogram) the PSD selection cuts applied. The shaded blue region indicates the B evaluation window with a constant count rate predicted by the background model, i.e. between 1930 and 2190 keV, excluding the 10 keV interval around $Q_{\beta\beta} = 2039$ keV, and the two energy intervals, 2099–2109 keV and 2114–2124 keV, where a substantial contribution from γ-ray lines due to background sources are expected.

Table 7.1: List of all events within $Q_{\beta\beta} \pm 5\,\text{keV}$ window in the GERDA Phase I energy spectrum.

Data set	Detector	Energy [keV]	Date	PSD passed
Golden	ANG5	2041.8	18 Nov 2011	no
Silver	ANG5	2036.9	23 Jun 2012	yes
Golden	RG2	2041.3	16 Dec 2012	yes
BEGe	GD32B	2036.6	28 Dec 2012	no
Golden	RG1	2035.5	29 Jan 2013	yes
Golden	ANG3	2037.4	02 Mar 2013	no
Golden	RG1	2041.7	27 Apr 2013	no

Table 7.2: Analysis parameters – namely, the total exposure ($\mathcal{E}$), the exposure-weighted average energy resolution at $Q_{\beta\beta}$ (FWHM), the optimum energy window for limit setting (ΔE_{opt}), the Gaussian efficiency within ΔE_{opt} (ε_{res}), the exposure-weighted average signal efficiency (ϵ), the background index at $Q_{\beta\beta}$ (B), the number of expected background (λ) and the number of observed events (n) in the $Q_{\beta\beta}\pm 5\,\text{keV}$ interval – for the *Golden*, *Silver*, *BEGe* and *Combined* data sets, both with and without PSD selection applied to data.

Data set	$\mathcal{E}$ [kg·yr]	FWHM [keV]	ΔE_{opt} [keV]	ε_{res}	ϵ	B [cts/(keV·kg·yr)]	λ [cts]	n [cts]
w/o PSD								
Golden	17.9	4.8 ± 0.2	7.5	0.934	0.688 ± 0.031	$(19 \pm 2) \cdot 10^{-3}$	3.2	5
Silver	1.3	4.8 ± 0.2	9.0	0.973	0.688 ± 0.031	$(64^{+16}_{-14}) \cdot 10^{-3}$	0.8	1
BEGe	2.4	3.2 ± 0.2	6.0	0.973	0.720 ± 0.019	$(42^{+10}_{-8}) \cdot 10^{-3}$	1.0	1
Combined	21.6	4.6 ± 0.2	7.0	0.927	0.692 ± 0.028	$(24 \pm 2) \cdot 10^{-3}$	5.2	7
with PSD								
Golden	17.9	4.8 ± 0.2	8.0	0.950	$0.619^{+0.044}_{-0.068}$	$(11 \pm 2) \cdot 10^{-3}$	2.0	2
Silver	1.3	4.8 ± 0.2	9.5	0.980	$0.619^{+0.044}_{-0.068}$	$(30^{+12}_{-9}) \cdot 10^{-3}$	0.4	1
BEGe	2.4	3.2 ± 0.2	8.0	0.997	0.663 ± 0.022	$(5^{+4}_{-3}) \cdot 10^{-3}$	0.1	0
Combined	21.6	4.6 ± 0.2	7.5	0.945	$0.624^{+0.039}_{-0.060}$	$(11^{+2}_{-1}) \cdot 10^{-3}$	2.4	3

7.2 Bayesian analysis of the GERDA Phase I data

The analysis for deriving a limit on $T^{0\nu}_{1/2}$ is carried out using the Bayesian approach described in Section 6.2 and performing the computations with the Bayesian analysis toolkit BAT [141]. Equal prior probabilities are assigned to the hypotheses H and $\bar{H}$, i.e. $P_0(H) = P_0(\bar{H}) = 0.5$. Three data sets are analyzed together by treating them separately in the likelihood functions. This option yields the best sensitivity for limit setting, as demonstrated in Section 6.7. Data are analyzed by defining the likelihood functions using both the counting method (Section 6.2.1) and the binned spectral fit (Section 6.2.2). The analysis is repeated to test the claim of ^{76}Ge $0\nu\beta\beta$ signal observation reported in [17], by

assuming an expected signal rate in $\bar{H}$ according to the claimed $T^{0\nu}_{1/2}$ value and comparing that $\bar{H}$ to the background only hypothesis H.

7.2.1 Results of the counting method

The analysis is performed on the Phase I data before and after the PSD selection cuts applied, and both in ΔE_{opt} determined for each data set in Section 6.6 and in the formerly 10 keV wide blinding window around $Q_{\beta\beta}$, the reason of which will become clear later. The prior for background contributions, $P_0(\vec{B})$, is given according to the according to the number of events observed in the 230 keV wide B evaluation window (Section 6.4) of the individual data sets. Whereas, a flat distribution between 0 and $10^{-24}\,\mathrm{yr}^{-1}$ is taken for $P_0(1/T^{0\nu}_{1/2})$. In all considered cases, there is no evidence for a $0\nu\beta\beta$ signal; data prefer background only hypothesis H, with a Bayes Factor (Eq. (6.8)) of $K < 1$. A 90% probability lower limit on $T^{0\nu}_{1/2}$ is derived from the marginalized posterior probability distribution, $P(1/T^{0\nu}_{1/2}|D,\bar{H})$. Results of the analysis are summarized in Table 7.3. The systematic uncertainties are included in the $T^{0\nu}_{1/2}$ results, which arise from the uncertainties on the analysis parameters – namely, on ϵ and FWHM (see Table 7.2). The uncertainties are folded in with a MC approach; the analysis is repeated with the parameters sampled randomly from their probability distributions. The 90% quantile of the averaged $P(1/T^{0\nu}_{1/2}|D,\bar{H})$ distribution is quoted as the limit including the systematic uncertainty. Fig. 7.2 shows the $P(1/T^{0\nu}_{1/2}|D,\bar{H})$ distribution resulting from the analysis carried out in the 10 keV window around $Q_{\beta\beta}$ and with PSD selection, superimposed with the one that includes the systematic uncertainty. The 90% quantile of the latter is $0.58 \cdot 10^{-25}\,\mathrm{yr}^{-1}$, corresponding to a $T^{0\nu}_{1/2}$ limit of $1.72 \cdot 10^{25}\,\mathrm{yr}$. The systematic uncertainty weakens the $T^{0\nu}_{1/2}$ limit by about 1%.

The $T^{0\nu}_{1/2}$ limits obtained from the analysis in ΔE_{opt} are worse compared to the ones in the 10 keV window around $Q_{\beta\beta}$. Due to the random nature of events, all observed events in the formerly 10 keV blinding window are confined within a 7 keV wide interval (see Table 7.1). The number of observed counts in the 10 keV window and in ΔE_{opt} (smaller than 10 keV) are same for all data sets. Thus, the larger window (10 keV) yields a better limit, since the background expectation increases, while observed number of events do not change. The comparison of the different results, due to choosing different analysis windows and/or applying additional cuts, demonstrates how the derived limit depends on the predefined analysis parameters and data selection cuts.

7.2.2 Results of the binned spectral fit

The energy spectra of GERDA Phase I data sets are fitted with a model accounting for the background and signal contributions, using 1 keV binning and in the 240 keV window where the background can be approximated as a flat distribution (Fig. 4.24). The fit model has four free parameters: B of the three data sets (related to λ_i as in Eq. (6.13)) for background contributions and one common $1/T^{0\nu}_{1/2}$ (related to ν_i as given in Eq. (6.14)) for the signal contributions. The spectral shape of the background, $f_B(E)$, is assumed as flat

Table 7.3: Number of expected background events (λ) in the analysis window ΔE according to B quoted in Table 7.2 and number of observed events in the same window (n) for the three data sets, the Bayes Factor (K) and 90% probability lower limit on $T^{0\nu}_{1/2}$ derived from the Bayesian analysis using the counting method, considering data both with and without PSD selection cuts applied. The analysis is carried out in $\Delta E = 10\,\text{keV}$ (no optimization) and in the optimum analysis windows: $\Delta E_{opt} = \{7.5, 9, 6\}\,\text{keV}$ (w/o PSD) and $\{8, 9.5, 8\}\,\text{keV}$ (with PSD) for $\{$*Golden*, *Silver*, *BEGe*$\}$ data sets. The $T^{0\nu}_{1/2}$ results include the systematic uncertainty arising from the uncertainties on B, ϵ and FWHM.

Selection	λ [cts]			n [cts]			K	$T^{0\nu}_{1/2}$ [10^{25} yr]
	Golden	*Silver*	*BEGe*	*Golden*	*Silver*	*BEGe*		
w/o PSD								
ΔE_{opt}	2.4 ± 0.3	0.8 ± 0.2	0.6 ± 0.1	5	1	1	0.47	> 0.97
$\Delta E = 10\,\text{keV}$	3.2 ± 0.4	0.8 ± 0.2	1.0 ± 0.2	5	1	1	0.31	> 1.17
with PSD								
ΔE_{opt}	1.6 ± 0.3	0.4 ± 0.1	$0.10^{+0.08}_{-0.06}$	2	1	0	$4 \cdot 10^{-3}$	> 1.59
$\Delta E = 10\,\text{keV}$	2.0 ± 0.4	0.4 ± 0.1	$0.12^{+0.10}_{-0.07}$	2	1	0	$3 \cdot 10^{-5}$	> 1.72

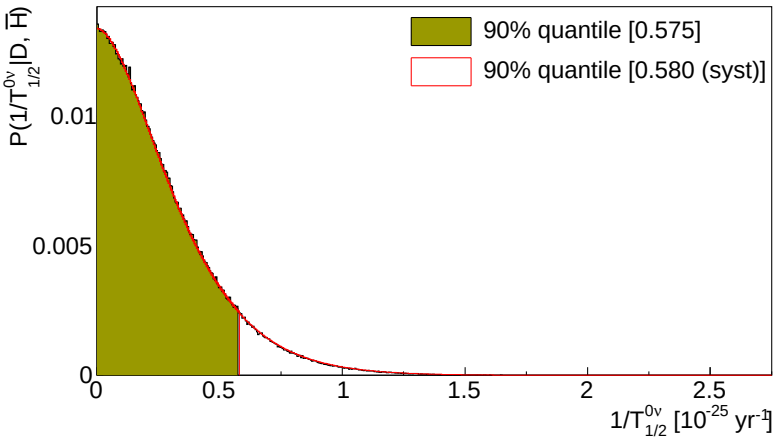

Figure 7.2: The marginalized posterior probability distribution, $P(1/T^{0\nu}_{1/2}|D, \bar{H})$, obtained from the Bayesian counting analysis carried out in the 10 keV window around $Q_{\beta\beta}$ and after PSD selection cuts were applied to data. The distribution is shown both without (black histogram) and with (red histogram) systematic uncertainties folded into the analysis. The 90% quantile of the latter, $0.58 \cdot 10^{-25}\,\text{yr}^{-1}$, corresponds to a limit of $T^{0\nu}_{1/2} > 1.72 \cdot 10^{25}\,\text{yr}$ at 90% C.I., which is about 1% worse than the limit without systematic uncertainty.

distribution for each data set and the parameters B are given flat priors. The signal shape, $f_S(E)$, is modeled as a Gaussian distribution with mean at $Q_{\beta\beta}$ and the corresponding standard deviation at $Q_{\beta\beta}$ for the individual data sets. A flat distribution between 0 and $10^{-24}\,\mathrm{yr}^{-1}$ is taken as $P_0(1/T^{0\nu}_{1/2})$.

The analysis is performed on the measured spectra both before and after PSD selection cuts applied. In both cases, data show no indication for a $0\nu\beta\beta$ signal. The Bayes Factor (Eq. (6.8)) is $K = 0.08$ without PSD and $K = 0.03$ with PSD; data strongly favor the background only hypothesis, H, over the signal plus background hypothesis, $\bar{H}$. A 90% probability lower limit on $T^{0\nu}_{1/2}$ is derived from the marginalized posterior probability distribution $P(1/T^{0\nu}_{1/2}|D,\bar{H})$ (Eq. (6.9)). The systematic uncertainties due to detector parameters and selection efficiencies (f_{76}, f_{AV}, ε_{FEP} and ε_{PSD}), energy resolution (FWHM) and energy scale ($\pm 0.2\,\mathrm{keV}$ shift) are included in the $T^{0\nu}_{1/2}$ results through a MC approach; the fit is repeated with the parameters sampled randomly from their probability distributions and the 90% quantile of the averaged $P(1/T^{0\nu}_{1/2}|D,\bar{H})$ distribution is quoted as the limit including the systematic uncertainty. The analysis performed on the spectra without PSD selection yields:

$$T^{0\nu}_{1/2} > 1.24 \cdot 10^{25}\,\mathrm{yr}\ (\nu < 6.66)\ \text{at}\ 90\%\,\mathrm{C.I.}\ , \tag{7.1}$$

and with PSD selection yields:

$$T^{0\nu}_{1/2} > 1.85 \cdot 10^{25}\,\mathrm{yr}\ (\nu < 4.02)\ \text{at}\ 90\%\,\mathrm{C.I.}\ , \tag{7.2}$$

including the systematic uncertainties. Fig. 7.3 shows the $P(1/T^{0\nu}_{1/2}|D,\bar{H})$ distribution resulting from the analysis (with PSD), superimposed with the one that includes the systematic uncertainty. The effect of the systematic uncertainty on the limit is about 1%.

Fig. 7.4 shows the sum energy spectrum of three data sets without (top) and with (bottom) PSD selection, together with the fit model: flat background distribution plus Gaussian $0\nu\beta\beta$ signal with an intensity corresponding to the 90% probability upper limit, i.e. $\nu < 6.66$ without PSD (Eq. (7.1)) and $\nu < 4.02$ with PSD (Eq. (7.2)) at 90% C.I. The upper limit on ν is calculated from the $T^{0\nu}_{1/2}$ limit derived from the analysis according to the relation between ν and $T^{0\nu}_{1/2}$ given in Eq. (6.2), and using the parameter values for the *Combined* data set in Table 7.2. Note that, the analysis was performed by treating each data set separately and considering their individual analysis parameters. Only for quoting ν limit and for the plots in Fig. 7.4, the combined (sum data) parameter values are used, i.e. $\mathcal{E} = 21.6\,\mathrm{kg{\cdot}yr}$, $\epsilon = 0.692$ (w/o PSD) and $\epsilon = 0.624$ (with PSD). The Gaussian signal is plotted with its mean at $Q_{\beta\beta} = 2039\,\mathrm{keV}$ and a standard deviation of $1.95\,\mathrm{keV}$ (FWHM $= 4.6\,\mathrm{keV}$).

7.2.3 Bayes Factors for the Claim

The outcome of the analyses described above is that, there is no indication of a $0\nu\beta\beta$ signal in GERDA Phase I data. The positive claim of observation of a ^{76}Ge $0\nu\beta\beta$ signal, with $T^{0\nu}_{1/2} = (1.19^{+0.37}_{-0.23}) \cdot 10^{25}\,\mathrm{yr}$ reported in [17] by parts of the HDM collaboration, is

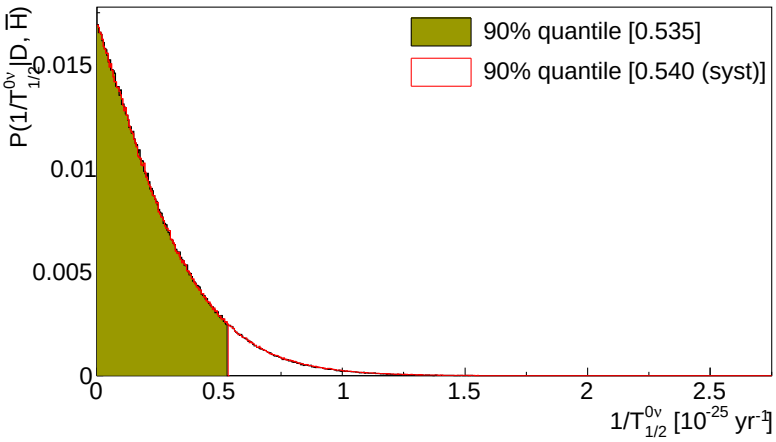

Figure 7.3: The marginalized posterior probability distribution, $P(1/T^{0\nu}_{1/2}|D,\bar{H})$, obtained from the Bayesian spectral fit carried out in the 240 keV constant background window and after PSD selection cuts were applied to data. The distribution is shown both without (black histogram) and with (red histogram) the systematic uncertainty folded into the analysis. The 90% quantile of the latter, $0.54 \cdot 10^{-25}\,\mathrm{yr}^{-1}$, corresponds to $T^{0\nu}_{1/2} > 1.85 \cdot 10^{25}$ yr at 90% C.I., which is about 1% worse than the limit without systematic uncertainty.

in strong tension with the findings of GERDA Phase I. The expected number of $0\nu\beta\beta$ signal events according to the claimed $T^{0\nu}_{1/2}$ in the $Q_{\beta\beta} \pm 2\sigma$ interval and for the ϵ after PSD selection is $\nu = 5.9 \pm 1.4$. In total 3 events are observed in GERDA Phase I energy spectrum in this energy window, where $\lambda = 2.0 \pm 0.3$ background events are expected. The Poisson probability to observe $n = 3$ events given the expectation of $\nu + \lambda = 7.9$ events is very low, i.e. $P(3|7.9) = 0.03$. Moreover, none of the observed three events in the GERDA Phase I spectrum are within $Q_{\beta\beta} \pm 1\sigma$ (Fig. 7.4).

In the Bayesian analysis of GERDA Phase I data described in Sections 7.2.1 and 7.2.2, a flat prior probability distribution was taken for the $0\nu\beta\beta$ signal rate, i.e. flat $P_0(1/T^{0\nu}_{1/2})$. For testing the claim, the observed spectrum after PSD is analyzed through binned spectral fit this time by taking $P_0(1/T^{0\nu}_{1/2})$ as a Gaussian distribution with mean of $0.84 \cdot 10^{-25}\,\mathrm{yr}^{-1}$ and standard deviation of $0.20 \cdot 10^{-25}\,\mathrm{yr}^{-1}$, which models the claimed $T^{0\nu}_{1/2}$ in [17]. Thus, the hypothesis $\bar{H}$ assumes the $0\nu\beta\beta$ signal with $\nu = 6.3 \pm 1.5$. As a result of the analysis, GERDA Phase I data strongly favor the background only hypothesis H over $\bar{H}$: the Bayes factor is:

$$K = P(\bar{H}|D)/P(H|D) = 0.02\ . \tag{7.3}$$

7.3 Bayesian analysis of the data from combined ^{76}Ge experiments

The analysis of $0\nu\beta\beta$ signal is extended to include the data from the two previous $0\nu\beta\beta$ decay experiments that were using the ^{76}Ge isotope, namely HDM and IGEX. The energy

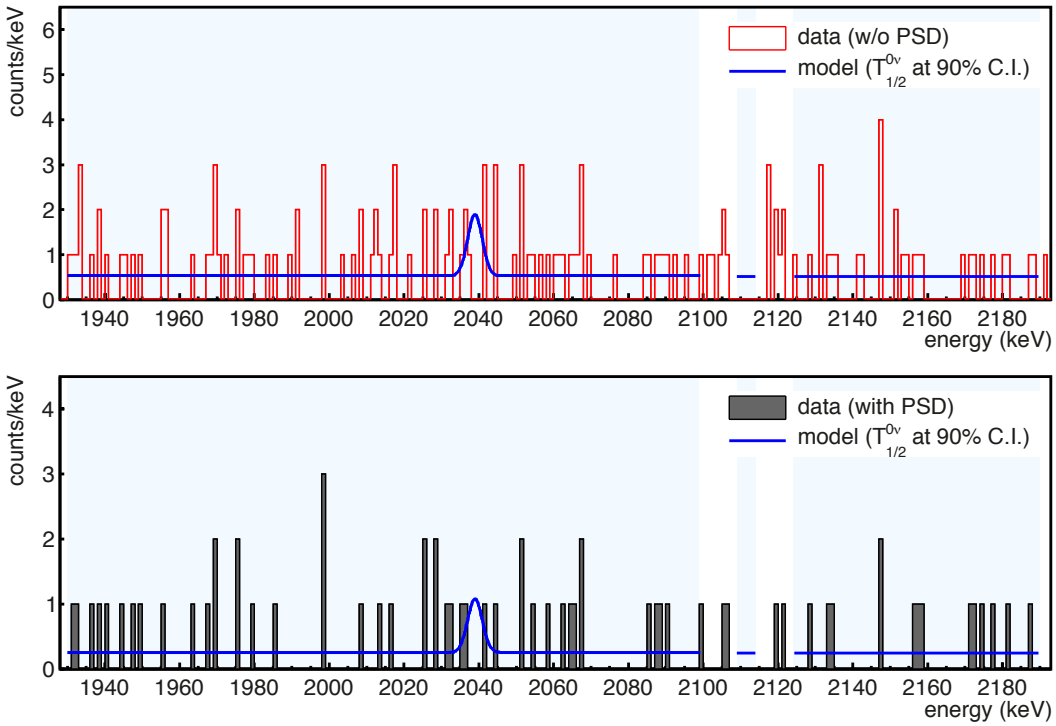

Figure 7.4: Sum energy spectrum of the GERDA Phase I data sets, without (top) and with (bottom) PSD, superimposed with the fit model. The shaded blue region indicates the 240 keV fit window, i.e. between 1930 and 2190 keV, excluding the two energy intervals 2099–2109 keV and 2114–2124 keV, where the background is assumed as a flat distribution. The fit model consists of a constant background plus a Gaussian $0\nu\beta\beta$ signal with an intensity corresponding to the $T^{0\nu}_{1/2}$ limit derived from the Bayesian spectral fit, i.e. $T^{0\nu}_{1/2} > 1.24 \cdot 10^{25}$ yr ($\nu < 6.66$) without PSD and $T^{0\nu}_{1/2} > 1.85 \cdot 10^{25}$ yr ($\nu < 4.02$) at 90% C.I. with PSD, including the systematic uncertainties. See text for further details.

spectrum of the HDM experiment after PSD selection is taken from Fig. 4 of [77], which is shown in the energy interval of 2000–2080 keV with 1 keV binning. The IGEX spectrum after PSD selection is obtained from Table 2 of [78], given in the 2020–2062 keV interval with 2 keV binning. The observations from the three ^{76}Ge experiments are analyzed using 5 data sets – namely, *Golden*, *Silver* and *BEGe* from GERDA, and the ones from HDM and IGEX – after PSD selection applied and by considering the individual analysis parameters of the data sets. For the GERDA Phase I data sets, the analysis parameters are listed in Table 7.2. For the HDM and IGEX data sets, the parameter values reported by the collaborations are assumed: $\mathcal{E} = 35.5$ kg·yr, FWHM $= 4.23 \pm 0.14$ keV, $\epsilon = 0.71$ after

PSD [1] for HDM; and $\mathcal{E} = 8.9\,\text{kg·yr}$, FWHM = 4.0 keV [2], $\epsilon = 0.92$ after PSD [3] for IGEX. When the uncertainties on the parameters of HDM and IGEX data sets were not available, they are extrapolated from the values used in GERDA for the following analysis.

7.3.1 Results of the binned spectral fit

A Bayesian spectral fit, as described in Section 6.2, is performed on the combined ^{76}Ge data. The fit window of each data set is different, since the energy spectra are available in different intervals: 240 keV window with 1 keV binning for the GERDA data sets, as in Section 7.2.2; 80 keV window (2000–2080 keV) with 1 keV binning for the HDM data set; and 62 keV window (2020–2062 keV) with 2 keV binning for the IGEX data set. The fit model has 6 free parameters: B of the 5 data sets for background contributions (related to λ_i as in Eq. (6.13)) and one common $1/T^{0\nu}_{1/2}$ for the signal contributions (related to ν_i as in Eq. (6.14)). The signal contribution of each data set is modeled as a Gaussian distribution with mean at $Q_{\beta\beta} = 2039$ keV and the corresponding standard deviation at $Q_{\beta\beta}$. A flat distribution between 0 and $10^{-24}\,\text{yr}^{-1}$ is given as $P_0(1/T^{0\nu}_{1/2})$. The background contribution is modeled as a flat distribution for each data set and the parameters B are given flat $P_0(\vec{B})$ distribution.

The best fit yields $\nu = 0$. The combined ^{76}Ge data data strongly favor background only hypothesis, H, with Bayes factor

$$K = P(\bar{H}|D)/P(H|D) = 2 \cdot 10^{-4} \ . \tag{7.4}$$

A lower limit on $T^{0\nu}_{1/2}$ as derived from the marginalized posterior probability distribution $P(1/T^{0\nu}_{1/2}|D,\bar{H})$ is

$$T^{0\nu}_{1/2} > 2.86 \cdot 10^{25}\,\text{yr} \ (\nu < 9.30) \text{ at } 90\%\,\text{C.I.} \ , \tag{7.5}$$

including the systematic uncertainty. The systematic uncertainty arising from the uncertainties on ϵ, FWHM and energy scale (± 0.2 keV shift) are folded into the analysis using a MC approach, which weaken the limit by about 1.5%. Fig. 7.5 shows the $P(1/T^{0\nu}_{1/2}|D,\bar{H})$ distribution resulting from the spectral fit, superimposed with the one that includes the systematic uncertainty.

Fig. 7.6 shows the energy spectrum of the combined ^{76}Ge data in 2020–2062 keV interval with 2 keV binning (due to the available IGEX spectrum), together with the fit model (blue line). The fit model consists of a constant background plus a Gaussian $0\nu\beta\beta$ signal with an intensity equal to the upper limit of $\nu < 9.30$ at 90% C.I. (Eq. (7.5)). The Gaussian signal is plotted with its mean at $Q_{\beta\beta} = 2039$ keV and standard deviation of 1.8 keV, given the exposure-weighted average FWHM = 4.3 keV for the combined ^{76}Ge data. The

[1] The efficiency without PSD is $\epsilon = 0.89$. After PSD selection, it reduces to $\epsilon = 0.71$, due to the given $\varepsilon_{PSD} = 0.80$ in [169]. The uncertainty on this parameter is not quoted in the reference. It is extrapolated from the value for GERDA $^{\text{enr}}$Ge-coax detectors, i.e. 10% uncertainty on ϵ with PSD.

[2] The uncertainty on FWHM is not given by the IGEX collaboration. For the systematic uncertainty evaluation 3% uncertainty is assumed here.

[3] The uncertainty on ϵ is assumed as 10% as for the GERDA $^{\text{enr}}$Ge-coax detectors.

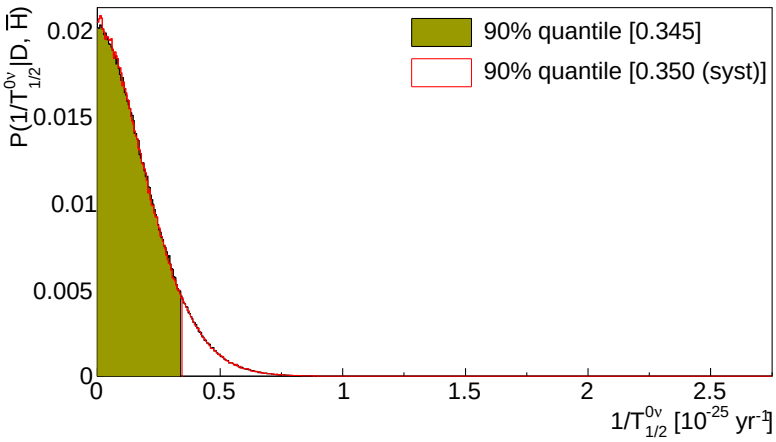

Figure 7.5: The marginalized posterior probability distribution, $P(1/T^{0\nu}_{1/2}|D,\bar{H})$, obtained from the Bayesian spectral fit of the combined ^{76}Ge data after PSD selection. The distribution is shown both without (black histogram) and with (red histogram) the systematic uncertainty folded into the analysis. The 90% quantile of the latter, $0.35 \cdot 10^{-25}\,\mathrm{yr}^{-1}$, corresponds to $T^{0\nu}_{1/2} > 2.86 \cdot 10^{25}\,\mathrm{yr}$ at 90% C.I., which is about 1.5% worse than the limit without systematic uncertainty.

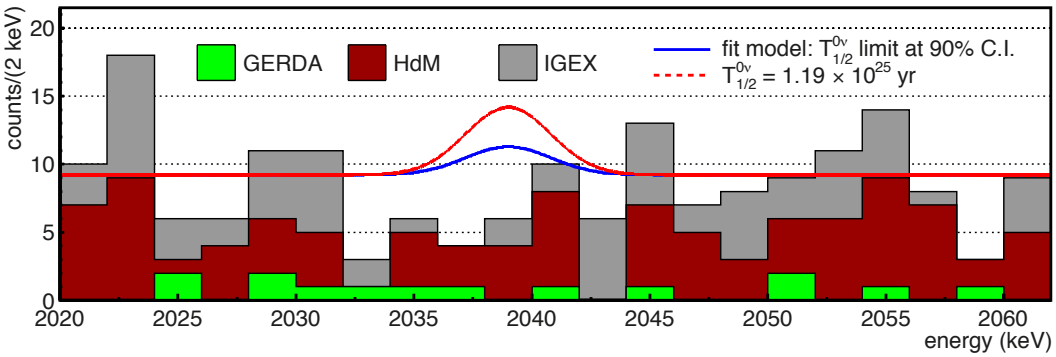

Figure 7.6: The energy spectrum of the combined ^{76}Ge data – GERDA Phase I (green) + HDM (red) + IGEX (gray) – after PSD selection, superimposed with the fit model (blue line): constant background plus Gaussian $0\nu\beta\beta$ signal with an intensity ν corresponding to the $T^{0\nu}_{1/2}$ limit derived from the Bayesian spectral fit, i.e. $T^{0\nu}_{1/2} > 2.86 \cdot 10^{25}\,\mathrm{yr}$ ($\nu < 9.30$) at 90% C.I. including the systematic uncertainty. The model that assumes the positive claim for observation of a $0\nu\beta\beta$ signal, i.e. a Gaussian signal with an intensity $\nu = 22.35$ corresponding to $T^{0\nu}_{1/2} = 1.19 \cdot 10^{25}\,\mathrm{yr}$ [17], is also shown (red dashed line), which is strongly disfavored ($K = 10^{-4}$) by combined ^{76}Ge data.

upper limit on ν is calculated given the $T^{0\nu}_{1/2}$ limit derived from the analysis and by using the relation between ν and $T^{0\nu}_{1/2}$ given in Eq. (6.2) with the parameter values of the combined ^{76}Ge data: a total exposure of $\mathcal{E} = 66.0\,\mathrm{kg{\cdot}yr}$; and an exposure-weighted average efficiency of $\epsilon = 0.73$ (with PSD). Note that, the spectral fit was performed by considering all data sets with their individual parameters and energy spectra in different intervals, and the combined parameters are only used for calculating ν limit and for plotting.

7.3.2 Bayes Factors for the Claim

For testing the claim of $0\nu\beta\beta$ signal observation, the binned spectral fit of the combined ^{76}Ge data is re-performed for the hypothesis $\bar{H}$ that assumes a $0\nu\beta\beta$ signal with $\nu = 22.35^{+5.36}_{-5.30}$, which corresponds to the claimed $T^{0\nu}_{1/2} = (1.19^{+0.37}_{-0.23}) \cdot 10^{25}\,\mathrm{yr}$ [17]. A Gaussian distribution with mean $0.84{\cdot}10^{-25}\,\mathrm{yr}^{-1}$ and standard deviation $0.20{\cdot}10^{-25}\,\mathrm{yr}^{-1}$ is taken as $P_0(1/T^{0\nu}_{1/2})$. As a result of the analysis, combined ^{76}Ge data strongly favor the background only hypothesis H; the Bayes factor is

$$K = P(\bar{H}|D)/P(H|D) = 10^{-4}\ . \tag{7.6}$$

The model that assumes the positive claim of a $0\nu\beta\beta$ signal with an intensity of $\nu = 22.35$ is shown on the same plot (red dashed line) in Fig. 7.6.

7.4 Frequentist analysis for GERDA Phase I and combined ^{76}Ge experiments

The analysis of GERDA Phase I data for deriving the $0\nu\beta\beta$ signal strength ν and the corresponding $T^{0\nu}_{1/2}$ value (or limit) was carried out by a profile likelihood fit as reported in [18, 24]. The method and the results of the analysis are briefly described here, using the same notation as in Section 6.2.

The energy spectra of GERDA Phase I data sets after PSD selection were fitted with a model accounting for the background and signal contributions in the 240 keV window, where the background is assumed to be a flat distribution (Fig. 4.24). The $0\nu\beta\beta$ signal contribution of each data set (i) is assumed as a Gaussian distribution with mean at $Q_{\beta\beta}$ and standard deviation σ_i at $Q_{\beta\beta}$ (according to the FWHM given in Table 7.2). The fit model has four free parameters: B of the three data sets for background contributions (related to λ_i as in Eq. (6.13)) and a common $1/T^{0\nu}_{1/2}$ for the $0\nu\beta\beta$ signal contributions (related to ν_i as in Eq. (6.14)). Assuming a Poisson fluctuation in the total number of observed events, N_i, around the mean value $\mu_i = \lambda_i + \nu_i$, the unbinned extended likelihood is defined as

$$L(\vec{B}, 1/T^{0\nu}_{1/2}) = \prod_i \frac{e^{-\mu_i}\mu^{N_i}}{N_i!} f_i(E|\vec{B}, 1/T^{0\nu}_{1/2})\ , \tag{7.7}$$

where the product runs over the three data sets and $f_i(E|\vec{B}, 1/T^{0\nu}_{1/2})$ is:

$$f_i(E|\vec{B}, 1/T^{0\nu}_{1/2}) = \frac{1}{\lambda_i + \nu_i} \prod_k \left(\frac{\lambda_i}{240} + \frac{\nu_i}{\sqrt{2\pi}\sigma_i} e^{\frac{(E_k - Q_{\beta\beta})^2}{2\sigma_i^2}} \right) , \tag{7.8}$$

where events are denoted with k. Having the nuisance parameters $\vec{B}$, the profile likelihood ratio, $\lambda(1/T^{0\nu}_{1/2})$, is used as the test statistics:

$$\lambda(1/T^{0\nu}_{1/2}) = \frac{\max\limits_{\vec{B}} L(\vec{B}, 1/T^{0\nu}_{1/2})}{\max\limits_{\hat{\vec{B}}, \hat{1/T^{0\nu}_{1/2}}} L(\hat{\vec{B}}, \hat{1/T^{0\nu}_{1/2}})} , \tag{7.9}$$

and is evaluated only for the physically allowed region; $\nu_i \geq 0$, implying $1/T^{0\nu}_{1/2} \geq 0$. The upper limit on the parameter $1/T^{0\nu}_{1/2}$ is obtained by defining $q = -2\ln\lambda(1/T^{0\nu}_{1/2})$ for $1/T^{0\nu}_{1/2} \geq 0$ ($q = 0$ otherwise). For 90% probability upper limit, the $1/T^{0\nu}_{1/2}$ value that corresponds to $q = 2.7$ is found (see Fig. 7.7). It was verified with MC that the method has sufficient coverage. The systematic uncertainty arising from the uncertainties on ϵ, σ (see Table 7.2) and energy scale (± 0.2 keV shift) are folded in with a MC approach, which takes correlations into account.

The best fit yields $1/T^{0\nu}_{1/2} = 0$, hence $\nu = 0$. The limit on $T^{0\nu}_{1/2}$ is [18]

$$T^{0\nu}_{1/2} > 2.1 \cdot 10^{25}\,\text{yr}\ (\nu < 3.5)\ \text{at}\ 90\%\,\text{C.L.}, \tag{7.10}$$

including the systematic uncertainty, which weakens the limit by about 1.5%.

The positive claim of a $0\nu\beta\beta$ signal with an intensity $\nu = 6.3 \pm 1.5$, which corresponds to $T^{0\nu}_{1/2} = (1.19^{+0.37}_{-0.23}) \cdot 10^{25}$ yr [17], was also tested with the Frequentist approach. The experimental spectra of the data sets were randomly generated from Poisson distributions with means given as the expected background and the expected signal strength according to the claimed $T^{0\nu}_{1/2}$. Each MC realization was analyzed using the profile likelihood fit described above. In the distribution of the best fit $1/T^{0\nu}_{1/2}$ values, only 1% of the results yields the GERDA Phase I result of $1/T^{0\nu}_{1/2} = 0$.

The spectral fit is extended to include the data from the HDM and IGEX experiments, as has been done in Section 7.3. Also for the combined ^{76}Ge data, the best fit yields $1/T^{0\nu}_{1/2} = 0$. The limit on $T^{0\nu}_{1/2}$ is [18]

$$T^{0\nu}_{1/2} > 3.0 \cdot 10^{25}\,\text{yr}\ (\nu < 8.9)\ \text{at}\ 90\%\,\text{C.L.}, \tag{7.11}$$

including the systematic uncertainty.

7.5 Limit on the effective Majorana neutrino mass

The range for the upper limit on effective Majorana neutrino mass is [18]:

$$\langle m_{\beta\beta} \rangle = (0.2 - 0.4)\,\text{eV} , \tag{7.12}$$

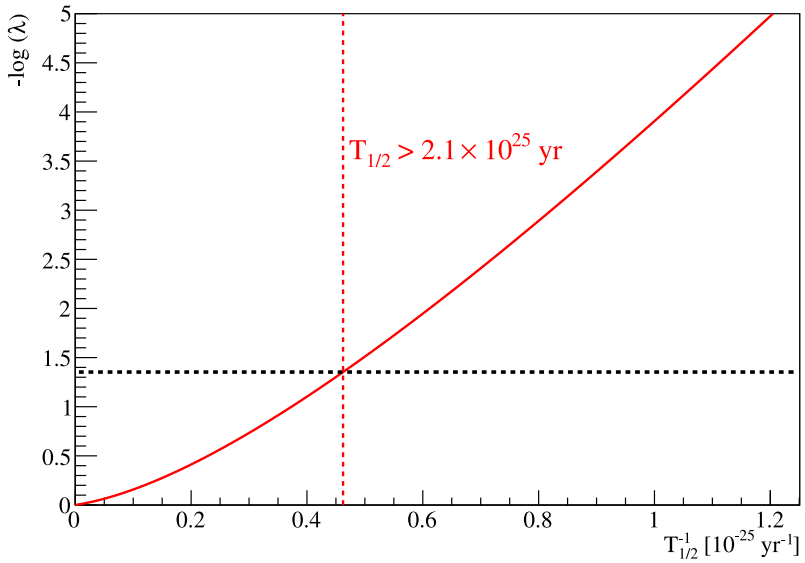

Figure 7.7: Profile likelihood distribution obtained from the analysis of GERDA Phase I data. The limit derived from the analysis is $T^{0\nu}_{1/2} > 2.1 \cdot 10^{25}$ yr at 90% C.L. [18, 24].

obtained using the $T^{0\nu}_{1/2}$ limit derived from combined ^{76}Ge data (Eq. (7.11)), $G_{0\nu}$ values of [29] and $M_{0\nu}$ calculations of [30, 72, 75, 76, 170–172]. Scaling due to different parameters g_A and r_A for $M_{0\nu}$ is obeyed as discussed in [173]. The achieved upper limit on $\langle m_{\beta\beta} \rangle$ is among the most stringent ones [14].

Conclusions and outlook

This dissertation presents the analysis of GERDA Phase I data, corresponding to a total exposure of 21.6 kg·yr, for the search of $0\nu\beta\beta$ decay of ^{76}Ge. The main focus of this work lies on the comprehensive background model that reproduces all the features of the measured energy spectrum. The analysis for background modeling was performed before the width of the initial $Q_{\beta\beta} \pm 20$ keV blinding window was reduced to $Q_{\beta\beta} \pm 5$ keV. The model predicts a flat energy distribution of background events in a 240 keV energy interval around $Q_{\beta\beta}$. The observed number of events in the $Q_{\beta\beta} \pm 5$ keV window after the unblinding, i.e. 7 before and 3 after PSD, are consistent with the expected number of background events given the flat background assumption, i.e. 5.2 before and 2.4 after PSD. A Bayesian analysis for setting a limit on the $0\nu\beta\beta$ decay rate was carried out on both data from GERDA alone and that in combination with data from the past HPGe $0\nu\beta\beta$ experiments HDM and IGEX. Bayes Factors for the claim of observation of a $0\nu\beta\beta$ decay signal, reported by a subgroup of the HDM collaboration, were calculated. Both GERDA Phase I and combined data strongly disfavor the claim. The background model, in addition to predicting the background in the $0\nu\beta\beta$ signal region, has also yielded many important results about background sources in the experimental setup and allowed for determining the $T^{2\nu}_{1/2}$ of ^{76}Ge. The results of the background and $0\nu\beta\beta$ signal studies are summarized in the following.

In the commissioning phase of GERDA, data taking was dedicated to the understanding of the background sources in the setup. The ^{228}Th specific activity in the heat exchanger was estimated to be $A < (33 \pm 6)$ mBq/kg using data from a particular run, during which the detector string was moved to a higher position in the setup, such that the detectors were surrounded by the heat exchanger located at the neck of the cryostat. The background contribution from the heat exchanger given the determined source activity is negligible in the nominal string position for Phase I. Also using commissioning data, the low energy region of the spectrum, dominated by the β spectrum of ^{39}Ar up to its Q-value of 565 keV, has been analyzed to determine the specific activity of ^{39}Ar. The analysis has yielded

$$A(^{39}\mathrm{Ar}) = (1.15 \pm 0.11)\,\mathrm{Bq/kg}\ ,$$

with the uncertainty dominated by the assumptions on the thickness of the dead layers on detector surfaces, particularly on the n^+ surface. The result is in good agreement with previous measurements.

The characterization of the background in Phase I was performed by determining the observed γ-ray lines and other prominent structures in the energy spectrum, and by taking into consideration the results of material screening measurements. Expected energy spectra from all the determined background sources in GERDA were obtained using the Monte Carlo simulation framework MAGE. A global fit of the measured energy spectrum with the simulated energy spectra was performed in the energy region between 570 keV (above ^{39}Ar spectrum) and 7500 keV. Different source locations were considered by repeating the analysis with a different set of components that takes into account the minor contributions as well.

According to the background model a total ^{226}Ra activity of $(3.0 \pm 0.9)\,\mu$Bq and a total initial ^{210}Po activity of (0.18 ± 0.01) mBq on the p^+ surfaces of the ^{enr}Ge-coax detectors are responsible for the observed high energy events induced by α decays in the sub-chains. The assumptions on the origin of these high energy ($E > 3.5$ MeV) events show consistency with the results from event rate analysis. Also, the model indicates a sizable contribution to the energy spectrum from ^{222}Rn decays in LAr close to the p^+ surfaces of the detectors.

The contribution from ^{42}K decays uniformly distributed in LAr to the background spectrum, as determined from the global model, corresponds to a ^{42}K (^{42}Ar) specific activity of

$$A(^{42}\mathrm{Ar}) = \left(106.2\,^{+12.7}_{-19.2}\right)\ \mu\mathrm{Bq/kg}.$$

The uncertainty is dominated by the assumption of a uniform ^{42}K distribution in LAr, which is not necessarily the case due to the drift of ^{42}K ions in the electric field dispersed in LAr. Previous measurements reported in literature provide only upper limits for the ^{42}Ar concentration in natural argon, which are in tension with the positive measurement of the ^{42}Ar concentration in the LAr of GERDA.

The half life of $2\nu\beta\beta$ decay of ^{76}Ge has been determined using the contribution from $2\nu\beta\beta$ decays to the measured energy spectrum as determined the global background model:

$$T^{2\nu}_{1/2}(^{76}\mathrm{Ge}) = \left(1.926^{+0.025}_{-0.022}\,\mathrm{stat}\ \pm 0.091\,\mathrm{syst}\right)\cdot 10^{21}\,\mathrm{yr} = (1.926 \pm 0.094)\cdot 10^{21}\,\mathrm{yr}.$$

The analyzed data corresponds to a total exposure of 17.9 kg·yr collected with the ^{enr}Ge-coax detectors. The major contribution to the systematic uncertainty arises from the uncertainties on the active volume and isotopic enrichment fractions of the detectors. The result is in good agreement with the one derived from the first 5 kg·yr exposure of the same data set and published by the GERDA collaboration. A significant reduction in the uncertainty due to the background model compared to the previous result has been achieved, thanks to better characterized and constrained background contributions with larger statistics and, as a result, more complete background model.

Another important outcome of the model is the decomposition of background in the energy region of interest around $Q_{\beta\beta}$. This enables the understanding of problematic background sources and initiates strategies for further mitigating the background in Phase II. According to the model, the background in the 10 keV window around $Q_{\beta\beta}$ is resulting from close-by decays of ^{214}Bi, ^{228}Th, ^{60}Co, ^{68}Ge (only for BEGes), ^{42}K and the α-emitting isotopes, i.e ^{210}Po and the isotopes in the ^{226}Ra sub-chain. Comparison of the models describing data with a minimum and a maximum number of model components shows that

the background contributions from contaminations at different source locations are model dependent. However, regardless of these assumptions on the source locations, the background spectrum is predicted to be a flat distribution in a 240 keV wide energy interval around $Q_{\beta\beta}$. The background index at $Q_{\beta\beta}$ is determined from observed events in this energy interval excluding the 10 keV wide blinding window:

$$B = (24 \pm 2) \cdot 10^{-3}\,\mathrm{cts}/(\mathrm{keV} \cdot \mathrm{kg} \cdot \mathrm{yr}) \text{ without PSD and}$$
$$B = (11^{+2}_{-1}) \cdot 10^{-3}\,\mathrm{cts}/(\mathrm{keV} \cdot \mathrm{kg} \cdot \mathrm{yr}) \text{ with PSD,}$$

which is in excellent agreement with results from the background model. The background index in GERDA Phase I is an order of magnitude lower compared to the previous HPGe experiments.

After all data selection cuts were frozen and the background model was determined, the blinding window was opened to analyze the energy spectrum including the events in the $0\nu\beta\beta$ signal region. No indication for a $0\nu\beta\beta$ signal has been found. A lower limit on $T^{0\nu}_{1/2}$ was derived using a Bayesian approach, as a consistent repetition of the published analysis which had contributions from this work. Two different methods for defining the likelihood were investigated: the counting method, by only considering the number of expected and observed events; and a binned spectral fit, by taking into account the spectral shapes of the background (flat) and signal (Gaussian) contributions. The effect of different choices of the analysis window width (optimized or not) and data selections cuts (with or without PSD) on the derived limits has also been investigated. Given the determined analysis parameters, the limit setting sensitivity, i.e. the median sensitivity for the 90% probability $T^{0\nu}_{1/2}$ lower limit, was evaluated for the different analysis options and for different ways of grouping data. The best sensitivity, i.e. $2.04 \cdot 10^{25}$ yr at 90% C.I., has been obtained from the spectral fit, using PSD selection cuts and analyzing all data grouped into subsets with similar characteristics (e.g. energy resolutions and background levels) but treated separately in the analysis. The Bayesian spectral fit of the measured energy spectrum yields:

$$T^{0\nu}_{1/2} > 1.85 \cdot 10^{25}\,\mathrm{yr} \text{ at } 90\%\,\mathrm{C.I.},$$

if data from GERDA Phase I is considered. The limit improves as

$$T^{0\nu}_{1/2} > 2.86 \cdot 10^{25}\,\mathrm{yr} \text{ at } 90\%\,\mathrm{C.I.}$$

when GERDA Phase I data in combination with data from the HPGe experiments HDM and IGEX are analyzed.

The longstanding claim for observation of a $0\nu\beta\beta$ signal reported by a subgroup of HDM collaboration has been strongly disfavored by data from both GERDA alone (D) and combined HPGe experiments (D_c); the Bayes factors for the claimed $0\nu\beta\beta$ signal rate (hypothesis $\bar{H}$) over the background only hypothesis (H) are

$$P(\bar{H}|D)/P(H|D) = 0.02 \qquad \text{and} \qquad P(\bar{H}|D_c)/P(H|D_c) = 10^{-4}\ .$$

In another work, similar $T^{0\nu}_{1/2}$ lower limits were derived using a Frequentist approach. An extended unbinned profile likelihood analysis has provided $T^{0\nu}_{1/2} > 2.1 \cdot 10^{25}$ yr at 90% C.L. using GERDA data, and $T^{0\nu}_{1/2} > 3.0 \cdot 10^{25}$ yr at 90% C.L. using data from combined HPGe experiments.

We note that by construction, frequentist intervals are not statements about probable values of the parameter, and therefore cannot be directly compared to a Bayesian credible interval. Since the goal of this analysis was to draw a conclusion on probable values of $T^{0\nu}_{1/2}$, we have focused on the Bayesian approach.

The lower limit on $T^{0\nu}_{1/2}$ determined in GERDA Phase I corresponds to one of the most stringent $\langle m_{\beta\beta} \rangle$ upper limits. Different nuclear matrix element calculations yield different upper limits for $\langle m_{\beta\beta} \rangle$ when translating the $T^{0\nu}_{1/2}$ limit to this quantity. These upper limit values on $\langle m_{\beta\beta} \rangle$ are in the range:

$$\langle m_{\beta\beta} \rangle = (0.2 - 0.4)\,\text{eV}.$$

The GERDA experiment is currently upgrading the setup for Phase II data taking. In Phase II, the source (and detector) mass is planned to be increased by employing additional ($\sim$ 20 kg) new custom-made BEGe detectors, which exhibit enhanced PSD capabilities for discriminating background- from signal-like events. Further background suppression is planned to be achieved through the detection of coincident scintillation light in the LAr. The goal is to improve the $T^{0\nu}_{1/2}$ sensitivity by an order of magnitude by achieving $B < 10^{-3}$ cts/(keV·kg·yr) and acquiring an exposure of 100 kg·yr ($\sim$ 3 years of data taking), which will allow for further exploration of the $0\nu\beta\beta$ decay process.

Appendix A

Background sources

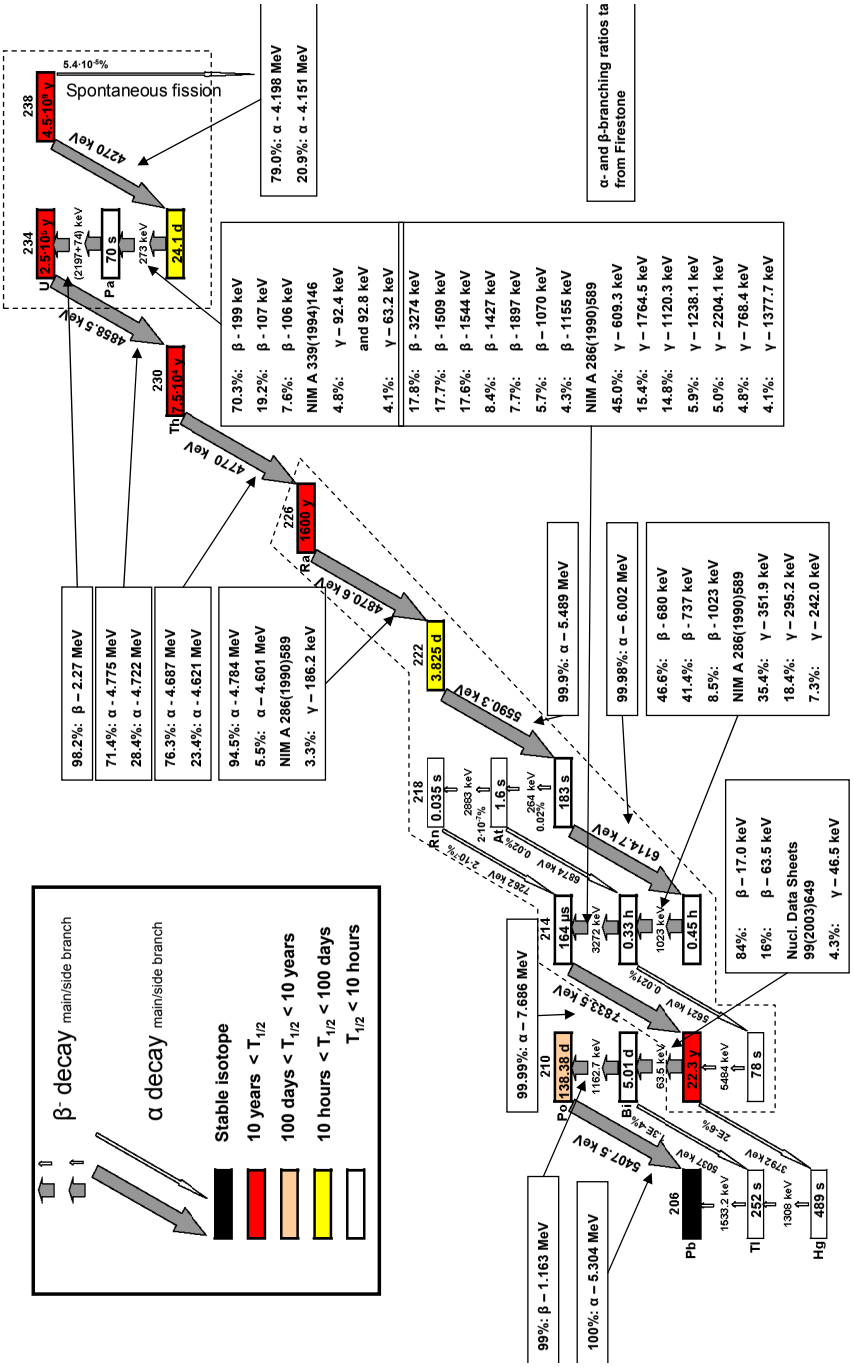

Figure A.1: ^{238}U decay chain [174].

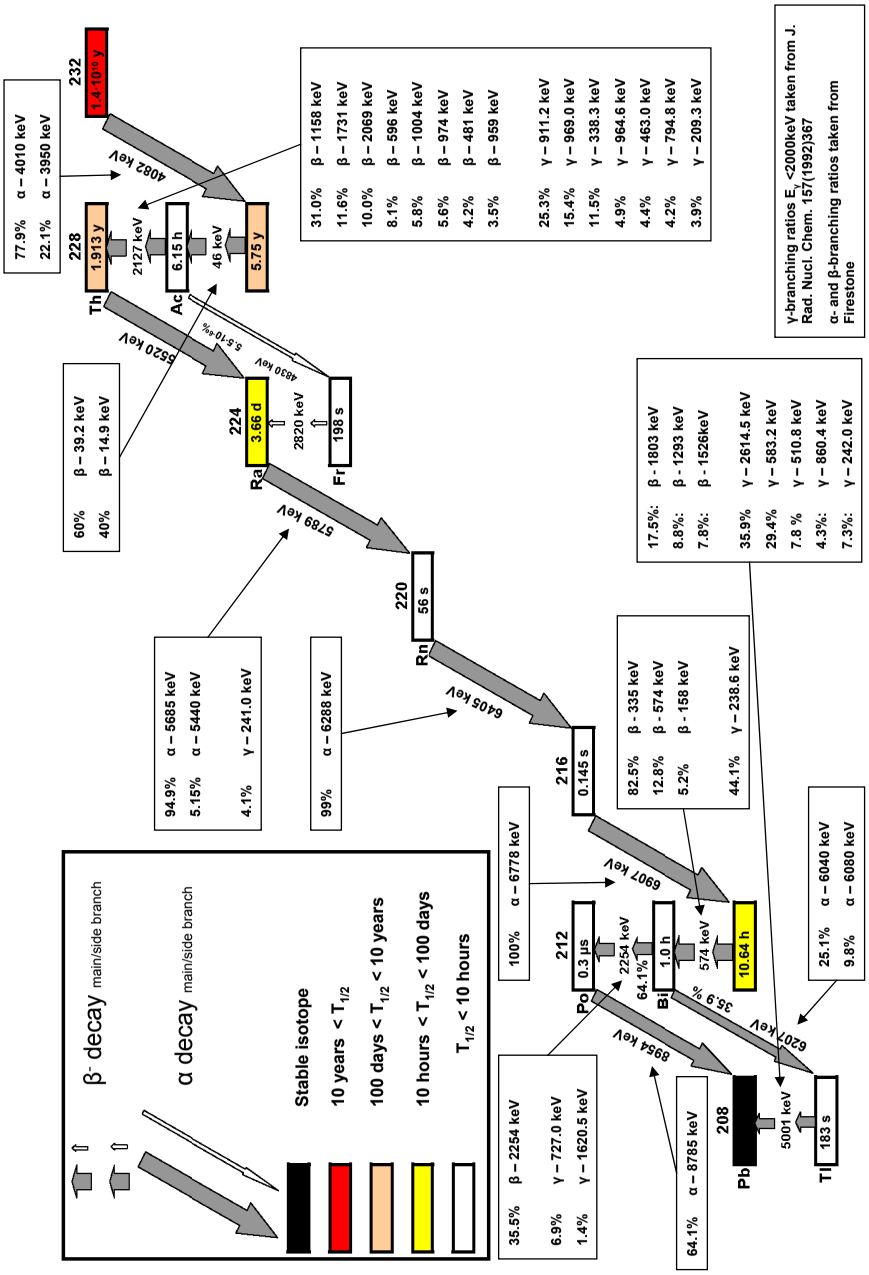

Figure A.2: ^{232}Th decay chain [174].

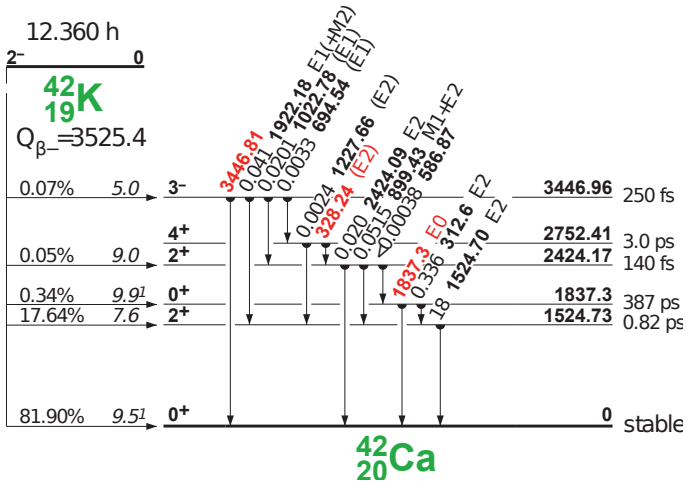

Figure A.3: ^{42}K decay scheme [144].

Bibliography

[1] P. A. M. Dirac, *The Quantum theory of electron*, Proc.Roy.Soc.Lond. **A117** (1928) 610–624.

[2] E. Majorana, *A symmetric theory of electrons and positrons*, Nuovo Cimento **14** (1937) 171–184.

[3] Particle Data Group, J. Beringer et al., *Review of Particle Physics (RPP)*, Phys.Rev. **D86** (2012) 010001.

[4] Planck Collaboration, P. Ade et al., *Planck 2013 results. XVI. Cosmological parameters*, 2013, `arXiv:1303.5076`.

[5] M. Gell-Mann, P. Ramond, and R. Slansky, *Complex Spinors and Unified Theories*, Conf.Proc. **C790927** (1979) 315–321.

[6] T. Yanagida, *Horizontal symmetry and masses of neutrinos*, Conf.Proc. **C7902131** (1979) 95–99.

[7] M. Fukugita and T. Yanagida, *Baryogenesis Without Grand Unification*, Phys.Lett. **B174** (1986) 45.

[8] P. Di Bari, *An introduction to leptogenesis and neutrino properties*, Contemp.Phys. **53** (2012) 315–338.

[9] B. R. Holstein, *The mysterious disappearance of Ettore Majorana*, Journal of Physics: Conference Series **173** (2009) 012019.

[10] S. Elliott and M. Franz, *Colloquium: Majorana Fermions in nuclear, particle and solid-state physics*, 2014, `arXiv:1403.4976`.

[11] J. Schechter and J. Valle, *Neutrinoless Double beta Decay in SU(2) x U(1) Theories*, Phys.Rev. **D25** (1982) 2951.

[12] A. Giuliani and A. Poves, *Neutrinoless double-beta decay*, Advances in High Energy Physics **2012** (2012).

[13] J. Gomez-Cadenas, J. Martin-Albo, M. Mezzetto, F. Monrabal, and M. Sorel, *The Search for neutrinoless double beta decay*, Riv.Nuovo Cim. **35** (2012) 29–98.

[14] A. Barabash, *Review of double beta decay experiments*, 2014, arXiv:1403.2870.

[15] L. Pandola, *Status of double beta decay experiments using isotopes other than Xe-136*, 2014, arXiv:1403.3329.

[16] EXO Collaboration, D. Tosi, *The search for neutrino-less double-beta decay: summary of current experiments*, 2014, arXiv:1402.1170.

[17] H. Klapdor-Kleingrothaus, I. Krivosheina, A. Dietz, and O. Chkvorets, *Search for neutrinoless double beta decay with enriched Ge-76 in Gran Sasso 1990-2003*, Phys.Lett. **B586** (2004) 198–212.

[18] GERDA Collaboration, M. Agostini et al., *Results on Neutrinoless Double-β Decay of ^{76}Ge from Phase I of the GERDA Experiment*, Phys.Rev.Lett. **111** (2013) 122503.

[19] GERDA Collaboration, K. Ackermann et al., *The GERDA experiment for the search of $0\nu\beta\beta$ decay in ^{76}Ge*, Eur.Phys.J. **C73** (2013) 2330.

[20] M. Agostini, *Signal and background studies for the search of neutrinoless double beta decay in GERDA*, Dissertation, Technische Universität München, Lehrstuhl E15 für Experimentalphysik und Astroteilchenphysik, Germany (2013), http://www.mpi-hd.mpg.de/gerda/public/2013/phd2013_matteoAgostini.pdf.

[21] S. Hemmer, *Study of Lepton Number Conserving and Non-Conserving Processes Using GERDA Phase I data*, PhD thesis, Dipartimento di Fisica e Astronomia, Universita di Padova, Padova, Italy (2014).

[22] GERDA Collaboration, M. Agostini et al., *The background in the $0\nu\beta\beta$ experiment GERDA*, Eur.Phys.J. **C74** (2014) 2764.

[23] GERDA Collaboration, M. Agostini et al., *Measurement of the half-life of the two-neutrino double beta decay of Ge-76 with the Gerda experiment*, J.Phys. **G40** (2013) 035110.

[24] B. Schwingenheuer, *Limit on neutrinoless double beta decay of ^{76}Ge by the GERDA experiment*, Physics Procedia. Proceedings of the TAUP 2013 Conference.

[25] M. Goeppert-Mayer, *Double beta-disintegration*, Phys.Rev. **48** (1935) 512–516.

[26] R. B. Firestone, V. S. Shirley, C. M. Baglin, S. F. Chu, and J. Zipkin, *Table of Isotopes*. Wiley & Sons, New York, 8th edition (1996).

[27] A. Barabash, *Double Beta Decay: Historical Review of 75 Years of Research*, Phys.Atom.Nucl. **74** (2011) 603–613.

[28] A. Barabash, *Precise half-life values for two neutrino double beta decay*, Phys.Rev. **C81** (2010) 035501.

[29] J. Kotila and F. Iachello, *Phase space factors for double-β decay*, Phys.Rev. **C85** (2012) 034316.

[30] J. Barea, J. Kotila, and F. Iachello, *Nuclear matrix elements for double-β decay*, Phys.Rev. **C87** (2013) 014315.

[31] G. Racah, *On the symmetry of particle and antiparticle*, Nuovo Cim. **14** (1937) 322–328.

[32] W. Furry, *On transition probabilities in double beta-disintegration*, Phys.Rev. **56** (1939) 1184–1193.

[33] I. Avignone, Frank T., S. R. Elliott, and J. Engel, *Double Beta Decay, Majorana Neutrinos, and Neutrino Mass*, Rev.Mod.Phys. **80** (2008) 481–516.

[34] W. Rodejohann, *Neutrinoless double beta decay and neutrino physics*, J.Phys. **G39** (2012) 124008.

[35] Particle Data Group, C. Amsler et al., *Review of Particle Physics*, Phys.Lett. **B667** (2008) 1–1340.

[36] Z. Maki, M. Nakagawa, and S. Sakata, *Remarks on the unified model of elementary particles*, Prog.Theor.Phys. **28** (1962) 870–880.

[37] B. Pontecorvo, *Neutrino Experiments and the Problem of Conservation of Leptonic Charge*, Sov.Phys.JETP **26** (1968) 984–988.

[38] S. M. Bilenky and S. Petcov, *Massive Neutrinos and Neutrino Oscillations*, Rev.Mod.Phys. **59** (1987) 671.

[39] M. Doi, T. Kotani, H. Nishiura, K. Okuda, and E. Takasugi, *CP Violation in Majorana Neutrinos*, Phys.Lett. **B102** (1981) 323.

[40] L. Wolfenstein, *Neutrino Oscillations in Matter*, Phys.Rev. **D17** (1978) 2369–2374.

[41] S. Mikheev and A. Y. Smirnov, *Resonance Amplification of Oscillations in Matter and Spectroscopy of Solar Neutrinos*, Sov.J.Nucl.Phys. **42** (1985) 913–917.

[42] G. Fogli, E. Lisi, A. Marrone, A. Palazzo, and A. Rotunno, *Hints of $\theta_{13} > 0$ from global neutrino data analysis*, Phys.Rev.Lett. **101** (2008) 141801.

[43] F. Capozzi, G. Fogli, E. Lisi, A. Marrone, D. Montanino, et al., *Status of three-neutrino oscillation parameters, circa 2013*, Phys.Rev. **D89** (2014) 093018.

[44] Daya Bay Collaboration, F. An et al., *Spectral measurement of electron antineutrino oscillation amplitude and frequency at Daya Bay*, Phys.Rev.Lett. **112** (2014) 061801.

[45] Reno Collaboration, H. Seo, *Recent Results from RENO*, talk at WIN 2013, XXIV International Workshops on Weak Interactions and Neutrinos (Natal, Brazil, 2013), `http://hep.if.usp.br/WIN13/`.

[46] T2K Collaboration, K. Abe et al., *Observation of Electron Neutrino Appearance in a Muon Neutrino Beam*, Phys.Rev.Lett. **112** (2014) 061802.

[47] MINOS Collaboration, P. Adamson et al., *Electron neutrino and antineutrino appearance in the full MINOS data sample*, Phys.Rev.Lett. **110** (2013) 171801.

[48] Reno Collaboration, E. Lisi, *Present status of neutrino parameters and near future prospects*, 26th Rencontres de Blois, France 2014.

[49] Y.-F. Li, *Overview of the Jiangmen Underground Neutrino Observatory (JUNO)*, Int.J.Mod.Phys.Conf.Ser. **31** (2014) 1460300.

[50] IceCube Collaboration, PINGU Collaboration, M. Aartsen et al., *PINGU Sensitivity to the Neutrino Mass Hierarchy*, 2013, `arXiv:1306.5846`.

[51] J. Bian, *The NOvA experiment: overview and status*, 2013, `arXiv:1309.7898`.

[52] C. Kraus, B. Bornschein, L. Bornschein, J. Bonn, B. Flatt, et al., *Final results from phase II of the Mainz neutrino mass search in tritium beta decay*, Eur.Phys.J. **C40** (2005) 447–468.

[53] Troitsk Collaboration, V. Aseev et al., *An upper limit on electron antineutrino mass from Troitsk experiment*, Phys.Rev. **D84** (2011) 112003.

[54] KATRIN Collaboration, R. H. Robertson, *KATRIN: an experiment to determine the neutrino mass from the beta decay of tritium*, 2013, `arXiv:1307.5486`.

[55] A. Nucciotti, *The MARE project*, J. of Low Temp.Phys. **151** (2008) 597–602.

[56] P.-O. Ranitzsch, J.-P. Porst, S. Kempf, C. Pies, S. Schäfer, D. Hengstler, A. Fleischmann, C. Enss, and L. Gastaldo, *Development of metallic magnetic calorimeters for high precision measurements of calorimetric ^{187}Re and ^{163}Ho spectra*, J. of Low Temp.Phys. **167** (2012) 1004–1014.

[57] G. Drexlin, V. Hannen, S. Mertens, and C. Weinheimer, *Current direct neutrino mass experiments*, Adv.High Energy Phys. **2013** (2013) 293986.

[58] S. Hannestad, *Neutrino physics from Cosmology*, Symposium in honour of Bruno Pontecorvo, 2013, `arXiv:1311.0623`.

[59] EUCLID Collaboration, R. Laureijs et al., *Euclid Definition Study Report*, 2011, `arXiv:1110.3193`.

[60] T. Basse, O. E. Bjaelde, J. Hamann, S. Hannestad, and Y. Y. Wong, *Dark energy properties from large future galaxy surveys*, JCAP **1405** (2014) 021.

[61] D. Forero, M. Tortola, and J. Valle, *Global status of neutrino oscillation parameters after Neutrino-2012*, Phys.Rev. **D86** (2012) 073012.

[62] KamLAND-Zen Collaboration, A. Gando et al., *Limit on Neutrinoless $\beta\beta$ Decay of Xe-136 from the First Phase of KamLAND-Zen and Comparison with the Positive Claim in Ge-76*, Phys.Rev.Lett. **110** (2013) 062502.

[63] A. Caldwell, *Example Analysis & Opening the Blinded Window(s)*, GERDA Scientific Technical Reports: GSTR-12-500v1 (2012).

[64] NEMO-3 Collaboration, R. Arnold et al., *Search for Neutrinoless Double-Beta Decay of ^{100}Mo with the NEMO-3 Detector*, Phys.Rev. **D89** (2014) 111101.

[65] E. Andreotti, C. Arnaboldi, F. Avignone, M. Balata, I. Bandac, et al., *^{130}Te neutrinoless double-beta decay with CUORICINO*, Astropart.Phys. **34** (2011) 822–831.

[66] Majorana Collaboration, N. Abgrall et al., *The MAJORANA DEMONSTRATOR Neutrinoless Double-Beta Decay Experiment*, Adv.High Energy Phys. **2014** (2014) 365432.

[67] K. Inoue, *Results from KamLAND-Zen*, Nucl.Phys.B - Proc. Suppl. **235-236** (2013) 249 –254. The XXV International Conference on Neutrino Physics and Astrophysics.

[68] G. Gratta and D. Sinclair, *Present Status and Future Perspectives for the EXO-200 Experiment*, Adv.High Energy Phys. **2013** (2013) 545431.

[69] SuperNEMO Collaboration, A. Barabash, *SuperNEMO double beta decay experiment*, J.Phys.Conf.Ser. **375** (2012) 042012.

[70] CUORE Collaboration, D. Artusa et al., *Searching for neutrinoless double-beta decay of ^{130}Te with CUORE*, 2014, `arXiv:1402.6072`.

[71] J. Suhonen and O. Civitarese, *Review of the properties of the $0\nu\beta^-\beta^-$ nuclear matrix elements*, J.Phys. **G39** (2012) 124005.

[72] F. Šimkovic, V. Rodin, A. Faessler, and P. Vogel, *$0\nu\beta\beta$ and $2\nu\beta\beta$ nuclear matrix elements, quasiparticle random-phase approximation, and isospin symmetry restoration*, Phys.Rev. **C87** (2013) 045501.

[73] J. Barea and F. Iachello, *Neutrinoless double-beta decay in the microscopic interacting boson model*, Phys.Rev. **C79** (2009) 044301.

[74] P. Rath, R. Chandra, K. Chaturvedi, P. Lohani, P. Raina, et al., *Neutrinoless $\beta\beta$ decay transition matrix elements within mechanisms involving light Majorana neutrinos, classical Majorons and sterile neutrinos*, Phys.Rev. **C88** (2013) 064322, `arXiv:1308.0460`.

[75] T. R. Rodriguez and G. Martinez-Pinedo, *Energy density functional study of nuclear matrix elements for neutrinoless $\beta\beta$ decay*, Phys.Rev.Lett. **105** (2010) 252503.

[76] J. Menendez, A. Poves, E. Caurier, and F. Nowacki, *Disassembling the Nuclear Matrix Elements of the Neutrinoless beta beta Decay*, Nucl.Phys. **A818** (2009) 139–151.

[77] H. Klapdor-Kleingrothaus, A. Dietz, L. Baudis, G. Heusser, I. Krivosheina, et al., *Latest results from the Heidelberg-Moscow double beta decay experiment*, Eur.Phys.J. **A12** (2001) 147–154.

[78] IGEX Collaboration, C. Aalseth et al., *The IGEX Ge-76 neutrinoless double beta decay experiment: Prospects for next generation experiments*, Phys.Rev. **D65** (2002) 092007.

[79] F. Feruglio, A. Strumia, and F. Vissani, *Neutrino oscillations and signals in β and $0\nu\beta\beta$ experiments*, Nucl.Phys. **B637** (2002) 345–377.

[80] O. Chkvorets, *Search for double beta decay with HPGe detectors at the Gran Sasso Underground Laboratory*, Dissertation, Combined Faculty for Natural Sciences and for Mathematics of the Ruperto-Carola University of Heidelberg, Germany (2008), `http://www.mpi-hd.mpg.de/gerda/public/2008/phd2008_chkvorets.pdf`, `arXiv:0812.1206`.

[81] B. Schwingenheuer, *Status and prospects of searches for neutrinoless double beta decay*, Annalen Phys. **525** (2013) 269–280.

[82] A. Gando, Y. Gando, K. Ichimura, H. Ikeda, K. Inoue, et al., *A study of extraterrestrial antineutrino sources with the KamLAND detector*, Astrophys.J. **745** (2012) 193.

[83] R. Brodzinski, H. Miley, J. Reeves, and I. Avignone, Frank T., *Further reduction of radioactive backgrounds in ultrasensitive germanium spectrometers*, Nucl.Instrum.Meth. **A292** (1990) 337–342.

[84] I. Avignone, Frank T., J. Collar, R. Brodzinski, H. Miley, J. Reeves, et al., *Theoretical and experimental investigation of cosmogenic radioisotope production in germanium*, Nucl.Phys.Proc.Suppl. **28A** (1992) 280–285.

[85] A. Peurrung, T. Bowyer, R. Craig, and P. Reeder, *Expected atmospheric concentration of ^{42}Ar*, Nucl.Instrum.Meth. **A396** (1997) 425–426.

[86] P. Cennini, S. Cittolin, J. Revol, C. Rubbia, W. Tian, et al., *A Neural network approach for the TPC signal processing*, Nucl.Instrum.Meth. **A356** (1995) 507–513.

[87] V. Ashitkov, A. Barabash, S. Belogurov, G. Carugno, S. Konovalov, et al., *A liquid-argon ionization detector for the study of double beta decay*, Instrum.Exp.Tech. **46** (2003) 153–160.

[88] A. Barabash, *Liquid Xe(Ar) low-background detectors, Russian activities*, Proc. Int. Workshop on Tech. and App. of Xe Detectors (2001) 101–114.

[89] G. F. Knoll, *Radiation detection and measurement*, vol. 3. Wiley, New York, 1999.

[90] O. Volynets, *Methods to improve and understand the sensitivity of high purity germanium detectors for searches of rare events*, Dissertation, Technische Universität München, Max-Planck-Institut für Physik, Germany (2012), `http://www.mpi-hd.mpg.de/gerda/public/2012/phd2012_olexandrVolynets.pdf`.

[91] F. Goulding et al. IEEE Trans. Nucl. Sci. **NS-31** (1984) 285.

[92] J. Roth et al. IEEE Trans. Nucl. Sci. **NS-31** (1984) 367.

[93] D. Gonzalez, J. Morales, S. Cebrian, E. Garcia, I. Irastorza, et al., *Pulse shape discrimination in the IGEX experiment*, Nucl.Instrum.Meth. **A515** (2003) 634–643.

[94] F. Petry, A. Piepke, H. Strecker, H. Klapdor-Kleingrothaus, A. Balysh, et al., *Background recognition in Ge detectors by pulse shape analysis*, Nucl.Instrum.Meth. **A332** (1993) 107–112.

[95] B. Majorovits and H. Klapdor-Kleingrothaus, *Digital pulse shape analysis by neural networks for the Heidelberg-Moscow Double Beta-Decay experiment*, Eur.Phys.J. **A6** (1999) 463–469.

[96] J. Hellmig and H. Klapdor-Kleingrothaus, *Identification of single-site events in germanium detectors by digital pulse shape analysis*, Nucl.Instrum.Meth. **A455** (2000) 638–644.

[97] GERDA Collaboration, M. Agostini et al., *Pulse shape discrimination for GERDA Phase I data*, Eur.Phys.J. **C73** (2013) 2583.

[98] M. Agostini, C. Ur, D. Budjas, E. Bellotti, R. Brugnera, et al., *Signal modeling of high-purity Ge detectors with a small read-out electrode and application to neutrinoless double beta decay search in Ge-76*, JINST **6** (2011) P03005.

[99] D. Budjas, M. Barnabe Heider, O. Chkvorets, N. Khanbekov, and S. Schonert, *Pulse shape discrimination studies with a Broad-Energy Germanium detector for signal identification and background suppression in the GERDA double beta decay experiment*, JINST **4** (2009) P10007.

[100] G. Heusser, *Low-radioactivity background techniques*, Ann.Rev.Nucl.Part.Sci. **45** (1995) 543–590.

[101] Broad Energy Germanium Detectors (BEGe) (URL, last access 27.6.2014), `http://www.canberra.com/products/485.asp`.

[102] D. Budjas, L. Pandola, P. Zavarise, *Rejection efficiency of muon-induced events in the commissiong GERDA array*, GERDA Scientific Technical Reports: GSTR-11-002 (2011).

[103] L. Pandola, P. Zavarise, *Estimate of the muon-induced background in the GERDA commissioning runs*, GERDA Scientific Technical Reports: GSTR-11-007 (2011).

[104] High Activity Disposal Experimental Site (HADES) of the Belgian Nuclear Research Center SCK·CEN, Boeretang 200, BE-2400 Mol, Belgium.

[105] M. B. Heider, *Performance and stability tests of bare high purity germanium detectors in liquid argon for the GERDA experiment*, Dissertation, Combined Faculty for Natural Sciences and for Mathematics of the Ruperto-Carola University of Heidelberg, Germany (2009), `http://www.mpi-hd.mpg.de/gerda/public/2009/phd2009_MarikHeider.pdf`.

[106] GERDA Collaboration, I. Abt et al., *The GERmanium Detector Array for the search of neutrinoless $\beta\beta$ decays of ^{76}Ge at LNGS*, Proposal to the LNGS **P38/04** (2004).

[107] I. Barabanov, S. Belogurov, L. B. Bezrukov, A. Denisov, V. Kornoukhov, et al., *Cosmogenic activation of germanium and its reduction for low background experiments*, Nucl.Instrum.Meth. **B251** (2006) 115–120.

[108] D. Lenz, *Pulse Shapes and Surface Effects in Segmented Germanium Detectors*, Dissertation, Technische Universität München, Max-Planck-Institut für Physik Germany, (2010), `http://www.mpi-hd.mpg.de/gerda/public/2010/phd2010_DanielLenz.pdf`.

[109] I. Barabanov, L. Bezrukov, E. Demidova, V. Gurentsov, S. Kianovsky, et al., *Shielding of the GERDA experiment against external gamma background*, Nucl.Instrum.Meth. **A606** (2009) 790–794.

[110] G. Zuzel and H. Simgen, *High sensitivity radon emanation measurements*, Appl. Rad. Isot. **67** (2009) 889 – 893. 5th International Conference on Radionuclide Metrology - Low-Level Radioactivity Measurement Techniques ICRM-LLRMT'08.

[111] L. Pandola, *Estimate of allowable ^{222}Rn emanation rate from the cryostat*, GERDA Scientific Technical Reports: GSTR-07-020 (2007).

[112] L. Pandola, K. T. Knöpfle, S. Schönert and B. Schwingenheuer, *Background from radon emanation of the GERDA cryostat*, GERDA Scientific Technical Reports: GSTR-09-001 (2009).

[113] M. Gunther, J. Hellmig, G. Heusser, M. Hirsch, H. Klapdor-Kleingrothaus, et al., *Heidelberg - Moscow beta-beta experiment with Ge-76: Full setup with five detectors*, Phys.Rev. **D55** (1997) 54–67.

[114] A. Morales, *Review on double beta decay experiments and comparison with theory*, Nucl.Phys.Proc.Suppl. **77** (1999) 335–345.

[115] H. Klapdor-Kleingrothaus, L. Baudis, A. Dietz, G. Heusser, B. Majorovits, et al., *GENIUS-TF: A Test facility for the GENIUS project*, Nucl.Instrum.Meth. **A481** (2002) 149–159.

[116] M. B. Heider, C. Cattadori, O. Chkvorets, A. Di Vacri, K. Gusev, et al., *Performance of bare high-purity germanium detectors in liquid argon for the GERDA experiment*, arXiv:0812.1907.

[117] MIZZI Computer Software GmbH (URL, last access 27.6.2014), http://www.mizzi-computer.de.

[118] R. Isocrate, M. Bellato, M. Bettini, R. Venturelli, C. Ur, and D. Bazzacco, *MD2S - Digital sampling electronics for the MARS detector*, Laboratori Nazionali di Legnaro, Annual Report (2004). http://www.lnl.infn.it/~annrep/read_ar/2004/contrib_2004/pdfs/FAA127T.pdf.

[119] C. Ur, C. R. Alvarez, C. Rusu, D. Bazzacco, M. Bellato, E. Farnea, and R. Isocrate, *A data acquisition system for the MD2S digital sampling electronics*, Laboratori Nazionali di Legnaro, Annual Report (2004). http://www.lnl.infn.it/~annrep/read_ar/2004/contrib_2004/pdfs/FAA128.pdf.

[120] M. Agostini, L. Pandola, P. Zavarise, and O. Volynets, *GELATIO: A General framework for modular digital analysis of high-purity Ge detector signals*, JINST **6** (2011) P08013.

[121] M. Agostini, L. Pandola, and P. Zavarise, *Off-line data processing and analysis for the GERDA experiment*, J.Phys.Conf.Ser. **368** (2012) 012047.

[122] S. W. Smith, *The scientist and engineer's guide to digital signal processing*. California Technical Publishing, San Diego, 1999.

[123] H. L. V. Trees, *Detection, Estimation, and Modulation Theory*. New York: John Wiley and Sons, 1968.

[124] P. Zavarise, M. Agostini, A. Machado, L. Pandola, and O. Volynets, *Off-line data quality monitoring for the GERDA experiment*, J.Phys.Conf.Ser. **375** (2012) 042028.

[125] P. Zavarise, *Analysis of the first data of the GERDA experiment at LNGS*, PhD thesis (2013), http://www.mpi-hd.mpg.de/gerda/public/2013/phd2013_paoloZavarise.pdf.

[126] I. MacKenzie and J. Campbell, *On the use of the single escape peak in Ge(Li) spectroscopy*, Nuclear Instruments and Methods **101** (1972) 149 – 152.

[127] C. O'Shaughnessy, E. Andreotti, D. Budjas, A. Caldwell, A. Gangapshev, et al., *High voltage capacitors for low background experiments*, Eur.Phys.J. **C73** (2013) 2445.

[128] L. Pandola, *Parameters and facts for the analysis dataset of the $0\nu\beta\beta$ decay of GERDA Phase I*, GERDA Scientific Technical Reports: GSTR-13-012 (2013).

[129] GERDA Collaboration, *Status report from the commissioning of GERDA*, GERDA Scientific Technical Reports: GSTR-10-004 (2010).

[130] N. Becerici-Schmidt, B. Majorovits, *Estimation of an upper limit on the Thorium activity in the Heat Exchanger*, GERDA Scientific Technical Reports: GSTR-12-008 (2012).

[131] R. Brugnera, A. Garfagnini, S. Hemmer , *Analysis of ^{60}Co decays in the heat exchanger*, GERDA Scientific Technical Reports: GSTR-12-005 (2012).

[132] A. Kirsch, *Simulation of ^{60}Co and ^{208}Tl decays in the Heat Exchanger*, GERDA Scientific Technical Reports: GSTR-12-006 (2012).

[133] WARP Collaboration, P. Benetti et al., *Measurement of the specific activity of AR-39 in natural argon*, Nucl.Instrum.Meth. **A574** (2007) 83–88.

[134] H. H. Loosli, *A dating method with ^{39}Ar*, Earth and Planetary Science Letters **63** (1983) 51–62.

[135] M. Boswell, Y.-D. Chan, J. A. Detwiler, P. Finnerty, R. Henning, et al., *MaGe-a Geant4-based Monte Carlo Application Framework for Low-background Germanium Experiments*, IEEE Trans.Nucl.Sci. **58** (2011) 1212–1220.

[136] LBNL Isotopes Project Nuclear Data Dissemination Home Page (URL, last access 27.6.2014), `http://ie.lbl.gov/toi.html`.

[137] N. Becerici-Schmidt, A. Caldwell, B. Majorovits, L. Pandola, *Analysis of the ^{226}Ra background in GERDA Phase-I*, GERDA Scientific Technical Reports: GSTR-12-012 (2012).

[138] M. Agostini, N. Becerici-Schmidt, L. Pandola and S. Schönert, *Decomposition of the GERDA Phase-I background at $Q_{\beta\beta}$ through pulse shape analysis and MC simulations*, GERDA Scientific Technical Reports: GSTR-12-015.

[139] N. Becerici-Schmidt, A. Caldwell, B. Majorovits, *Background decomposition around $Q_{\beta\beta}$ for the $^{\mathrm{enr}}Ge$-coax detectors in GERDA Phase-I*, GERDA Scientific Technical Reports: GSTR-13-004 (2013).

[140] GERDA collaboration, N. Becerici-Schmidt, *Background modeling for the GERDA experiment*, AIP Conf. Proc. **1549** (2013) 156–160.

[141] A. Caldwell, D. Kollar, and K. Kroninger, *BAT: The Bayesian Analysis Toolkit*, Comput.Phys.Commun. **180** (2009) 2197–2209.

[142] Bayesian Analysis Toolkit, Measuring a decay rate - tutorial for BAT 0.9 (URL, last access 27.6.2014), `https://www.mppmu.mpg.de/bat/?page=tutorials&version=0.9&name=counting_experiment`.

[143] R. Aggarwal and A. Caldwell, *Error Bars for Distributions of Numbers of Events*, Eur.Phys.J.Plus **127** (2012) 24.

[144] R. B. Firestone, V. S. Shirley, C. M. Baglin, S. F. Chu, and J. Zipkin, *Table of Isotopes*. Wiley & Sons, New York, 8th edition (1996).

[145] G. Meierhofer, P. Grabmayr, L. Canella, P. Kudejova, J. Jolie, et al., *Prompt gamma rays in (77)Ge and (75)Ge after thermal neutron capture*, Eur.Phys.J. **A48** (2012) 20.

[146] L. Pandola, M. Bauer, K. Kroninger, X. Liu, C. Tomei, et al., *Monte Carlo evaluation of the muon-induced background in the GERDA double beta decay experiment*, Nucl.Instrum.Meth. **A570** (2007) 149–158.

[147] D.-M. Mei, S. Elliott, A. Hime, V. Gehman, and K. Kazkaz, *Neutron inelastic scattering processes as a background for double-beta decay experiments*, Phys.Rev. **C77** (2008) 054614.

[148] M. J. Berger, J. S. Coursey, M. A. Zucker, and J. Chang, *Stopping-Power and Range Tables for Electrons, Protons, and Helium Ions*, NIST, Physical Measurement Laboratory (URL, last access 27.06.2014). `http://www.nist.gov/pml/data/star/`.

[149] I. Barabanov, S. Belogurov, L. B. Bezrukov, A. Denisov, V. Kornoukhov, et al., *Cosmogenic activation of germanium and its reduction for low background experiments*, Nucl.Instrum.Meth. **B251** (2006) 115–120, `nucl-ex/0511049`.

[150] GEANT4, S. Agostinelli et al., *GEANT4: A Simulation toolkit*, Nucl.Instrum.Meth. **A506** (2003) 250–303.

[151] O. Ponkratenko, V. Tretyak, and Y. Zdesenko, *Event generator DECAY4 for simulating double-beta processes and decays of radioactive nuclei*, Phys.Atom.Nucl. **63** (2000) 1282–1287.

[152] B. Lehnert, *In print*, Dissertation, TU Dresden.

[153] MAJORANA Collaboration, E. Aguayo et al., *Characteristics of Signals Originating Near the Lithium-Diffused N+ Contact of High Purity Germanium P-Type Point Contact Detectors*, Nucl.Instrum.Meth. **A701** (2013) 176–185.

[154] R. Brugnera et al., *Measurement of the ^{42}Ar contamination in natural argon with GERDA*, GERDA Scientific Technical Reports: GSTR-12-004 (2012).

[155] N. Becerici-Schmidt et al., *Measurement of the half life of the two-neutrino $\beta\beta$ decay with GERDA*, GERDA Scientific Technical Reports: Addendum to GSTR-12-009 (2012), GSTR-12-010.

[156] V. Tretyak and Y. Zdesenko, *Tables of double beta decay data*, Atom.Data Nucl.Data Tabl. **61** (1995) 43–90.

[157] Dörr, C. and Klapdor-Kleingrothaus, H.V., *New Monte-Carlo simulation of the HEIDELBERG-MOSCOW double beta decay experiment*, Nucl.Instrum.Meth. A **513** (2003) 596–621.

[158] K. Amako, S. Guatelli, V. Ivanchenko, M. Maire, B. Mascialino, et al., *Comparison of Geant4 electromagnetic physics models against the NIST reference data*, IEEE Trans.Nucl.Sci. **52** (2005) 910–918.

[159] M. Agostini et al., *Performance of the quality cuts in GERDA Phase-I*, GERDA Scientific Technical Reports: GSTR-13-022 (2013).

[160] A. Bakalyarov, A. Y. Balysh, S. Belyaev, V. Lebedev, and S. Zhukov, *Results of the experiment on investigation of Germanium-76 double beta decay: Experimental data of Heidelberg-Moscow collaboration November 1995 - August 2001*, Phys.Part.Nucl.Lett. **2** (2005) 77–81, `arXiv:hep-ex/0309016`.

[161] A. Vasenko, I. Kirpichnikov, V. Kuznetsov, A. Starostin, A. Dzhanian, et al., *New Results in the ITEP/YePI Double Beta Decay Experiment With Enriched Germanium Detectors*, Mod.Phys.Lett. **A5** (1990) 1299–1306.

[162] H. Miley, R. Brodzinski, J. Reeves, F. Avignone, and J. Collar, *Suggestive evidence for the two neutrino double beta decay of Ge-76*, Phys.Rev.Lett. **65** (1990) 3092–3095.

[163] F. Avignone, C. Guerard, R. Brodzinski, H. Miley, J. Reeves, et al., *Confirmation of the observation of 2 neutrino beta-beta decay of Ge-76*, Phys.Lett. **B256** (1991) 559–561.

[164] F. Avignone, *Double-beta decay: Some recent results and developments*, Prog.Part.Nucl.Phys. **32** (1994) 223–245.

[165] A. Morales, J. Morales, and S. Cebrian, *Proceedings, 30th International Meeting on Fundamental Physics (IMFP 2002)*, Nucl.Phys.Proc.Suppl. **114** (2003) pp.1–308.

[166] B. Pritychenko Proc. Nuclear Structure (East Lansing, MI, 3–6 June 2008).

[167] A. Barabash, *Precise half-life values for two neutrino double beta decay*, Phys.Rev. **C81** (2010) 035501.

[168] A. Caldwell and K. Kröninger, *Signal discovery in sparse spectra: A Bayesian analysis*, Phys. Rev. D **74** (2006) 092003.

[169] J. Hellmig and H. Klapdor-Kleingrothaus, *Identification of single-site events in germanium detectors by digital pulse shape analysis*, Nucl.Instrum.Meth. **A455** (2000) 638–644.

[170] M. Mustonen and J. Engel, *Large-scale calculations of the double-β decay of ^{76}Ge,^{130}Te,^{136}Xe, and ^{150}Nd in the deformed self-consistent Skyrme quasiparticle random-phase approximation*, Phys.Rev. **C87** no. 6, (2013) 064302.

[171] J. Suhonen and O. Civitarese, *Effects of orbital occupancies and spin-orbit partners on $0\nu\beta\beta$-decay rates*, Nucl.Phys. **A847** (2010) 207–232.

[172] A. Meroni, S. Petcov, and F. Simkovic, *Multiple CP Non-conserving Mechanisms of $\beta\beta_{0\nu}$-Decay and Nuclei with Largely Different Nuclear Matrix Elements*, JHEP **1302** (2013) 025.

[173] A. Smolnikov and P. Grabmayr, *Conversion of experimental half-life to effective electron neutrino mass in $0\nu\beta\beta$ decay*, Phys.Rev. **C81** (2010) 028502.

[174] B. Majorovits, *Limitations of next generation neutrinoless double beta-decay germanium experiments*, Habilitation, Technische Universität München, Max-Planck-Institut für Physik, Germany (2011).

Acknowledgements

It is a great moment of realization; I was never left alone throughout this happy but also equally challenging and demanding period. Having reached this page, I want to compliment those who contributed to the realization of this work, if I succeeded in reporting it properly, and thank in any case for helping and being there for me along the way.

I was very lucky to be part of the GERDA+GeDet group of MPP, the members of which made my life during working hours as natural and enjoyable as real life. It was also very fortunate for sure to meet with my postdoc Dimitris here, instead of at some random Physics conference. For the most interesting group dynamics, joyous and teaching coffee breaks, long meetings and friendship, a huge thanks goes to the present and former members: Iris Abt, Béla Majorovits, Hans Seitz, Franz Stelzer, Christopher O'Shaughnessy, Chris Gooch, Dimitris Palioselitis, Laura Vanhoefer, Fabiana Cossavella, Oleksandr Volynets, Heng-Ye Liao, Sabine Irlbeck, Lucia Garbini, Matteo Palermo, Oliver Schulz, Burcin Dönmez, Jian Tang and Xiang Liu.

Many thanks go to Béla Majorovits for his guidance, support and for all he has taught me, although he always said it is his job whenever I thanked him. I happily remember his encouragements that helped me to gain confidence and get more engaged in the analysis, the outcome of which would be not half as meaningful without his contribution. Equally many thanks to Allen Caldwell, who miraculously always found time for teaching and for guiding me throughout this work.

As I promised him one sunny afternoon, while listening to his comments about the last two chapters which had been one chapter before that discussion: "I am grateful for the invaluable comments from Matteo Agostini, which have significantly improved the content of this thesis". I am glad that our friendship has surpassed this constructive knowledge exchange, and luckily without hindering it.

I am very thankful to the BATmen Frederik Beaujean and Daniel Greenwald, who generously spend their time to help me using the Bayesian Analysis Toolkit and contributed to my progress in data analysis.

Thanks to the GERDA members for the fruitful collaboration, for the great GERDA meetings and social dinners with unlimited alcohol and never-ending toast sessions, for the "blinding" procedure and the "unblinding" excitement, and for all the exchange during the last three years. I owe a special thanks to Luciano Pandola, the best analysis coordinator ever, for his constant help in the analysis issues and for his support as a friend when the spirits went down; and to those with whom I got the chance to share more, whether

work-related or not: Peter Grabmayr, Stefan Schönert, Bernhard Schwingenheuer, Andrea Kirsch, Carla Cattadori, Carla Macolino, Björn Lehnert, Nuno Barros, Alex Hegai, Kai Freund, Sabine Hemmer, Giovanni Benato, Katharina von Sturm, Mark Heisel, Michal Tarka, Manuel Walter, Andrea Lazzaro, Tobias Bode, and Dusan Budjáš.

Thanks for the cover page, technical help, editing, correcting, baby-sitting, especially for the support in the unforgettable last week: Max Schmidt, Johanna Bronner, Jonathan Burdalo, Meral Heinik, Jürgen Heinik, Martina Kupser, Thomas Kupser, Ayça Beygo, Chris Gooch, Dimitris Palioselitis, Edith Nerke, Jürgen Bauer, Wolfgang Schmidt and Matteo Agostini.

I am grateful to my families Becericis, Schmidts and Webers, and to all my dear friends for the unconditional support and love.

Final thanks goes to Max. But it is hard to simply tell the reasons, since any specification will be an oversimplification.